Trace elemental and multi-isotopic (δ^{98}Mo, δ^{34}S, δ^{15}N) study of Proterozoic shales: Implications to ocean euxinia and productivity patterns

विद्या वाचस्पति की
उपाधि की अपेक्षाओं की आंशिक पूर्ति में प्रस्तुत शोध प्रबंध

A thesis submitted in partial fulfillment of the requirements of the degree of Doctor of Philosophy

द्वारा
अच्युत वेणुगोपाल
By
Achyuth Venugopal

पंजीकरण सं. / Registration No.: **20193685**

शोध प्रबंध पर्यवेक्षक / Thesis Supervisor:
Dr. Gyana Ranjan Tripathy

भारतीय विज्ञान शिक्षा एवं अनुसंधान संस्थान पुणे
INDIAN INSTITUTE OF SCIENCE EDUCATION AND RESEARCH PUNE
2025

भारतीय विज्ञान शिक्षा एवं अनुसंधान संस्थान पुणे
INDIAN INSTITUTE OF SCIENCE EDUCATION AND RESEARCH PUNE
डॉ. होमी भाभा मार्ग, पुणे 411008, महाराष्ट्र, भारत | Dr. Homi Bhabha Road, Pune 411008, Maharashtra, India
T +91 20 2590 8001 W www.iiserpune.ac.in

IISER PUNE

Certificate

Certified that the work incorporated in the thesis entitled "**Trace elemental and multi-isotopic (δ^{98}Mo, δ^{34}S, δ^{15}N) study of Proterozoic shales: Implications to ocean euxinia and productivity patterns**" submitted by **Mr. Achyuth Venugopal** was carried out by the candidate, under my supervision. The work presented here or any part of it has not been included in any other thesis submitted previously for the award of any degree or diploma from any other University or Institution.

Date: 08/Jan/2025

Place: Pune

Dr. Gyana Ranjan Tripathy

(Supervisor)

भारतीय विज्ञान शिक्षा एवं अनुसंधान संस्थान पुणे
INDIAN INSTITUTE OF SCIENCE EDUCATION AND RESEARCH PUNE
डॉ. होमी भाभा मार्ग, पुणे 411008, महाराष्ट्र, भारत | Dr. Homi Bhabha Road, Pune 411008, Maharashtra, India
T +91 20 2590 8001 W www.iiserpune.ac.in

IISER PUNE

Declaration

Name of Student: **Achyuth Venugopal**

Reg. No.: **20193685**

Thesis Supervisor(s): **Dr. Gyana Ranjan Tripathy**

Department: **Earth and Climate Science**

Date of joining program: **01.08.2019**

Date of Pre-Synopsis Seminar: **22.07.2024**

Title of Thesis: **Trace elemental and multi-isotopic (δ^{98}Mo, δ^{34}S, δ^{15}N) study of Proterozoic shales: Implications to ocean euxinia and productivity patterns**

I declare that this written submission represents my idea in my own words and where others' ideas have been included; I have adequately cited and referenced the original sources. I declare that I have acknowledged collaborative work and discussions wherever such work has been included. I also declare that I have adhered to all principles of academic honesty and integrity and have not misrepresented or fabricated or falsified any idea/data/fact/source in my submission. I understand that violation of the above will be cause for disciplinary action by the Institute and can also evoke penal action from the sources which have thus not been properly cited or from whom proper permission has not been taken when needed. The work reported in this thesis is the original work done by me under the guidance of Dr. Gyana Ranjan Tripathy.

Date: 08.01.2025

Signature of the student

Acknowledgement

I want to extend my sincere gratitude to my supervisor, Dr. Gyana Ranjan Tripathy, for his persistent support and guidance throughout my doctoral work. Your mentorship helped me become a more diligent student and challenged me to strive for high standards. Your dedication and approach towards research have always been a constant motivator. Thank you for allowing me to pursue my research interests and providing helpful advice and suggestions whenever I encountered challenges.

I want to thank my RAC members Dr. Aninda Mazumdar from the National Institute of Oceanography (NIO) Goa, Dr. Arvind Singh from the Physical Research Laboratory (PRL) Ahmedabad, and the members of the PMRF review committee for their critical suggestions and constructive inputs throughout my Ph.D. tenure. I am indebted to Dr. Vineet Goswami for his insightful discussions and invaluable support during my stay at the Physical Research Laboratory, Ahmedabad. Thanks are also due to Mr. Deependra Singh and Mahesh Goud for their aid in all the sample preparation processes and instrumental assistance at PRL.

I thank my collaborators, Dr. B.P. Singh from Banaras Hindu University (BHU), Dr. Tavheed Khan and Dr. Sreenivas Sarma from the National Geophysical Research Institute (NGRI), and Dr. Santosh Kumar Rai and Dr. Sumit. K. Ghosh from Wadia Institute of Himalayan Geology (WIHG) for extending their support in the fieldwork. I also thank Dr. Lukáš Ackerman from the Institute of Geology of the Czech Academy of Sciences, Prague, for providing the Re-Os datasets. Logistical assistance provided by the DGM and Geologists at the Mangampeta Mines and all the other personnel who played a key role in completing my field trips is thankfully acknowledged.

Thanks are due to Dr. Shreyas Managave for his helpful guidance and support during the IRMS analysis. All the faculty members of the Earth and Climate Science Department at IISER Pune are thanked for their input and suggestions. The administrative support and technical assistance provided by Ms. Ruby Soni, Mr. Vikrant Bartakke and Mr. Vibhas Shevde are gratefully acknowledged. I also thank the staff and members of the IISER Pune community for making my stay at IISER Pune pleasant.

I am highly indebted to my seniors, Anirban Mandal, Mohd Danish and Anupam Samanta, for familiarizing me with different wet-chemical procedures and proper handling of various analytical instruments. All your criticisms, concerns and suggestions significantly

helped develop my scientific and analytical capabilities. This work would not have been complete without the support and help offered by my dear colleagues at the GRASP Lab: Rakesh, Kruttika, and Shuvashree. Your friendship and encouragement made every challenge easier to overcome, and I'll miss all the great times we shared. I also thank the present and past members of the GRASP lab for all the stimulating discussions and helpful participation. I also appreciate the good moments shared with Rashi, Venu, Avinash, Shashank, Hardik, Arijeet, Mahi, Sindoora, Visrutha, Dileep, Shreya, Daniel, and many other fellow mates at the ECS Department.

I thank the Ministry of Education, Government of India, and the Council of Scientific and Industrial Research (CSIR) for financially supporting my doctoral work. I also appreciate the additional financial support from the IISER Pune-Trimurti Research Grant. I am grateful to all the taxpayers of our country whose invaluable contributions support and sustain these research and educational infrastructures.

Finally, I thank all my family members for their unwavering support and encouragement.

Abstract

Oxygenation of the ocean-atmosphere system had a profound effect on the origin and evolution of multicellular life on the Earth. Available geological and geochemical studies document significant fluctuations in Proterozoic seawater redox state and biogeochemical cycling, capable of imparting primary control on eukaryotic expansion. However, the exact linkage between environmental changes and the emergence of complex life is not well-established due to temporal gaps. This thesis work presents a detailed geochemical and isotopic study of organic-rich shales from three major Proterozoic sedimentary successions (Cuddapah Supergroup, Vindhyan Supergroup and the Lesser Himalaya) to (a) reconstruct the depositional environment, (b) quantify the areal extent of ocean euxinia, and (c) evaluate the modes of nitrogen cycling in these basins. A multi-proxy approach using redox-sensitive trace elemental abundances (e.g., Mo, U, Mn and Cd), stable isotopic compositions ($\delta^{15}N$, $\delta^{34}S$ and $\delta^{98}Mo$), and Fe-speciation data has been adopted to achieve these objectives.

The ^{187}Re–^{187}Os radiometric dating of organic-rich shales from the Cumbum Formation (Nallamalai Group, Cuddapah Supergroup) have yielded their direct depositional age (1658 ± 50 Ma (2σ, n = 10)). Distributions of multiple redox indices (Mo/TOC, Mo_{EF}/U_{EF} and Cd/Mo) for these shales and their comparison with datasets from modern-day settings indicate a limited productivity regime with restricted basinal settings during the shale deposition. Further, high Fe_{HR}/Fe_T (0.61 ± 0.18) and Fe_{Py}/Fe_{HR} (0.72 ± 0.14) ratios support a fluctuating (euxinic to ferruginous) bottom-water condition in this basin. The $\delta^{98}Mo$ values of these shales (+0.68 ± 0.13‰) and their mass balance modelling (for euxinic shales) suggest a wide extent of ocean euxinia (~5% of seafloor area) at 1.66 Ga, an order of magnitude higher than that observed for modern oceans (0.1% to 0.3%). A similar modelling effort using previously reported $\delta^{98}Mo$ data of euxinic shales from other global sections supports a relatively stable but high (average 5 ± 4%) extent of Proterozoic oceanic euxinia. These evaluations also reveal episodes of intensified oceanic euxinia during the Proterozoic, which often follow the fluctuations in atmospheric oxygen levels.

Shale $\delta^{98}Mo$ data and their mass balance calculations have also been used to quantify the extent of euxinia around the Precambrian-Cambrian (Pc-C) transition. These shales belong to the Tal Formation (Lesser Himalaya), and their Iron speciation and Mo/U data point to anoxic and ferruginous deep water conditions. Calculations involving the $\delta^{98}Mo$ (1.5 ± 0.2‰)

data for these shales estimate ~4 times higher pyrite burial rates and ~2 times extensive extent of sulfidic conditions during the Pc-C transition when compared to that for present-day oceanic conditions. Further, these shales were also characterized by isotopically heavier pyrite-$\delta^{34}S$ values (3.6‰ to 8.3‰) compared to modern-day sedimentary pyrites (~ −21‰). Earlier reported $\delta^{34}S$ values for early Cambrian seawater, measured $\delta^{34}S$ pyrite data and their empirical relationship estimate the seawater sulfate concentration (8 ± 3 mM) during their deposition. This sulfate value for the Tal basin is higher than that reported for the late Neoproterozoic ocean (<5 mM), potentially related to the increasing oxygen availability and continental supply during the Pc-C transition.

Further, the effect of the temporal and spatial redox heterogeneities in the primary productivity was investigated by comparing the nitrogen isotopic compositions of organic-rich shale sequences from these different basins. The (molar) TOC/TN ratios of these shales vary between 12 and 52 and are systematically higher than the Redfield ratio. The $\delta^{15}N$ values for these shales are consistently positive and range from +0.8‰ to +8.6‰. The lack of correlations between $\delta^{15}N$-TN, $\delta^{15}N$-TOC/TN and $\delta^{15}N$-$\delta^{13}C$ suggests a limited role of thermal effects, post-depositional alterations and mobilization processes in affecting the isotopic signals. The bulk nitrogen isotopic composition ($\delta^{15}N_{bulk}$) of the Bijaigarh and Lower Tal shales (~1−2‰) overlap with sedimentary $\delta^{15}N$ values characteristic of environments where N-fixing processes using Mo-nitrogenase are dominant. The highly enriched $\delta^{15}N_{bulk}$ values (>3‰) for the Tadpatri, Kajrahat and Cumbum shales suggest the occurrence of aerobic modes of nitrogen cycling in these basins, where processes such as nitrification, denitrification/*anammox* and ammonium assimilation were active. Further, a steady-state box model using the measured shale $\delta^{15}N$ values establishes the prevalence of nitrate rich-waters and the dominance of nitrate assimilators in most of these sections.

Table of Contents

Title Page……i

Certificate……iii

Declaration……v

Acknowledgement……vii

Abstract……ix

Table of Contents……xi

List of Tables……xiv

List of Figures……xvii

Chapter 1 – Introduction 1

1.1. Introduction 3

1.2. Aims and Objectives 9

1.3. Structure of the thesis 9

Chapter 2 – Materials and Methods 11

2.1. Geological setting 14

2.1.1. Cuddapah Basin 14

2.1.1.1. The Cuddapah Supergroup 15

2.1.1.2. The Kurnool Group 17

2.1.1.3. The Nallamalai Fold Belt 17

2.1.2. Vindhyan Basin 18

2.1.2.1. Lower Vindhyans 18

2.1.2.2. Upper Vindhyans 20

2.1.3. Lesser Himalaya 22

2.1.3.1. Inner Lesser Himalaya 24

2.1.3.2. Outer Lesser Himalaya 24

2.2. Sampling 26
2.2.1. Cuddapah Basin 26
2.2.2. Vindhyan Basin 26
2.2.3. Lesser Himalaya 29
2.3. Analytical methods 30
2.3.1. Sampling protocol 30
2.3.2. Geochemical analyses 30
2.3.3. Isotopic analyses 41
Chapter 3 – Extent of ocean euxinia during the late Paleoproterozoic: Constraints from Re–Os and Mo isotopes 47
3.1. Results 49
3.2. Discussion 56
3.2.1. Re–Os geochronology of Cumbum shales 56
3.2.2. Basinal redox state and hydrography 57
3.2.3. Areal extent of ocean euxinia at 1.66 Ga 61
3.2.4. Proterozoic ocean euxinia and its implication for biological stasis 65
3.3. Conclusions 67
Chapter 4 – Oceanic redox state during the early Cambrian: Insights from Mo-S isotopes and geochemistry of Himalayan Shales 69
4.1. Results 71
4.2. Discussion 77
4.2.1. Redox setting of the Tal basin: Chemical and isotopic constraints 79
4.2.1.1 Trace elements and Iron speciation data 79
4.2.1.2. Molybdenum isotopic constraints 84
4.2.2 Sulfur cycling during the Pc-C transition 88
4.2.3 Ocean biogeochemical cycle of the Tal basin during the Pc-C transition 89
4.3. Conclusions 91

Chapter 5 – Proterozoic Nitrogen cycling in the shallow water environments: An isotopic and modelling perspective from Indian shales 93

5.1. The Modern Nitrogen Cycle 95

5.2. Results 97

5.3. Discussion 106

5.3.1. Evaluating post-depositional and metamorphic effects 106

5.3.2. Possible Modes of Nitrogen cycling during the Proterozoic 109

5.3.2.1. Aerobic Nitrogen cycling 109

5.3.2.2. Anaerobic cycling 110

5.3.3. Effect of redox conditions on primary productivity 111

5.4. Conclusions 115

Chapter 6 – Summary and Future Perspectives 117

6.1. Summary 119

6.2. Future Perspectives 121

References 123

Appendix 161

A5.1. Nitrogen isotopic Model details 171

List of Publications 177

List of Tables

Table 2.1. General stratigraphy of Cuddapah Basin (after Nagaraja Rao et al., 1987) along with the major lithology and environment of deposition (Valdiya, 2015)……**16**

Table 2.2. Generalized stratigraphy of the Vindhyan Supergroup (after Sastry and Moitra, 1984) along with the major lithology and depositional environment (Sarkar and Banerjee, 2020)……..……**21**

Table 2.3. Generalized stratigraphic details of Neoproterozoic-Cambrian succession of outer Lesser Himalaya (after Ghosh et al., 2016; Hughes, 2016)……**23**

Table 2.4. Typical operating parameters and settings of Q-ICPMS instrument during trace element analyses……**33**

Table 2.5. Comparison of measured and reported trace elemental composition of USGS certified reference materials BHVO-2 and SGR-1b……..**34**

Table 2.6. Comparison of trace elemental data for replicate samples.……...**35**

Table 2.7. REE concentration data of replicate digestion aliquots……**36**

Table 2.8. Overview of the iron extraction protocol followed in this study (after Poulton and Canfield, 2005)……..**38**

Table 2.9. Comparison of measured and reported iron speciation dataset of reference material WHIT……**40**

Table 2.10. Replicate analyses of bulk Nitrogen ($\delta^{15}N_{bulk}$), organic carbon ($\delta^{13}C_{org}$) and pyrite-S ($\delta^{34}S_{Py}$) isotopic data.....**43**

Table 2.11. Molybdenum purification scheme adopted in this study (after Pearce et al., 2009)..……..……..……..**44**

Table 2.12. Results of replicate δ^{98}Mo measurements of sample aliquots……**45**

Table 2.13. Total analytical blank for Mo isotopic measurements……**45**

Table 2.14. δ^{98}Mo values for USGS reference material SDO-1 measured during this study……...…….…..……**46**

Table 3.1. Elemental, iron-speciation, and Mo isotopic data for black shales from the Cumbum Formation, Cuddapah Supergroup (India)……**54**

Table 3.2. Re and Os concentrations, and isotopic data for the black shales from the Cumbum Formation……..**55**

Table 4.1. Elemental and sulfur (δ^{34}S) isotopic data for black shale samples from the (lower) Tal Formation, Lesser Himalaya. For comparison, these data for a Neoproterozoic shale sequence (Chandpur Formation) from Lesser Himalaya have also been included……**72**

Table 4.2. Iron speciation data for studied samples from the (lower) Tal Formation and Chandpur Formation, Lesser Himalaya…….……**73**

Table 4.3. Mo elemental and isotopic (δ^{98}Mo) data for the Tal shales along with the estimated Mo flux fractions (f_{oxic}, f_{interm}, f_{eux}) and areal extent (A_{oxic}, A_{interm}, A_{eux}) for oxic, intermediate, and euxinic sinks……...……**77**

Table 5.1. Elemental and isotopic data for shale samples from selected sedimentary successions of India ……....…….**99**

Appendix

Table A3.1. Additional geochemical data for the Cumbum shales……**163**

Table A3.2. Input parameters used for the Mo isotopic modelling……..…**164**

Table A3.3. Summary of the δ^{98}Mo compilation data for shales deposited in euxinic settings.....**165**

Table A3.4. Estimated areal extent of ocean redox state for the Proterozoic Eon. These model results are based on present and literature-available δ^{98}Mo data for shales deposited in euxinic settings…….……..……**166**

Table A4.1. Additional geochemical data for black shale samples from the (lower) Tal Formation and Neoproterozoic shale sequence (Chandpur Formation) from Lesser Himalaya…….**168**

Table A4.2. REE concentration data for black shale samples from the (lower) Tal Formation and the Neoproterozoic shale sequence (Chandpur Formation) from Lesser Himalaya…….**169**

Table A4.3. Results from Principal Component Analysis (PCA) of the geochemical data for the black shales from the Tal Formation…….……**170**

Table A5.1. Model parameters used for the box model calculations..... **174**

List of Figures

Figure 1.1. Compilation of trends in various biological, geological and geochemical factors since the Archean Eon; these trends include **(a)** major glaciations, snowball Earth episodes (Hoffman et al., 2017) and time intervals of Supercontinent assembly (Hawkesworth et al., 2009) **(b)** atmospheric oxygenation (Kendall and Ostrander, 2024) **(c)** temporal variations in seawater redox structure (Lowenstein et al., 2013) and trace element inventories (after Robbins et al., 2016 and references therein) **(d)** changes in biovolume (Payne et al., 2009) along with Iron Formation abundance and mode of deposition (Bekker et al., 2010) **(e)** sulfur mass fractionations (after Uveges et al., 2023) and **(f)** organic and carbonate carbon isotopic compositions (after Krissansen-Totton et al., 2015)……**4**

Figure 2.1. Spatial distribution of major Archean Cratons and Proterozoic Basins of India (modified after Deb and Paul, 2015). The red boxes denote the targeted sedimentary basins……..……**13**

Figure 2.2. Simplified geological map of the Cuddapah Basin (modified after Nagaraja Rao et al., 1987; Bhukosh-Geological Survey of India)……**14**

Figure 2.3. Geological Map of the Vindhyan Basin (after Soni et al., 1987; Bhukosh-Geological Survey of India)……..……**19**

Figure 2.4. Simplified geological map of the Lesser Himalaya showing the distribution of Proterozoic sedimentary successions in the Outer Lesser Himalaya (OLH) and Inner Lesser Himalaya (ILH) (modified after Rai and Singh, 1983; Ghosh et al., 2016). ……**22**

Figure 2.5. Generalized stratigraphy of the Cuddapah Basin (modified after Nagaraja Rao et al., 1987; Ramakrishnan and Vaidyanathan, 2008). Geochronological data are from (1) Wabo et al., 2022; (2) Collins et al., 2015; (3) Mukherjee et al., 2023; (4) Chalapathi Rao et al., 1999; (5) Chalapathi Rao et al., 1996; (6) Khelen et al., 2020; (7) Sheppard et al., 2017; (8) Bhaskar Rao et al., 1995; (9) French et al., 2008; (10) Anand et al., 2003; (11) Murthy et al., 1987; (12) Rai et al., 2015; (13) Absar et al., 2016; (14) Sesha Sai et al., 2016; (15) Jayananda et al., 2013)……..……**27**

Figure 2.6. Generalized stratigraphy of the Vindhyan Basin at Son Valley (after Sastry and Moitra, 1984). Geochronological data are from (1) Malone et al., 2008; (2) Gopalan et al., 2013;

(3) Ray et al., 2003; (4) Colleps et al., 2021; (5) Tripathy and Singh, 2015; (6) Sarangi et al., 2004; (7) Bengston et al., 2009; (8) Rasmussen et al., 2002; (9) Lan et al., 2021; (10) Ray et al., 2002; (11) Bickford et al., 2017; (12) Mishra et al., 2018; (13) Mondal et al., 2002……**28**

Figure 2.7. Generalized stratigraphic details of Neoproterozoic-Cambrian succession of the outer Lesser Himalaya (after Ghosh et al., 2016; Hughes, 2016). Age information from Richards et al. (2005) and Etienne et al. (2011)……**29**

Figure 2.8. Flowchart depicting the analytical methods followed in this study……**31**

Figure 2.9. Comparison of measured and reported major oxide values for USGS-certified reference materials **(a)** BCR-2 and **(b)** BHVO-2. The dotted diagonal line represents the 1:1 line……**32**

Figure 2.10. Flow chart illustrating the iron speciation methodology followed in this study (after Poulton and Canfield, 2005)……**38**

Figure 2.11. Schematics of **(a)** Chromic to chromous chloride conversion and **(b)** the experimental setup for pyrite extraction (after Canfield et al., 1986)……**40**

Figure 2.12. Measured bulk **(a)** nitrogen and **(b)** carbon isotopic data for USGS SGR-1b. The grey-shaded region represents the 2σ interval……**42**

Figure. 3.1. Variation of selected geochemical parameters of the Cumbum shales collected in a stratigraphic order (n = 16). For reference, average values of Al in the UCC (Rudnick and Gao, 2003), modern aqueous seawater Mo/U (Algeo and Tribovillard, 2009), Fe-speciation thresholds (Raiswell et al., 2018), Cd/Mo values of modern restricted and upwelling settings (Sweere et al., 2016), and average δ^{98}Mo for Paleoproterozoic shales (Qin et al., 2022) are shown……**50**

Figure 3.2. Enrichment factors (X_{EF}) for selected major and trace elements of the Cumbum shales. The red dashed line indicates an enrichment factor of 1……**51**

Figure 3.3. Re–Os isochron of black shales from the Cumbum Formation, Nallamalai Group, Cuddapah Supergroup using **(a)** the entire sample set (n = 10), and **(b)** subset of samples (n = 4) from a stratigraphic depth of ~3 m. The sample subset yields a precise Model 1 age for the shales.……**52**

Figure 3.4. Frequency distribution of the δ^{98}Mo values for the Cumbum shales. The global δ^{98}Mo distribution for Paleoproterozoic shales is also shown (Qin et al., 2022 and references therein) for comparison. Expected isotopic fractionation factors for removal pathways and ranges of δ^{98}Mo for modern sedimentary deposits from different depositional settings are provided (Dahl et al., 2021 and references therein)……**53**

Figure 3.5. (a) Co-variation of Mo_{EF} and U_{EF} for the Cumbum shales. The data are compared with the Mo/U ratios for modern seawater (SW) and its multiples (0.3 and 3; Tribovillard et al., 2012). **(b)** Frequency distribution of Cd/Mo ratio for the Cumbum shales. The vertical lines represent expected ratios for different modern upwelling and restricted settings (Sweere et al., 2016)……..……**58**

Figure 3.6 (a) Comparison of black shale [Mo] and [TOC] concentrations with average Mo/TOC ($\times10^{-4}$) ratios for modern anoxic silled basins with different deep-water renewal times (τ) (Algeo and Lyons, 2006). **(b)** Relative abundances of highly reactive and pyritic (Fe_{HR}/Fe_T and Fe_{Py}/Fe_{HR}) iron phases in the Cumbum shale compared with that expected for different redox states (Raiswell et al., 2018). The symbol size here represents the S/Mn ratio of the sample. Note that samples falling in the euxinic regions also show systematically higher S/Mn ratios than those for ferruginous deposition……...……**60**

Figure 3.7. Sensitivity test for modern seafloor areal extent using a Mo isotopic model for known $\Delta^{98}Mo_{oxic}$ (−3.0‰ to −2.8‰), $\Delta^{98}Mo_{eux}$ (−0.8‰ to 0‰), and euxinic shale (δ^{98}Mo ~1.8‰; Kendal et al., 2017) compositions. These modelled results converge to observed values for $\Delta^{98}Mo_{interm}$ ranging between −1.0‰ and −0.9‰…….……**63**

Figure 3.8. Estimated ranges for oxygenated, intermediate and euxinic seafloor extent at ~1.66 Ga. The solid lines represent possible combinations of areal extent for a given seawater δ^{98}Mo value……..**64**

Figure 3.9. Compilation of **(a)** global biogeochemical changes, **(b)** black shale Mo/TOC ratios (Farrell et al., 2021) and **(c)** sedimentary δ^{98}Mo values with the estimated euxinic seafloor extents from Paleoproterozoic through early Cambrian (500 Ma). Data for the shale δ^{98}Mo taken from Qin et al. (2022), with new data added from Scheller et al. (2018), Tan et al. (2021), and Pan et al. (2021). For reference, literature data for major biospheric innovations (Lyons et al., 2021), atmospheric oxygen levels (Lyons et al., 2024), periods of supercontinents assembly

(Campbell and Allen, 2008), and modern seawater δ^{98}Mo (Nägler et al., 2014) are also shown.....**66**

Figure 4.1. UCC-normalized **(a)** elemental ratios and **(b and c)** enrichment factors of selected trace elements (Rudnick and Gao, 2003) for Pc-C (Tal Fm) and Neoproterozoic (Chandpur Fm) shales. Red dashed lines represent an enrichment factor of 1……**74**

Figure 4.2. Frequency distribution of δ^{98}Mo isotopes of the Pc-C shales from the Himalaya. For reference, the global Mo isotopic data for early Cambrian (550 – 530 Ma; Farrell et al., 2021) are also shown. Expected isotopic fractionation factors for molybdenum isotopes (Poulson et al., 2006) in sedimentary systems are also depicted……**75**

Figure 4.3. Frequency distribution of pyrite δ^{34}S of the Pc-C shales from the Himalaya. For reference, the global pyrite S isotopic data for early Cambrian (550 – 530 Ma; Farrell et al., 2021) are also shown. Expected isotopic fractionation factors for sulfur (Lyons et al., 2009) in sedimentary systems are also depicted……...……**76**

Figure 4.4. Compiled chemo-stratigraphic data for shale sequences from the Lower Tal Formation (Data source: present study, Banerjee et al. (1997) and Liu et al. (2021)). Red dashed lines represent average UCC values (Rudnick and Gao, 2003)……**78**

Figure 4.5. Factor loadings for four major factors extracted from the principle component analysis of the geochemical dataset……...……**81**

Figure 4.6. Co-variation plots of **(a)** Mo_{EF}–U_{EF} and **(b)** Iron speciation (Fe_{HR}/Fe_T and Fe_{Py}/Fe_{HR}) parameters for Pc-C (Tal Fm) and Neoproterozoic (Chandpur Fm) shales. For comparison, modern seawater Mo/U molar ratio (solid line) and compiled Fe-speciation data (Grey circle) for early Cambrian (550 – 530 Ma; Farrell et al., 2021) shales are also shown……**83**

Figure 4.7. Ternary diagrams of estimated **(a)** Mo removal fluxes and **(b)** seafloor areal extents of oxic, intermediate, and euxinic sinks (based on burial rates from Scott et al., 2008; Asael et al., 2018). Solid lines in the diagrams represent calculated values for different seawater δ^{98}Mo values, whereas the (red-coloured) dashed lines depict calculation for modern seawater δ^{98}Mo (+2.34‰) value……**87**

Figure 4.8. (a) Estimation of seawater [SO_4^{2-}] for the Tal Basin using $\Delta^{34}S_{sulfate\text{-}sulfide}$ values using the MSR trend method (Algeo et al., 2015). Compiled data (grey circles) for modern aqueous systems and seawater sulfate concentration are also shown (Algeo et al., 2015). **(b)** Comparison of our estimated sulfate concentrations with compiled seawater sulfate data from other synchronous global sections and estimates (Horita et al., 2002; Lowenstein et al., 2003; Brennan et al., 2004; Ries et al., 2009; Canfield and Farquhar, 2009; Loyd et al., 2012; Wotte et al., 2012; Algeo et al., 2015; Wu et al., 2015; Zhu et al., 2021; Li et al., 2023)…….**90**

Figure 5.1. Simplified illustration of the modern marine nitrogen cycle showing the different transformation pathways and associated isotopic fractionation ($\varepsilon \approx \delta^{15}N_{reactant} - \delta^{15}N_{product}$) between various nitrogen species (after Stüeken et al., 2024 and references therein). Blue and orange pathways mark oxic and suboxic-anoxic processes (Stüeken et al., 2016)…….……**96**

Figure 5.2. Cross plots between TN, TOC and TP. The expected Redfield ratio associated with normal phytoplankton biomass is also shown for comparison ……**98**

Figure 5.3. Molar ratio of total organic carbon (TOC) and total phosphorus (TP) in the studied sections. Median values observed for different modern marine environments (after Algeo and Ingall, 2007) are also depicted……..……..**103**

Figure 5.4. Crossplots between **(a)** Mo_{EF} and U_{EF} **(b)** Fe-speciation parameters. Dashed lines in (a) represent the 0.3×, 1× and 3× seawater Mo/U molar ratio……..…….**104**

Figure 5.5. Histogram plot showing the $\delta^{15}N_{bulk}$ distribution of the studied samples along with the global data reported from other (a) Paleoproterozoic, (b) Mesoproterozoic and (c) Pc-C boundary (550−530 Ma) sections (after Stüeken et al., 2024). Additional available data for the Bijaiagarh shales (Gilleaudeau et al., 2020) are also included. The typical range of sedimentary $\delta^{15}N$ values associated with N-fixation-dominated ecosystems (Stüeken et al., 2024) and the average value of modern marine sediments (~6.6‰; Tesdal et al., 2013) are also shown.……..……**105**

Figure 5.6. Cross plots showing relations between **(a)** TN and TOC, **(b)** $\delta^{15}N_{bulk}$ and TN, **(c)** $\delta^{15}N_{bulk}$ and TOC/TN, and **(d)** $\delta^{15}N_{bulk}$ and $\delta^{13}C_{org}$. The black arrows depict expected trends resulting from alteration. The grey-shaded region denotes the typical $\delta^{15}N_{bulk}$ values associated with N-fixation (Zhang et al., 2014)……**107**

Figure 5.7. Variation of modelled bulk-rock sedimentary $\delta^{15}N$ values as a function of **(a)** water-column anoxia and **(b)** the contribution of nitrogen assimilators ($f_{assimilators}$) to the sedimentary nitrogen pool. The black solid line represents mean values, and the grey shaded regions represent the 2σ range of the modelled result. The f_{an_sub} and $f_{assimilators}$ ranges depicted for the modern-day ocean are based on the results of the Monte Carlo simulation under modern-day parametrization (Table A5.1)……..……**113**

Figure A5.1. Box model framework of the marine nitrogen cycle (after Kipp et al., 2018)…….……..…….……...……...……**171**

Figure A5.2. Frequency distribution showing the results of the Monte Carlo simulation under modern-day parametrization. The red dashed line depicts the average value of this population……....**175**

Chapter 1

Introduction

1.1. Introduction

The Proterozoic Eon (2500 to 539 Ma) represents a transitional phase of our Earth, separating the biologically primitive low-oxygen Archean conditions from the complex multicellular and well-oxygenated Phanerozoic Eon. This change in the habitability of the Earth has been widely attributed to the progressive oxygenation of the atmosphere, which broadly occurred in two steps near the beginning (the Great Oxidation Event (GOE); ~2.4 to 2.1 Ga; Holland, 2002) and the end (the Neoproterozoic Oxygenation Event (NOE); 0.8 to 0.5 Ga; Och and Shields-Zhou, 2012) of the Proterozoic Eon. The GOE marked the permanent rise in atmospheric oxygen contents to $>10^{-5}$ present atmospheric levels (PAL), after which the ocean-atmospheric system transitioned into one characterized by a stratified ocean structure and low atmospheric oxygen levels (Fig. 1.1; Lowenstein et al., 2013; Lyons et al., 2014; Lyons et al., 2024). The GOE was followed by a complex period marked by oxygen level fluctuations in the atmosphere and oceans (Wang et al., 2022; Kendall and Ostrander, 2024). This post-GOE period, often termed the "boring billion" (~1.8 Ga to 0.8 Ga; Buick et al., 1995; Holland, 2006), has been of considerable interest due to its dynamic oxygenation history, which fundamentally influenced the cycling of redox-dependent elements on the land and in the oceans (Lyons et al., 2021; Kendall and Ostrander, 2024). This period witnessed a growth in the oceanic inventories of phosphorus and many redox-sensitive trace elements associated with higher oxidative weathering and riverine supply into the oceans (Scott et al., 2008; Robbins et al., 2016; Reinhard et al., 2017). However, fluctuations in the oceanic redox state regulated the bioavailability of elements in the oceans and are considered to have influenced primary productivity in the marine ecosystems, with a possible control on biological evolutionary pathways (Javaux et al., 2001; Frausto da Silva and Williams, 2001; Anbar and Knoll, 2002). While available studies indicate an origin of life by ~3.5 Ga (Hofmann et al., 1999; Allwood et al., 2006), the emergence of complex life forms occurred much later with the appearance of eukaryotic life by ~1.6 Ga (Pang et al., 2015; Agić; 2021), and complex multicellular life by ~0.8 Ga (Knoll and Carroll, 1999; Zhu et al., 2006; Love et al., 2009; Erwin et al., 2011). Although still debated, low oxygen contents and associated nutrient delivery have been invoked as prime environmental drivers that led to this evolutionary stasis of the early eukaryotes and their protracted diversification (Sperling et al., 2013; Javaux and Lepot, 2018; Cole et al., 2020; Lyons et al., 2021; Mills et al., 2024). Assessing the exact role oxygen played in the advent of biological expansion thus requires a more robust understanding of the stability and distribution of oxygen contents in oceanic systems during this interval.

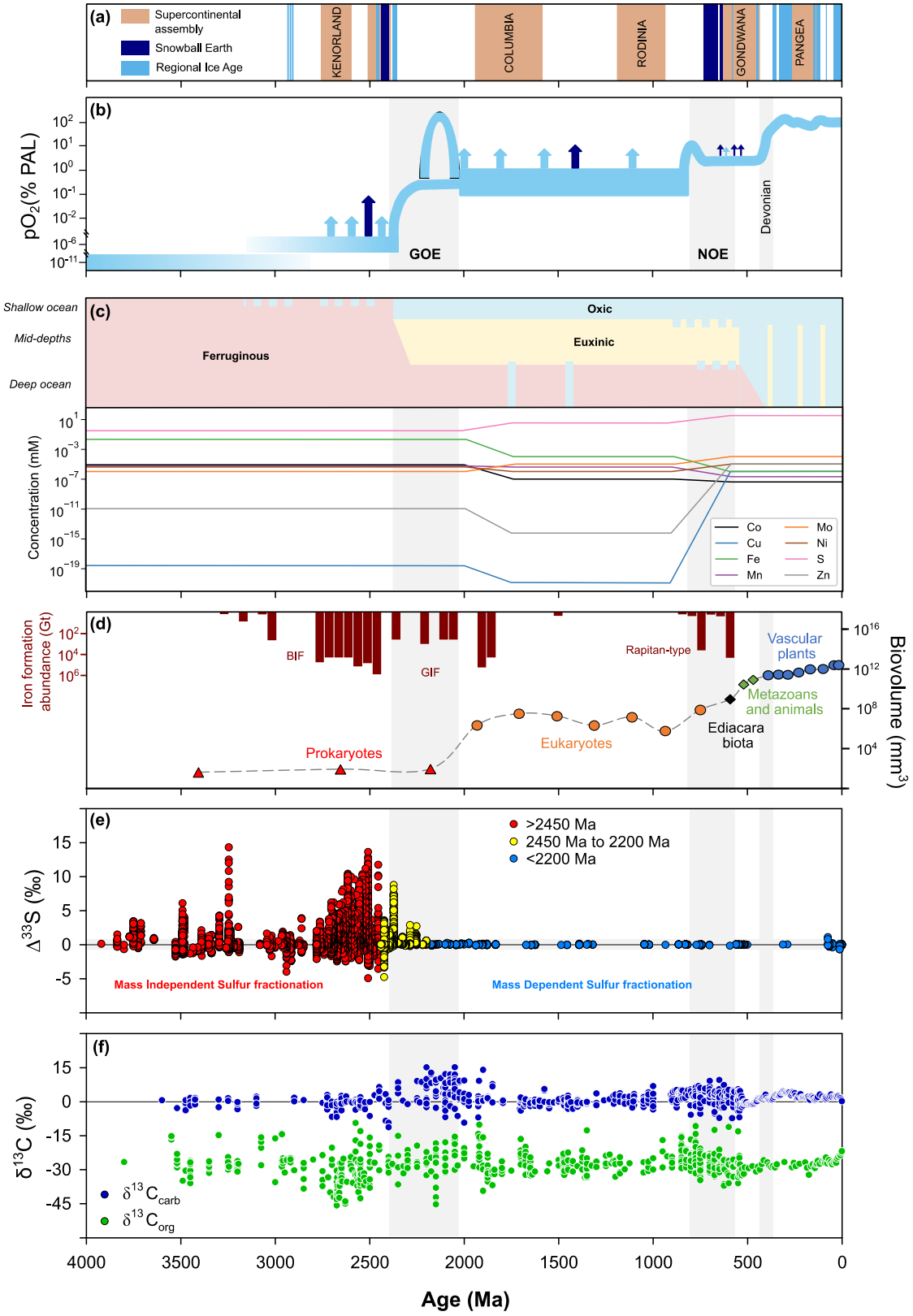

Figure 1.1. *Compilation of trends in various biological, geological and geochemical factors since the Archean Eon; these trends include* ***(a)*** *major glaciations, snowball Earth episodes (Hoffman et al., 2017) and time intervals of Supercontinent assembly (Hawkesworth et al., 2009)* ***(b)*** *atmospheric oxygenation (Kendall and Ostrander, 2024)* ***(c)*** *temporal variations in seawater redox structure (Lowenstein et al., 2013) and trace element inventories (after Robbins et al., 2016 and references therein)* ***(d)*** *changes in biovolume (Payne et al., 2009) along with Iron Formation abundance and mode of deposition (Bekker et al., 2010)* ***(e)*** *sulfur mass fractionations (after Uveges et al., 2023) and* ***(f)*** *organic and carbonate carbon isotopic compositions (after Krissansen-Totton et al., 2015).*

Although the oxygenation history of the atmosphere is broadly constrained, the evolution of the redox state of the oceans is still unclear. The Proterozoic oceans were initially considered to be pervasively oxygenated by ~1.85 Ga based on the disappearance of Banded Iron Formations (BIFs) in the rock record (Cloud, 1973; Holland, 1984). However, Canfield (1998) linked the BIF disappearance to transitioning from a Fe-rich (ferruginous) to a euxinic deep-water ocean. This 'Canfield Ocean' model received support from several proxies, such as C-S-Fe systematics (Poulton et al., 2004), molybdenum isotope relationships (Arnold et al., 2004), and biomarker studies (Brocks et al., 2005). Further studies proposed ferruginous conditions in subsurface waters during the Mesoproterozoic, with euxinia restricted only to productive margins (e.g., Poulton et al., 2010). The current understanding is that the Proterozoic oceans were stratified, where oxic surface layers overlaid ferruginous layers in deeper oceans and euxinic layers in shallow productive continental margins of high organic matter production and epicontinental seas (Poulton et al., 2004; Poulton et al., 2010; Poulton and Canfield, 2011; Planavsky et al., 2011; Lyons et al., 2014; Li et al., 2020).

Recent studies provide increasing evidence for a more dynamic Proterozoic ocean-atmospheric redox state and identify the occurrence of transient oxygenation events. Combined Mo and Tl isotopic studies reveal the presence of oxygenated continental shelves at ~2.5 Ga (Ostrander et al., 2019). Multi-sulfur isotopic signatures from Paleoproterozoic black shales indicate a rapid rise in seawater sulfate reservoir at ~2.3 Ga and its subsequent contraction at ~2.05 Ga (Scott et al., 2014). The ~1.7 Ga ironstones from the North China Craton show highly fractionated chromium and unfractionated iron isotopes, suggesting shallow water oxygenation (Qiu et al., 2022). Sulfur isotopic composition of Carbonate-Associated Sulfur ($\delta^{34}S_{CAS}$) and Ce anomalies from ~1.6 Ga carbonates point towards pulses of seawater oxygenation in the early Mesoproterozoic (Ma et al., 2023). Rare earth element compositions, I/(Ca+Mg) ratios and paired carbon isotopes reveal the occurrence of redox stratification and deep water oxygenation at ~1.64 Ga, ~1.56 Ga and ~1.4 Ga (Zhang et al., 2018; Shang et al., 2019; Wei et al., 2021; Yang et al., 2024). Modelling studies using Fe^{3+} content of ophiolites have estimated O_2 concentrations for Proterozoic deep oceans to be about an order of magnitude lower than the modern day (Stopler and Keller, 2018).

Towards the end of the Proterozoic Eon, coinciding with the second significant rise in atmospheric oxygen levels, there were drastic changes in the marine system characterized by significant heterogeneity in redox state at global and regional scales. Multi-proxy trace

elemental, iron speciation and Mo-U isotopic datasets suggest a transition from euxinic deep waters during the Ediacaran-Cambrian transition to oxygenated oceans towards Cambrian Stage 4 (Wille et al., 2008; Wang et al., 2012; Chen et al., 2015). The Ediacaran-Cambrian sections from China (Li et al., 2009), Oman (Amthor et al., 2003), Mongolia (Brasier et al., 1996), Namibia (Grotzinger et al., 1995), and India (Aharon et al., 1987; Banerjee et al., 1997) document a global negative $\delta^{13}C$ excursion (magnitude 5 – 10‰) in carbonates, signifying a change in carbon cycling and seawater chemistry during this time span. Occurrence of widespread chert and phosphate deposits (Cook and Shergold, 1984), extreme enrichments of redox-sensitive trace elements (e.g., Ni, Mo, V, Cr and Zn; Wille et al., 2008; Pi et al., 2013), and an increase in marine strontium isotopic ratios (Shields, 2007) point to elevated continental influx and a reducing/anoxic oceanic condition during this interval.

Available isotopic records of sulfur (Wang et al., 2012; Feng et al., 2014; Jin et al., 2016; Sahoo et al., 2016; He et al., 2019) and selenium (Wen et al., 2014; Pogge von Strandmann et al., 2015) provide support for pulsed oxygenation of Precambrian-Cambrian (Pc-C) oceans, with regional anoxic conditions and shallower chemoclines in the continental margins. The Mo isotopic signatures of organic-rich shales show near-modern seawater $\delta^{98}Mo$ (up to ~ +2.1‰) values during the Pc-C transition (Wen et al., 2011). Variations in $\delta^{98}Mo$ across the Pc-C boundary in different global sections indicate transitions from a redox-stratified (oxic shallow and anoxic deep water) to an oxic ocean (Wille et al., 2008; Wen et al., 2011; 2014; Xu et al., 2012; Chen et al., 2015; Kendall et al., 2015; Yin et al., 2018). Consistently, sulfur isotopic studies of pyrites and carbonate-associated sulfur have also documented a fluctuating seawater sulfate reservoir with variable sulfate concentrations (<2 to 10 mM) across the Pc-C transition (Loyd et al., 2012; Feng et al., 2014; Algeo et al., 2015; Jin et al., 2016; Li et al., 2023). All these studies suggest a dynamic ocean-atmospheric oxygenation history during the Proterozoic, interspersed with transient peaks and oxygenation episodes.

Attempts to quantify the changing redox conditions in the Proterozoic oceans use the abundance and isotopic compositions of redox-sensitive trace elements to model the global extent of oxic, anoxic or euxinic seafloors. The enrichment of Mo and Cr in sedimentary deposits estimates the extent of ocean anoxia (~40%) and euxinia (~1–10%) for the mid-Proterozoic period (Reinhard et al., 2013). A similar mass balance modelling using Re enrichment in organic-rich mud rocks indicates extensive seafloor anoxia during this time frame (Sheen et al., 2018). Uranium isotopic modelling using data from carbonates spanning the same

interval suggests that <7% of global seafloor was euxinic (Gilleaudeau et al., 2019). A statistical analysis of Fe-speciation data from shale records between ~2.3 Ga and ~1 Ga shows that more than half of the shale deposition occurred under anoxic oceanic conditions (Sperling et al., 2015). Independent estimates using Mo and Tl isotope modelling suggest global seafloor euxinia of <9.6% at ~1.6 Ga (Xu et al., 2023), 1–10% at ~1.56 Ga (Luo et al., 2021) and <4% at ~1.36 Ga (Li et al., 2021). While providing significant insights on the broader spatio-temporal evolution of the Proterozoic oceans, such efforts require more additions to understand the short-term fluctuations punctuating this interval.

The bioavailability of nitrogen, due to its redox-dependent transformations in marine systems, has also been of considerable interest. Temporal changes in nitrate availability have been investigated using the bulk and kerogen nitrogen isotopic signatures of various sedimentary lithologies. Nitrogen isotopic signatures from different Paleoproterozoic sections largely support the presence of stable nitrate-rich surface waters (Kipp et al., 2018; Zerkle et al., 2017; Luo et al., 2018; Cheng et al., 2019; Motomura et al., 2024). In contrast, regional variations with enriched $\delta^{15}N$ values (up to 32‰) also suggest N-limited conditions and the occurrence of ammonium assimilation (Papineau et al., 2009). Studies evaluating shore-to-basinal transects have suggested spatial gradients in nitrogen cycling during the Mesoproterozoic, which were controlled by contraction in oxygenated surface waters (Godfrey et al., 2013; Stüeken, 2013). In these sections, aerobic modes of nitrogen cycling, involving direct nitrate assimilation or assimilation of upwelled ammonium, occurred close to shore. In contrast, the offshore regions in such basins exhibit $\delta^{15}N$ values related to nitrate limitations, which were compensated by N-fixation processes. Compilation of sedimentary $\delta^{15}N$ has shown a stepwise enrichment in sedimentary $\delta^{15}N$ values during late Paleoproterozoic and early Neoproterozoic (Kipp et al., 2018; Kang et al., 2023), where the initial rise was attributed to the post-GOE expansion of oxygenated water (Kipp et al., 2018). The later rise in sedimentary $\delta^{15}N$ at ~800 Ma has been attributed to a ~50% increase in marine nitrate availability and eukaryotic contribution in the aquatic ecosystem (Kang et al., 2023). Further, high-resolution nitrogen isotopic datasets for the Ediacaran-Cambrian transition provide strong evidence for the coupling between sporadic oxygenation episodes and evolutionary events (Wang et al., 2018).

Limited studies from the Proterozoic Basins of India have attempted to understand Proterozoic ocean chemistry and productivity patterns (Chakraborty et al., 2020; Sharma and Chakraborty, 2024). Redox-sensitive elemental enrichments and Ce-anomaly in carbonates

from the Bastar Craton suggest the prevalence of anoxic surface water in their depositional basin at ~2.0 Ga. Banerjee (1985), based on the presence of phosphatic laminae and beds in the late Paleoproterozoic to early Mesoproterozoic strata of the Vindhyan, Cuddapah, and Chhattisgarh Basins, proposed a relatively oxygenated/suboxic shallow marine condition in these basins. Sulfur isotopic data from pyrites in these basins support the existence of a global Mesoproterozoic sulfidic deep ocean (Sarkar et al., 2010). Mitra et al. (2018) suggest a broadly oxic depositional environment for the ~1.8 Ga Tadpatri shales based on U/Th, Cu/Zn, Ni/Co and V/Cr ratios. A suboxic condition for the Gwalior Sea at ~1.7 Ga was suggested by Paul (2017) based on rare earth element (REE) patterns of the BIFs from the Morar Formation, Gwalior Group. The occurrence of euxinic depositional environment has been inferred based on the geochemical investigation of carbonaceous phyllites from the Cuddapah Basin (Sindhuja et al., 2022). Trace elemental and isotopic studies of the argillaceous sections of the Vindhyan Basin suggest euxinic depositional environments for the Arangi, Rampur and Bijaigarh shales and suboxic to anoxic environments during the Sirbu, Koldaha and Rewa shale depositions (Singh et al., 2018; Ansari et al., 2023). Sedimentary pyrite texture and heavy sulfur isotopic signatures reveal strongly anoxic depositional conditions for the Bijaigarh shales (Mukherjee et al., 2020). The Fe-speciation data for this Formation reveal the existence of locally ferruginous waters below the zone of wave-mixing (Gilleaudeau et al., 2020). This study also shows a reduced supply of sulfate, Mo and Cr to this shallow to deep basin, where a progressive reduction in Mo content was recorded. The organic carbon and nitrogen isotopic values from this Formation support an oxygen-rich surface layer and anaerobic nitrogen cycling in this setting (Gilleaudeau et al., 2020). Redox fluctuations and changes in nutrient inputs were reported for the Marwar Basin towards the late Neoproterozoic (Ansari et al., 2020). Redox-sensitive trace element ratios from the Lower Bander Sandstone suggest a transition from oxic to suboxic depositional environment during the deposition of glauconitic layers (Mandal et al., 2022). REE compositions and carbon isotopic study from the Pc-C sections from the Lesser Himalaya sections reveal stratified basinal conditions with oxic surface layers and anoxic deep layers (Mazumdar et al., 1999).

A substantial amount of evidence, both global and national, thus indicates a dynamic atmosphere-ocean-biosphere system during the Proterozoic time frame, with spatial-temporal variations and a possible cause-effect relationship. Though considerable work has been done in this aspect, a comprehensive understanding of the co-evolving ocean-biosphere system is still lacking. Temporal gaps in Proterozoic records, primarily due to a lack of well-preserved and

well-dated sections, still challenge our understanding of the biogeochemical changes accompanying the varying redox states. Identifying and investigating basinal and near-shore environments, which could have been the site for eukaryotic diversification, is required to improve our understanding of the linkage between life and environments during this interval. Further, the inter-basinal correlation of these redox fluctuations and productivity patterns can help constrain large-scale oceanic conditions and their influence on metazoan diversification. The well-preserved and weakly deformed sedimentary deposits from the Proterozoic Basins of India offer a scope for tracking these hydrosphere and atmosphere changes. Organic-rich shales could be one of the prime targets for such studies due to their abundance in the rock record, the presence of modern depositional analogues and the availability of well-calibrated chemical proxies.

1.2. Aims and Objectives

This thesis aims to carry out a detailed chemical and isotopic investigation of organic-rich shales from three different Proterozoic Basins (Cuddapah Basin, Vindhyan Basin and the Lesser Himalaya succession) of India.

The main objectives of this work are:

1. To reconstruct the depositional environment in these basins using abundance and distribution of organic carbon, redox-sensitive elements, and Fe-speciation.

2. To quantify the areal extent of ocean euxinia/anoxia and its temporal changes using Mo isotopic compositions.

3. To understand the productivity pattern and modes of nitrogen cycling in these basins by utilizing the carbon and nitrogen isotopic data.

1.3. Structure of the thesis

The thesis is organized into six chapters.

Chapter 1 reviews the current knowledge of the Proterozoic ocean-atmospheric system. It also identifies the research gaps and objectives for this study.

Chapter 2 provides details on samples and their geological settings. The analytical procedures adopted for chemical and isotopic analyses are also included.

Chapter 3 presents the chemical (trace elements and Fe speciation), chronological, and Mo isotopic datasets for late Paleoproterozoic shales from the Cumbum Formation, Cuddapah Supergroup. These data were used to establish the depositional age and environment for this succession.

Chapter 4 establishes the oceanic redox state and seawater sulfate inventory during the Precambrian-Cambrian transition. These outcomes were mainly constrained using geochemical and Mo-S isotopic data of the lower Tal shales from the Lesser Himalaya.

Chapter 5 focuses on the nitrogen isotopic study of shales from the Vindhyan, Cuddapah, and Lesser Himalaya sedimentary successions. These datasets are employed to evaluate the linkage between nitrate availability and basinal redox state.

Chapter 6 summarizes the major conclusions from this study and identifies the future scope of research on the co-evolution of seawater chemistry and early life.

Chapter 2

Materials and Methods

The main objective of this thesis work, as mentioned earlier, is to reconstruct the extent of the ocean euxinia and sulfate inventory during the deposition of shales in three Proterozoic sedimentary successions from India. This chapter provides geological details for these basins and the analytical methods employed in this work. Efforts were made to collect less-altered organic-rich shale sequences from the Cuddapah Basin, Vindhyan Basin and the Lesser Himalaya (Fig. 2.1). These sequences cover depositional periods ranging from the Paleoproterozoic to the Precambrian-Cambrian transition. The collected samples were subjected to comprehensive geochemical and isotopic investigation; details on these analytical methodologies are also described below.

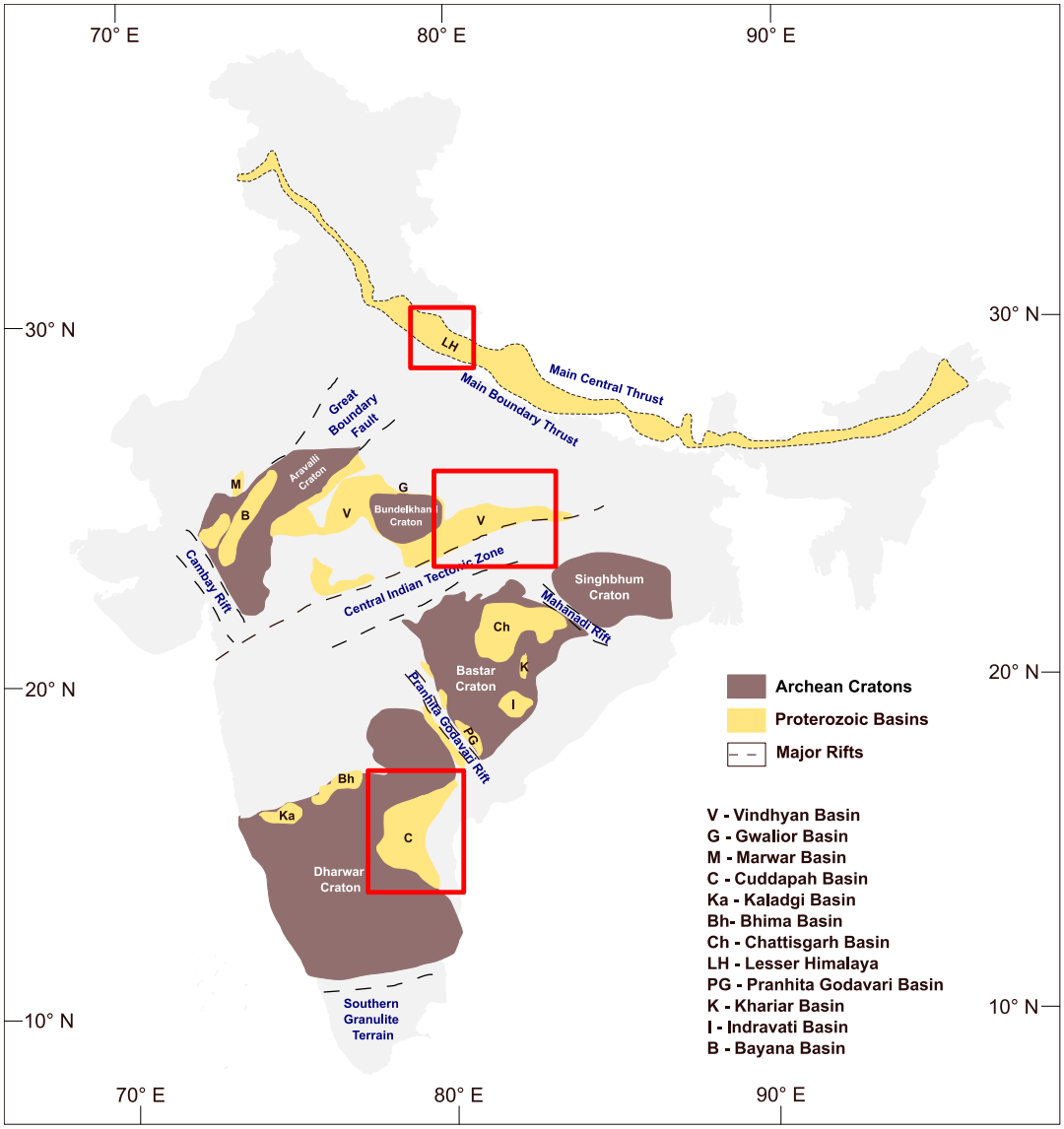

Figure 2.1. *Spatial distribution of major Archean Cratons and Proterozoic Basins of India (modified after Deb and Paul, 2015). The red boxes denote the targeted sedimentary basins.*

2.1. Geological setting

2.1.1. Cuddapah Basin

The intracratonic Cuddapah Basin is a crescent-shaped, northerly plunging, polyphase basin consisting of unconformity-bound shale-sandstone-limestone sequences deposited in varying fluvial to shallow marine settings (Ramakrishnan and Vaidyanathan, 2008; Fig. 2.2; Table 2.1). The sedimentary succession lies non-conformably over the Mesoarchean to Neoarchean tonalite-trondhjemite-granodiorite (TTG) gneisses, Neoarchean greenstone belts and granites, and the Paleoproterozoic granites and basic dykes of the Eastern Dharwar Craton (Saha and Patranabis-Deb, 2014).

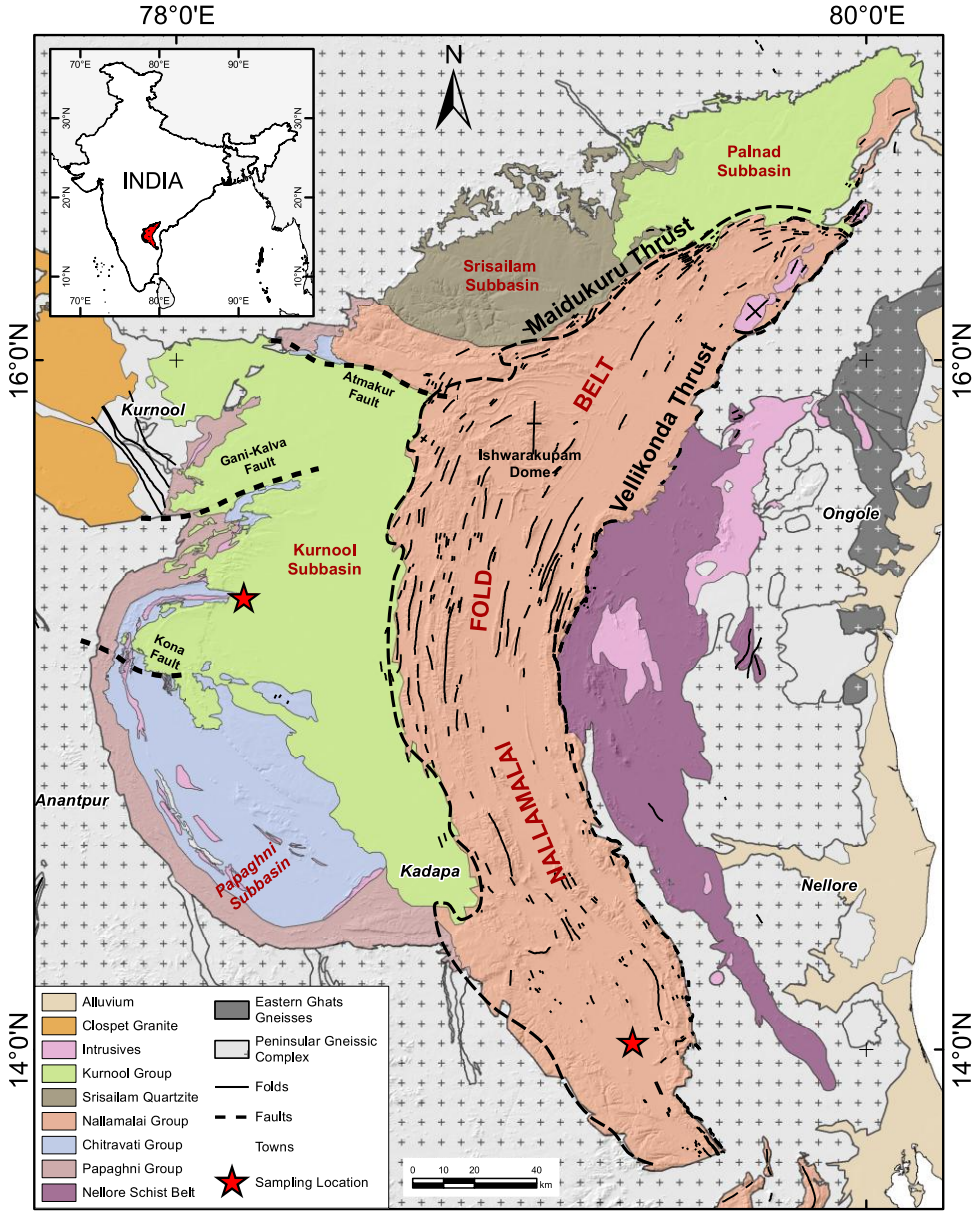

Figure 2.2. *Simplified geological map of the Cuddapah Basin (modified after Nagaraja Rao et al., 1987; Bhukosh-Geological Survey of India)*

The Cuddapah Basin consists of four major cycles of sedimentation represented by unconformity to thrust-bound sequences and is broadly divided into the Paleoproterozoic Cuddapah Supergroup and the Neoproterozoic Kurnool Group (Table 2.1; Nagaraja Rao et al., 1987; Saha and Tripathy, 2012; Patranabis-Deb et al., 2012). Based on the sedimentation pattern and spatial distribution, the Cuddapah Basin is classified into Palnad, Srisailam, Kurnool and Papaghni subbasins (Nagaraja Rao et al., 1987; Fig. 2.2). The western part of the Cuddapah Basin consists of the Papaghni and Srisailam subbasins, which host the Papaghni and Chitravati Groups (of Paleoproterozoic age) of the Cuddapah Supergroup, and the Palnad and Kurnool subbasins which host the (Neoproterozoic) Kurnool Group (Table 2.1; Fig. 2.2). The Nallamalai subbasin in the eastern part of the Cuddapah Basin hosts the deformed rocks of the Nallamalai Fold Belt (NFB), constituting the Nallamalai Group successions.

2.1.1.1. The Cuddapah Supergroup

The basal Papaghni Group is composed of conglomerates and sandstones of the Gulcheru Quartzite and the stromatolitic dolomites-sandstone-shales of the Vempalle Formation. The siliciclastic-dominated Gulcheru Quartzite was deposited in an alluvial fan to shallow marine settings, while the carbonate-dominated Vempalle Formation represents a shallow shelf depositional environment (Kale et al., 2020). The upper part of the Vempalle Formation consists of mafic flows, tuffs and intrusives, which yield a radiometric age of 1841 ± 71 Ma (K−Ar; Murthy et al., 1987). Pb−Pb age of 1752 ± 41 Ma (Zachariah et al., 1999) has also been reported from the Vempalle dolomites. Detrital zircons from the Gulcheru and Vempalle Formations provide a maximum depositional age of ~2.4 Ga (Collins et al., 2015).

The Papaghni Group is unconformably overlain by the Chitravati Group, comprising Pulivendla Quartzite, Tadpatri Formation and Gandikota Quartzite (Nagaraja Rao et al., 1987). The quartz-arenites of the Pulivendla Quartzite represent recycled Archean crustal components that were deposited in a passive margin environment (Saha et al., 2016; Somashekhar et al., 2018). The Tadpatri Formation is composed of heterolithic shale-sandstone-dolomitic successions with mafic-ultramafic sills, which record a transition from outer shelf to inner shelf depositional environment (Ramakrishnan and Vaidyanathan, 2008). A depositional age between ~1920 Ma and 1882 Ma has been constrained for the Pulivendla and Tadpatri Formations based on Pb−Pb detrital zircon (1923 ± 22 Ma; Collins et al., 2015), Ar−Ar phlogopite (1899 ± 20 Ma; Anand et al., 2003) and U−Pb baddeleyite ages (1885 ± 3 Ma; French et al., 2008). The quartzitic sandstones of the Gandikota Quartzite represent deposition

in a tide-dominated open shelf environment (Lakshminarayana and Bhattacharjee, 2000). Pb−Pb detrital zircon age of 1181 ± 29 Ma (Collins et al., 2015) has been reported from the Gandikota Formation. The Srisailam Quartzite overlies the Chitravati Group and is composed of sub-horizontal quartzite sequences with siltstone and shale intercalations. These sediments were deposited in a stable cratonic shelf under a fluvio-marine environment with minor aeolian input (Lakshminarayana et al., 2001; Patranabis-Deb et al., 2012; Kale et al., 2020). The U−Pb dating of quartzites from the Srisailam subbasin provides a depositional age between 1840 Ma and 1770 Ma for this sequence (Mukherjee et al., 2023).

Table 2.1. General stratigraphy of Cuddapah Basin (after Nagaraja Rao et al., 1987) along with the major lithology and environment of deposition (Valdiya, 2015).

Group	Formation	Lithology	Depositional Environment
Kurnool	Nandyal Shale	Shale, Calcareous shale	Outer shelf
	Koikuntla Limestone	Siliceous limestone with quartzite	Carbonate Platform
	Paniam Quartzite	Massive quartzite and siliceous shale	Shelf Bar
	Auk Shale	Laminated shale with siltstone	Outer shelf
	Narji Limestone	Limestone, glauconitic sandstone	Carbonate platform
	Banganapalle Quartzite	Oligomict conglomerate grit, quartzite, shale	Fan delta to shallow shelf
----------*Unconformity*----------			
Cuddapah Supergroup			
	Srisailam Quartzite	Pebbly grit, quartzite, heterolithic shales and sandstone	Fluvial to shallow marine with minor aeolian component
-x-x-x-x-x-x-x-x-x-x-Tectonic contact-x-x-x-x-x-x-x-x-x-x-x-			
Nallamalai	Cumbum/Pullampet Formation	Phyllite, slate, quartzite, dolomite, shale, felsic and mafic intrusives	Subtidal bars to peritidal
	Bairenkonda/Nagari Quartzite	Quartzite, quartz wacke, shale, conglomerate	Fan delta to peritidal
-x-x-x-x-x-x-x-x-x-x-Tectonic contact-x-x-x-x-x-x-x-x-x-x-x-			
Chitravati	Gandikota Quartzite	Alternate shale-quartzite beds, glauconitic quartzite	Shelf bar (intertidal to subtidal)
	Tadpatri Formation	Shale with arenite, dolomite, limestone, chert, tuff and ultramafic flows	Storm-dominated shallow shelf
	Pulivendla Quartzite	Quartzite, Conglomerate	Fluvial to shallow marine transition
----------*Unconformity*----------			
Papaghni	Vempalle Formation	Stromatolitic dolomite, chert, shale, quartzite, basic sills and flows	Carbonate platform (intertidal playa to subtidal basin)
	Gulcheru Quartzite	Basal Conglomerate, arkose, quartzite with shale interbeds	Tide and storm influenced fan-delta and delta front setting
----------*Unconformity*----------			
Crystalline basement of Dharwar Craton with Archean granite, gneiss and greenstones			

2.1.1.2. The Kurnool Group

The Neoproterozoic Kurnool Group lies unconformably over the lower Cuddapah Supergroup in the western part and the basement granite-gneiss in the northern part of the basin. This Group is composed of conglomerates-orthoquartzite-carbonate-shale associations deposited in shallow-marine depositional environments ranging between beach, littoral, tidal-flat and lagoonal environments (Lakshminarayana et al., 1999). The appearance of organic-walled microfossil assemblage from the Owk Shale constrains a Neoproterozoic age for the Kurnool Group (Sharma and Shukla, 2012; Shukla et al., 2020).

2.1.1.3. The Nallamalai Fold Belt

The Nallamalai Fold Belt (NFB), situated in the eastern part of the basin, is mainly composed of folded and faulted metasedimentary rocks of the Nallamalai Group. This Group comprises sandstone-shale-carbonate sequences with felsic tuff, debris-flow conglomerate and slumped beds (Chaudhuri et al., 2002). The NFB is thrust over the undeformed Chitravati and Papaghni Groups of the Cuddapah Supergroup in the west and the Kurnool Group in the north along the Maidukuru Thrust (or the Rudravaram Line; Meijerink et al., 1984; Saha et al., 2010; Patranabis-Deb et al., 2012). The NFB is bound in the east by the Vellikonda Thrust (Venkatakrishnan and Dotiwalla, 1987), along which the Nellore Schist Belt is juxtaposed against the NFB. Three phases of deformation have been recognized from the northern part of the NFB, which include (i) N-S trending tight to isoclinal folds associated with slaty cleavage, (ii) NNW to NE-SW trending large tight to open folds with crenulation cleavage and (iii) E-W trending folds and cleavage (Saha, 2002; Tripathy and Saha, 2010).

The Nallamalai Group is classified into the sandstone-dominated Bairenkonda Quartzite and the shale-limestone-dominated Cumbum Formation. These sequences are considered to be formed in an independent basin east of the Papaghni subbasin and hence allochthonous to the other sedimentary succession in the Cuddapah Supergroup (Saha et al., 2010; Saha and Tripathy, 2012). Lithological associations in the NFB successions indicate subtidal to peritidal depositional settings, possibly in a marginal basin with open ocean connectivity (Saha and Tripathy, 2012; Kale et al., 2020). Provenance studies based on Pb−Pb and Hf isotopes indicate that sediments from the Nallamalai Group were supplied from the Krishna Orogen (~1.78 Ga; Vadlamani et al., 2014; Chatterjee et al., 2016), and got deposited in a foreland basin (Collins et al., 2015; Joy et al., 2015). U−Pb dating of detrital zircons constrains maximum depositional ages of 1659 ± 22 Ma (Collins et al., 2015) and ~1550 Ma (Joy et al., 2015) for the Nallamalai

Group. The minimum age for this Group has also been provided using radiometric dating of the lamproite intrusions at Chelima (1418 ± 8 Ma; Chalapathi Rao et al., 1999) and syenite intrusions at Racherla (1326 ± 73 Ma; Chalapathi Rao et al., 2012).

2.1.2. Vindhyan Basin

The intracratonic Vindhyan Basin, exposed within the Bundelkhand Craton, represents the largest Proterozoic basin of India and consists of mostly unmetamorphosed and mildly deformed siliciclastic-carbonate sedimentary rocks deposited predominantly in shallow marine conditions (Ramakrishnan and Vaidyanathan, 2008). The Basin is bounded by the Aravalli-Delhi orogenic belt (the Great Boundary Fault) in the northwest and the Son-Narmada lineament in the southeast. The eastern margin of the basin is bordered by the low-grade metamorphic rocks of the Mahakoshal (~2.4 Ga) and the Bijawar (~2.1 Ga) Supergroups (Ramakrishnan and Vaidyanadhan 2008). The basin is thought to have originated due to (i) an intracontinental sag-continental extension (e.g. Bickford et al., 2017) or (ii) the subduction zone-foreland deposition (e.g. Chakrabarti et al., 2007). The sedimentation of the Vindhyan rocks occurred within an epicratonic sea with an open ocean connection to the northwest (Chanda and Bhattacharya, 1982). A significant part of the basin is currently covered under Gangetic alluvium in the north and the Deccan traps in the southwest (Chakraborty, 2006; Ray, 2006). The Bundelkhand Granite Complex (BGC; ~2.5 Ga; Azmi, 1998; Malone et al., 2008) separates the rocks in this Basin into the eastern (Son Valley) and the western (Rajasthan) outcrop sectors (Shukla et al., 2020; Fig. 2.3). Samples from this study are from the Son valley region of the Vindhyan basin. The Vindhyan sedimentary rocks unconformably overlie the Bundelkhand igneous complex and metamorphosed Paleoproterozoic rocks of the Bijawar and Gwalior Groups (Sarkar and Banerjee, 2020). The sedimentary sequences are divided into the Lower Vindhyans (Semri Group) and the Upper Vindhyans (Kaimur, Rewa and Bhander Groups), separated by an unconformity (Table 2.2; Fig. 2.3).

2.1.2.1. Lower Vindhyans

The Lower Vindhyans are dominated by sandstones, limestone, porcellanite, and shales and are regarded as the Semri Group of rocks. This Group is further classified into three subgroups, namely, the Mirzapur, Kheinjua and Rohtas Subgroups (Sastry and Moitra, 1984). The Mirzapur Subgroup consists of arenaceous rocks of the Deoland Formation, argillaceous

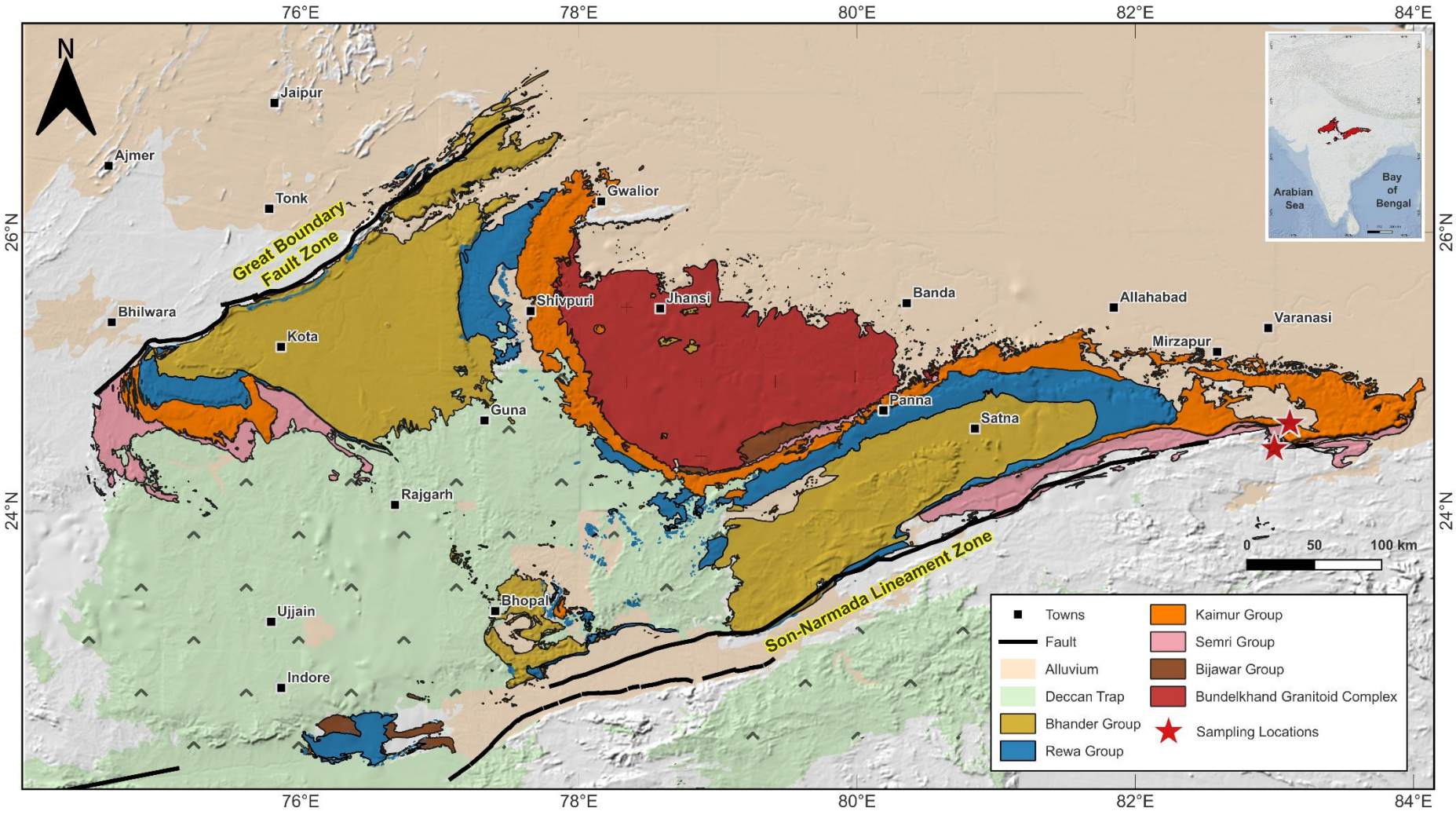

Figure 2.3. *Geological Map of the Vindhyan Basin (after Soni et al., 1987; Bhukosh-Geological Survey of India)*

layers of the Arangi Formation, stromatolitic carbonates of the Kajrahat Limestone, and the silicified tuff (porcellanites) and sandstones of the Deonar Formation. The occurrence of domal, laminated forms of stromatolites has been reported from the Kajrahat Limestone (Valdiya, 1969). The porcellanites of this subgroup are considered to represent submarine and terrestrial volcanoclastic sediments deposited in tidal flat regions (Srivastava et al., 2003). The overlying Kheinjua Subgroup is composed of the olive shales of the Koldaha Formation, stromatolitic carbonates of the Salkhan Limestone and the glauconitic sandstones of the Rampur Formation. The stromatolite assemblage of the Salkhan Limestone is characteristic of the Lower Riphean age (1650–1350 Ma; Valdiya, 1969). The Rohtas Subgroup overlies the Kheinjua Subgroup and is dominated by the greyish-to-black limestone and shales of the Rohtasgarh Limestone and the shale-sandstone sequences of the Bhagwar shale. The sedimentation of the Lower Vindhyan is constrained between 1750 and 1500 Ma based on the available age constraints. These include Rb−Sr model ages between 1504 to 1409 Ma for glauconites from Kheinjua Subgroup (Kumar et al., 2001), whole rock carbonate Pb−Pb ages of 1729 ± 110 Ma for Kajrahat and 1601 ± 130 Ma for the Rohtas Limestone (Sarangi et al., 2004; Ray et al., 2003), Pb−Pb and SHRIMP age between 1647 and 1599 Ma for magmatic zircons from the Deonar Porcellanites (Rasmussen et al., 2002; Bickford et al., 2017; Mishra et al., 2018) and TIMS U−Pb zircon age of 1599 ± 8 Ma for the Rampur Shale (Rasmussen et al., 2002).

2.1.2.2. Upper Vindhyans

The Upper Vindhyans are separated from the Lower Vindhyans by a major (~500 Ma) regional hiatus in the Son Valley (Mishra, 2011). The Upper Vindhyan are further classified into the Kaimur, Rewa and Bhander Groups. The lowermost (Kaimur) Group is dominated by the argillaceous-arenaceous rocks with a conglomerate layer at its base. The intrusion of Kimberlite pipes (Majhgawan) into the Kaimur Group has been observed near Panna (Valdiya, 2015). The Rewa Group overlies the diamondiferous conglomerate horizon and consists of sandstones and shales indicative of shallow shelf deposition. The topmost (Bhander) Group is composed of shale-limestone-sandstone sequences and shows the occurrence of columnar to domal stromatolites. These rocks represent deposition in lagoonal to storm-dominated tidal flat environments (Chakraborty, 2006; Ramakrishnan and Vaidyanadhan, 2008). The Upper Vindhyan sequences are considered to have been deposited in the late Mesoproterozoic to Neoproterozoic based on radiometric, chemostratigraphic and biostratigraphic evidence. These include phlogopite Ar−Ar age (1074 ± 14 Ma) and paleomagnetic signatures of the Majhgawan

kimberlite intruding the Kaimur Group (Gregory et al., 2006; Malone et al., 2008), Re−Os depositional age of 1210 ± 52 Ma for the Bijaigarh shales (Tripathy and Singh, 2015), absence of detrital zircon ages above 1000 Ma (Malone et al., 2008; McKenzie et al., 2011; 2013; Turner et al., 2014), occurrence of Ediacaran-type fossils (Pandey et al., 2024 and references therein), carbon and strontium isotopic stratigraphy (Ray et al., 2003; Gilleaudeau et al., 2018), and Pb−Pb ages of 908 ± 72 Ma and 1073 ± 210 Ma for the Bhander limestone (Gopalan et al., 2013).

Table 2.2. Generalized stratigraphy of the Vindhyan Supergroup (after Sastry and Moitra, 1984) along with the major lithology and depositional environment (Sarkar and Banerjee, 2020)

Group	Formation		Lithology	Depositional Environment
Upper Vindhyan				
Bhander Group	Maihar Sandstone		Sandstone, shale	Tide-storm-influenced coastal flat
	Sirbu Shale		Shale, siltstone with sandstone intercalation	Lagoonal, outer to inner shelf
	Bhander Limestone		Dark grey limestone and greyish shale	Supratidal to tidal flat
	Ganugarh Shale		Shale, calcareous siltstone and fine-grained sandstone	Tide-affected, coastal flat system
Rewa Group	Govindgarh Sandstone		Pebbly to coarse-grained Sandstone	Fluvial
	Jhiri Shale		Shale with minor sandstone	Inner shelf
	Asan Sandstone		Glauconitic sandstone	Inner shelf
	Panna Shale		Laminated grey, green and brown shales	Inner shelf
Kaimur Group	Dhandraul Quartzite		Sandstone	Fluvial delta
	Mangesar Formation		Sandstone with minor shales	Storm-influenced inner shelf
	Bijaigarh Shale		Grey black shale, siltstone and sandstone	Proximal to distal shelf
	Ghaghar Sandstone		Sandstone with shale intercalation	Wave-tide-influenced inner shelf
	Sasaram Formation		White to grey massive bedded sandstone	Storm-tide-influenced inner shelf
----------*Unconformity*----------				
Lower Vindhyan				
Semri Group	Rohtas Subgroup	Bhagwar Shale	Silicified shale, sandstone and carbonaceous shale	Carbonate Lagoon
		Rohtasgarh Limestone	Greyish black limestone and shales	Carbonate platform
	Kheinjua Subgroup	Rampur Shale	Glauconitic sandstone, minor shales	Inner to outer shelf
		Salkhan Limestone	Siliceous and cherty limestone with minor shale	Peritidal
		Koldaha Shale	Olive shale, siltstone and minor sandstones	Distal to proximal shelf
	Mirzapur Subgroup	Deonar Formation	Silicified tuff and sandstone	Outer shelf environment
		Kajrahat Limestone	Limestone with shale intercalation	Distal to proximal shelf
		Arangi Formation	Shale	Inner to outer shelf
		Deoland Formation	Shale, Sandstone, conglomerate, limestone	Alluvial fan to fan delta
----------*Unconformity*----------				
Bijawar, Aravalli and Pre-Aravalli Group/Bundelkhand Granite Basement				

2.1.3. Lesser Himalaya

The Lesser Himalaya sedimentary successions represent Paleoproterozoic to Early Paleozoic sedimentary formations consisting of autochthonous to para-autochthonous sedimentary successions bound by the Main Central Thrust (MCT) in the north and the Main Boundary Thrust (MBT) in the south (Valdiya, 1980; Fig. 2.4). These successions comprise sediments derived from the passive Indian margin intercalated with granites and acid volcanics (Valdiya, 2015). Based on lithological and geochronological constraints, they are divided into the Inner Lesser Himalaya and the Outer Lesser Himalaya, separated by the south-dipping Tons Thrust (Richards et al., 2005; Valdiya, 1980; Table 2.3; Fig. 2.4). The Inner and Outer Lesser Himalayan Sequence zones were juxtaposed along the Tons Thrust prior to the emplacement of the Main Central Thrust sheet atop the Lesser Himalayan Sequence (Célérier et al., 2009a).

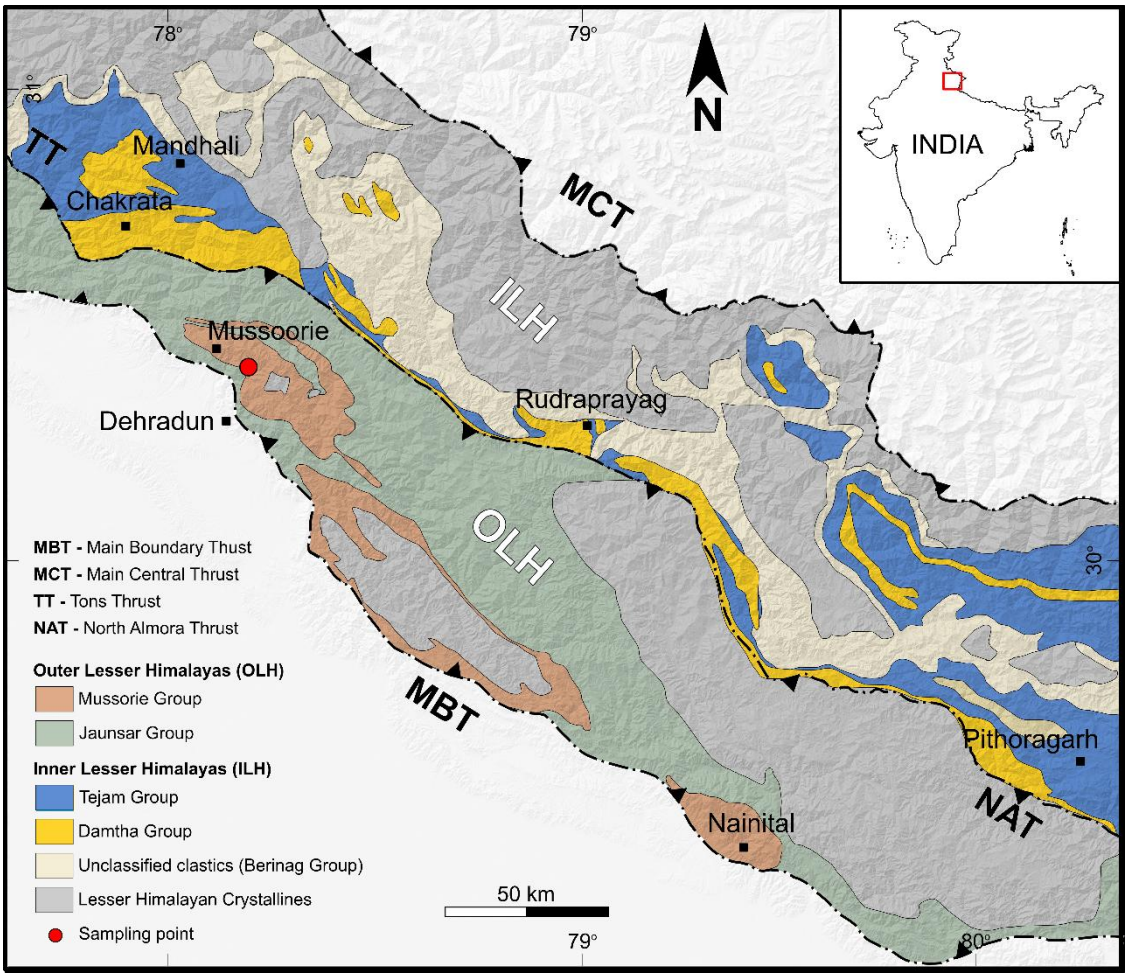

Figure 2.4. *Simplified geological map of the Lesser Himalaya showing the distribution of Proterozoic sedimentary successions in the Outer Lesser Himalaya (OLH) and Inner Lesser Himalaya (ILH) (modified after Rai and Singh, 1983; Ghosh et al., 2016).*

Table 2.3. Generalized stratigraphic details of Neoproterozoic-Cambrian succession of outer Lesser Himalaya (after Ghosh et al., 2016; Hughes, 2016).

Group	Formation	Member	Lithology	Depositional Environment
Mussoorie	Tal	Upper Tal	Sandstone–siltstone interbedded with purple, brown, and grey shales	Supratidal to intertidal zones
		Lower Tal	Carbonaceous–pyritic black shale, stromatolitic limestone	Supratidal to lower intertidal/upper subtidal
	Krol	Krol E	Limestone with calcareous shale, siltstone	Tidal flat to shallow subtidal
		Krol D	Microbial cherty limestone, calcareous shale, siltstone and minor sandstone	Lagoonal subtidal to deep subtidal
		Krol C	Massive dark grey and blue dolomite, brecciated	Lagoonal to shallow subtidal
		Krol B	Purple green shale, limestones with biohermal stromatolitic dolomite	Proximal tidal flat and rimmed shelf
		Krol A	Dolomitic limestone chert, shale	Deep to shallow subtidal
	Infra Krol		Shale, slate, quartzite with pyrite and nodules of phosphate	Tidal-flat, lagoonal environment
	Blaini		Conglomerate, quartzite, diamictite	Supratidal to intertidal environment
----------*Unconformity*----------				
Jaunsar	Nagthat		White, fawn, pink and purple quartzite, variegated slates	Shoreface to proximal inner shelf deposit with tide and storm influence
	Chandpur		Lithic wacke, sublitharenite, siltstone and shale	Storm-dominated progradational shelf
-x-x-x-x-x-x-x-x-x-x-x-Tectonic contact-x-x-x-x-x-x-x-x-x-x-x-				
Tejam	Mandhali		Shale, slate interbedded with marlites and argillaceous limestones	Shallow water littoral environment
	Deoban		Blue to greyish black dolomitic limestone, dolostone with bedded chert and shale intercalations	Subtidal to intertidal
----------*Unconformity*----------				
Damtha	Rautgara		Quartz-arenites/sublitharenite	Inter-tidal to supratidal/tidal flat
	Chakrata		Quartz wacke–siltstone–shale assemblage	Inter-tidal to supratidal/tidal flat
Basement not exposed				

2.1.3.1. Inner Lesser Himalaya

The sedimentary successions of the Inner Lesser Himalaya consist of Paleoproterozoic to Mesoproterozoic autochthonous siliciclastic rocks of the Damtha and Tejam Groups. These rocks are dominantly shallow marine argillo-arenaceous sequences associated with intrusive granites, basic magmatism seismites and acid tuff deposited in a shallowing near-shore environment (Ghosh et al., 2012, 2016). These sequences have undergone a high degree of diagenesis and low-grade metamorphism (greenschist to upper amphibolite grade; Célérier et al., 2009b; Ghosh et al., 2016). The Damtha Group is comprised of turbiditic flysch of the Chakrata Formation at its base, which grades upwards to a slate-quartzite assemblage of the Rautgara Formation. An age of ~1.8 Ga (Pb−Pb single zircon age) has been determined for interbedded mafic volcanics of the Rautgara Formation, constraining a Paleoproterozoic age for the Damtha Group (Miller et al., 2000). This Group is conformably overlain by the Tejam Group, which comprises the carbonate-dominated Deoban Formation and argillo-calcareous Mandhali Formation. The Deoban sequence consists of stromatolitic carbonates deposited in a shallow marine stable tidal-flat condition (Virdi, 1995). Based on the presence of stromatolites, a Mesoproterozoic (Riphean) age has been assigned for this Group (Valdiya, 1980; Bhargava et al., 2011). The Mandhali Formation consists of carbonaceous shales intercalated with dolomites deposited in a poorly ventilated shallow marine environment that experienced periodic anoxicity (Valdiya, 2015). A late Neoproterozoic age (upper Riphean to Vendian) has been assigned to this Group (Valdiya, 1980).

2.1.3.2. Outer Lesser Himalaya

Overlying the autochthonous Inner Lesser Himalayan zone is the para-autochthonous Outer Lesser Himalayan Krol belt succession spanning the Neoproterozoic to early Cambrian interval. These strata occur as a series of doubly plunging synclines comprised of the Nigalidhar, Mussoorie, Nainital and Garhwal synclines. The Outer Lesser Himalayan rocks have undergone low degrees of thermal metamorphism, as evidenced by the Raman Spectra analysis of carbonaceous matter from the Mussoorie syncline (Célérier et al., 2009b). The Krol nappe consists of two groups of sedimentary rocks, the Neoproterozoic Jaunsar Group and the Neoproterozoic to Cambrian Mussoorie Group. The Jaunsar Group represents a coarsening upward stratigraphic sequence constituted by the phyllites and siltstones of the Chandpur Formation at the base and the slates-orthoquartzites of the Nagthat Formation. This Group represents a changing depositional environment from deep water to a progradational shelf

affected by occasional storms and transgressive events (Pant and Goswami 2002). The stratigraphic position below the ~692 Ma Blaini Formation and the occurrence of detrital zircons of ~0.8 Ga constrain a Neoproterozoic age for the Jaunsar Group (Celerier et al., 2009a; Etienne et al., 2011). The Jaunsar Group is conformably overlain by the glaciomarine-arenaceous-argillaceous sequence of the Mussoorie Group consisting of the Blaini, Infra Krol, Krol and Tal successions, representing the inner part of a passive continental margin (Brookfield, 1993). The Blaini Formation consists of diamictite units separated by shale-sandstone alternations (Brookfield 1987). A maximum depositional age of 692 ± 18 Ma (Pb−Pb detrital zircon age) has been provided for the Blaini diamictites (Etienne et al., 2011). The uppermost unit of the Blaini Formation is the Infra Krol succession, consisting of carbonaceous shales and pyritiferous phosphates deposited in a euxinic lagoonal environment (Valdiya, 2015). The Infra Krol succession grade into the shallow marine carbonates and siliciclastics of the Krol and Tal units (Valdiya 1980). The Krol Formation is dominated by argillaceous limestones, marls, and slates in the lower parts (Krol A, B, C) and microbial dolomites (Krol D and E) in the upper parts representing a supratidal to shallow-subtidal environment (Valdiya 1980; 2015). Sequence and carbon isotopic stratigraphy of the Krol Group has been correlated with the Dengying and Doushantuo Formations in South China (Aharon et al., 1987; Jiang et al., 2003; Kaufman et al., 2006).

The Tal Formation overlies the Krol Formation and represents a transition to the early Cambrian. The lower member of the Tal Formation is comprised of carbonaceous–pyritic black shales, stromatolites, chert-phosphorite horizons and subordinate black limestone with the occurrence of penecontemporaneous deformation structures. The upper member consists of ripple-marked sandstone-siltstone sequences interbedded with purple, brown and grey shales. The Tal Formation was deposited in a barred basin with an open ocean connection where restricted circulation, episodic anoxicity and basin upwelling were prevalent (Valdiya, 2015; Mazumdar et al., 1999; Bhargava et al., 2021). This succession is also characterized by assemblages of small shelly fauna such as *Anabarites, Protohertzina*, and *Maldeotaia* (Bhatt et al., 1985; Brasier and Singh, 1987). Both chemostratigraphic (carbon and oxygen isotopes) and biostratigraphic evidence (acritarchs, small shelly fauna, trilobites, and brachiopods) support the presence of the Precambrian-Cambrian boundary within the Krol-Tal succession (Azmi 1983; Aharon et al., 1987; Banerjee et al., 1997; Jiang et al., 2003). Re−Os dating of black shales from the Lower Tal Formation have yielded an age of 535 ± 11 Ma (Singh et al., 1999).

An older Rb−Sr age of 626 ± 13 Ma (Sharma et al., 1991) has also been reported from the Lower Tal, which may have been influenced by sediment provenance age.

2.2. Sampling

2.2.1. Cuddapah Basin

Samples from the Cuddapah Basin come from the Cumbum (Nallamalai Group) and the Tadpatri (Chitravati Group) Formations (Fig. 2.5). Shales from the Cumbum Formation were collected from an open cast mine section at Mangampeta village, Andhra Pradesh (14°01'27" N, 79°19'16"E; Fig. 2.2). This shale sequence had an overall thickness of ~100 m and overlaid dolomite and barite ore body. The targeted region was above the northern lens of the barite ore body and consists of freshly excavated black shales with minimal to no surface alterations. Sampling was carried out both spatially and stratigraphically from different parts of the mine away from the ore body. Occurrences of cm-sized pyrite grains were observed in the lower part of the shale sequences close to the ore body, which were avoided during sampling to prevent the nugget effect. The Tadpatri shales were collected from an abandoned mine near Yagantipalle village, Andhra Pradesh (15°19'02"N, 78°11'41"E; Fig. 2.2). The shale exposure was ~1.5 m thick and was exposed below a large dolerite sill body. The shale layers close to the intrusive body were characterized by small-scale veins and were avoided during sampling.

2.2.2. Vindhyan Basin

Representative samples from the Vindhyan Basin were collected from the Kajrahat Limestone (Semri Group) and Bijaigarh Shale (Kaimur Group) sequences (Fig. 2.6). Shales from the Kajrahat Formation (24°26'49.0"N, 82°59'59.1"E; Fig. 2.3) were collected from a limestone quarry near Dalla village, Uttar Pradesh. The shale layers in the quarry section were found intercalated between limestone beds. The collected samples from these layers were very fresh, with their thickness varying between ~20 cm and ~1 m. The Bijaigarh Shale samples were collected from a railway cutting exposure close to the Churk Railway Bridge, Uttar Pradesh (24°37'37.7"N, 83°06'42.0"E; Fig. 2.3). The entire shale sequence was ~50 m in length with a thickness of ~8 m. Representative samples were collected from different parts of the exposed section.

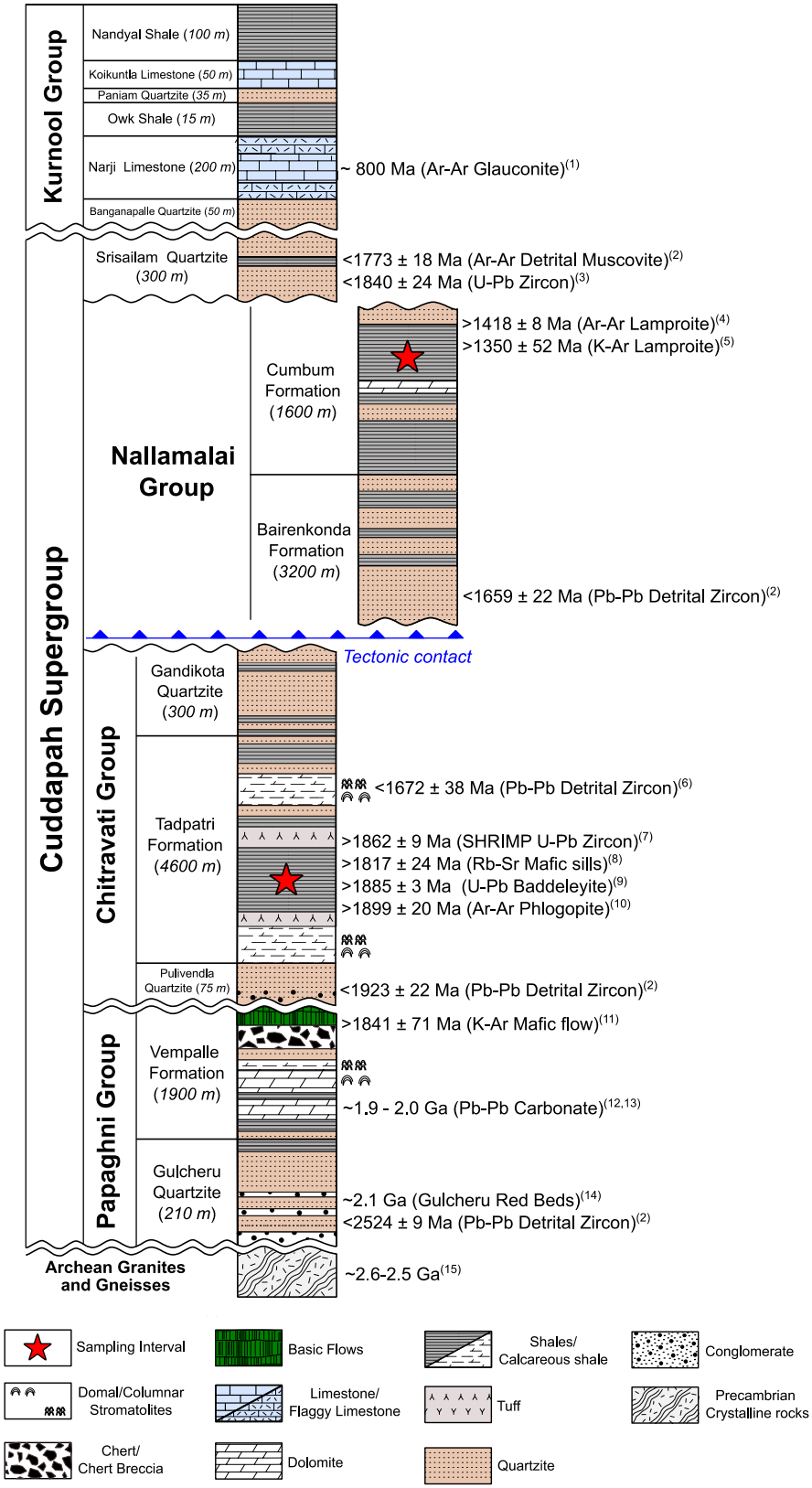

Figure 2.5. *Generalized stratigraphy of the Cuddapah Basin (modified after Nagaraja Rao et al., 1987; Ramakrishnan and Vaidyanathan, 2008). Geochronological data are from (1) Wabo et al., 2022; (2) Collins et al., 2015; (3) Mukherjee et al., 2023; (4) Chalapathi Rao et al., 1999; (5) Chalapathi Rao et al., 1996; (6) Khelen et al., 2020; (7) Sheppard et al., 2017; (8) Bhaskar Rao et al., 1994; (9) French et al., 2008; (10) Anand et al., 2003; (11) Murthy et al., 1987; (12) Rai et al., 2015; (13) Absar et al., 2016; (14) Sesha Sai et al., 2016; (15) Jayananda et al., 2013).*

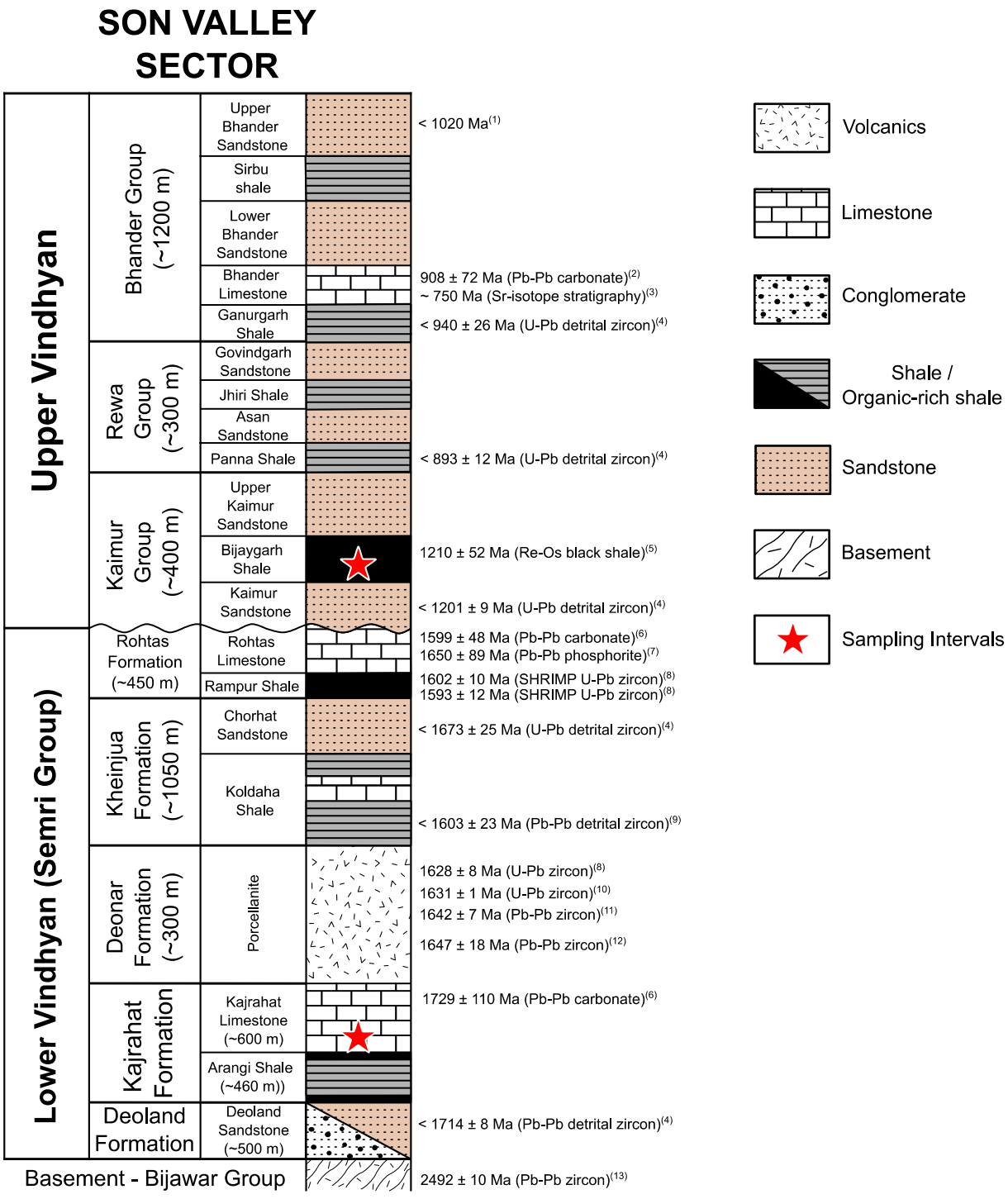

Figure 2.6. *Generalized stratigraphy of the Vindhyan Basin at Son Valley (after Sastry and Moitra, 1984). Geochronological data are from (1) Malone et al., 2008; (2) Gopalan et al., 2013; (3) Ray et al., 2003; (4) Colleps et al., 2021; (5) Tripathy and Singh, 2015; (6) Sarangi et al., 2004; (7) Bengston et al., 2009; (8) Rasmussen et al., 2002; (9) Lan et al., 2021; (10) Ray et al., 2002; (11) Bickford et al., 2017; (12) Mishra et al., 2018; (13) Mondal et al., 2002.*

2.2.3. Lesser Himalaya

Organic-rich shale samples belonging to the lower Tal Formation were collected from an abandoned mine section near the Maldeota village, Uttarakhand (30°21'50.17"N, 78° 8'30.11"E; Fig. 2.7). These rocks were well laminated, and disseminated pyrite grains (mm-sized) were observed in hand specimens of these shales. Shale samples from the underlying Chandpur Formation (Jaunsar Group) of Neoproterozoic age (Richards et al., 2005; Negi et al., 2022) were collected from a road-cut section near the Yamuna River bridge, Lohari Village, Uttarakhand (30°30'50.40"N, 77°59'49.20"E). All the collected samples were mostly undeformed and least metamorphosed. During sampling, care was taken to expose fresh surfaces and collect samples with no observable veins, fractures or surficial weathering.

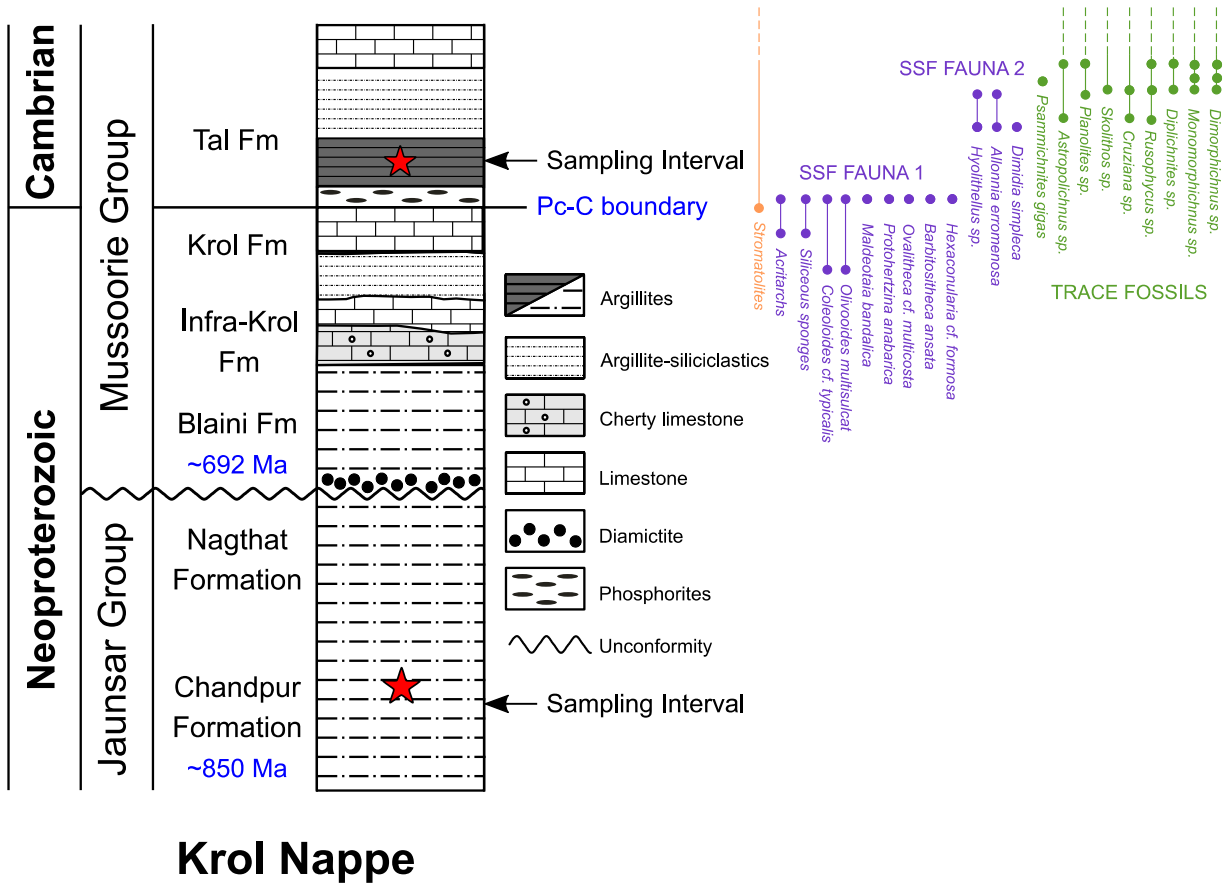

Figure 2.7. *Generalized stratigraphic details of Neoproterozoic-Cambrian succession of the outer Lesser Himalaya (after Ghosh et al., 2016; Hughes, 2016). Age information from Richards et al. (2005) and Etienne et al. (2011).*

2.3. Analytical methods

2.3.1. Sampling protocol

The samples used in this work include both archived and newly collected organic-rich shales from two field campaigns. As mentioned earlier, these samples, with no observable surface alteration, were collected from freshly excavated road cuts and mine sections. Further, the samples were collected from regions away from veins, intrusion contacts, and weathered domains. About 2 kg of bulk rock samples were collected from the outcrops, properly packed, and transported to IISER Pune for further processing. At IISER Pune, the shale samples were further chipped into *cm*-sized fragments, and these chips were washed using de-ionized water and dried overnight at 60°C in a hot air oven. About 90 g of these chips were powdered to <100 μm size using an agate mortar and pestle, and properly stored in polypropylene containers. Preparation of reagents and subsequent dilutions was always done using de-ionized water (18.2 MΩ; Millipore systems). The detailed workflow of the analytical methods adopted in this study is provided in Fig. 2.8.

2.3.2. Geochemical analyses

2.3.2.1. Major and Trace elemental analyses

Major oxide concentrations were determined on fusion beads of samples using a wavelength-dispersive X-ray fluorescence Spectrometer (WD-XRF; Bruker S8 Tiger) at IISER Pune using our established methodology (Samanta et al., 2022). Prior to bead preparation, samples were combusted at 950°C in quartz crucibles and the weight loss was noted to determine the Loss on Ignition (LOI) of the samples. For fusion bead preparation, about 500 mg of these ashed samples was mixed with lithium tetraborate-metaborate flux (66% $Li_2B_4O_7$ and 34% $LiBO_2$; FLUXANA) at a fixed proportion (1:17), and this mixture was fused in a platinum crucible at 1050°C. The resultant bead was introduced into the XRF machine, and the characteristic fluorescent wavelengths were quantified to determine oxide compositions. The instrument was calibrated using the GEO-QUANT ADVANCED package (Bruker), which includes a set of 32 reference standards comprising geological materials of different compositions. Quality check specimens (n = 5) were analyzed prior to the initiation of any batch to check instrumental performance.

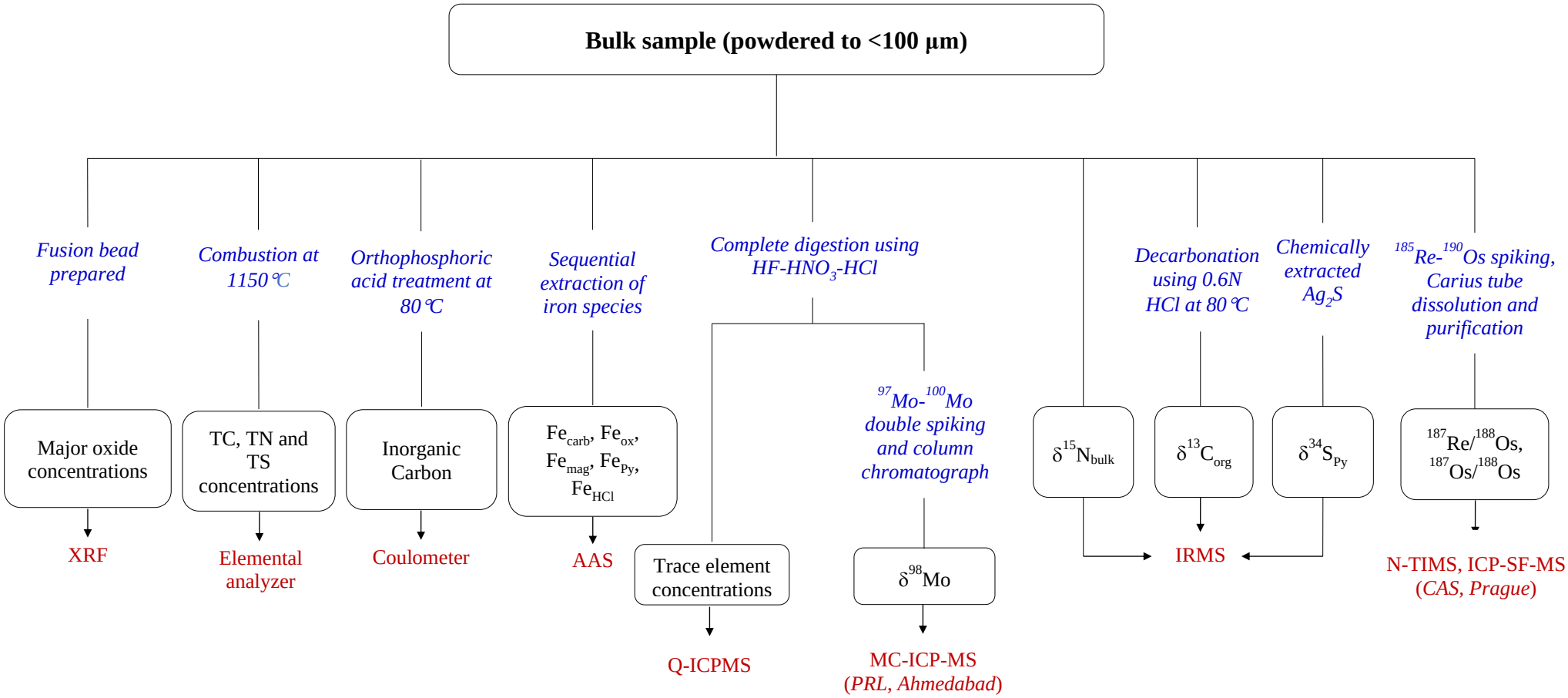

Figure 2.8. *Flowchart depicting the analytical methods followed in this study.*

To determine the accuracy of the measurements, USGS rock standards BHVO-2 and BCR-2 were prepared and analyzed using the same methodology. Results from these measurements for all oxides match within ±1% of their reported values (Fig. 2.9). Also, average sample reproducibility, based on repeat analysis of sample aliquots, was found to be ~ ±1% (n = 8).

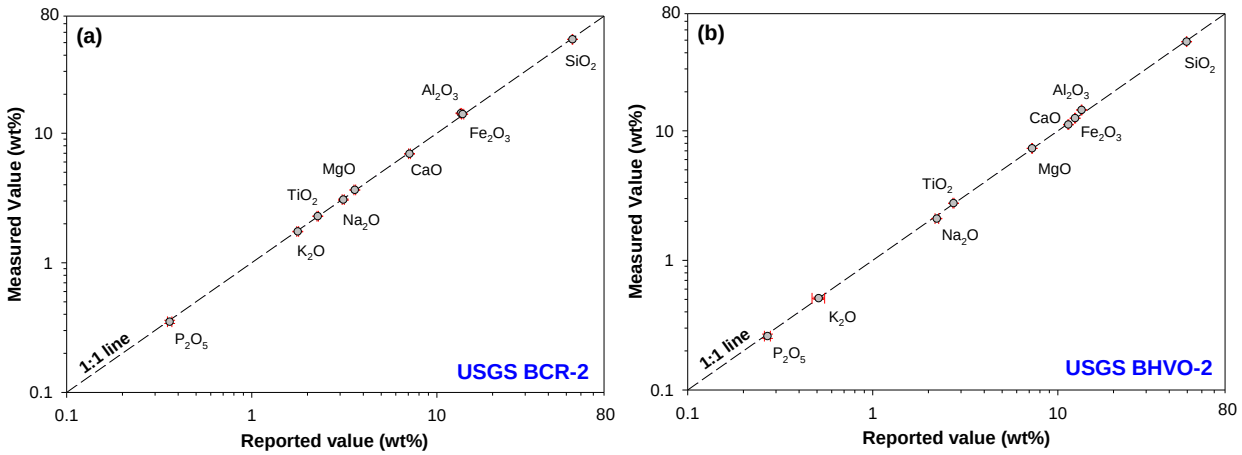

Figure 2.9. *Comparison of measured and reported major oxide values for USGS-certified reference materials* ***(a)*** *BCR-2 and* ***(b)*** *BHVO-2. The dotted diagonal line represents the 1:1 line.*

For trace elemental (including REE) analysis, ~100 to 200 mg of powdered samples were weighed into 100 ml PFA liners and digested completely using HF-HCl-HNO_3 acids in a microwave digestion unit (Anton Paar Multiwave Pro). This digestion method spanned ~90 min, which involved 30 min of ramp time at 0.3 bar/s pressure increments (to attain power of 1200W) and 60 min of hold time. The vessel temperature and pressure during the microwave digestion were typically ~190°C and 50 bar, respectively. After this procedure, the entire solution was transferred to a pre-cleaned PFA beaker (50 ml; Savillex), dried to a drop, and then treated with *aqua regia* for 12 hours. The solution was further dried and diluted using 0.3N HNO_3 and stored in pre-cleaned polypropylene bottles. Ultrapure grade (HF; Sigma Aldrich) or double-distilled (HNO_3 and HCl) acids were used during the digestion procedure. The digested solutions were diluted (~500 times) using 0.3N HNO_3 and measured for their trace elemental concentrations using a quadrupole ICPMS (Thermo iCAP Q) in Kinetic Energy Discrimination (KED) mode. The typical instrument parameters during these measurements are given in Table 2.4. In addition, the phosphorus concentration of the digested solutions for the Vindhyan and Cuddapah samples were also measured using an ICP-OES instrument and are used for the Redfield ratio comparison (cf. Chapter 5).

Table 2.4. Typical operating parameters and settings of Q-ICPMS instrument during trace element analyses.

Instrumental Parameters	Details
Mode	Kinetic Energy Discrimination
Plasma Power	1550 W (Hot Plasma)
RF Frequency	1.95 MHz
RF Amplitude	1100 V
Sample Uptake rate	1 ml/min
Uptake and Wash Time	60s and 60s
Spray Chamber temperature	2°C
Carrier Gas	Argon
Carrier Flow	14 ml/min
Auxiliary Flow	0.8 ml/min
Nebulizer Flow	1.12 ml/min
Additional Gas	Helium
Additional Gas flow	4.5 ml/min

A standard calibration line was created using different dilutions of the dissolved USGS rock standard BCR-2 to estimate the elemental concentrations. Samples were normally analyzed in batches of 10, where each batch was bracketed by standards and knowns to check for internal precision and instrumental drift. In addition to the samples, certified USGS reference materials BHVO-2 and SGR-1b were processed and measured to constrain the data accuracy (average ~6%; Table 2.5). Replicate digestions of sample aliquots (n = 8) were carried out to determine the external reproducibility of these measurements (average ~4%; Table 2.6 and 2.7).

The measured elemental concentrations (X) were used to compute the elemental enrichment factors (X_{EF}) with respect to the upper continental crust (UCC) compositions (Rudnick and Gao, 2003). The X_{EF} is computed as (Tribovillard et al., 2006):

$$X_{EF} = \frac{\left({}^{X}/_{Al}\right)_{sample}}{\left({}^{X}/_{Al}\right)_{UCC}} \tag{2.1}$$

Further, the Ce-anomaly for the samples was computed (Taylor and McLennan, 1985) as follows:

$$\frac{Ce}{Ce^{*}} = \frac{\frac{Ce_{sample}}{Ce_{PAAS}}}{\sqrt{\frac{La_{sample}}{La_{PAAS}} \times \frac{Pr_{sample}}{Pr_{PAAS}}}} \tag{2.2}$$

Table 2.5. Comparison of measured and reported trace elemental compositions for USGS-certified reference materials (BHVO-2 and SGR-1b).

Element	USGS BHVO-2		USGS SGR-1b	
	Measured	**Reported***	**Measured**	**Reported***
	(µg/g)	**(µg/g)**	**(µg/g)**	**(µg/g)**
Sc	31.9 ± 1.8	31.8 ± 0.3	5.0 ± 0.2	4.6 ± 0.7
V	319 ± 13	318 ± 2	120 ± 2	128 ± 6
Cr	286 ± 25	287 ± 3	31 ± 3	30 ± 3
Mn	1333 ± 55	1309 ± 15	250 ± 6	263 ± 31
Co	45.4 ± 2.4	44.9 ± 0.3	11.4 ± 0.1	11.8 ± 1.5
Ni	120 ± 4	120 ± 1	30.2 ± 1.3	-
Cu	124 ± 3	120 ± 1	69 ± 5	66 ± 9
Zn	102 ± 3	104 ± 1	72 ± 2	74 ± 9
Rb	9.1 ± 0.2	9.3 ± 0.1	79 ± 3	83 ± 6
Sr	394 ± 9	394 ± 2	398 ± 6	420 ± 30
Mo	4.1 ± 0.6	4.1 ± 0.2	35.5 ± 1.2	35.1 ± 0.9
Cd	-	-	1.16 ± 0.13	1.14[#]
Ba	132 ± 5	131 ± 1	300 ± 17	290 ± 40
Th	1.18 ± 0.04	1.22 ± 0.02	4.8 ± 0.4	4.8 ± 0.2
U	0.41 ± 0.02	0.41 ± 0.04	5.3 ± 0.1	5.4 ± 0.4
La	15.3 ± 0.5	15.2 ± 0.1	19.1 ± 0.3	20.3 ± 1.8
Ce	37.4 ± 1.7	37.5 ± 0.2	33.2 ± 0.4	36 ± 4
Pr	5.38 ± 0.26	5.34 ± 0.03	-	-
Nd	24.1 ± 0.9	24.3 ± 0.2	14.7 ± 0.2	15.5 ± 1.7
Sm	6.05 ± 0.26	6.02 ± 0.06	2.6 ± 0.1	2.7 ± 0.3
Eu	2.06 ± 0.08	2.04 ± 0.01	0.52 ± 0.10	0.56 ± 0.09
Gd	6.15 ± 0.26	6.21 ± 0.04	-	-
Tb	0.94 ± 0.04	0.94 ± 0.01	0.33 ± 0.01	0.36 ± 0.04
Dy	5.31 ± 0.24	5.28 ± 0.03	-	-
Ho	1.00 ± 0.04	0.99 ± 0.01	-	-
Er	2.52 ± 0.09	2.51 ± 0.01	-	-
Tm	0.338 ± 0.012	0.335 ± 0.003	-	-
Yb	1.99 ± 0.09	1.99 ± 0.03	-	-
Lu	0.281 ± 0.007	0.275 ± 0.002	-	-

**USGS Reference Information sheet [#]Hu and Gao, 2008*

Table 2.6. Comparison of trace elemental data for replicate samples.

Sample ID*	Aliquot	Sc	V	Cr	Mn	Co	Ni	Cu	Zn	Zr	Mo	Y	Th	U	Sr	Ba
		µg/g														
HM15-11B	(i)	11.1	102	63	264	11.6	56	35	84	187	15.9	24.9	12.7	7.8	83	392
	(ii)	11.6	101	64	264	11.6	55	34	89	197	15.9	22.9	13.4	7.6	87	336
HM15-13B	(i)	11.5	103	66	259	10.3	40	33	80	187	15.9	24.6	12.7	7.1	65	467
	(ii)	10.6	105	66	262	11.3	42	34	85	195	16.3	24.9	13.1	7.2	68	460
HM15-20A	(i)	11.9	96	63	307	10.7	43	28	96	183	13.4	24.9	13.5	8.1	91	651
	(ii)	11.6	97	61	310	9.9	41	27	93	179	13.3	25.0	12.9	8.0	86	693
CDP21-17	(i)	5.2	191	74	76	9.5	41	24	49	258	6.7	13.1	7.8	2.7	15	406
	(ii)	5.4	198	75	74	9.6	42	26	52	269	6.9	13.2	8.4	2.6	16	416
CDP21-23	(i)	5.4	184	95	17	10.3	46	41	63	309	7.1	12.3	10.3	2.7	10	1074
	(ii)	5.3	186	94	17	10.0	45	39	57	285	7.1	11.6	10.3	2.5	10	1011
CDP21-108A	(i)	18.0	140	115	532	15.3	49	8	160	156	0.6	24.2	14.2	3.5	25	309
	(ii)	17.0	140	114	542	15.4	50	8	175	160	0.6	24.1	13.7	3.5	25	301
VIN22-25A	(i)	8.4	48	52	212	8.8	28	14	73	83	0.2	9.7	10.0	2.2	37	189
	(ii)	8.8	49	54	221	9.1	29	15	75	88	0.2	10.0	10.0	2.2	39	194
VIN22-07A	(i)	9.6	186	35	31	4.0	26	13	55	165	23.1	47.9	9.9	20.4	51	462
	(ii)	8.8	177	34	30	3.8	26	13	52	161	23.7	47.2	10.2	20.9	48	450

**A, B and C represent different powdering aliquots of the same sample*

Table 2.7. REE concentration data of replicate digestion aliquots.

Sample ID*	Aliquot	La	Ce	Pr	Nd	Sm	Eu	Gd	Tb	Dy	Ho	Er	Tm	Yb	Lu
		µg/g													
HM15-11B	(i)	35.9	72.5	8.6	30.6	5.6	1.0	5.0	0.7	4.3	0.9	2.6	0.4	2.4	0.4
	(ii)	35.0	66.8	8.1	29.4	5.3	1.0	4.6	0.7	4.0	0.8	2.5	0.4	2.3	0.4
HM15-13B	(i)	32.2	64.5	7.4	27.3	5.3	1.0	4.2	0.7	3.9	0.8	2.6	0.4	2.2	0.4
	(ii)	34.2	68.8	8.0	28.7	5.6	1.0	4.5	0.7	3.8	0.8	2.5	0.4	2.3	0.4
HM15-20A	(i)	28.4	55.3	6.8	24.4	5.4	1.0	4.6	0.7	4.1	0.8	2.5	0.4	2.2	0.4
	(ii)	26.6	53.0	6.4	23.3	5.4	1.0	4.3	0.7	4.0	0.8	2.6	0.4	2.1	0.4
CDP21-17	(i)	9.9	17.5	2.3	8.8	2.0	0.5	2.0	0.3	1.9	0.4	1.2	0.2	1.4	0.2
	(ii)	8.9	15.1	2.2	8.4	1.9	0.5	2.0	0.3	2.0	0.4	1.3	0.2	1.4	0.2
CDP21-23	(i)	32.6	59.4	7.2	24.2	4.1	0.8	3.4	0.4	2.3	0.5	1.34	0.2	1.3	0.2
	(ii)	30.5	54.8	6.6	22.2	3.8	0.7	3.3	0.4	2.2	0.4	1.24	0.2	1.3	0.2
CDP21-108A	(i)	40.3	76.9	8.8	31.2	5.6	1.2	5.1	0.7	4.1	0.8	2.35	0.4	2.2	0.3
	(ii)	37.5	73.5	8.5	29.7	5.4	1.2	4.9	0.6	4.0	0.8	2.35	0.3	2.2	0.3
VIN22-25A	(i)	5.8	13.4	1.7	6.2	1.4	0.3	1.3	0.2	1.40	0.3	1.0	0.2	1.0	0.2
	(ii)	5.9	13.5	1.6	6.2	1.4	0.3	1.3	0.2	1.39	0.3	0.9	0.2	1.0	0.2
VIN22-07A	(i)	40.8	80.6	10.3	35.5	5.5	1.2	6.0	1.1	7.25	1.7	5.3	0.8	5.3	0.8
	(ii)	40.3	80.4	10.3	34.9	5.7	1.2	6.0	1.0	7.32	1.7	5.3	0.9	5.4	0.8

**A, B and C represent different powdering aliquots of a sample*

2.3.2.2. Carbon, Nitrogen and Sulfur analysis

Total Carbon (TC), Total Nitrogen (TN) and Total Sulfur (TS) measurements were carried out using an elemental analyzer (Elementar vario Pyro Cube) at IISER Pune. For this, a known amount (~30 mg) of bulk sample powder, along with an oxidant (WO_3), was packed in tin foil and combusted at 1150°C. The amounts of CO_2, N_2, and SO_2 gases that evolved during this process were calibrated using a linear fit between the analyte quantity and the measured peak areas for a standard to determine the concentrations for the samples. The accuracy of the analysis was estimated by repeat analysis (n = 26) of shale standard SGR-1b which yield overlapping TC (26.98 ± 0.30 wt%), TN (0.84 ± 0.04 wt%) and TS (1.50 ± 0.06 wt%) values to its reported values (TC = 27.24 ± 0.31 wt%, TN = 0.88 to 0.91 wt% and TS = 1.46 ± 0.12 wt%; Han et al., 2017; Stüeken et al., 2020). The average precision of these measurements, based on replicate sample analyses, was found to be ±4% (n = 24).

The Total Inorganic Carbon (TIC) content of the samples was determined using a coulometer (UIC Inc. CO_2 Coulometer; Tripathy et al., 2014). For this experiment, ~30 mg of bulk sample powder was treated with 5% ortho-phosphoric acid at 80°C. The amount of CO_2 liberated during this process was passed into a coulometer cell and quantified using electrochemical titration. The calibration of the instrument was done using known amounts of Na_2CO_3, which was also used to check the accuracy and reproducibility of the experiment between sample measurements. Repeat analysis of samples produced a precision of ~4% (n = 10).

2.3.2.3. Iron Speciation and Degree of Pyritisation (DOP)

Iron Speciation analysis was carried out following the analytical methodology of Poulton and Canfield (2005) and is outlined in Table 2.8. In this method, the amount of biogeochemically active Fe (Fe_{HR}) is calculated by sequential extraction and quantification of iron pools associated with sulfide (Fe_{Py}), carbonate (Fe_{carb}), oxide (Fe_{ox}) and magnetite (Fe_{mag}) phases. Towards this, about 50 to 100 mg of bulk sample powders were weighed into 50 ml centrifuge tubes and sequentially treated with a fixed volume (15 ml) of sodium acetate, sodium dithionite and ammonium oxalate solutions (Fig. 2.10). After each step, the samples were centrifuged, and the supernatants were collected to determine their Fe contents. The first step involved treatment with 1M sodium acetate solution (buffered to a pH of 4.5 using acetic acid) for 48 hours at a temperature of 50°C in a water bath. This step extracts iron associated with

carbonate (Fe_{carb}) phases such as siderite and ankerite. During this step, the samples were periodically sonicated and degassed to remove the CO_2 during initial carbonate dissolution. The residues from this step were then treated with 0.05% sodium dithionite solution (pH = 4.8) buffered with 0.35M acetic acid and 0.2M sodium citrate for 2 hours. The sodium dithionite solution was always prepared immediately prior to use in order to avoid the oxidation of the solution and reduction in its extraction potential. This step extracts iron associated with oxides (Fe_{ox}) such as goethite, akaganeite, and hematite. The last step involved treatment of the residues from step 2 with 0.2M ammonium oxalate/0.17M oxalic acid solution (pH = 3.2) for 6 hours. This step extracts Fe associated with magnetite (Fe_{mag}) phases. During the extraction period, the samples were always kept under constant agitation by means of a shaker table. The solutions collected after each extract were diluted (~5 to 10 times) using 0.3N HNO_3, and their Fe contents were determined using an Atomic Absorption Spectrometer (ThermoFisher iCE 3500) using a standard calibration approach. Different dilutions of a single-element standard solution were prepared and measured to create a standard calibration line for Fe. All the solutions were aspirated into an air-acetylene flame (T = 2300°C) and quantified using the characteristic absorption line of Fe (248.33 nm).

Table 2.8. Overview of the iron extraction protocol followed in this study (after Poulton and Canfield, 2005).

Iron Phase	Reagent/Methodology	Terminology
Carbonates (Siderite, Ankerite)	Sodium acetate (pH = 4.5 ± 0.1)	Fe_{carb}
Oxides (Ferrihydrite, Hematite, Goethite)	Sodium dithionite (pH = 4.8 ± 0.1)	Fe_{ox}
Magnetite	Ammonium oxalate (pH = 3.2 ± 0.1)	Fe_{mag}
Pyrite	Chromous chloride distillation	Fe_{Py}
Reactive Iron	Boiled concentrated HCl	Fe_R
Total Iron	XRF	Fe_T

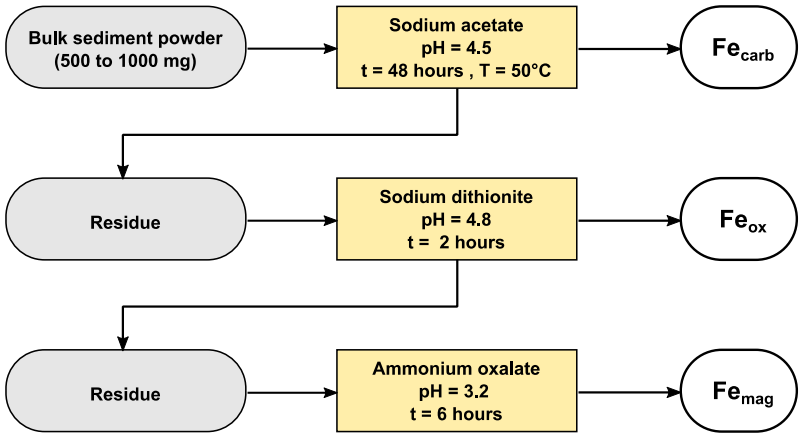

Figure 2.10. *Flow chart illustrating the iron speciation methodology followed in this study (after Poulton and Canfield, 2005).*

Pyrite-bound Iron (Fe_{Py}) was determined separately on bulk powders by quantifying the amount of Fe extracted during a chromous chloride distillation (Canfield et al., 1986). For this, 1M chromium chloride prepared in 0.5N HCl solution was used. Prior to analysis, this solution was added into a glass flask containing ~50 g of zinc shots/granular zinc and purged with N_2 for ~2 hours to enable the conversion of chromium chloride to chromous chloride (Fig. 2.11a). The chromous chloride solution was stored in glass BOD bottles (Borosil) and was always used within 48 hours. The distillation apparatus consists of a reaction vessel made of a three-neck glass round bottom flask (Borosil) kept over a heating mantle (Fig. 2.11b). The main aperture of the vessel was connected to a water-cooled condensation unit, which led to a sulfide trap composed of 40 ml solution of 10% NH_4OH and 5% $AgNO_3$ mixture. The other apertures were connected to a gas line for N_2 (99.99%) bubbling and a dropping funnel for reagent introduction. For the extraction, 500 to 1000 mg of sample (estimated based on sulfur content) along with 10 ml of ethanol was taken in the reaction vessel, connected to the apparatus and flushed with N_2 gas to remove traces of air. The occurrence of Acid Volatile Sulfur (AVS) was checked by the addition of ~10 ml 6N HCl solution and subsequent heating of the reaction vessel. If no precipitates were found in the trap solution, a mixture of 1M chromous chloride (35 ml) and 12M HCl (15 ml) was added to the reaction vessel for 2 hours. The liberated H_2S from this reaction was trapped as silver sulfide (Ag_2S) by bubbling through the silver nitrate trap solution. These precipitates were filtered using a vacuum filtration system, thoroughly washed with de-ionized water and dried at 60°C. Fe associated with pyrite (Fe_{Py}) was then calculated gravimetrically by weighing the silver sulfide precipitates, assuming a stoichiometry of FeS_2. The amount of highly reactive iron pool (Fe_{HR}) is calculated by adding the Fe content of the individual extractions ($Fe_{HR} = Fe_{carb} + Fe_{ox} + Fe_{mag} + Fe_{Py}$). The amount of HCl reactive iron (Fe_{HCl}) was determined by treating samples with boiling 12N HCl (Berner, 1970). The Degree of Pyritization (DOP) value for these samples was computed (Berner, 1970) as follows:

$$DOP = \frac{Fe_{Py}}{Fe_{Py}+Fe_{HCl}} \quad (2.3)$$

The efficiency of all the Fe-extractions was monitored by replicate extractions of reference material WHIT (Alcott et al., 2020), which gave an accuracy within ±7% (n = 15) from the reported values (Table 2.9). Replicate extractions of sample aliquots gave a reproducibility within ±5% (n = 11).

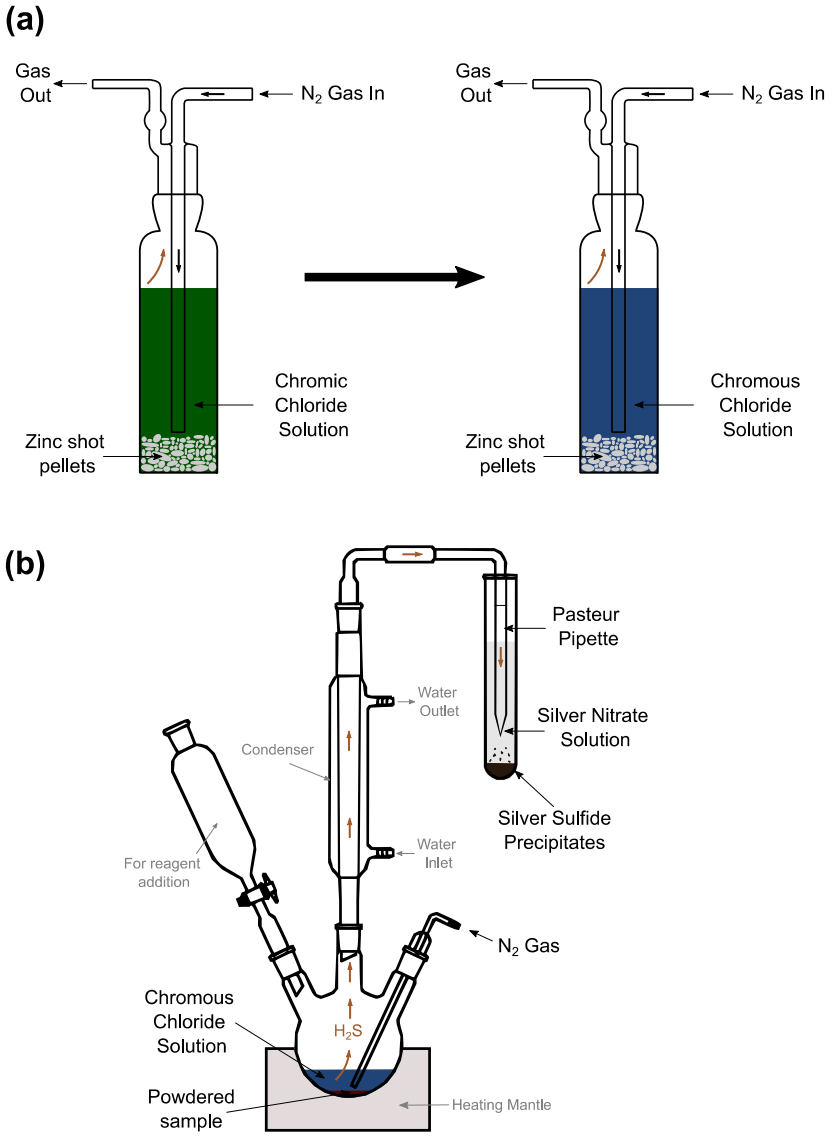

Figure 2.11. *Schematics of* ***(a)*** *chromic to chromous chloride conversion and* ***(b)*** *the experimental setup for pyrite extraction (after Canfield et al., 1986).*

Table 2.9. Comparison of measured and reported iron speciation dataset of reference material WHIT.

Iron phase	Measured value (wt%)	Reported Value* (wt%)
Fe_{carb}	0.56 ± 0.02	0.58 ± 0.03
Fe_{ox}	0.064 ± 0.004	0.062 ± 0.009
Fe_{mag}	0.10 ± 0.01	0.10 ± 0.01
Fe_{Py}	1.93 ± 0.09	1.97 ± 0.09
Fe_{HCl}	1.00 ± 0.05	0.97 ± 0.10

**Alcott et al., 2020; Errors are reported in 1σ.*

2.3.3. Isotopic analyses

2.3.3.1. Bulk Nitrogen, Organic Carbon and Pyrite Sulfur isotopic measurements

Carbon, Nitrogen and Sulfur isotopic compositions were determined using the EA-IRMS facility at IISER Pune following published protocols (Venugopal et al., 2023). Nitrogen isotopic compositions ($\delta^{15}N_{bulk}$) were determined on the bulk sample powders. For organic carbon isotopic analysis, the samples were first decarbonated to obtain carbonate-free fractions. Towards this, ~1 g of powdered sample was treated with 0.6N HCl at ~80°C for 2 hours, followed by rinsing with de-ionized water. This step was repeated thrice to completely remove traces of carbonate minerals in the samples. The residue was dried at 60°C in a hot air oven, homogenized using an agate mortar and stored. This powder was then used for determining the isotopic composition of organic carbon ($\delta^{13}C_{org}$) in the samples. For obtaining the pyrite-sulfur isotopic compositions ($\delta^{34}S_{Py}$), analyses were carried out on the dried and homogenized silver sulfide extracts obtained during the chromous chloride distillation process (cf. Section 2.3.2.3).

For all the isotopic determinations, the powdered fractions were packed in tin foil and mixed with equal amounts (by weight) of an oxidation catalyst (Tungsten oxide) and combusted at 1150°C in an elemental analyzer (Elementar vario Pyro Cube) that was coupled to a continuous flow Isotope Ratio Mass Spectrometer (Elementar Isoprime precisION). Isotopic signals of sample and reference gases were detected at masses 28, 29 and 30 for nitrogen; 44, 45 and 46 for carbon; 64 and 66 for sulfur. The isotopic measurements are reported in delta notation (in ‰ units) as follows:

$$\delta = \left(\frac{R_{sample} - R_{standard}}{R_{standard}}\right) \times 1000 \quad (2.4)$$

where, R is either $^{15}N/^{14}N$, $^{13}C/^{12}C$ or $^{34}S/^{32}S$. Nitrogen isotopes are expressed as $\delta^{15}N$ relative to atmospheric N_2 (Air), carbon isotopes as $\delta^{13}C$ relative to Vienna Pee Dee Belemnite (V-PDB), and sulfur isotopes as $\delta^{34}S$ relative to Vienna Cañon Diablo Troilite (V-CDT). The measured isotopic values were calibrated against several laboratory standards (Sulfanilamide, Merck Sucrose, Fluka Sucrose, Silver Sulfide, Barium Sulfate and Ammonium Sulfate), which were already calibrated with respect to international standards. The reported isotopic compositions for the international standards are as follows: IAEA-CH-3 ($\delta^{13}C$ = −24.72 ± 0.04‰), IAEA NO_3 ($\delta^{15}N$ = +4.7 ± 0.2‰), USGS 25 ($\delta^{15}N$ = −31.40 ± 0.27‰), IAEA-S1 (−0.30 ± 0.03‰), IAEA-S2 (+22.62 ± 0.08‰) and IAEA-S3 (−32.49 ± 0.08‰).

Samples, bracketed by the laboratory standards, were run in batches of 10. The long-term precision of these internal standards, measured over the course of the analysis, was found to be better than 0.09‰ for carbon (1σ, n = 82), 0.28‰ for nitrogen (1σ, n = 49), and 0.31‰ for sulfur (1σ, n = 52). The accuracy of these measurements was constrained by measuring USGS reference material SGR-1b (Fig. 2.12) which yield $\delta^{15}N$ = +17.43 ± 0.14‰ (1σ, n = 18) and $\delta^{13}C$ = −24.79 ± 0.14‰ (1σ, n = 15), consistent with the reported values ($\delta^{15}N$ = +17.43 ± 0.17‰ and +17.80 ± 0.35‰; $\delta^{13}C$ = −25.02 ± 0.47‰; Han et al., 2017; Stüeken et al., 2020). Reproducibility of the isotopic analysis, determined by replicate sample analysis, was 0.28‰ for nitrogen (1σ, n = 12), 0.09‰ for carbon (1σ, n = 13), and 0.31‰ for sulfur (1σ, n = 11) measurements (Table 2.10).

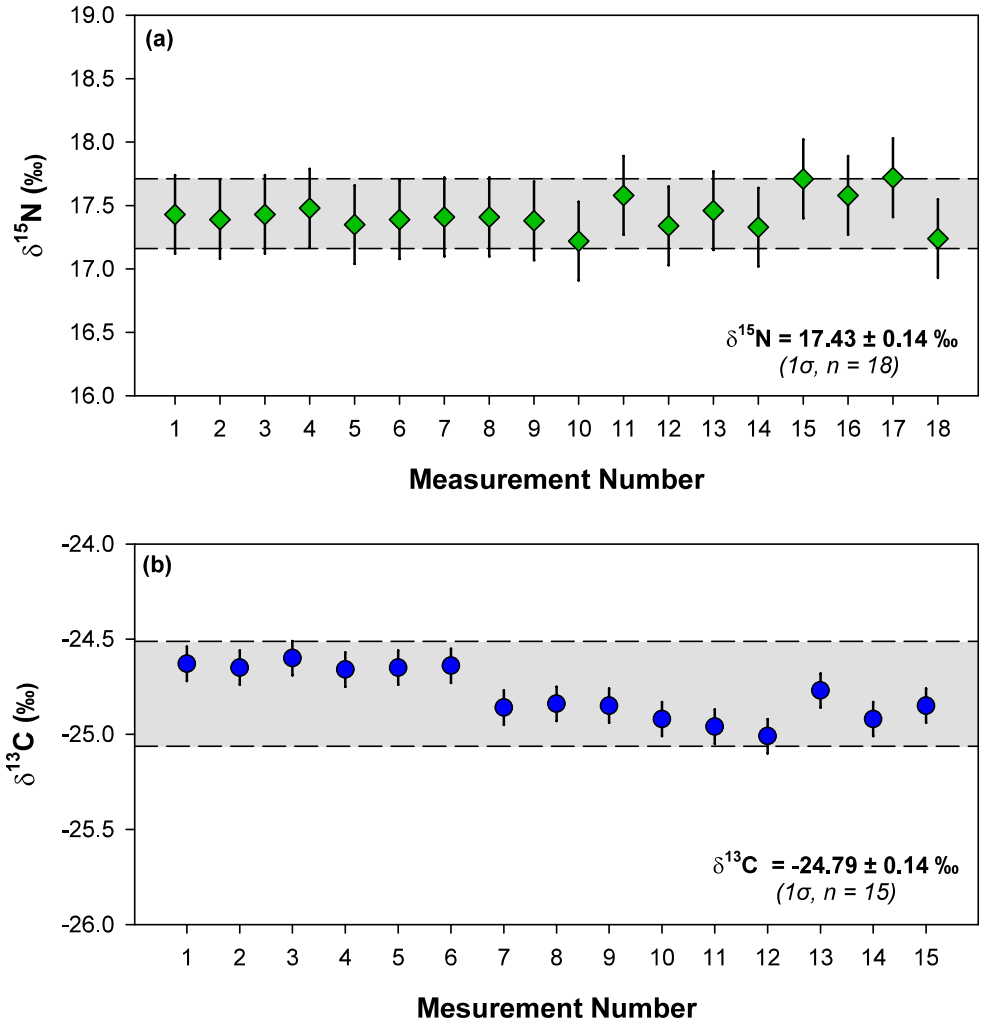

***Figure 2.12**. Measured bulk **(a)** nitrogen and **(b)** carbon isotopic data for USGS SGR-1b. The grey-shaded region represents the 2σ interval.*

Table 2.10. Replicate analyses of bulk Nitrogen ($\delta^{15}N_{bulk}$), organic carbon ($\delta^{13}C_{org}$), and pyrite-S ($\delta^{34}S_{Py}$) isotopic data.

Sample ID	Aliquot	$\delta^{15}N_{bulk}$ (Air) ‰
HM15-10A	(i)	1.16
	(ii)	0.90
HM15-11A	(i)	0.96
	(ii)	0.97
HM15-12A	(i)	0.70
	(ii)	0.74
HM15-14A	(i)	1.26
	(ii)	1.09
HM15-17A	(i)	0.85
	(ii)	1.00
CDP21-17	(i)	7.60
	(ii)	7.33
CDP21-128	(i)	7.96
	(ii)	8.12
CDP21-135	(i)	7.65
	(ii)	7.65
CDP21-140	(i)	6.97
	(ii)	6.88
CDP21-137	(i)	6.35
	(ii)	6.66
VIN22-29C	(i)	2.27
	(ii)	2.07
VIN22-11B	(i)	1.77
	(ii)	1.55

Sample ID	Aliquot	$\delta^{13}C_{org}$ (V-PDB) ‰
HM15-12A	(i)	–31.14
	(ii)	–31.15
HM15-17B	(i)	–29.70
	(ii)	–29.70
HM15-01B	(i)	–28.00
	(ii)	–27.99
HM15-10B	(i)	–31.14
	(ii)	–31.15
HM15-16A	(i)	–29.94
	(ii)	–30.00
HM15-16B	(i)	–29.94
	(ii)	–30.00
CDP21-23	(i)	–30.21
	(ii)	–30.19
CDP21-128	(i)	–30.85
	(ii)	–30.83
CDP21-135	(i)	–30.56
	(ii)	–30.38
CDP21-99A	(i)	–33.08
	(ii)	–33.07
VIN22-29B	(i)	–24.36
	(ii)	–24.21
VIN22-33A	(i)	–32.69
	(ii)	–32.67
VIN22-07A	(i)	–31.70
	(ii)	–31.79

Sample ID	Aliquot	$\delta^{34}S_{Py}$ (V-CDT) ‰
HM15-21B	(i)	7.95
	(ii)	7.98
HM15-16B	(i)	5.06
	(ii)	5.25
HM15-16A	(i)	4.43
	(ii)	4.31
HM15-13B	(i)	4.72
	(ii)	4.91
HM15-21A	(i)	7.42
	(ii)	7.20
HM15-10A	(i)	4.86
	(ii)	4.50
CDP21-22	(i)	13.94
	(ii)	13.90
CDP21-37	(i)	8.02
	(ii)	7.94
CDP21-132	(i)	23.79
	(ii)	23.69
CDP21-142	(i)	10.45
	(ii)	10.16
CDP21-17	(i)	15.31
	(ii)	15.10

2.3.3.2. Molybdenum isotopic analysis

Mo isotopic analyses were carried out in the acid-digested sample solutions used for trace element measurements following a double spike method (Siebert et al., 2001; Rudge et al., 2009; Rahaman et al., 2014; Goswami et al., 2022) at the Physical Research Laboratory, Ahmedabad, India. Based on the measured Mo concentration, precisely weighed sample solutions were mixed with an appropriate amount of ^{97}Mo–^{100}Mo double spike solution and allowed for sample-spike equilibration. Subsequently, pure Mo was extracted from the sample-spike mixture using anion exchange chromatography (Biorad AG1-X8 resin; Pearce et al., 2009; Table 2.11).

Table 2.11. Molybdenum purification scheme adopted in this study (after Pearce et al., 2009).

Step	Reagent	Volume
		ml
Cleaning	1N HCl	32
Conditioning	1N HF + 0.5 N HCl	4
Sample Loading	1N HF + 0.5 N HCl	6
Washing/Rejection	1N HF + 0.5 N HCl	8
	4N HCl	16
Collection	3N HNO_3	10

The Mo isotopic composition of samples was measured using a MC-ICP-MS (Thermo Neptune Plus) in low-resolution mode. Sample solutions having Mo concentration of ~50ng/ml were introduced into the MC-ICP-MS instrument through an APEX-HF (Elemental Scientific Inc.) desolvating nebulizer system. The measurement was carried out in blocks of 10, each with 10 cycles per block. For each cycle, the integration time was set to 8s with an idle time of 3s. All seven Mo isotopes, ^{92}Mo, ^{94}Mo, ^{95}Mo, ^{96}Mo, ^{97}Mo, ^{98}Mo, and ^{100}Mo, were measured using a static multi-collection mode. In addition, signals of ^{91}Zr and ^{99}Ru were also constantly monitored to check the isobaric interference on Mo isotopes. After each sample analysis, the system was rinsed with 0.4N HNO_3 until the signals matched the initial background levels. The measured data was corrected offline employing the MATLAB algorithms of Rudge et al. (2009) for instrumental mass bias to obtain the Mo isotopic abundances of samples (Goswami et al., 2022). Finally, the Mo isotopic composition is reported in a delta notation relative to NIST SRM 3134 with a positive offset of +0.25‰ (Nägler et al., 2014):

$$\delta^{98}Mo = \left[\frac{\left(^{98}Mo/^{95}Mo\right)_{sample}}{\left(^{98}Mo/^{95}Mo\right)_{SRM3134}} - 1\right] \times 1000 + 0.25\ ‰ \quad (2.5)$$

The internal precision of the measurements was always better than ±0.04‰ ($2\sigma_\mu$). External precision of Mo isotopic analyses was constrained by measuring replicate samples and was found to be ±0.05‰ (Table 2.12). Procedural blanks, determined by using the Mo double spike solution, yield values that were two orders of magnitude lower than the total Mo processed and hence, were unlikely to have any measurable impact on the Mo isotopic data within its precision level (Table 2.13). A certified reference material, USGS SDO-1, was also measured repeatedly during the course of the analyses. The average δ^{98}Mo values of this standard is found to be 1.04 ± 0.15‰ (1σ, n = 5; Table 2.14), and this is consistent with the values reported by other studies, which range from 0.98‰ to 1.41‰ (Duan et al., 2010; Barling et al., 2001; Goldberg et al., 2013; Goswami et al., 2022).

Table 2.12. Results of replicate δ^{98}Mo measurements of sample aliquots.

Sample ID	Aliquot	δ^{98}Mo*
		‰
CDP21-23	(i)	0.66 ± 0.02
	(ii)	0.64 ± 0.02
CDP21-129	(i)	0.60 ± 0.03
	(ii)	0.59 ± 0.02
CDP21-140	(i)	0.77 ± 0.03
	(ii)	0.75 ± 0.03

**Errors are in $2\sigma_\mu$*

Table 2.13. Total analytical blank for Mo isotopic measurements.

Sample ID	Mo
	ng
TAB 1	1.9
TAB 2	1.4
TAB 3	1.1
TAB 4	1.3
TAB 5	1.3
TAB 6	1.2
TAB 7	1.3
Average	**1.4 ± 0.3**

Table 2.14. δ^{98}Mo values for USGS reference material SDO-1 measured during this study.

Sample ID	δ^{98}Mo
	‰
SDO-1-A	1.30
SDO-1-B	1.01
SDO-1-C	0.94
SDO-1-D	0.95
SDO-1-E	1.00
Average	**1.04 ± 0.15**

2.3.3.3. Re−Os concentrations and isotopic measurements

The Re–Os isotopic measurements were carried out on a commercial basis at the Institute of Geology of the Czech Academy of Sciences following the protocol outlined in Ackerman et al. (2019). In brief, about 0.1 g of powdered sample, along with a known amount of ^{185}Re–^{190}Os spike solution, was dissolved in a sealed Carius tube using CrO_3–H_2SO_4 mixture at 240°C for ~72 hours (Selby and Creaser, 2003). A solvent extraction approach involving CH_3Cl and HBr solutions was adopted to extract the osmium fraction from the digested solution, which was further purified using a micro-distillation method (Birck et al., 1997). Rhenium was isolated using a combination of acetone–sodium solution extraction followed by conventional anion-exchange (AG1-X8 resin) chromatography. Osmium isotopic analyses were carried out by negative thermal ionization mass spectrometry (Völkening et al., 1991; Creaser et al., 1991) using Thermo Triton Plus. The collected data were corrected for isobaric interferences, spike/blank contribution, and mass fractionation, whereas Os contents were calculated by an isotopic dilution. Rhenium concentrations were measured using a sector field ICP-MS instrument (Thermo Element 2) with precision on isotopic ratios always better than ±0.5% (2σ). The external reproducibility of Re–Os protocol monitored through the analyses of SBC-1 reference material (black shale; USGS) yielded values of Re = 10.95 ppb, Os = 99.3 ppt and ^{187}Os/^{188}Os of 5.23 ± 0.01, with all these values matching well with previously reported values (Li and Yin, 2019). The total procedural blanks for Re (18 pg) and for Os (1.7 pg) were insignificant, and hence no blank correction was carried out.

Chapter 3

Extent of ocean euxinia during the late Paleoproterozoic: Constraints from Re–Os and Mo isotopes

The Paleoproterozoic rise of atmospheric oxygen had a profound effect on eukaryotic life and seawater chemistry. Whilst this environmental transition provided sufficient molecular oxygen for eukaryotic emergence (Mentel and Martin, 2008; Albani et al., 2010; Mills et al., 2014; Butterfield, 2015), the prevalence of sulfidic seawater conditions during this period was hostile for complex life and possibly delayed the emergence of complex life for about 1000 Myr (Reinhard et al., 2016; Lyons et al., 2021; Fakhraee et al., 2023). The intensity of global sulfidic conditions during this time can be tracked by investigating the Mo isotopic composition of euxinic black shales. However, such studies for this period are still sparse, limiting a global comparison. This chapter presents the geochemical (major and trace elements, and iron-speciation) and Re–Os and Mo isotopic data for black shales from the late Paleoproterozoic Cumbum Formation, Cuddapah Basin. These datasets are used to constrain the (i) depositional age of the Cumbum Formation, (ii) the redox state of this semi-restricted basin, and (iii) the global extent of oceanic euxinia for the late Paleoproterozoic ocean. Discussions based on shale chemistry and isotopic datasets and their modelling are described below to establish the depositional age and environment for the basin.

3.1. Results

The geochemical and isotopic datasets for the Cumbum shales, Cuddapah Supergroup are provided in Tables 3.1, 3.2 and Appendix (Table A3.1). The TOC (1.1 ± 0.2 wt%) and TS (1.3 ± 0.4 wt%) concentrations of these shales are comparable to the Paleoproterozoic shale average (0.8 ± 0.8 wt% (n = 148) and 0.5 ± 0.7 wt% (n = 151); cf. Farrell et al., 2021). The TS contents show a general decrease in the stratigraphic section, while the TOC values mostly show limited variation (Fig. 3.1). Consequently, the TS/TOC ratios also vary from 0.3 and 1.6, hinting at changes in the depositional redox state of these shales. The TOC values exhibit a significant positive correlation with Al ($r = 0.61$, $p < 0.001$) but lack correlation with Si, Th, and Zr. The TIC values range from 0.1 to 3.0 wt% (average 0.9 ± 0.7 wt%) and show a general decrease up the stratigraphic section. TIC also shows positive correlations with Ca, Mg, Mn, and Sr ($r > 0.95$, $p < 0.001$). The total iron (Fe_T) concentrations (average 2.32 ± 0.23 wt%) and Fe_T/Al ratios (0.31 ± 0.07) are lower than that reported for the UCC (Fe_T ~3.9 wt%; Fe_T/Al ~0.48; Rudnick and Gao, 2003). The total iron contents of these shales are mainly comprised of pyritic phases (Fe_{Py} ~45%) with minimal contributions from oxides (e.g., goethite, hematite) and magnetite (Fe_{ox} and Fe_{mag} <2%) phases. The Fe_{Py} concentrations exhibit a positive correlation ($r = 0.87$, $p < 0.001$) with sulfur. The proportion of iron associated with reactive phases ($Fe_{HR} = Fe_{carb} + Fe_{ox} + Fe_{mag} + Fe_{Py}$) in the total iron pool (Fe_T) shows a general decrease

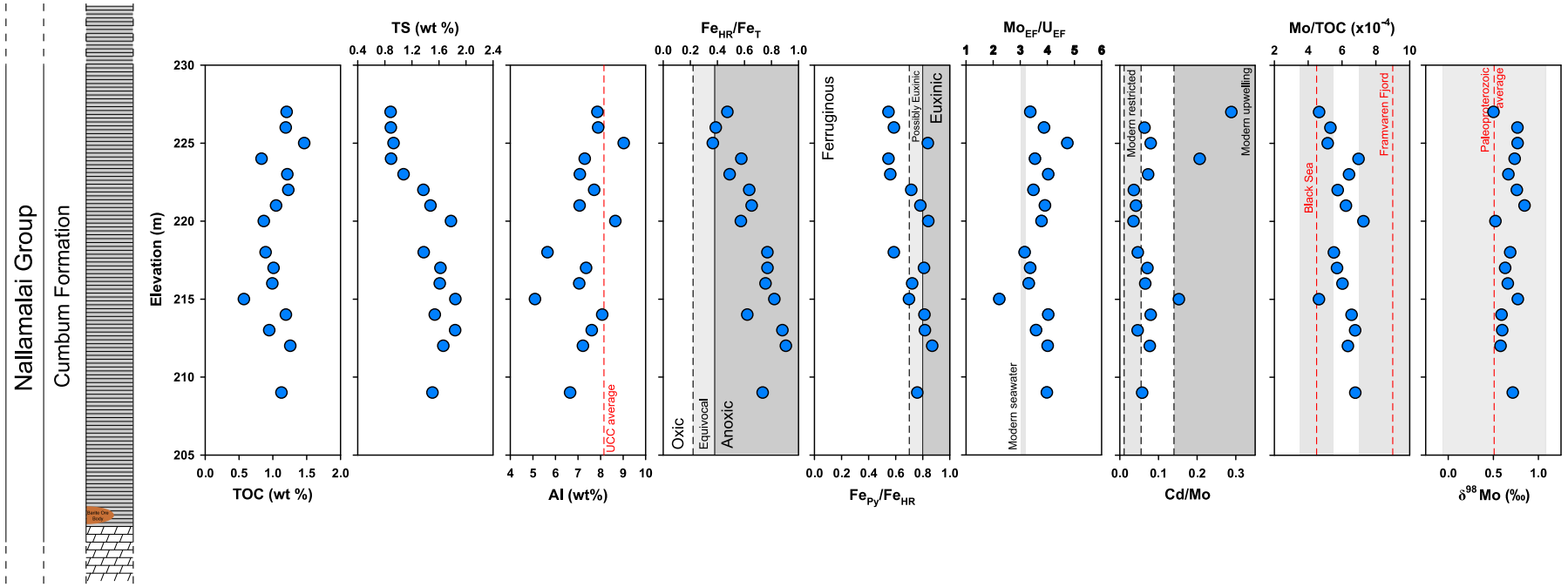

Figure 3.1. *Variation of selected geochemical parameters of the Cumbum shales collected in a stratigraphic order (n = 16). For reference, average values of Al in the UCC (Rudnick and Gao, 2003), modern aqueous seawater Mo/U (Algeo and Tribovillard, 2009), Fe-speciation thresholds (Raiswell et al., 2018), Cd/Mo values of modern restricted and upwelling settings (Sweere et al., 2016), and average δ^{98}Mo for Paleoproterozoic shales (Qin et al., 2022) are shown.*

up the stratigraphic section (Fig. 3.1). Figure 3.2 depicts enrichment factors for selected elements for the Cumbum shales, where a high degree of enrichment can be observed for several redox-sensitive elements (U, V, Mo, Cu, and Cd). The average enrichment factor for Mo (~6.5) is about four times higher than that observed for U (~1.5; Fig. 3.2). The Mo_{EF}/U_{EF} ratios of these samples, with no major stratigraphic variation, fall closer to that of the modern-day seawater values (Fig. 3.1). Additionally, the EFs for alkaline earth metals (Mg and Ba) are also higher than unity for these shales, which stratigraphically overlie a barite sequence.

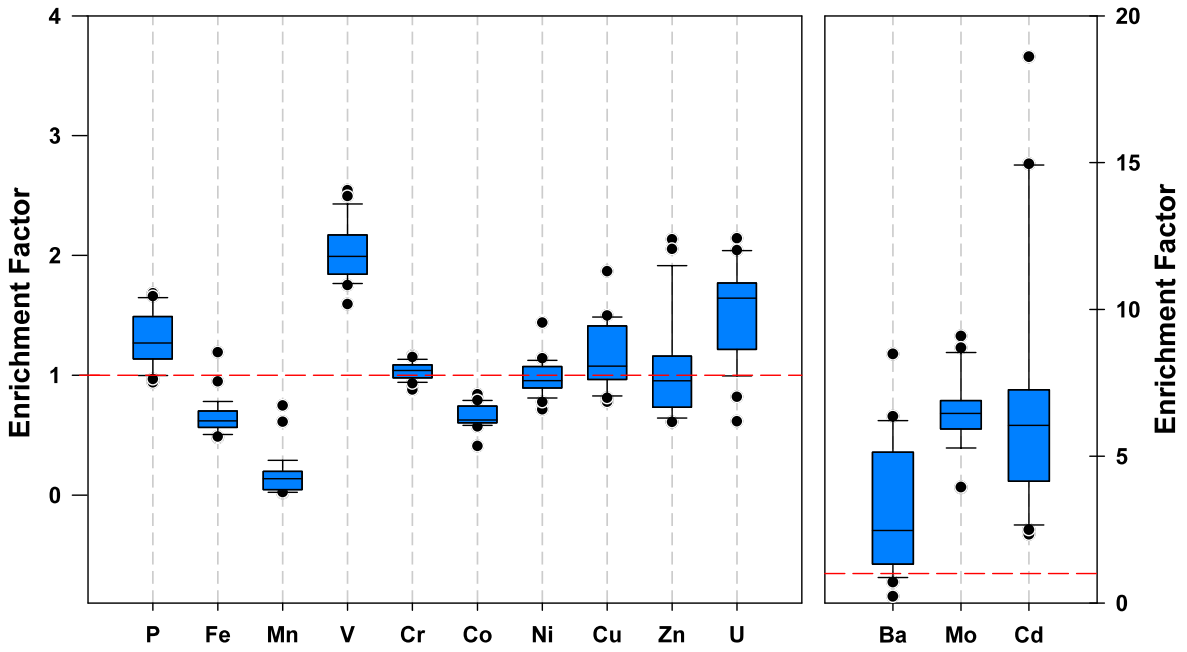

Figure 3.2. *Enrichment factors (X_{EF}) for selected major and trace elements of the Cumbum shales. The red dashed line indicates an enrichment factor of 1.*

The Re and Os concentrations vary between 11.6 and 17.7 ng/g, and 299 and 446 pg/g, respectively (Table 3.2). Both these elements exhibit a significant positive correlation with TOC ($r = 0.76$, $p < 0.01$ (for Re); $r = 0.69$, $p < 0.05$ (for Os)). The slope of the Re–TOC plot (~7.6 ppb/wt%) is comparable with that compiled for shales of overlapping (~0.6–2.0 Ga) age (~7 ppb/wt%; Sheen et al., 2018). Further, the average ^{192}Os/TOC value of these samples (49 ± 18 ppt/wt%) also overlaps with that for the Proterozoic shales (32 ± 16 ppt/wt%; Lu et al., 2017). The $^{187}Re/^{188}Os$ ratios of the Cumbum shale samples vary between 422 and 834, with an average value of 640 ± 128. The $^{187}Os/^{188}Os$ ratios span a large range between 11.96 and 23.53. These ratios are higher by an order of magnitude than that of the average crustal value (0.8 to 1.4; Esser and Turekian, 1993; Peucker-Ehrenbrink and Jahn, 2001). In addition, the $^{187}Os/^{188}Os$ ratios show a linear correlation with $^{187}Re/^{188}Os$ ratios. A bidirectional-uncertainty weighted

regression line between these two parameters (IsoplotR; Vermeesch, 2018) yields a Model 3 age of 1658 ± 50 Ma (2σ, MSWD = 69; n = 10, Fig. 3.3a) with an initial $^{187}Os/^{188}Os$ (Os_i) ratio of 0.03 ± 0.53 (2σ). The Model 3 age, here, indicates that the observed large uncertainty (MSWD > 1) in the age is not only due to analytical variabilities but also to geological factors. The Re−Os isochron for a subset of stratigraphically closer (~3 m) samples from the lower part of the section yields a precise Model 1 age of 1638 ± 21 Ma (2σ, n = 4, MSWD = 1.7; Fig. 3.3b) for the Cumbum shales. The Os_i ratio for this subset (0.27 ± 0.12; 2σ) falls intermediate to the modern riverine sources (~1.4), hydrothermal ($^{187}Os/^{188}Os$ = 0.11 to 0.39) and cosmic (~0.13) sources (Peucker-Ehrenbrink and Ravizza, 2000).

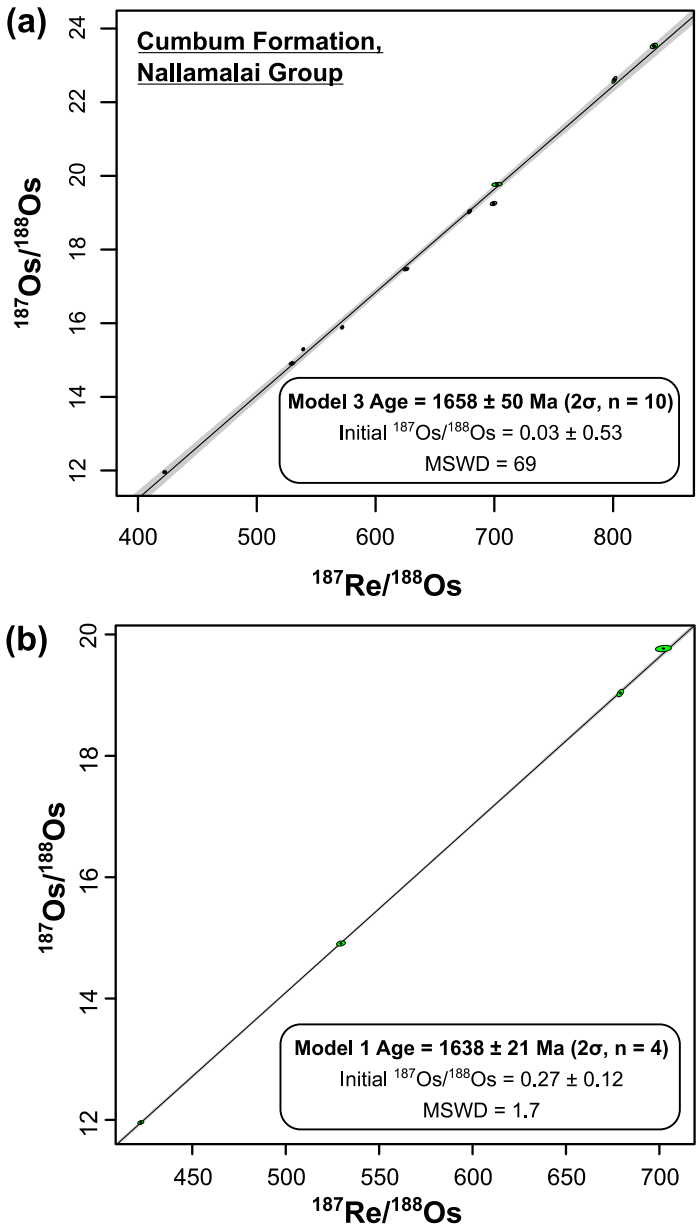

Figure 3.3. *Re–Os isochron of black shales from the Cumbum Formation, Nallamalai Group, Cuddapah Supergroup using* ***(a)*** *the entire sample set (n = 10), and* ***(b)*** *subset of samples (n = 4) from a stratigraphic depth of ~3 m. The sample subset yields a precise Model 1 age for the shales.*

The Mo concentrations of the shales vary widely (2.7 to 9.1 μg/g), and its average value (6.7 ± 1.2 μg/g) is about six times higher than that of the UCC (~1.1 μg/g; Rudnick and Gao, 2003). The Mo contents of the Cumbum shales correlate positively with TOC ($r = 0.57$; $p < 0.01$) and negatively with Mn ($r = -0.49$; $p < 0.01$). Molybdenum isotopic compositions ($\delta^{98}Mo$) range from +0.43‰ to +1.02‰ with an average value of +0.68 ± 0.13‰ (Fig. 3.4). This value is comparable to the average Paleoproterozoic shale value (+0.51 ± 0.57‰; n = 269; Qin et al., 2022), and about ~1.7‰ lower than the modern seawater $\delta^{98}Mo$ value (+2.34 ± 0.10‰; Nägler et al., 2014). The $\delta^{98}Mo$ values for the Cumbum shales show a good positive correlation with Mo/Al ($p < 0.01$) but are not correlated with Mn/Al, Fe_T/Al and Fe_{ox} ($p > 0.05$).

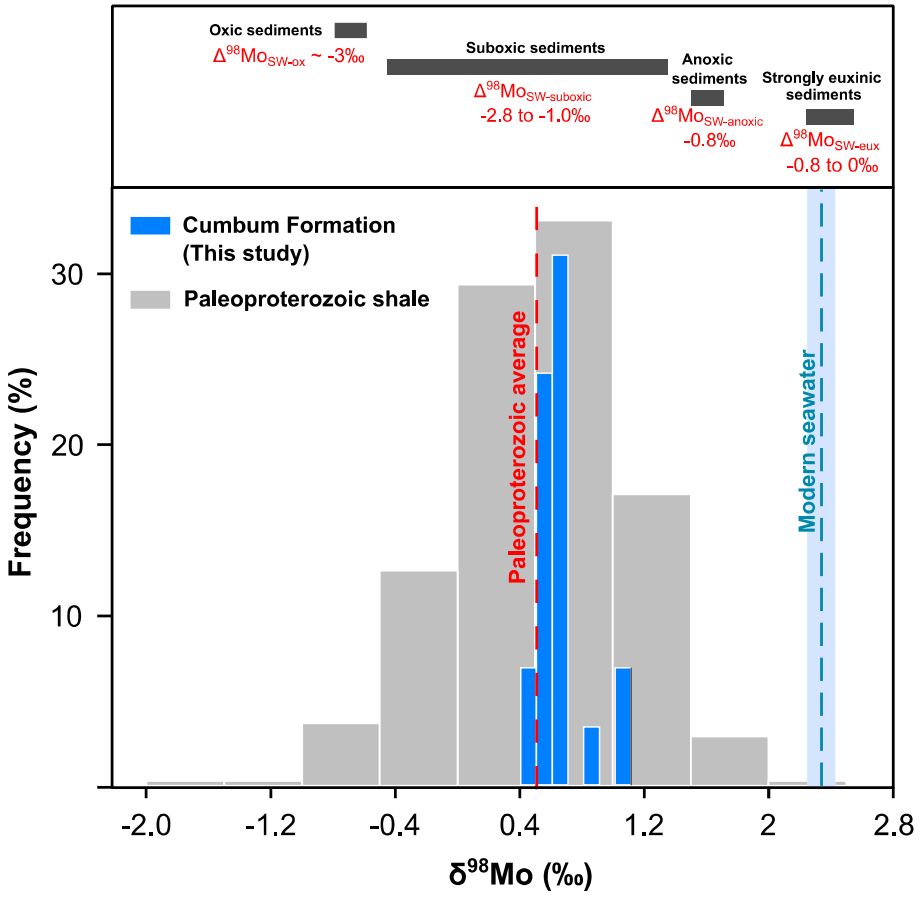

Figure 3.4. *Frequency distribution of the $\delta^{98}Mo$ values for the Cumbum shales. The global $\delta^{98}Mo$ distribution for Paleoproterozoic shales is also shown (Qin et al., 2022 and references therein) for comparison. Expected isotopic fractionation factors for removal pathways and ranges of $\delta^{98}Mo$ for modern sedimentary deposits from different depositional settings are provided (Dahl et al., 2021 and references therein).*

Table 3.1. Elemental, iron-speciation, and Mo isotopic data for black shales from the Cumbum Formation, Cuddapah Supergroup (India)

Sample ID	TOC	TIC	TS	Al	Fe_T	Mn	Co	Cd	U	Mo	Fe_{HR}/Fe_T	Fe_{Py}/Fe_{HR}	$\delta^{98}Mo$*
	wt%					µg/g							‰
CDP21-17	1.00	0.49	0.93	7.43	2.35	76	9.5	0.4	2.7	6.7	0.55	0.63	0.74 ± 0.02
CDP21-18	1.41	0.12	0.87	9.38	2.15	14	8.2	0.6	1.9	5.0	0.38	0.78	0.43 ± 0.02
CDP21-19	0.97	0.19	0.92	7.82	2.16	34	10.2	1.0	2.6	7.0	0.43	0.77	0.59 ± 0.02
CDP21-20	0.95	0.25	0.97	8.00	2.20	34	10.2	0.6	2.7	7.0	0.41	0.76	0.58 ± 0.02
CDP21-21	0.98	0.13	0.98	7.97	2.14	23	10.2	0.7	4.3	6.5	0.53	0.88	0.66 ± 0.02
CDP21-22	0.98	0.14	0.91	8.05	2.11	23	9.8	0.6	4.5	6.4	0.37	0.81	0.70 ± 0.02
CDP21-23	1.14	0.09	1.16	7.94	2.23	17	10.3	0.6	2.7	7.1	0.43	0.86	0.65 ± 0.02
CDP21-24	1.14	0.06	1.08	8.10	2.25	18	10.7	0.5	2.2	7.1	0.67	0.92	0.66 ± 0.02
CDP21-35	1.15	0.81	0.80	7.37	2.41	108	9.5	0.4	4.1	8.6	0.46	0.50	1.02 ± 0.02
CDP21-36	1.18	0.97	0.85	7.44	2.51	126	10.1	0.5	3.8	9.1	0.60	0.40	1.01 ± 0.02
CDP21-37	1.12	0.86	0.86	7.67	2.41	100	10.2	1.3	3.1	6.5	0.61	0.45	0.54 ± 0.02
CDP21-38	1.09	0.82	1.77	7.93	2.71	91	12.8	0.2	3.2	7.3	0.91	0.84	0.69 ± 0.02
CDP21-39	1.15	0.65	2.09	7.99	2.69	86	13.4	0.2	3.8	7.5	0.91	0.86	0.71 ± 0.02
CDP21-127	1.13	1.71	1.50	6.65	2.32	180	10.4	0.4	4.7	7.7	0.74	0.76	0.72 ± 0.02
CDP21-128	1.26	0.86	1.66	7.22	2.17	98	11.5	0.6	4.9	8.0	0.91	0.87	0.58 ± 0.02
CDP21-129	0.95	1.30	1.84	7.61	2.27	158	10.7	0.3	4.4	6.4	0.88	0.82	0.60 ± 0.02
CDP21-130	1.19	0.41	1.54	8.07	2.14	61	10.9	0.6	4.8	7.8	0.62	0.81	0.59 ± 0.02
CDP21-131	0.57	3.00	1.84	5.09	2.92	362	8.2	0.4	3.0	2.7	0.82	0.70	0.77 ± 0.02
CDP21-132	0.99	1.79	1.61	7.06	2.15	195	10.1	0.4	4.4	6.0	0.76	0.72	0.66 ± 0.02
CDP21-133	1.01	1.16	1.62	7.36	2.03	106	11.1	0.4	4.2	5.8	0.77	0.81	0.63 ± 0.02
CDP21-134	0.89	2.65	1.37	5.65	2.57	328	9.5	0.2	3.8	4.9	0.77	0.59	0.69 ± 0.02
CDP21-135	0.87	0.32	1.78	8.65	2.03	46	11.2	0.2	4.1	6.3	0.57	0.84	0.52 ± 0.02
CDP21-136	1.05	0.88	1.47	7.07	2.16	107	11.4	0.3	4.1	6.5	0.65	0.78	0.85 ± 0.02
CDP21-137	1.23	0.85	1.37	7.71	2.04	130	10.3	0.3	5.0	7.1	0.64	0.71	0.76 ± 0.02
CDP21-138	1.21	0.96	1.08	7.08	2.46	150	11.1	0.6	4.7	7.8	0.49	0.56	0.67 ± 0.02
CDP21-139	0.83	1.57	0.89	7.30	2.74	195	13.0	1.2	4.0	5.8	0.58	0.55	0.74 ± 0.02
CDP21-140	1.46	0.26	0.93	9.03	2.19	24	11.2	0.6	3.9	7.5	0.37	0.84	0.77 ± 0.02
CDP21-141	1.19	0.47	0.89	7.89	2.35	100	10.1	0.4	4.0	6.3	0.39	0.59	0.77 ± 0.04
CDP21-142	1.20	0.91	0.89	7.86	2.34	131	10.4	1.6	4.1	5.6	0.47	0.55	0.50 ± 0.02

**Errors are reported as $2\sigma_\mu$*

Table 3.2. Re and Os concentrations, and isotopic data for the black shales from the Cumbum Formation

Sample ID	Re	Os	^{192}Os	^{187}Re / ^{188}Os	^{187}Os / ^{188}Os	Rho#
	ng/g	pg/g	pg/g			
CDP21-128	17.74	445.68	56.41	625.6 ± 2.0	17.47 ± 0.04	0.33
CDP21-129	13.44	323.64	38.24	699.3 ± 2.2	19.25 ± 0.05	0.33
CDP21-130	16.32	434.78	61.31	529.6 ± 1.9	14.91 ± 0.03	0.29
CDP21-131	12.12	351.57	57.08	422.4 ± 1.3	11.96 ± 0.03	0.33
CDP21-132	15.52	379.40	43.97	702.2 ± 3.4	19.77 ± 0.04	0.21
CDP21-133	13.65	335.77	39.99	679.1 ± 1.4	19.03 ± 0.05	0.50
CDP21-134	14.13	334.16	35.08	801.0 ± 1.6	22.61 ± 0.07	0.62
CDP21-135	11.61	298.85	40.38	571.9 ± 1.0	15.89 ± 0.04	0.66
CDP21-136	16.93	396.14	40.36	834.3 ± 2.5	23.53 ± 0.06	0.37
CDP21-137	14.69	390.97	54.20	539.1 ± 0.7	15.29 ± 0.03	0.83

**Errors are in 2σ #Rho is the error correlation function*

3.2. Discussion

3.2.1. Re–Os geochronology of Cumbum shales

Re and Os in organic-rich shales, owing to their redox-sensitive nature, are mostly authigenic in nature. The radioactive ingrowth of ^{187}Os through β^- decay of ^{187}Re in these sedimentary deposits, therefore, serves as a reliable tool to determine their direct depositional age (Ravizza and Turekian, 1989; Kendall et al., 2009; Rooney et al., 2010; Georgiev et al., 2011; Tripathy and Singh, 2015; Rooney et al., 2024). This systematic in shales mostly remains unaltered during thermal metamorphism (up to greenschist facies; Kendall et al., 2004; Rooney et al., 2011) and organic matter maturation (Creaser et al., 2002; Selby and Creaser, 2005). Therefore, several studies have utilized the $^{187}Re–^{187}Os$ geochronometer successfully to date sedimentary sequences with depositional ages varying from Archean to Mesozoic (e.g., Yang et al., 2009; Kendall et al., 2009; Georgiev et al., 2011; Tripathy et al., 2018; Mandal et al., 2021).

A Re–Os isochron for the Cumbum shales, computed using IsoplotR (Vermeesch, 2018), provides a Model 3 age of 1658 ± 50 Ma (2σ, n = 10; Fig. 3.3a) whereas a subset of four samples with limited stratigraphic thickness (~3 m) provides a Model 1 age (1638 ± 21 Ma (2σ) Fig. 3.3b). The Model 1 age confirms that the data spread in the isochron is only due to analytical errors and, hence, represents the direct depositional age for the shales. This age is also in accordance with most of the existing chronological records (Fig. 2.5), except for one maximum age constraint for the underlying Bairenkonda Quartzite (~1550 Ma; Joy et al., 2015). The reported minimum ages for the Group, based on Rb−Sr age for (Vellaturu) granitic intrusion (1575 ± 20 Ma; Crawford and Compston, 1973), K−Ar age for phlogopite (1350 ± 52 Ma; Chalapathi Rao et al., 1996) and Ar−Ar age for phlogopite from (Chelima) lamproites (1418 ± 8 Ma; Chalapathi Rao et al., 1999), and Sm−Nd dating of apatite grains in syenites (1326 ± 73 Ma; Chalapathi Rao et al., 2012), are lower compared to the direct age obtained in this study (Fig. 2.5). Further, our Re−Os age is consistent with the age speculated earlier (late Paleoproterozoic to early Mesoproterozoic; Saha, 2002) for the timing of the deformation of the Nallamalai Group of rocks (~1600 Ma), acquired by correlating the structural features of xenoliths within the ~1575 Ma Vellaturu Granite (Crawford and Compston, 1973). Further, the youngest U–Pb ages for detrital zircon for the Group confirm deposition of the Nallamalai sediment around 1650 Ma (Collins et al., 2015), which is consistent with the depositional age (1638 ± 21 Ma) obtained for the Cumbum shales (Fig. 3.3).

The Re–Os isochron of Cumbum shales yields Os_i values of 0.03 ± 0.53 (2σ, n = 10) and 0.27 ± 0.12 (2σ, n = 4; Fig. 3.3). The (former) low Os_i value, with high uncertainty, overlaps with that reported for other Paleoproterozoic sections (0.11 to 0.13; Hannah et al. 2004, 2006), suggesting dominant Os supply from non-radiogenic magmatic/hydrothermal sources. Further, this value may also be attributed to riverine Os supply from juvenile crusts with a lower isotopic ratio than that of the present-day continental crust. A juvenile provenance has indeed been suggested for an underlying (Bairenkonda) Formation using Hf isotopic values of detrital zircons (Collins et al., 2015), which can partly explain the observed low Os_i value for the Model 3 isochron. The Model 1 isochron, however, provides a higher Os_i value for this restricted basin. Earlier studies have also reported elevated $^{187}Os/^{188}Os$ values for restricted basins than that of the open ocean, which was attributed to basinal restriction and related riverine supply at a regional scale (Dickson et al., 2022; Tanaka et al., 2022). For instance, Dickson et al. (2022) have used elevated Os_i values to quantify salinity drop in basins with limited seawater exchange. Consistently, the observed higher Os_i value for the Cumbum shale (~0.27) may also be related to the restricted character of the studied basin, where enhanced continental runoff with radiogenic $^{187}Os/^{188}Os$ signature may have played an important role. A mass balance calculation involving $^{187}Os/^{188}Os$ and salinity of river and seawater end-members, however, could not be attempted for the Cumbum basin due to a lack of well-constrained riverine composition and relative contribution from juvenile sources (Collins et al., 2015).

3.2.2. Basinal redox state and hydrography

The depositional environment for the Cumbum basin has been reconstructed using multi-elemental proxies (Table 3.1 and Table A3.1). The Mo/U ratios of shales serve as a reliable proxy for the redox state, mainly due to their differential redox-dependent removal mechanisms (Algeo and Tribovillard, 2009). While scavenging of uranium from seawater ($UO_2(CO_3)_3^{4-}$) mainly occurs under suboxic to anoxic conditions (Klinkhammer and Palmer, 1991; Zheng et al., 2002), removal of Mo (MoO_4^{2-}) is largely linked to conversion of particle-reactive thiomolybdate (MoO_xS_{4-x}) in euxinic conditions (Erickson and Helz, 2000). Consequently, the sedimentary Mo/U values are lower than the seawater ratio in an anoxic basin and are comparable to or higher than seawater values in euxinic conditions (Algeo and Tribovillard, 2009). As mentioned earlier, the enrichment factor of Mo (6.5 ± 1.2) is about four times higher than that of U (1.5 ± 0.4; Fig. 3.2). Thus, the average Mo_{EF}/U_{EF} ratio (5 ± 1) determined for the Cumbum shales is closer to the modern seawater value (Fig. 3.5a), which indicates preferentially more Mo removal than U, possibly in a sulfidic (euxinic) environment.

Further, we have also employed sedimentary Cd/Mo data to reconstruct the basinal settings (Fig. 3.5b). The Cd abundance in organic-rich shales is largely associated with biogenic debris, while Mo abundance is more regulated by authigenic removal mechanisms. The Cd/Mo ratio, therefore, is expected to have a higher (>0.1; Sweere et al., 2016) value for continental marginal settings with higher productivity than restricted basins with limited productivity (~0.1; Sweere et al., 2016). The Cd/Mo ratio (0.09 ± 0.06; n = 29) for the Cumbum shales is compared with that for modern restricted (Cd/Mo <0.06) and upwelling (Cd/Mo >0.1) settings (Fig. 3.5b). This data comparison (Fig. 3.5b) indicates that the Cumbum Cd/Mo ratios are closer to that of the Saanich Inlet and Cariaco basin sediments, pointing to a limited productivity regime with restricted basinal settings during the deposition of the Cumbum shales.

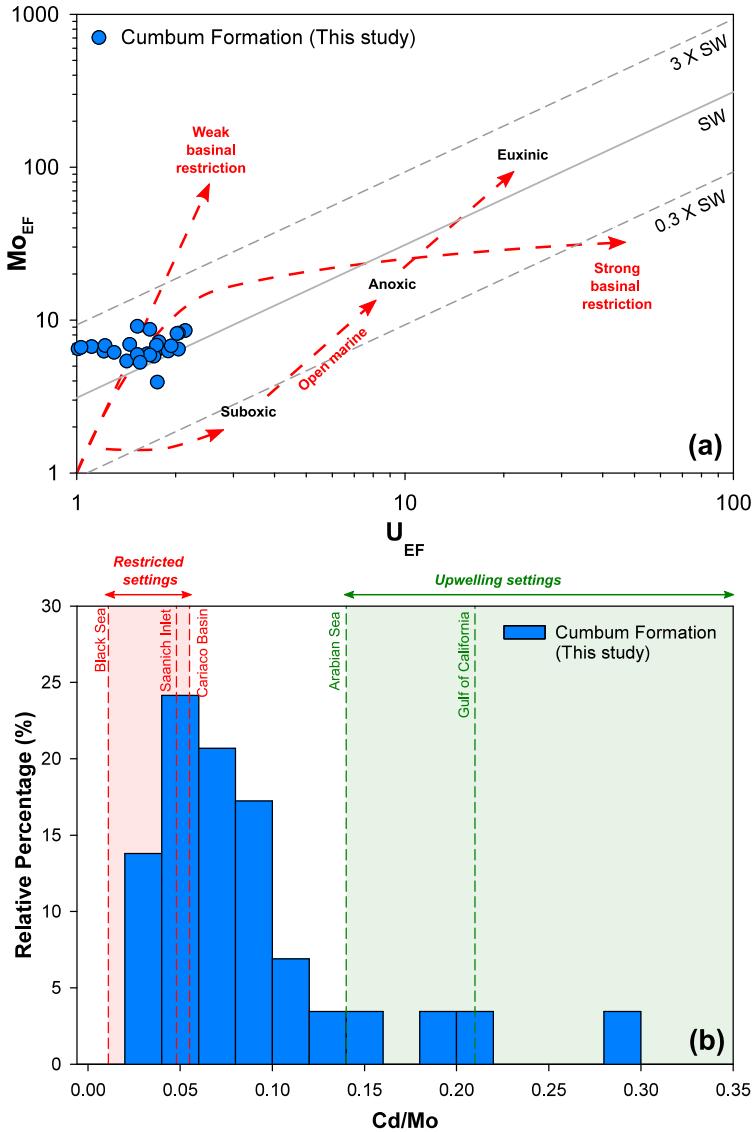

Figure 3.5. (a) *Co-variation of Mo_{EF} and U_{EF} for the Cumbum shales. The data are compared with the Mo/U ratios for modern seawater (SW) and its multiples (0.3 and 3; Tribovillard et al., 2012).* ***(b)*** *Frequency distribution of Cd/Mo ratio for the Cumbum shales. The vertical lines represent expected ratios for different modern upwelling and restricted settings (Sweere et al., 2016).*

The Mo/TOC ratios provide additional evidence for a reducing basin with limited open ocean connectivity (Algeo and Lyons, 2006). In restricted basins, the sedimentary Mo/TOC values are proportional to the aqueous Mo concentrations in deep water, which are affected by basinal restriction and deep-water renewal times (Algeo and Rowe, 2012). The Mo/TOC ($\times 10^{-4}$) ratios for the Cumbum shales vary from 3.6 to 7.7. The average Mo/TOC (5.6 ± 1.0) of these samples is closer to that reported for the Black Sea (Mo/TOC = 4.5 ± 1), a modern perennial euxinic basin with low aqueous Mo concentrations and limited connectivity with the open ocean (Fig. 3.6a; Algeo and Rowe, 2012). Comparison of the present Mo/TOC data with those of modern silled basins suggests the presence of low Mo inventory in the basin, possibly similar to values observed in the modern Black Sea. This comparison also suggests a low seawater [Mo] value for the Cumbum basin, in accordance with those estimated for the mid-Proterozoic seawater (~11 to 22 nmol/L; Scott et al., 2008).

The ratio of reactive (Fe_{HR}) to total (Fe_T) iron in sedimentary deposits (Raiswell and Canfield, 1998; Poulton and Raiswell, 2002) is another reliable proxy for bottom-water redox conditions. During reducing conditions, the reactive mineral phases (iron carbonates, oxyhydroxides and magnetite) present in the sedimentary column get converted to sulfide phases during early diagenesis (Raiswell et al., 2018). This increase in the total reactive iron pool leads to a higher Fe_{HR}/Fe_T value for anoxic basins (>0.38; Poulton and Canfield, 2011) compared to that for oxic settings (<0.22). The proportion of pyrite-associated iron (Fe_{Py}) phases in the reactive iron (Fe_{HR}) pool can be further used to distinguish between ferruginous (Fe_{Py}/Fe_{HR} <0.7) and euxinic (Fe_{Py}/Fe_{HR} >0.7; Poulton and Canfield, 2011) conditions. The Fe_{HR}/Fe_T values for the Cumbum shales (0.37 to 0.91; Fig. 3.6b) mainly fall in the zone of anoxic conditions, whereas the Fe_{Py}/Fe_{HR} ratios (0.40 to 0.92) fluctuate between the ferruginous and euxinic fields. Consistently, the euxinic shales are also found to have higher S/Mn ratios than those deposited in the ferruginous basin (Fig. 3.6b). The S/Mn value in shales reflects a balance between the formation of sulfidic minerals in euxinic conditions and Fe-Mn hydroxides in an oxygenated environment. The S/Mn distribution, together with Fe_{Py}/Fe_{HR} ratios, confirm shale deposition in ferruginous to sulfidic basinal conditions. These redox fluctuations may occur due to the deposition of sediments closer to the chemocline and/or variable seawater exchange (Raiswell et al., 2018). Collectively, these evidence suggests that the Cumbum black shales were deposited in a restricted basin with fluctuating redox states.

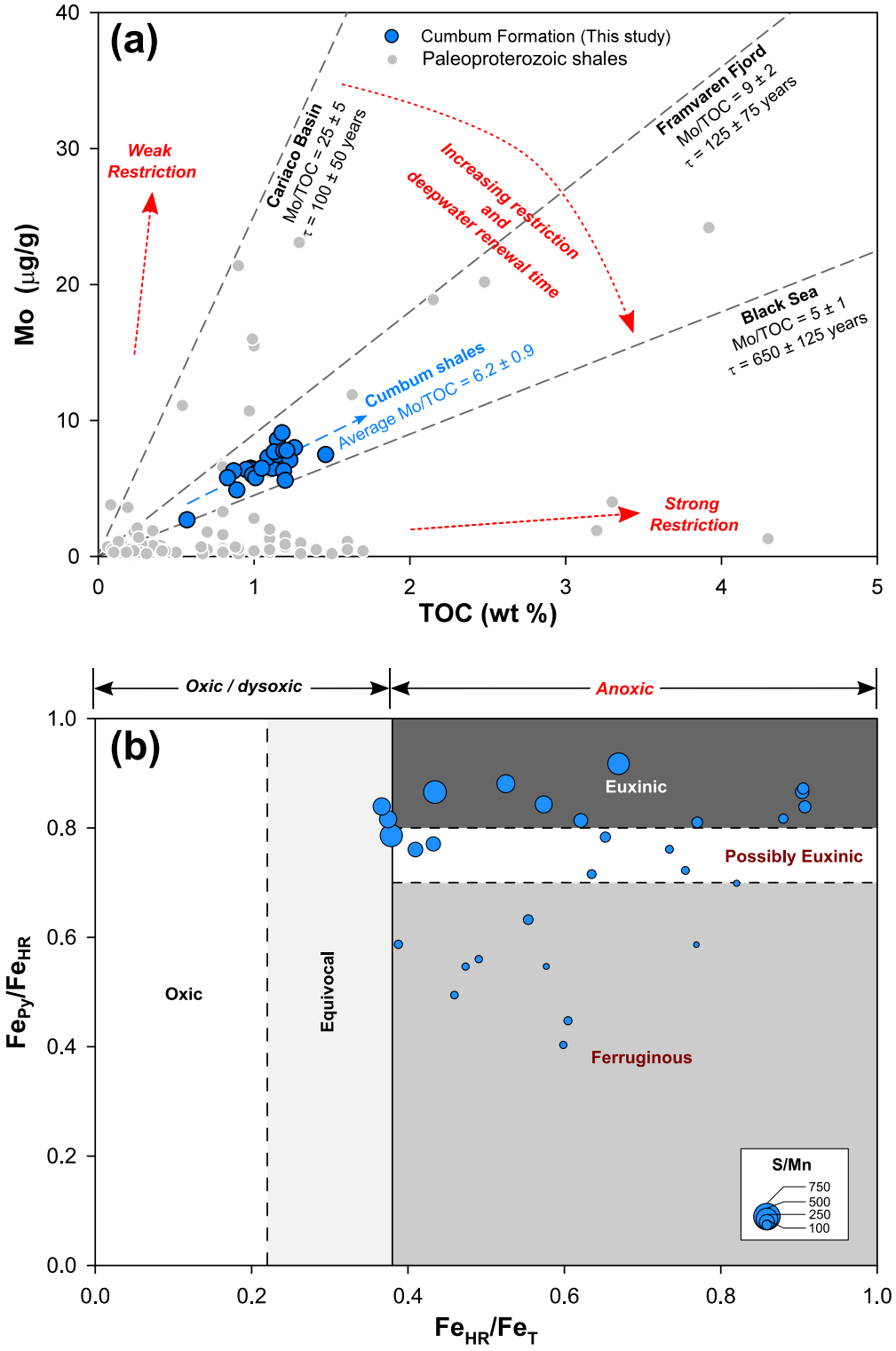

Figure 3.6 (a) *Comparison of black shale [Mo] and [TOC] concentrations with average Mo/TOC ($\times 10^{-4}$) ratios for modern anoxic silled basins with different deep-water renewal times (τ) (Algeo and Lyons, 2006).* ***(b)*** *Relative abundances of highly reactive and pyritic (Fe_{HR}/Fe_T and Fe_{Py}/Fe_{HR}) iron phases in the Cumbum shale compared with that expected for different redox states (Raiswell et al., 2018). The symbol size here represents the S/Mn ratio of the sample. Note that samples falling in the euxinic regions also show systematically higher S/Mn ratios than those for ferruginous deposition.*

3.2.3. Areal extent of ocean euxinia at 1.66 Ga

Shale δ^{98}Mo serves as a reliable proxy for the past redox state of the global ocean. This is largely due to (i) the redox-sensitive nature of Mo (Morford and Emerson 1999), (ii) its high oceanic residence time (~440 kyr; Miller et al., 2011), and (iii) quantifiable isotopic fractionation during different scavenging processes (Barling et al., 2001; Poulson et al., 2006; Poulson Brucker et al., 2009; Goldberg et al., 2012; Dickson et al., 2014; Dahl et al., 2017; Kendall et al., 2017). In particular, the Mo isotopic signatures of sedimentary successions deposited under strongly euxinic (where $[H_2S]_{aq} > 10\mu M$) and restricted environments are near-equal to global seawater value during deposition (Barling et al., 2001; Neubert et al., 2008; Noordmann et al., 2015), which reflects the balance between oceanic Mo sources and sinks (Kendall et al., 2017). Here, we have utilized the Mo mass balance model developed by Stockey et al. (2020) to calculate the areal extent for different redox settings. This modelling methodology has been successfully used for different Paleozoic sections (Lu et al., 2023; Yang et al., 2023). The model assumes a well-mixed oceanic reservoir where the Mo concentration and isotopic values are described by the following mass balance equations:

$$\frac{d[Mo]_{sw}}{dt} = F_{inputs} - \sum F_i \quad (3.1)$$

$$\frac{d[Mo]_{sw}\delta^{98}Mo_{sw}}{dt} = F_{inputs} \times \delta^{98}Mo_{inputs} - \sum F_i(\delta^{98}Mo_{sw} + \Delta^{98}Mo_i) \quad (3.2)$$

Here, the subscripts *SW*, *inputs*, and *i* stand for seawater, input (riverine + groundwater) source and three sinks (*i* stands for oxygenated (oxic), intermediate (interm) and euxinic (eux)), respectively. F_{inputs} and F_i represent input (riverine and groundwater) and output Mo fluxes, respectively. The $\Delta^{98}Mo_i$ (= $\delta^{98}Mo_i - \delta^{98}Mo_{SW}$) stands for the isotopic offset between seawater and the sinks *i*.

The Mo flux for sink *i* is defined as:

$$F_i = b_i A f_i \alpha_i \frac{[Mo]_{modelled}}{[Mo]_{modern}} \quad (3.3)$$

where *A* represents the total modern seafloor area, b_i and f_i represent the burial flux and proportion of global seafloor area for sink *i*, respectively. The α_i is the pseudo-spatial scaling coefficient that relates the burial rate and seafloor area for the sink *i*. The $[Mo]_{modern}$ and $[Mo]_{modelled}$ reflect the mean modern-day and model-predicted Mo concentrations for seawater.

The scaling factor (α) considers the effect of organic matter re-mineralization and the changes in Mo burial rates associated with bathymetry and expanding redox settings (Menard and Smith, 1966; Middelburg et al., 1996; Reinhard et al., 2013). The burial in oxic settings are considered to vary linearly (i.e., $\alpha_{oxic} = 1$), whereas the burial rates in euxinic environments depend on the basinal remineralization and its bathymetry (Reinhard et al., 2013), and the associated scale, therefore, may be defined as:

$$\alpha_{eux} = \frac{\sum_{\min(z_{eux})}^{\max(z_{eux})} 1.58 - 0.16ln(z_{eux})}{N(z_{eux}) \times (1.58 - 0.16ln(\min(z_{eux})))} \quad (3.4)$$

Here, N(z_{eux}) describes the number of depths modelled (n = 10,000). The minimum (min(z_{eux})) and maximum (max(z_{eux})) values for this parameter were calibrated based on the LOESS model, which replicates the modern ocean depth-area relationship (Menard and Smith, 1966; Reinhard et al., 2013).

Estimation of the scaling factor for the intermediate environments (α_{interm}), consisting of both ferruginous and suboxic settings, must incorporate relative transition between euxinia and intermediate seafloor area. For this, the model assumes that the minimum depth for the intermediate setting (min(z_{interm})) is similar/equal to the max(z_{eux}), whereas its maximum depth (max(z_{interm})) is a function of A_{interm} + A_{eux} (Menard and Smith, 1966; Reinhard et al., 2013). Based on this approximation, the α_{interm} value may be computed as:

$$\alpha_{interm} = \frac{\sum_{\min(z_{interm})}^{\max(z_{interm})} 1.58 - 0.16ln(z_{interm} + \max(z_{eux}))}{N(z_{interm}) \times (1.58 - 0.16ln(\min(z_{eux})))} \quad (3.5)$$

A time-dependent Monte Carlo model involving equations 3.1 to 3.5 iterates from a defined set of input parameters and their ranges (Table A3.2) to attain a frequency distribution of the global euxinic extents compatible with the observed oceanic δ^{98}Mo value. This computation was carried out using R packages *deSolve* (Soetaert et al., 2010) and *FME* (Soetaert and Petzoldt, 2010) modules.

The input parameters for this model require δ^{98}Mo values for sources and fractionation factors associated with each sink (Table A3.2). Molybdenum supply to the modern-day ocean is dominated by riverine and groundwater fluxes (>90%), which has a range of δ^{98}Mo values from ~ +0.2‰ to +0.8‰ (Archer and Vance, 2008; Neely et al., 2018). This range has been used as the δ^{98}Mo value for sources in this study. This range also covers the typical δ^{98}Mo value for hydrothermal systems (~ +0.8‰), which is a minor (<10%) source for oceanic Mo

(McManus et al., 2002; Reinhard et al., 2013). Removal of seawater Mo occurs by sedimentary (authigenic) accumulation in different redox settings, which is accompanied by diverse isotopic fractionations. In oxygenated settings, Mo gets adsorbed onto Mn and Fe oxides with a large isotopic fractionation of ~ −3‰ to −2.8‰ (Barling and Anbar, 2004; Goldberg et al., 2009). In sulfidic settings, the degree of isotopic fractionation depends on the basinal restriction and water renewal rates (Kendall et al., 2017). Small offsets (−0.8‰ to 0‰) are observed in deeper parts of highly restricted euxinic basins where the bottom water $[H_2S]_{aq}$ concentration is >11μM, while intermediate (−1.6‰ to −1.0‰) to high offsets (up to −3‰) are observed during sediment deposition near chemocline and more open basinal settings in euxinic basins (Neubert et al., 2008; Dahl et al., 2010; Nägler et al., 2011). For the model, we have used a $\Delta^{98}Mo_{eux}$ range of −0.8‰ to 0‰ for strongly euxinic sinks. In weakly-oxygenated environments (including the pore-water regimes with mild H_2S content), variable isotopic fractionation factors ($\Delta^{98}Mo_{interm}$ = −0.3‰ to −1.8‰) have been reported, which is linked to Mo sulfidization from both the seawater and various Fe-Mn oxides (Siebert et al., 2003; Goldberg et al., 2012; Kendall et al., 2017). To better constrain the $\Delta^{98}Mo_{interm}$, we have used the model to find the most probable $\Delta^{98}Mo_{interm}$ range, which can reproduce the modern-day areal extent for different settings. This approach yields $\Delta^{98}Mo_{interm}$ values of −1.0‰ to −0.9‰, which have been used for model calculations (Fig. 3.7).

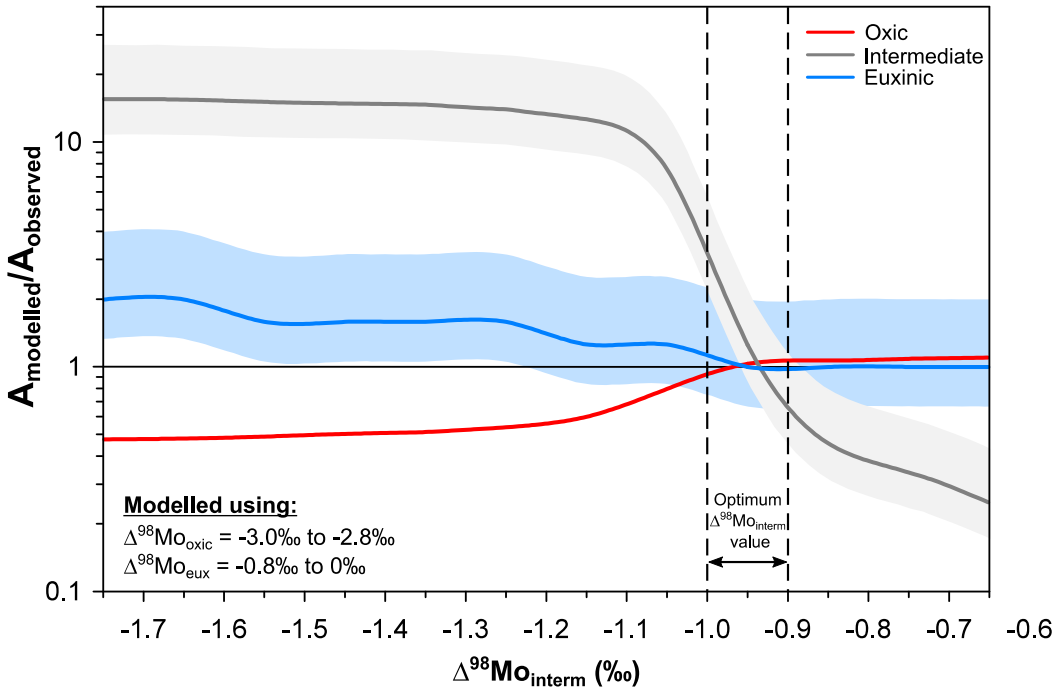

Figure 3.7. *Sensitivity test for modern seafloor areal extent using a Mo isotopic model for known $\Delta^{98}Mo_{oxic}$ (−3.0‰ to −2.8‰), $\Delta^{98}Mo_{eux}$ (−0.8‰ to 0‰), and euxinic shale ($\delta^{98}Mo$ ~1.8‰; Kendall et al., 2017) compositions. These modelled results converge to observed values for $\Delta^{98}Mo_{interm}$ ranging between −1.0‰ and −0.9‰.*

We have used the data for Cumbum shales (with Fe_{HR}/Fe_T >0.38 and Fe_{Py}/Fe_{HR} >0.7) deposited only in euxinic settings for the model calculation, as these shales are expected to provide the best estimate for past seawater δ^{98}Mo. We, here, recognize that this selection criterion is likely to provide only a minimum estimate for the global seawater δ^{98}Mo and hence maximum extents for global euxinic seafloor extent during this period. The δ^{98}Mo values for the euxinic shales vary between +0.52‰ and +0.85‰ (Fig. 3.4), constraining the seawater δ^{98}Mo for the late Paleoproterozoic interval. Model results based on these data estimate the median A_{eux} of ~5% (32nd quantile = 1.6%; 68th quantile = 15.8%), A_{oxic} of ~28% (32nd quantile = 12.6%; 68th quantile =45.9%), and A_{interm} of ~41% (32nd quantile = 24.6%; 68th quantile =58.4%) for the Cumbum basin (Fig. 3.8; Table A3.4). These values are consistent with that reported earlier for Paleo- and mid-Proterozoic sections, confirming a globally reducing oceanic environment during this time interval. The A_{eux} and A_{interm} were about an order of magnitude higher than that of the modern ocean (A_{eux} ~0.1% to 0.3% and A_{interm} ~1% to 4%; Reinhard et al., 2013; Tissot and Dauphas, 2015; Owens et al., 2016; Sheen et al., 2018; Lu et al., 2023). The A_{oxic} was about three times lower than the modern oceans (~85%). These estimates suggest that oceanic environments, while predominantly reducing, also had a substantial extent of oxygenated seafloor during the late Paleoproterozoic.

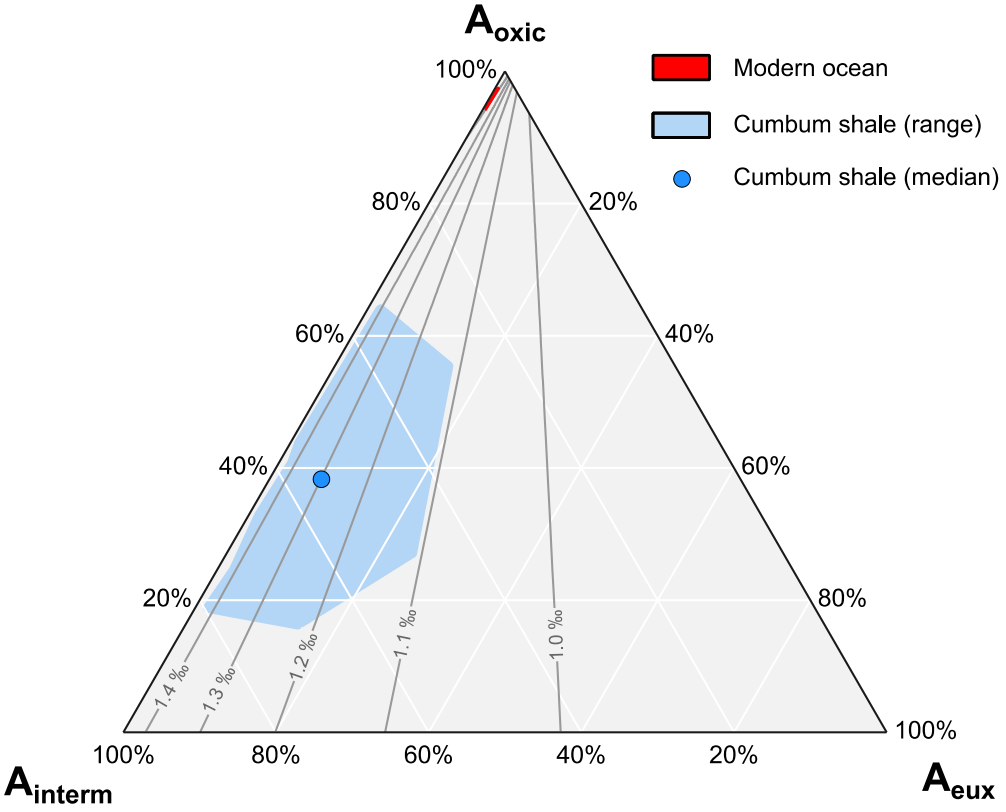

Figure 3.8. *Estimated ranges for oxygenated, intermediate and euxinic seafloor extent at ~1.66 Ga. The solid lines represent possible combinations of areal extent for a given seawater δ^{98}Mo value.*

3.2.4. Proterozoic ocean euxinia and its implication for biological stasis

The progressive changes in atmosphere-ocean oxygenation during the Proterozoic had fundamental effects on redox-dependent elemental cycling, which may have influenced the biological diversification and expansion (Anbar and Knoll, 2002; Robbins et al., 2016; Lyons et al., 2021; Lyons et al., 2024). Specifically, the existence of pervasive ocean euxinia created an evolutionary barrier for the early eukaryotes and subsequent metazoans by limiting the availability of key nutrients (such as Mo and Cu; Buick, 2007). Quantitative constraints on the spatial extent and temporal distribution of different marine environments, hence, are critical for evaluating the role of changing oxygen contents and toxic sulfide levels in modulating complex life. While earlier studies have attempted to quantify temporal changes in anoxia extent using Re (Sheen et al., 2018) and Cr (Reinhard et al., 2013) contents, and U isotopes (Gilleaudeau et al., 2019), the Mo isotopes of euxinic shales provide an additional handle to compute the euxinia extent, data on which is sparse. In this respect, we have compiled earlier-reported δ^{98}Mo data for organic-rich shales (Table A3.3) for the Proterozoic Eon and used the same modelling approach to quantify the extent of oceanic euxinia (Fig. 3.9). Mo isotopic data for shales deposited in euxinic settings (Fe_{HR}/Fe_T >0.38 and Fe_{Py}/Fe_{HR} >0.7) were only used for this evaluation. The outcome of this exercise, although limited in temporal resolution, shows that the estimated euxinia extent through the Proterozoic Eon varies between 1.3% (at 2150 Ma) and 15.9% (at 633 Ma), with an average value of 5 ± 4% (Table A3.4).

Excluding a few episodic excursions, the Proterozoic ocean was mostly steady with a high magnitude of sulfidic areal extent, which was about ten times greater than the modern oceanic settings. The high sulfidicity is consistent with the reported low sulfate content of the Proterozoic seawater (<1 mM to ~4 mM; Luo et al., 2015). In addition to this broad stable ocean state, episodes of increased euxinia were also observed, which often follow atmospheric pO_2 excursions (Fig. 3.9). In particular, the ocean euxinia following the Neoproterozoic oxygenation event (~13% to 16%) increases by about two times than the average Proterozoic extent (~5%) and about sixty times compared to the modern sulfidicity (0.1 to 0.3%). The pronounced intensification of oceanic euxinia towards the end of such oxygen excursions is attributable to the intensification of pyrite burial rates, promoted by enhanced primary productivity and continental sulfate supply to the anoxic oceans (e.g., Ossa Ossa et al., 2018; Wang et al., 2020; Xu et al., 2024). The development of large-scale ocean euxinia, following these oxygenation episodes, could ultimately develop a nutrient-poor oceanic environment, which sustained

throughout the major part of the Proterozoic. In turn, such a chemical state of the oceans, despite sufficient atmospheric oxygen availability, may have served as the prime constraint for eukaryotic metabolism and its diversification.

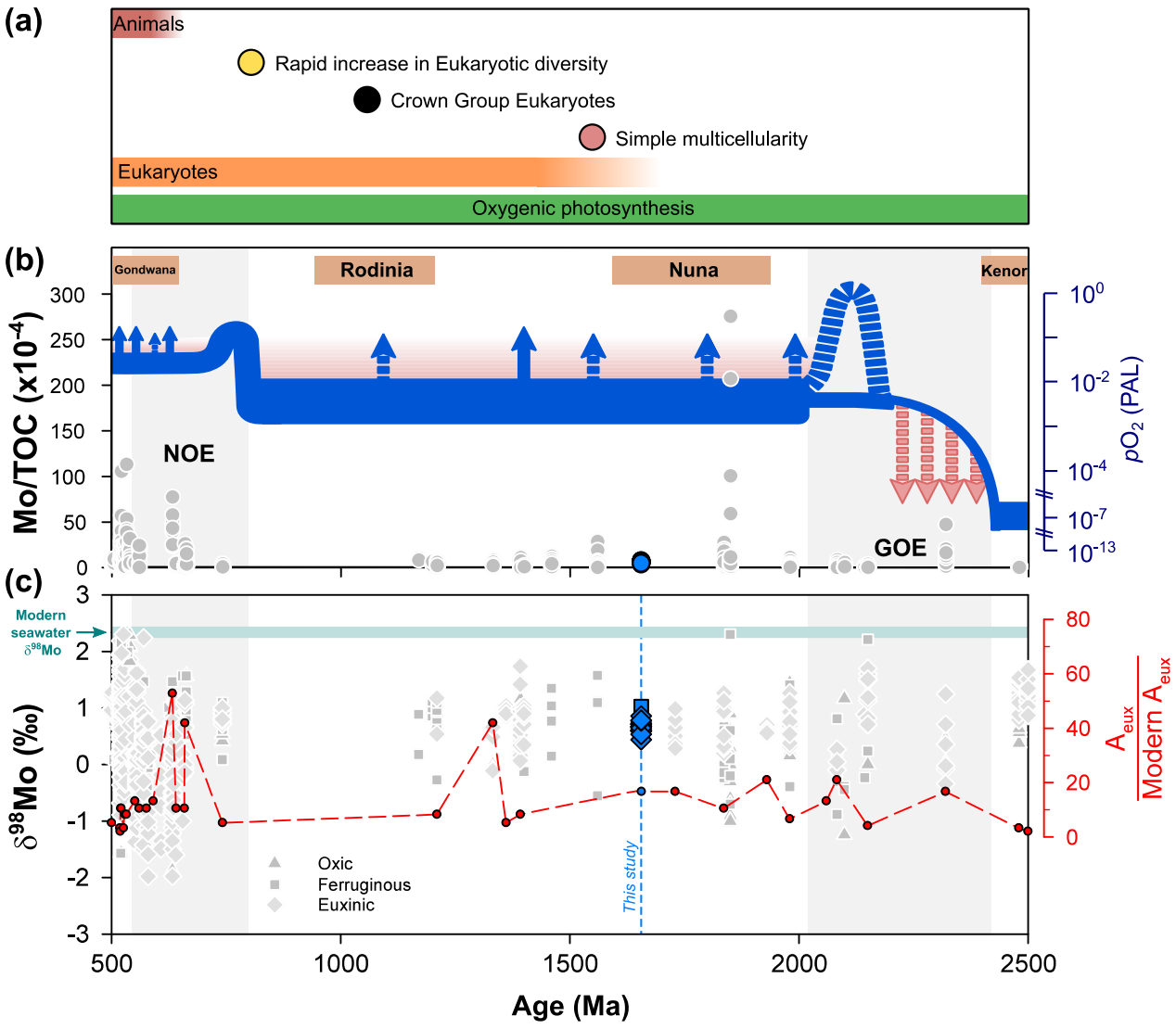

Figure 3.9. *Compilation of* ***(a)*** *global biogeochemical changes,* ***(b)*** *black shale Mo/TOC ratios (Farrell et al., 2021) and* ***(c)*** *sedimentary δ^{98}Mo values with the estimated euxinic seafloor extents from Paleoproterozoic through early Cambrian (500 Ma). Data for the shale δ^{98}Mo taken from Qin et al. (2022), with new data added from Scheller et al. (2018), Tan et al. (2021), and Pan et al. (2021). For reference, literature data for major biospheric innovations (Lyons et al., 2021), atmospheric oxygen levels (Lyons et al., 2024), periods of supercontinents assembly (Campbell and Allen, 2008), and modern seawater δ^{98}Mo (Nägler et al., 2014) are also shown.*

3.3. Conclusions

Shale chronology and chemistry of the Cumbum Formation, Cuddapah Supergroup was investigated to constrain the depositional age, environment, and the extent of euxinia for the late Paleoproterozoic ocean. The Re–Os chronometer provides the first direct depositional age for the Cumbum shales and confirms their Paleoproterozoic (1658 ± 50 Ma) deposition. Trace elemental and iron speciation data suggest a fluctuating depositional environment for these shales varying between euxinic to ferruginous conditions in a restricted basin. Molybdenum isotopic data and their modelling confirm significantly higher euxinia (~5%) for the late Paleoproterozoic than the modern oceanic (0.1% to 0.3%) settings. These sulfidic waters might have been responsible for the reduced availability of bio-essential nutrients and hence, could have contributed to the billion-year-long biological stasis.

Chapter 4

Oceanic redox state during the early Cambrian: Insights from Mo-S isotopes and geochemistry of Himalayan Shales

This chapter discusses the geochemical and isotopic compositions of organic-rich shales overlying the Pc-C boundary from the Tal Formation, Lesser Himalaya. As mentioned in Chapter 2, the organic-rich shales were collected from the Krol-Tal succession of the Lesser Himalayan sedimentary succession. The occurrence of the Pc-C boundary in the Krol-Tal succession of the Lesser Himalayan sedimentary succession has been previously established based on chemo-, chrono-, and bio-stratigraphic records (Aharon et al., 1987; Bhargava et al., 1998; Singh et al., 1999). Existing geochemical (Banerjee et al., 1997; Mazumdar et al., 1999; Mazumdar and Banerjee, 2001) and mercury isotopic (Liu et al., 2021) records of the Lesser Himalayan shales provide evidence for transitional suboxic-anoxic conditions and the influence of continental erosion and upwelling processes on these varying redox states during the Pc-C transition. Here, we utilize the geochemical data of these shales and their principal component analyses to constrain the major carrier phases of redox-sensitive elements. By utilizing an inversion approach, the Mo isotopic data of these shales and their mass balance calculations were used to reconstruct the extent of various seafloor depositional environments during the Pc-C transition. The measured $\delta^{34}S$ pyrite data, along with the earlier-reported $\delta^{34}S$ values for early Cambrian seawater, were used to estimate the seawater sulfate concentration of the Tal basin. Further information regarding these datasets, as well as their interpretations and implications, are discussed below.

4.1. Results

Geochemical and Mo-S isotopic data for the Himalayan shales (Tal Formation) overlying the Pc-C boundary are provided in Tables 4.1, 4.2 and Appendix (Tables A4.1, A4.2). For comparison, these data for a Neoproterozoic shale sequence from an underlying (Jaunsar) Group are also included. Concentrations for most of the major oxides for the Tal shales match well with those reported for the UCC (Rudnick and Gao, 2003; Fig. 4.1). The total carbon in these shales, on average, is comprised of ~60% of organic and ~40% of inorganic carbon content. The average TOC for these shales is 1.3 ± 0.1%, about an order of magnitude higher than that of the Neoproterozoic shales (0.14 ± 0.06%; Table 4.1) from the Himalaya. The total nitrogen (TN) concentrations (0.092 ± 0.003%) of these samples exhibit a good correlation with TOC ($r = 0.43$, $p < 0.05$) and Al ($r = 0.71$, $p < 0.001$). The (atomic) TOC/TN ratios for the Pc-C shales vary between 15.2 and 17.8, with an average value of 16 ± 1. These TOC/TN ratios, although higher than the Redfield ratio (~7), are consistent with that reported for shales with similar depositional ages (e.g., Cremonese et al., 2014; Kikumoto et al., 2014).

Table 4.1. Elemental and sulfur ($\delta^{34}S$) isotopic data for black shale samples from the (lower) Tal Formation, Lesser Himalaya. For comparison, these data for a Neoproterozoic shale sequence (Chandpur Formation) from Lesser Himalaya have also been included.

Sample ID[#]	TOC	TIC	TN	TS	Al	Fe_T	$\delta^{34}S_{Py}$ (V-CDT)	P	Mn	V	Cr	Co	Ni	Cu	Zn	Mo	U
	wt%						‰	µg/g									
Tal Formation, Lesser Himalaya (Shale sequence overlying the Pc-C boundary)																	
HM15-10A	1.28	1.03	0.09	1.54	7.46	3.53	4.86	670	420	119	64	12.3	67	37	95	15.8	8.0
HM15-10B	1.35	0.97	0.09	1.51	7.41	3.54	5.19	662	413	113	63	12.0	57	34	110	16.0	7.9
HM15-11A	1.36	1.01	0.10	1.49	7.51	3.54	4.46	665	412	112	66	11.9	65	34	109	15.7	8.2
HM15-11B	1.38	1.01	0.09	1.53	7.35	3.55	5.25	643	421	106	63	11.6	56	35	84	15.9	7.8
HM15-12A	1.23	1.06	0.09	1.56	7.44	3.58	5.62	654	408	106	64	12.0	45	35	86	15.9	7.5
HM15-12B	1.36	0.95	0.09	1.45	7.41	3.55	5.50	658	421	97	61	11.0	42	33	82	15.8	7.2
HM15-13A	1.24	0.93	0.10	1.48	7.49	3.61	5.05	668	423	94	68	10.4	40	32	76	15.8	7.8
HM15-13B	1.28	0.89	0.09	1.44	7.50	3.60	4.72	664	417	96	66	10.3	40	33	80	15.9	7.1
HM15-14A	1.27	0.96	0.10	1.68	7.56	3.66	6.77	665	409	100	66	11.5	44	35	78	16.3	7.7
HM15-14B	1.26	0.94	0.09	1.69	7.41	3.69	8.34	691	422	98	54	11.6	45	35	98	16.1	6.6
HM15-15A	1.36	1.02	0.09	1.54	7.28	3.52	4.89	664	421	67	72	7.40	41	22	82	15.5	8.1
HM15-15B	1.31	1.08	0.09	1.56	7.25	3.50	5.27	645	422	95	68	11.1	56	32	94	15.5	8.1
HM15-16A	1.40	0.94	0.09	1.44	7.39	3.46	4.43	638	420	97	66	10.7	56	32	84	15.7	7.8
HM15-16B	1.35	0.96	0.09	1.43	7.35	3.51	5.06	666	394	103	63	11.2	59	33	94	15.7	7.6
HM15-17A	1.32	1.03	0.09	1.53	7.32	3.46	3.93	670	413	103	65	10.8	63	31	90	16.8	8.1
HM15-17B	1.28	1.07	0.09	1.59	7.29	3.50	4.61	665	398	99	64	10.7	61	31	91	16.1	7.6
HM15-18A	1.21	1.06	0.09	1.50	7.56	3.63	3.64	704	418	108	60	11.3	65	33	95	16.6	7.8
HM15-18B	1.31	1.00	0.09	1.59	7.38	3.49	3.61	688	427	108	66	11.3	65	31	94	17.0	8.3
HM15-20A	1.21	0.98	0.09	1.53	7.21	3.43	7.99	688	412	87	63	10.7	43	28	96	13.4	8.1
HM15-20B	1.23	1.01	0.09	1.70	7.14	3.66	7.51	699	400	87	63	10.2	42	29	76	14.7	7.5
HM15-21A	1.23	1.02	0.09	1.70	7.08	3.46	7.42	668	386	91	51	10.5	38	32	64	13.0	5.0
HM15-21B	1.19	1.00	0.08	1.53	7.21	3.53	7.95	662	400	90	62	10.9	37	33	70	14.2	5.8
Chandpur Formation, Lesser Himalaya																	
HM15-01A	0.12	0.09	0.12	0.02	13.17	3.86	-	1284	442	173	93	11.0	37	9	44	1.2	2.3
HM15-01B	-	0.10	0.12	0.02	13.20	3.88	-	1158	421	172	101	11.3	38	17	41	1.2	2.1
HM15-01C	-	0.10	0.12	0.01	13.15	3.88	-	1108	427	184	97	12.2	39	13	51	1.2	2.4
HM15-02A	0.09	0.09	0.09	0.05	9.62	3.86	-	467	433	133	78	11.8	35	8	72	1.1	1.9
HM15-02B	-	0.09	0.12	0.02	12.64	3.83	-	1104	418	174	90	10.4	36	11	52	1.1	1.9
HM15-02C	-	0.09	0.12	0.02	13.49	3.85	-	1037	420	194	101	9.2	37	8	37	1.0	1.6
HM15-03A	0.2	0.10	0.09	0.08	9.17	4.42	-	443	417	127	74	12.2	37	35	87	1.1	2.0
HM15-03B	-	0.12	0.09	0.18	9.23	4.48	-	448	418	115	72	16.0	37	35	109	1.0	2.3
HM15-03C	-	0.12	0.09	0.12	9.62	4.37	-	438	429	118	74	14.0	36	37	85	1.2	2.0

[#]A, B, and C stand for different powdering aliquots of the shale sample.

Table 4.2. Iron speciation data for studied samples from the (lower) Tal Formation and Chandpur Formation, Lesser Himalaya.

Sample ID[#]	F_{carb}	Fe_{ox}	F_{mag}	Fe_{Py}	Fe_R	Fe_{HR}	Fe_{HR}/Fe_T	Fe_{Py}/Fe_{HR}	DOP
	wt%								
Tal Formation, Lesser Himalaya (Shale sequence overlying the Pc-C boundary)									
HM15-10A	0.45	0.07	0.08	1.15	1.00	1.75	0.50	0.66	0.54
HM15-10B	0.40	0.09	0.08	1.17	1.25	1.73	0.49	0.67	0.48
HM15-11A	0.40	0.10	0.06	1.21	1.20	1.76	0.50	0.69	0.50
HM15-11B	0.38	0.08	0.07	1.23	1.20	1.76	0.49	0.70	0.51
HM15-12A	0.43	0.07	0.06	1.16	1.10	1.72	0.48	0.67	0.51
HM15-12B	0.40	0.08	0.07	1.08	1.19	1.64	0.46	0.66	0.48
HM15-13A	0.38	0.17	0.06	1.15	1.19	1.75	0.49	0.65	0.49
HM15-13B	0.35	0.16	0.07	1.18	1.23	1.76	0.49	0.67	0.49
HM15-14A	0.43	0.09	0.07	1.32	1.07	1.91	0.52	0.69	0.55
HM15-14B	0.41	0.08	0.07	1.13	1.21	1.68	0.46	0.67	0.48
HM15-15A	0.40	0.06	0.07	1.13	1.12	1.66	0.47	0.68	0.50
HM15-15B	0.38	0.06	0.07	1.18	1.18	1.69	0.48	0.70	0.50
HM15-16A	0.40	0.11	0.07	0.98	1.17	1.56	0.45	0.63	0.46
HM15-16B	0.37	0.11	0.07	0.97	1.07	1.52	0.43	0.64	0.48
HM15-17A	0.43	0.08	0.07	1.09	1.03	1.67	0.48	0.65	0.51
HM15-17B	0.37	0.08	0.07	1.13	1.08	1.65	0.47	0.68	0.51
HM15-18A	0.40	0.07	0.06	1.16	1.04	1.69	0.46	0.69	0.53
HM15-18B	0.41	0.08	0.07	1.10	1.03	1.67	0.48	0.66	0.52
HM15-20A	0.39	0.07	0.07	1.02	0.96	1.55	0.45	0.66	0.52
HM15-20B	0.47	0.08	0.07	1.23	1.14	1.84	0.50	0.67	0.52
HM15-21A	0.38	0.09	0.06	1.24	0.94	1.77	0.51	0.70	0.57
HM15-21B	0.44	0.09	0.07	1.30	1.03	1.90	0.54	0.69	0.56
Chandpur Formation, Lesser Himalaya									
HM15-01A	0.10	0.13	0.19	0.03	-	0.44	0.11	0.07	-
HM15-01B	0.10	0.14	0.18	0.02	-	0.44	0.11	0.05	-
HM15-01C	0.13	0.18	0.20	0.01	-	0.51	0.13	0.02	-
HM15-02A	0.23	0.08	0.30	0.03	-	0.63	0.16	0.04	-
HM15-02B	0.10	0.12	0.20	0.02	-	0.44	0.11	0.04	-
HM15-02C	0.11	0.16	0.16	0.02	-	0.45	0.12	0.04	-
HM15-03A	0.49	0.06	0.27	0.07	-	0.89	0.20	0.08	-
HM15-03B	0.65	0.07	0.29	0.15	-	1.15	0.26	0.13	-
HM15-03C	0.56	0.05	0.27	0.09	-	0.97	0.22	0.10	-

[#]A, B, and C stand for different powdering aliquots of the shale sample.

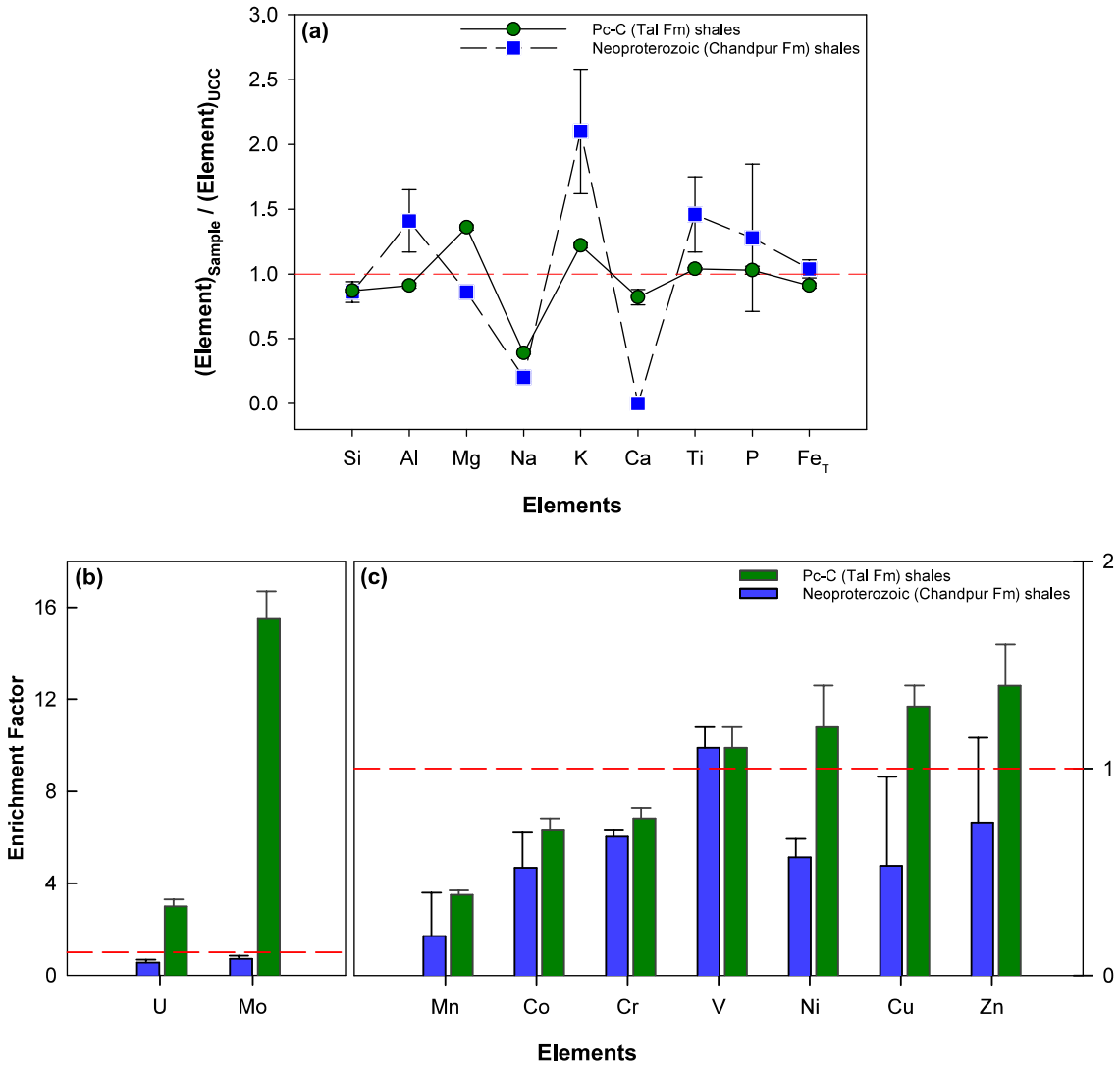

Figure 4.1. *UCC-normalized* ***(a)*** *elemental ratios and* ***(b and c)*** *enrichment factors of selected trace elements (Rudnick and Gao, 2003) for Pc-C (Tal Fm) and Neoproterozoic (Chandpur Fm) shales. Red dashed lines represent an enrichment factor of 1.*

The average phosphorus concentration in these samples is 668 µg/g. Phosphorus concentrations show a good correlation with Ca ($r = 0.49$, $p < 0.05$), Mg ($r = 0.65$, $p < 0.01$), and Ti ($r = 0.50$, $p < 0.05$). The total iron (Fe_T) content of the samples ranges from 3.4 to 3.7% with an average value of 3.5 ± 0.1%, which is lower than the UCC (3.9%; Rudnick and Gao, 2003). The average Fe_T/Al ratio (0.48 ± 0.01) for these samples is lower than those reported for Paleozoic oxic marine shales (0.53 ± 0.11; Raiswell et al., 2008) and modern marine sediments (0.55 ± 0.11; Clarkson et al., 2014). Iron, manganese, potassium, and other trace elements (V and Cu) show a positive correlation with the Al concentrations. Most of the trace elements, except Mo and U, show limited variations, with enrichment factors of ≤1 (Fig. 4.1b). The Mo concentrations of these shales vary between 13 and 17 µg/g, whereas U concentrations vary

between 5.1 and 8.3 µg/g. The U concentrations correlate well with the TOC (r = 0.45, p < 0.05). In contrast, the Mo concentrations show a good correlation with Mn and Al, with no significant correlation with S. The Molybdenum isotopic (δ^{98}Mo) values of the Tal samples range from +0.99‰ to +1.89‰ with an average value of +1.47 ± 0.21‰ (n = 11; Table 4.3). Excluding two samples, the δ^{98}Mo values exhibit minimal variations with a mean value of +1.48 ± 0.07‰, which is ~0.8‰ depleted than modern-day seawater value (+2.34 ± 0.1‰; Nakagawa et al., 2012; Goswami et al., 2022). The δ^{98}Mo values of Tal shales are comparable to that reported across the Pc-C transitions (Fig. 4.2). However, these values are systematically depleted than that reported for shales deposited in sulfidic environments during the Pc-C boundary (~ +1.9‰; Wille et al., 2008) and early Cambrian (~ +2.1‰ at ~535 Ma; Wen et al., 2011) period.

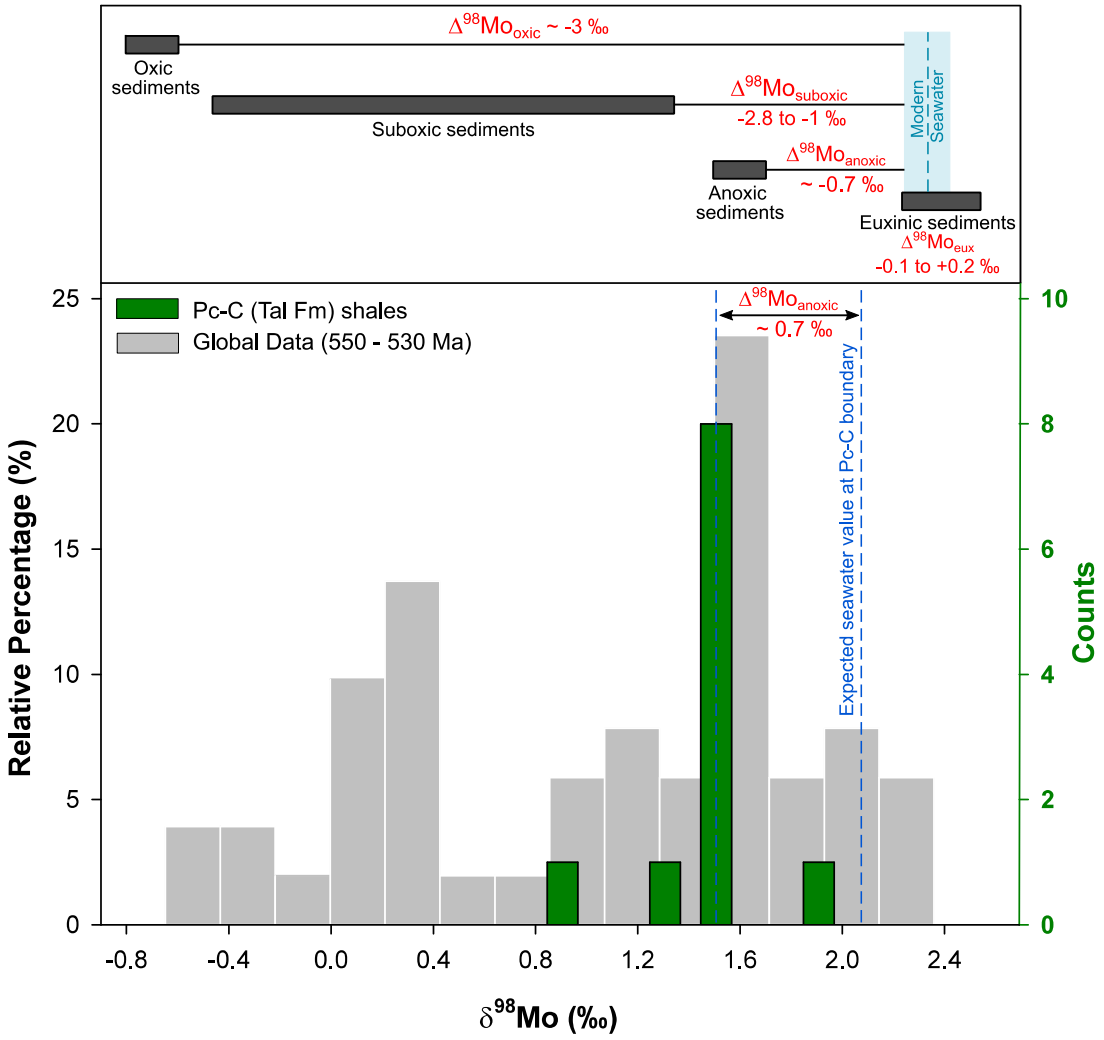

Figure 4.2. *Frequency distribution of δ^{98}Mo isotopes of the Pc-C shales from the Himalaya. For reference, the global Mo isotopic data for early Cambrian (550 – 530 Ma; Farrell et al., 2021) are also shown. Expected isotopic fractionation factors for molybdenum isotopes (Poulson et al., 2006) in sedimentary systems are also depicted.*

The average S concentrations of the Pc-C shales (1.5 ± 0.1%) are higher by two orders of magnitude than that of the UCC (~0.0621%; Rudnick and Gao, 2003) and Neoproterozoic (0.06 ± 0.06%; Table 4.1) shales. The sulfur concentrations show a significant correlation with the Fe_T concentrations ($r = 0.60$, $p < 0.01$). The pyrite $\delta^{34}S_{Py}$ of the Tal shales ranges from +3.6‰ to +8.4‰ (Fig. 4.3). The average $\delta^{34}S_{Py}$ (+5.5 ± 1.4‰) for these shales overlap with the mean of earlier-reported $\delta^{34}S_{Py}$ data for the early Cambrian from Himalayan (−25‰ to +45‰; Mazumdar et al., 1999) and other global (−27‰ to +53‰; Canfield and Farquhar, 2009) sections, despite their large variations (Fig. 4.3). However, the Tal $\delta^{34}S_{Py}$ is less depleted than that of the modern-day pyrites formed by microbial sulfide reduction ($\delta^{34}S_{Py} \sim -21$‰; Fike et al., 2015).

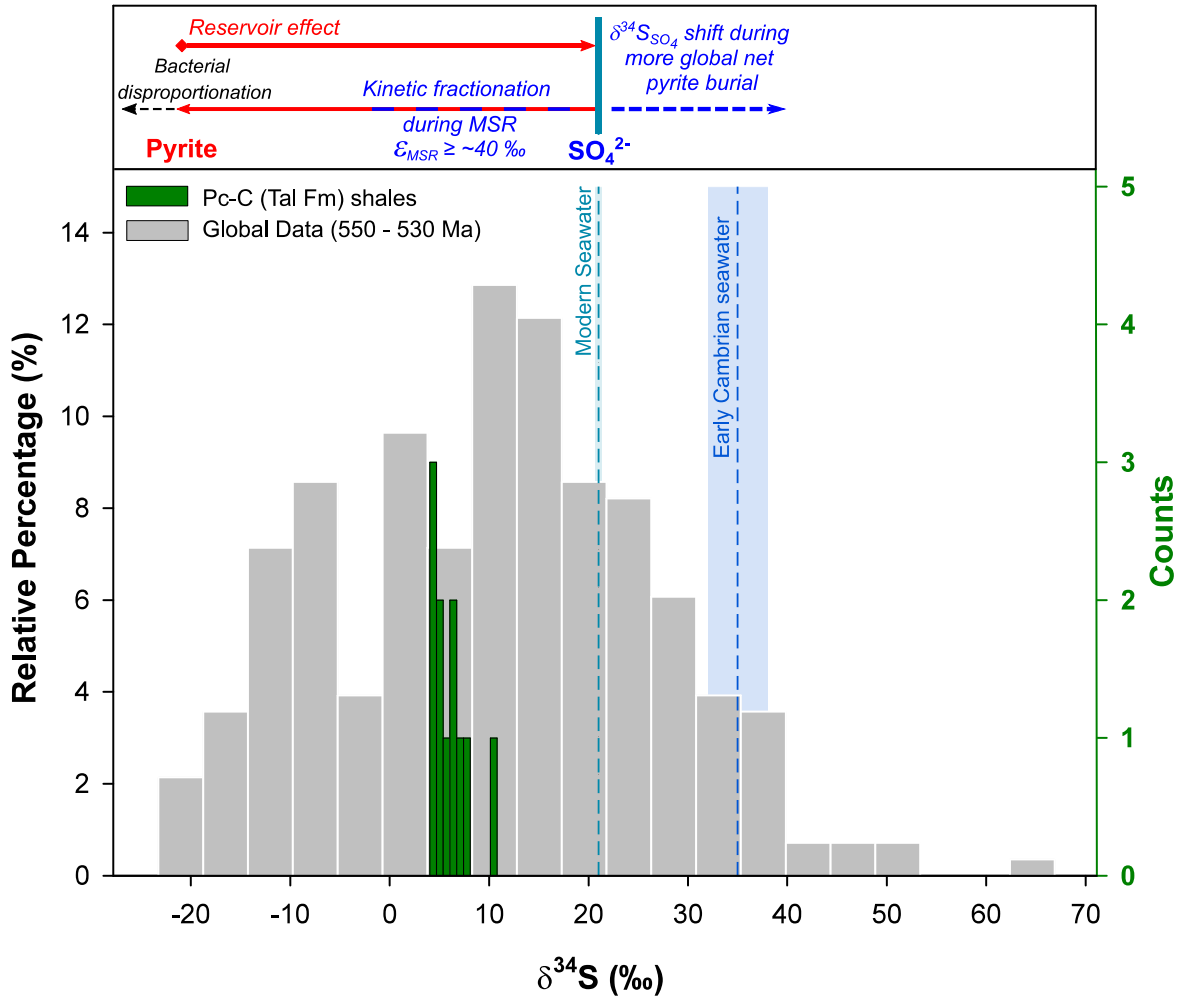

Figure 4.3. *Frequency distribution of pyrite $\delta^{34}S$ of the Pc-C shales from the Himalaya. For reference, the global pyrite S isotopic data for early Cambrian (550 – 530 Ma; Farrell et al., 2021) are also shown. Expected isotopic fractionation factors for sulfur (Lyons et al., 2009) in sedimentary systems are also depicted.*

Table 4.3. Mo elemental and isotopic (δ^{98}Mo) data for the Tal shales along with the estimated Mo flux fractions (f_{oxic}, f_{interm}, f_{eux}) and areal extent (A_{oxic}, A_{interm}, A_{eux}) for oxic, intermediate, and euxinic sinks.

Sample ID	Mo	δ^{98}Mo[a]	f_{oxic}	f_{interm}	f_{eux}	A_{oxic}	A_{interm}	A_{eux}
	µg/g	‰				%		
HM15-10A	15.8	0.99 ± 0.04	0.22	0.36	0.42	98.39	1.30	0.31
HM15-11A	15.7	1.37 ± 0.02	0.35	0.32	0.33	99.10	0.74	0.16
HM15-12A	15.9	1.57 ± 0.03	0.42	0.29	0.29	99.32	0.56	0.12
HM15-13A	15.8	1.55 ± 0.03	0.41	0.30	0.29	99.30	0.58	0.12
HM15-14A	16.3	1.55 ± 0.03	0.41	0.29	0.29	99.31	0.57	0.12
HM15-15A	15.5	1.42 ± 0.03	0.37	0.31	0.32	99.17	0.68	0.15
HM15-16A	15.7	1.44 ± 0.02	0.37	0.31	0.32	99.19	0.67	0.14
HM15-17A	16.8	1.46 ± 0.03	0.38	0.31	0.31	99.21	0.65	0.14
HM15-18A	16.6	1.44 ± 0.03	0.37	0.31	0.32	99.19	0.67	0.14
HM15-20A	13.4	1.54 ± 0.03	0.41	0.3	0.29	99.30	0.58	0.12
HM15-21A	13.0	1.89 ± 0.03	0.53	0.24	0.23	99.57	0.36	0.07
Modern estimates[b]								
Scott et al., 2008			0.35	0.50	0.15	98.79	1.14	0.07
Poulson Brucker et al., 2009			0.5	0.45	0.05	99.26	0.72	0.02
Kendall et al., 2009			0.35	0.60	0.05	98.62	1.36	0.02

[a]*The uncertainties for Mo isotopic data are reported as $2\sigma_{\mu}$.*
[b]*The areal coverage has been computed using the reported f_{oxic}, f_{interm} and f_{eux} values*

4.2. Discussion

Elemental and isotopic compositions of organic-rich shales serve as reliable proxy for deep water redox state, primary productivity, and nutrient cycling (Tribovillard et al., 2006; Tripathy et al., 2014). The Tal Formation, as mentioned in Chapter 2, is mainly comprised of chert-phosphorites, carbonates, and sandstones with the occurrence of a shale horizon above the Pc-C boundary. Chemo-stratigraphic investigation of this section, which has already been reported (Banerjee et al., 1997), is compiled in Fig. 4.4. This study focuses on Mo-S isotopic and trace elemental distributions for the shale horizon.

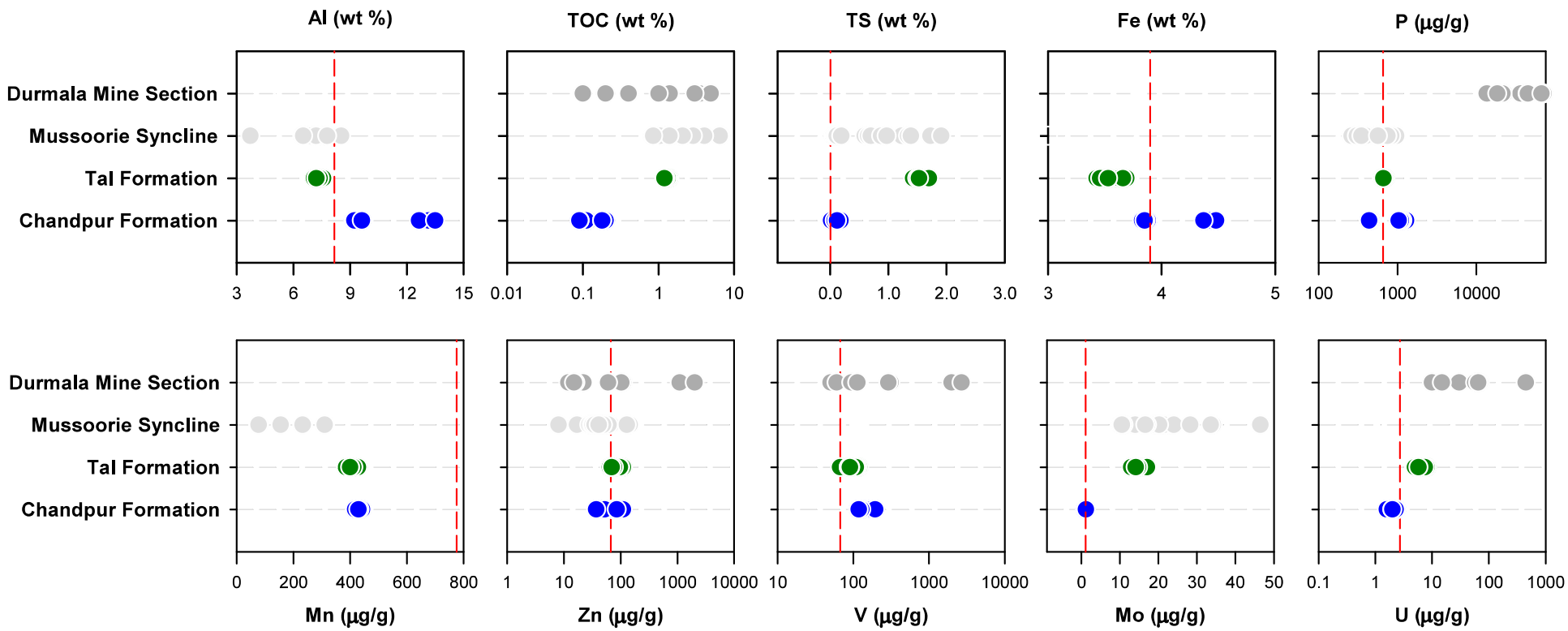

Figure 4.4. *Compiled chemo-stratigraphic data for shale sequences from the Lower Tal Formation (Data source: present study, Banerjee et al. (1997) and Liu et al. (2021)). Red dashed lines represent average UCC values (Rudnick and Gao, 2003).*

4.2.1. Redox setting of the Tal basin: Chemical and isotopic constraints

4.2.1.1 Trace elements and Iron speciation data

Trace element abundances in organic-rich shales are mostly regulated by their redox-dependent scavenging from the water column and subsequent enrichment in underlying sediments. For instance, redox-sensitive elements (e.g., U, Mo, V, and Cr) remain mostly soluble in oxygenated conditions and get removed by forming organo-metallic complexes/sulfides in reducing conditions (Tribovillard et al., 2006). For the Tal shales, only selected trace elements (Mo, U, and Zn) exhibit high (>1) enrichment factors (Fig. 4.1). In addition to authigenic enrichment, the abundances of these elements in marine sediments also depend on continental input, hydrothermal supply, post-depositional alteration, hydrographic restriction, and particulate shuttling (Tribovillard et al., 2006; Algeo and Maynard, 2008; Algeo and Rowe, 2012). We have carried out a principal component analysis (PCA) of the geochemical dataset using the PAST (Paleontological Statistics; v. 4.08; Hammer et al., 2001) software to better constrain the major mechanisms affecting the trace element distribution. The PCA analysis identifies six principle components (PC) with Eigen values >1, which accounts for ~86% of the observed data variance (Table A4.3). Factor loadings for different elements from these components are shown in Fig. 4.5. The PC-1, which explains ~26% of the total variance, has high factor loadings for TOC, TN, Al, K, Mn, and several redox-sensitive trace elements (V, Cr, Co, Ni, Zn, Mo, Th, U). The observed elemental grouping possibly suggests an authigenic source for these major and trace elements. It is intriguing to observe high loading for aluminium, which mostly reflects lithogenic sources, in this factor. High TOC-trace elements association and low loading for other lithogenic indices (such as Si and Na) establish that these Al loadings may also be linked to hydrogenous processes. We, therefore, hypothesize that an appreciable amount of aluminium in this factor may also be linked to Al adsorption onto clay surfaces (Timothy and Calvert, 1998). The PC-1 shows low loading for sulfur and hence, may not account for the removal of elements in euxinic conditions. In contrast, the PC-2 is characterized by high S loading and explains ~20% of the variance. This factor also has high loadings for Fe_T, Co, and Cu, which are usually taken up by pyrites or other sulfide phases during diagenesis (Morse and Luther, 1999). The PC-3 (variance ~15%) has high loadings for TIC, Ca, Sr, and P, suggesting a carbonate phase association. The association of P with Ca and TIC for this component also hints at the presence of carbonate-fluorapatite minerals, which can form authigenically due to P-supersaturation in pore waters (Ruttenberg

and Berner, 1993). The PC-4 (variance ~14%) shows high factor loading for Si, Ti, Fe_T, K, and Mg. These elements are typically found enriched in clastic sediments, and hence, the component can be identified as continental input to the basin. In addition to these four major principal components, which together explain ~75% of the data variance, two more components relating to macronutrients (PC-5 with variance ~6% for Si, Ni, K, TIC, TOC, and TN) and carbonate-rich clastic fluxes (PC-6 with variance ~5% for TIC, Th, Al, Si, Ti, and S) are observed. PCA analysis thus gives an indication that the elements associated with the PC-1 and PC-2 can provide better insights into reconstructing the redox state of the basin.

Covariation of Mo and U in sediments and its comparison with seawater Mo/U ratios have been successful in understanding (1) bottom water redox condition, (2) particulate shuttle in the water column, (3) hydrographic restriction, and (4) renewal of bottom water (Algeo and Lyons, 2006; Algeo and Tribovillard, 2009). Uranium enrichment occurs in the sediments when the soluble uranyl tricarbonate ions ($UO_2(CO_3)_3^{4-}$) diffuse into the sediments and get either adsorbed or precipitated as uraninite and related oxides (UO_2, U_3O_7, U_3O_8; Klinkhammer and Palmer, 1991; Zheng et al., 2002). In the case of molybdenum, the aqueous Mo species (molybdate (MoO_4^{2-})) gets converted to particle reactive thiomolybdate species ($MoO_xS^{2-}_{(4-x)}$, x = 0 to 3) in sulfidic conditions and gets scavenged by sulfur-rich organic matter and iron sulfides (Erickson and Helz, 2000; Tribovillard et al., 2004). The U enrichment exceeds that of Mo in oceanic basins with suboxic bottom water, leading to a lower Mo/U ratio in sediments compared to that of the overlying seawater. During highly reducing and occasional sulfidic conditions, the relative enrichment of Mo matches that of U, leading to a sediment Mo/U ratio comparable to the seawater value (Algeo and Tribovillard, 2009). Additionally, Mo can adsorb onto Mn-Fe-oxyhydroxides formed in oxic waters and get transported to the sediment-water interface. In bottom water conditions where O_2 content falls below 10 μM (Calvert and Pedersen, 1996), reductive dissolution of these oxides can also enhance Mo burial in the sediments. To assess this proposition, we have evaluated the Ce anomaly for the Tal shale samples. This rare earth element gets adsorbed onto Mn-Fe-oxyhydroxides in oxic layers, which subsequently may get released during their reductive dissolution in anoxic conditions, leading to its enrichment in bottom waters/pore waters and chemical sedimentary phases (German and Elderfield, 1990; Tostevin et al., 2016). The Tal shales show insignificant Ce-anomaly ($Ce/Ce^* = 1.01 \pm 0.08$) and, hence, record no appreciable signature for reductive dissolution. This proposition based on cerium data, however, cannot be ascertained as this anomaly may be influenced by both terrigenous and hydrogenous components in shales.

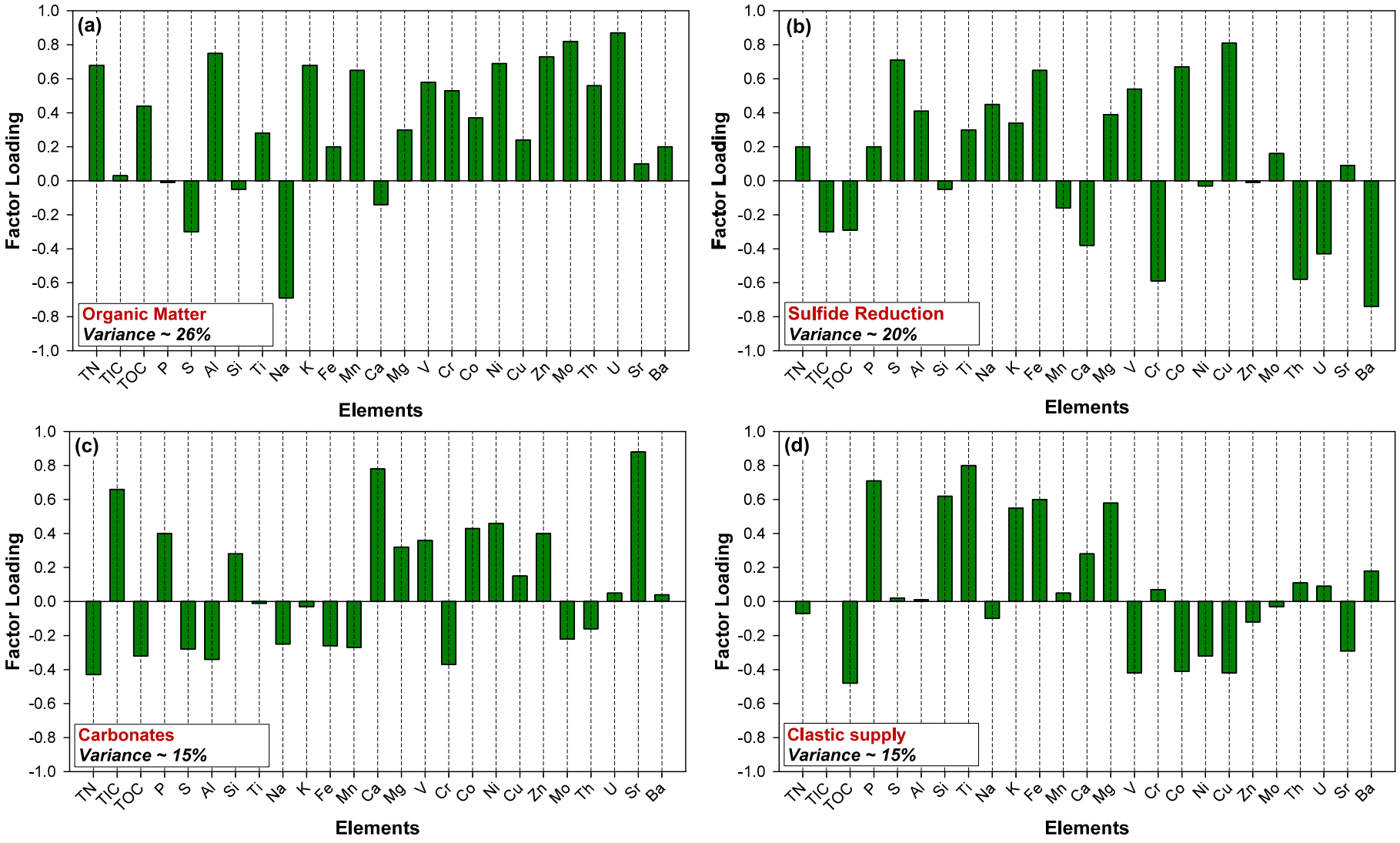

Figure 4.5. *Factor loadings for four major factors extracted from the principle component analysis of the geochemical dataset.*

To confirm this, we have also evaluated the co-variation between Mo_{EF} and U_{EF} (Fig. 4.6a) to better constrain the depositional condition. The Tal shales display a positive correlation between Mo_{EF} and U_{EF} ($r = 0.52$, $p < 0.05$), and these data fall closer to the modern seawater Mo/U value, suggesting a reducing depositional condition for the basin. The Mo/TOC ratios ($\times 10^{-4}$) of these shales (12 ± 1) are close to the Framvaren Fjord (9 ± 2; Algeo and Lyons, 2006), which is a semi-restricted and stratified basin with bottom water renewal time of ~125 years (Algeo and Rowe, 2012). Strong Mo_{EF}–U_{EF} correlations and Mo_{EF} <25 for the Tal shales hint at an anoxic bottom-water condition with euxinic condition, which is restricted to pore waters (Scott and Lyons, 2012; Kendall et al., 2017).

Iron speciation data for shales provide additional insight regarding the bottom-water anoxia (Poulton and Canfield, 2005). This approach relies on the abundance of reactive iron and pyrites in the shales, which depend on the basin anoxia and euxinia, respectively (Poulton and Canfield, 2005; Raiswell et al., 2018). The Fe-speciation data of the Tal shales show that about one-third of the sedimentary Fe is of pyritic nature, whereas the iron associated with carbonate (~11%), oxide (~3%), and magnetite (~2%) phases are minimal. Figure 4.6b compares the Fe_{HR}/Fe_T and Fe_{Py}/Fe_{HR} ratios for the Tal shales. The threshold values for various depositional settings shown in Fig. 4.6b are from the earlier-reported data for modern and Phanerozoic marine sediments (e.g., Raiswell and Canfield, 1998; Poulton and Raiswell, 2002). Based on these datasets, the Fe_{HR}/Fe_T ratios are generally low (below 0.2) for oxic conditions, which increase to >0.38 in anoxic settings (Poulton and Canfield, 2011). High sedimentation rates or transfer of Fe_{HR} to poorly reactive silicates during diagenesis can yield intermediate ratios (0.22 - 0.38; Poulton and Canfield, 2011). The Fe_{Py}/Fe_{HR} ratios increase significantly in euxinic deposition due to the pyritization of reactive iron species and hence, are higher (>0.7; März et al., 2008) in euxinic water conditions. The iron speciation data for the Chandpur shales, with lower Fe_{HR}/Fe_T (~0.16) and Fe_{Py}/Fe_{HR} (~0.06) ratios, indicate their deposition in modern-like oxic depositional settings. In contrast, the Tal shales have an average Fe_{HR}/Fe_T value of 0.48, which is greater than the oxic threshold (Fig. 4.6b). These shales also show a range of Fe_{Py}/Fe_{HR} values from 0.63 to 0.70 with an average ratio of 0.67, which falls close to the ferruginous-euxinic transition threshold. Further, these samples have an average DOP value of 0.51, falling in the range for ferruginous deposition (0.45 to 0.75). Consistent with the Mo–U trend, the iron speciation data for the Tal shales also confirm an anoxic and ferruginous depositional environment.

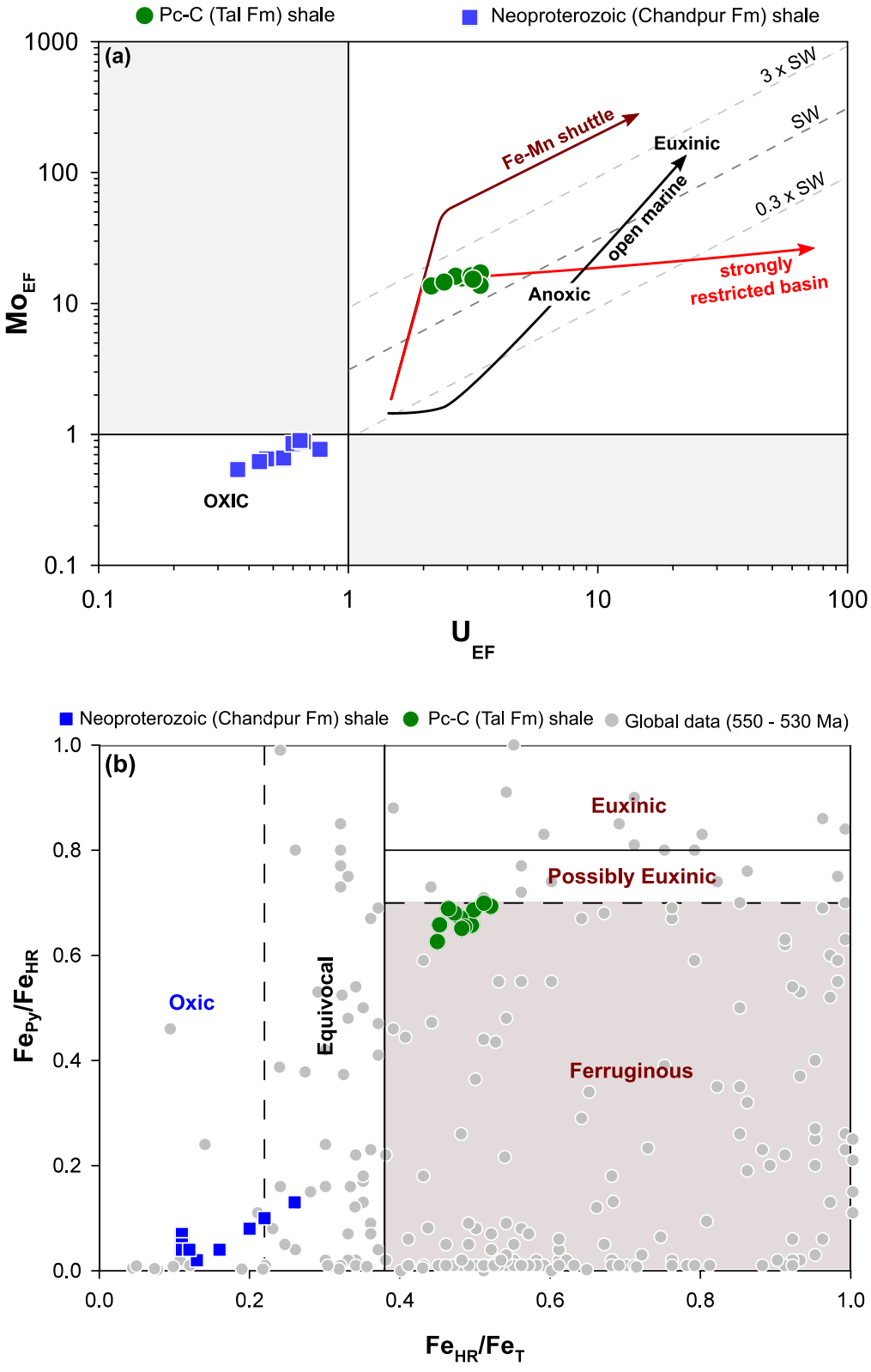

Figure 4.6. *Co-variation plots of* ***(a)*** Mo_{EF}–U_{EF} *and* ***(b)*** *Iron speciation* (Fe_{HR}/Fe_T *and* Fe_{Py}/Fe_{HR}) *parameters for Pc-C (Tal Fm) and Neoproterozoic (Chandpur Fm) shales. For comparison, modern seawater Mo/U molar ratio (solid line) and compiled Fe-speciation data (Grey circle) for early Cambrian (550 – 530 Ma; Farrell et al., 2021) shales are also shown.*

4.2.1.2. Molybdenum isotopic constraints

The molybdenum isotopic signature of organic-rich shales has been widely used to reconstruct past seawater δ^{98}Mo value and areal extent of redox state (e.g., Arnold et al., 2004; Kendall et al., 2011; Chen et al., 2015). The seawater δ^{98}Mo (modern-day value ~ +2.34‰; Nakagawa et al., 2012) is mainly regulated by its input and removal pathways. The major sources of Mo are riverine (~ +0.7‰; Archer and Vance, 2008) and hydrothermal (−3.5‰ to +2.06‰; McManus et al., 2002; Neely et al., 2018) inputs, whereas Mo removal from the oceans occurs through its association with Fe-Mn oxyhydroxides in oxic settings, and as thiomolybdate complexes in sulfidic waters. The distinctive isotopic fractionation factors occurring during oxic (~ −3‰; Poulson et al., 2006), anoxic (−0.7‰ to −3‰; Poulson et al., 2006; Neubert et al., 2008), and euxinic (−0.1‰ to +0.2‰; Siebert et al., 2003) scavenging processes makes δ^{98}Mo a reliable proxy for oceanic redox state. Here, we have considered the anoxic condition as the intermediate reducing Mo sink with low (<11μM; Helz et al., 1996) H_2S abundance and particulate shuttling/generation possibilities, where a complete conversion of molybdate ions to thiomolybdate complexes is unlikely.

The δ^{98}Mo values of the Tal shales range from +0.99‰ to +1.89‰ with an average of +1.5 ± 0.2‰. These values are marginally lower than those reported for euxinic shales during this period (~ +1.9‰; Wille et al., 2008; ~ +2.1‰; Wen et al., 2011). This difference is likely linked to isotopic fractionation between seawater and shale in anoxic and ferruginous depositional setting of the Tal shales (cf. section 4.2.1; Fig. 4.6b). Observations based on limited dataset from modern anoxic basins hint that sediments deposited in weakly reducing basins and continental margins may display an isotopic depletion of ~0.7‰ from the contemporaneous seawater value (Poulson et al., 2006; Poulson Brucker et al., 2009; Dickson et al., 2014; Eroglu et al., 2020). Considering this offset from our mean δ^{98}Mo value of +1.5‰, a qualitative estimate of the global ocean during the deposition of the Tal shales is found to be ~ +2.2‰. This inferred seawater δ^{98}Mo for the Pc-C is consistent with that reported earlier for other global sections (Fig. 4.2). The measured seawater Mo isotopic composition and related isotopic balance equations, hence, can be used to quantify the relative Mo removal proportions for different redox pathways.

A steady-state Mo isotopic balance approach has been adopted to quantify the areal extent of oxic, intermediate reducing (or Sulfidic At Depth; SAD), and sulfidic conditions for

the early Cambrian ocean (Kendall et al., 2017). The approach taken in this case is different from that adopted for the Cumbum shales (cf. Chapter 3) since the Tal shales were deposited in ferruginous conditions. This methodology parametrizes the oceanic Mo isotopic mass balance alone and hence provides a more first-order approximation. Towards this, it is assumed that the Mo supply via riverine input is balanced by its removal in oxic (oxic), intermediate reducing (interm), and euxinic (eux) settings. The related mass balance equations are provided below:

$$\delta^{98}Mo_{input} = f_{oxic} \times \delta^{98}Mo_{oxic} + f_{interm} \times \delta^{98}Mo_{interm} + f_{eux} \times \delta^{98}Mo_{eux} \quad (4.1)$$

Or,

$$\delta^{98}Mo_{SW} - \delta^{98}Mo_{input} \approx \delta^{98}Mo_{samples} = f_{oxic} \times \Delta_{oxic} + f_{interm} \times \Delta_{interm} + f_{eux} \times \Delta_{eux} \quad (4.2)$$

$$f_{oxic} + f_{interm} + f_{eux} = 1 \quad (4.3)$$

Here, f_{oxic}, f_{interm}, and f_{eux} represent the fraction of Mo removed to oxic, intermediate reducing, and euxinic sinks, respectively. The $\delta^{98}Mo_{input}$, $\delta^{98}Mo_{oxic}$, $\delta^{98}Mo_{interm}$, and $\delta^{98}Mo_{eux}$ stand for the isotopic compositions associated with respective sources and sinks. The Δ_{oxic}, Δ_{interm}, and Δ_{eux} represent Mo isotopic fractionation factors for oxic, intermediate reducing, and euxinic sinks, respectively. Here, $\delta^{98}Mo_{SW} - \delta^{98}Mo_{input} \approx \delta^{98}Mo_{samples}$ since both the isotopic offset in anoxic settings and the assumed riverine input value are ~ +0.7‰.

In this calculation, the $\delta^{98}Mo_{river}$ value has been assumed to be the same as that of the modern-day value (with ~ +0.7‰; Archer and Vance, 2008; King and Pett-Ridge, 2018). Support for this proposition comes from the seawater $^{187}Os/^{188}Os$ ratio, which also depends on the degree of oxidative weathering on the continents. Available Os isotopic ratios show that the initial $^{187}Os/^{188}Os$ ratios for Pc-C shales (0.8 to 1.2; Singh et al., 1999; Jiang et al., 2007; Kendall et al., 2009; Zhu et al., 2013; Fu et al., 2016) are similar to the modern seawater $^{187}Os/^{188}Os$ ratio (~1.05; Lu et al., 2017), indicating a modern-like oceanic budget for osmium and hence, a modern-like riverine composition and flux. This observation, however, may not be strictly valid as $\delta^{98}Mo_{river}$ values are regulated by multiple factors such as incongruent weathering, $\delta^{98}Mo$ value of exposed rocks, oxidative weathering rate, and Mo adsorption, which may have varied in the past (Kendall et al., 2015).

Equations (4.2 and 4.3) involving observed (left side of the equation) and model (right side) parameters were constructed for the eleven samples analyzed for Mo isotopes during this study (Table 4.3). Here, the observed parameters stand for the $\delta^{98}Mo$ values for the samples,

whereas the Δ values (Δ_{oxic}, Δ_{interm}, and Δ_{eux}) and Mo fractions (f_{oxic}, f_{interm}, and f_{eux}) serve as the model parameters. These parameters are assumed to follow log-normal distribution for the inversion. Further, modern-like values for $\delta^{98}Mo_{river}$ and seawater Mo concentrations have been assumed for the Tal basin. We have adopted an inverse model with a Quasi-Newton optimization algorithm to find the best-fit solution for the model parameters. The computational model used here has already been successfully employed to constrain solute sources for water (Tripathy and Singh, 2010; Goswami et al., 2014; Danish et al., 2020) samples. The model starts an iteration from a-priori values provided for the model parameters (Δ_{oxic} = 3.00 ± 0.14‰; Barling et al., 2001; Siebert et al., 2003; Barling and Anbar, 2004; Δ_{interm} = 0.70 ± 0.14‰, Poulson et al., 2006; Δ_{eux} = 0.50 ± 0.30‰; Arnold et al., 2004; Chen et al., 2015; Kendall et al., 2017) to yield corresponding a-posteriori values (Δ_{oxic} = 2.99 ± 0.01‰, Δ_{interm}= 0.67 ± 0.05‰, Δ_{eux} = 0.39 ± 0.11‰) that can explain the equations with least residual. Using the inversion outcomes, the fraction of Mo removed (f_{oxic}, f_{interm}, and f_{eux}) can be related to the seafloor area represented for each sink (A) using the following equation.

$$f = \frac{A \times B}{F_{input}} \tag{4.4}$$

where *A* represents the seafloor area covered by the sinks (in cm^2), *B* is the Mo burial flux for each sink (in nmol cm^{-2} yr^{-1}), and F_{input} represents the Mo input flux (3.1×10^{17} nmol yr^{-1}; Miller et al., 2011). In this evaluation, the average Mo burial flux (B) for modern-day oxic (0.021 nmol cm^{-2} yr^{-1}), intermediate (2.61 nmol cm^{-2} yr^{-1}), and euxinic (12.51 nmol cm^{-2} yr^{-1}) oceanic settings were considered (Scott et al., 2008). The assumed burial fluxes and seawater Mo inventory may have varied in the past depending on the ocean redox state, continental Mo supply, and its removal intensities. These possible changes in these parameters may also introduce uncertainties to our calculation.

Results from the inversion show that the average Mo removal fractions for oxic (0.22 – 0.53), intermediate reducing (0.24 – 0.36), and euxinic (0.23 – 0.42) fractions are comparable (Fig. 4.7a). While the average oxic removal fractions (~0.39) are close to those estimated for the modern-oceanic settings (f_{oxic} ~0.40), the average euxinic removal fractions (~0.31) is about four times higher than the modern oceans (f_{eux} ~0.08; Scott et al., 2008; Poulson Brucker et al., 2009; Kendall et al., 2009). Evaluation of the relative seafloor extent during the Tal shale deposition (A_{oxic} = 99.19%; A_{interm} = 0.67%; A_{eux} = 0.14%) and its comparison with respect to modern values (A_{oxic} = 98.94%; A_{interm} = 1.03%; A_{eux} = 0.03%) indicate enhanced Mo removal

and euxinic areal extent during the Pc-C transition (Fig. 4.7b). The high sulfidic removal of Mo in this anoxic basin is intriguing. We hypothesize limited availability of H_2S in pore waters, which can trigger the conversion of molybdates to particle-reactive thiomolybdate complexes in the shallow sub-surface.

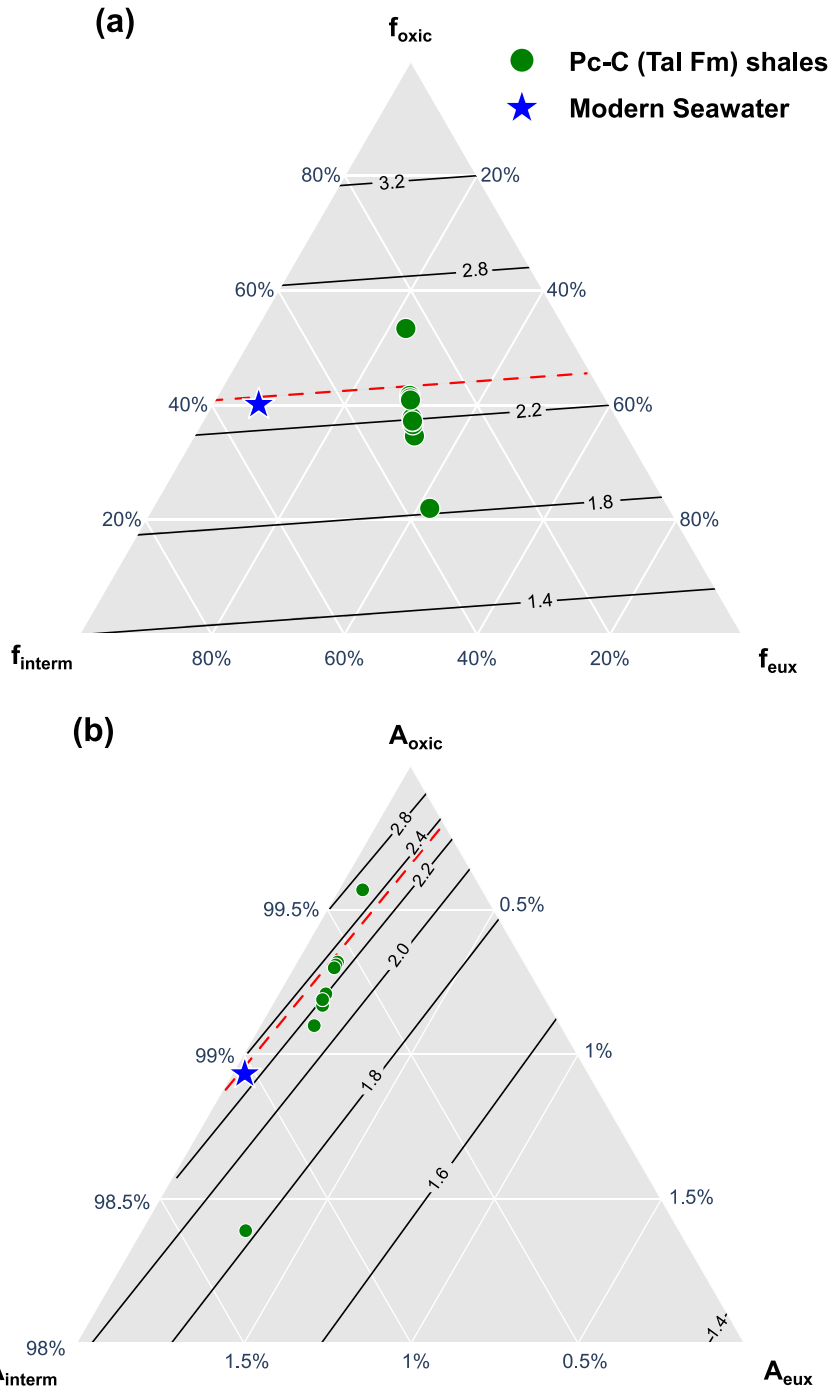

Figure 4.7. *Ternary diagrams of estimated* ***(a)*** *Mo removal fluxes and* ***(b)*** *seafloor areal extents of oxic, intermediate, and euxinic sinks (based on burial rates from Scott et al., 2008; Asael et al., 2018). Solid lines in the diagrams represent calculated values for different seawater* δ^{98}*Mo values, whereas the (red-coloured) dashed lines depict calculation for modern seawater* δ^{98}*Mo (+2.34‰) value.*

4.2.2 Sulfur cycling during the Pc-C transition

The present-day seawater sulfate concentration is ~28 mM with a higher residence time (~20 Myr; Claypool et al., 1980) than the ocean mixing time (~1 kyr). These sulfate ions are mainly supplied by rivers (~2.6 Tmol yr^{-1}; Raiswell and Canfield, 2012) with subordinate contributions from hydrothermal (0.1 Tmol yr^{-1}; Kagoshima et al., 2015) and volcanic (0.7 Tmol yr^{-1}; Kagoshima et al., 2015) inputs. The average $\delta^{34}S$ value for riverine source is ~ +4.8‰ (Burke et al., 2018), whereas the S input flux has a combined value of ~ +3‰ (Canfield, 2004). The removal of seawater sulfate mainly occurs via the formation of sulfides (pyrites) and sulfates (gypsum). Mass balance calculations for present-day values suggest that ~10–45% of S gets removed through pyrite burial (Tostevin et al., 2014). Additionally, sulfur associated with organic matter and carbonate phases also serve as minor sulfate sinks. The burial of sulfide minerals is a consequence of sulfate reduction through biological pathways and the subsequent conversion of released H_2S into pyrites. This microbial sulfate reduction (MSR) process involves preferential incorporation of lighter (^{32}S) isotopes with varying degrees of isotopic fractionation (≥40‰; Canfield, 2001; Canfield et al., 2010). Additionally, the $\delta^{34}S$ of sulfides are also regulated by overlying water $\delta^{34}S$ value, sulfate concentration, basin restriction, reactive iron availability, diagenesis, and biological uptake rates (Canfield, 2001; Fike and Grotzinger, 2010; Gomes and Hurtgen, 2013). In contrast to sulfides, the $\delta^{34}S$ value of sulfate minerals (e.g., gypsum anhydrite, barites) mostly retain the seawater $\delta^{34}S$ signature, with minimal (~1.6‰) fractionation (Raab & Spiro 1991).

Seawater sulfate concentration and its variation are mainly linked to oceanic oxygenation and continental oxidative weathering. Previous studies on seawater sulfate estimation have adopted several approaches, such as (i) mass balance modelling (Kah et al., 2004; Fike and Grotzinger, 2008; Canfield and Farquhar, 2009; Loyd et al., 2012), (ii) isotopic discrimination between co-genetic sulfides and sulfates (Song et al., 2014; Algeo et al., 2015; Wu et al., 2015), (iii) numerical modelling (Zhu et al., 2021; Li et al., 2023) or (iv) direct estimations from halites (Horita et al., 2002; Lowenstein et al., 2003; Brennan et al., 2004). The isotopic-balance approach requires information on multiple parameters, which include sulfate inventory and related input/output fluxes, rate of sulfur isotopic changes ($\partial^{34}S/\partial t$), (open/closed) diagenetic settings, and organic substrate type and reduction rates (Song et al., 2014; Algeo et al., 2015). In the absence of these data, we have utilized the MSR trend method (Algeo et al., 2015) to estimate the sulfate concentration of the Tal basin. This approach has

been established by correlating modern-day aqueous sulfate concentration [SO_4^{2-}] and isotopic fractionation ($\delta^{34}S_{sulfate\text{-}sulfide} = \delta^{34}S_{sulfate} - \delta^{34}S_{pyrite}$) data. This empirical relation, therefore, is less sensitive to organic substrate type, strain-specific fractionation, and sulfate reduction rates (Algeo et al., 2015). The following equation (Algeo et al., 2015) has been used for sulfate estimation for the Tal basin:

$$log[SO_4^{2-}] = \frac{\left(log\left(\Delta^{34}S_{sulfate-sulfide}\right) - 1.10 \pm 0.08\right)}{0.42 \pm 0.02} \quad (4.5)$$

The calculation yields sulfate concentrations ranging from 4 to 15 mM for the Tal basin, with an average value of 8 ± 3 mM (1σ; Fig. 4.8a). Our calculation relies on earlier-reported seawater $\delta^{34}S$ value for this period (35 ± 3‰ (1σ); Kampschulte and Strauss, 2004), as co-genetic sulfate $\delta^{34}S$ data were not available. In an earlier study, Mazumdar et al. (2008) have reported $\delta^{34}S$ for both sulfate and pyrites for the Tal basin. Using these literature data, an average [SO_4^{2-}] concentration of ~7 mM is computed, which is also similar to our estimates (~8 mM). Further, these estimates match well with compiled [SO_4^{2-}] data (6 ± 5 mM; 1σ; n = 111; Algeo et al., 2015) for 550−520 Ma (Fig. 4.8b). These data during the Pc-C transition are systematically higher than that reported for the Precambrian. Higher [SO_4^{2-}] can be linked to its increased continental supply via oxidative weathering during this period. Further, Fig. 4.8b also exhibits large variability in the sulfate estimates from Tal and other global sections. For instance, the estimated [SO_4^{2-}] across the Pc-C transition for the Yangtze platform (~2–6 mM; Li et al., 2023) is lower than that obtained for the Tal basin (~8 mM). As both the sites had similar paleogeographic locations (Jiang et al., 2003), these differences may have a linkage to the restricted connection of the Tal basin (unlike the Yangtze) to the open ocean. More studies with precise information on basinal setting, seawater $\delta^{34}S$ and paleogeography can constrain causative factors for spatial variability in sulfate concentrations.

4.2.3 Ocean biogeochemical cycle of the Tal basin during the Pc-C transition

The above discussion establishes a sulfate concentration of ~8 mM for the Pc-C ocean (Fig. 4.8). Assuming modern-like fluxes for sources and sinks, this concentration corresponds to a residence time of ~5 Myr for sulfates. These concentrations and residence time are higher compared to that for the Neoproterozoic Era but lower than the modern ocean (~28 mM and ~20 Myr). This comparison confirms the high nutrient supply (compared to the Neoproterozoic) and reactive iron (Fe_{HR}) in the early Cambrian oceans due to intense oxidative weathering in the continents. A high nutrient flux could enhance oceanic productivity, increasing OM export

to the seafloor and thereby facilitating the expansion of sulfidic water masses in the ocean. Our modelling efforts utilising Mo isotopes show elevated areal extent (~3–4 times the modern area; Fig. 4.7b) for sulfidic waters in the global oceans, confirming this proposition. Further, the observed anoxic-ferruginous bottom water condition (Fig. 4.6) in the Tal basin could be a result of increased reactive iron supply sourced from either riverine supply (Raiswell and Anderson, 2005) or marine incursions into the shelf regions (Mazumdar et al., 1999; Hughes et al., 2005). Previous studies from the same section (Mazumdar et al., 1999; Liu et al., 2021), as well as global records (Hughes et al., 2005), provide evidence for these processes. Fossil evidence of small shelly fauna, acritarchs, brachiopods, and trilobites in the overlying sections of the Lower Tal Formation further ascertains that environmental conditions in the Tal basin eventually became conducive for ecological expansion and sustained complex organisms.

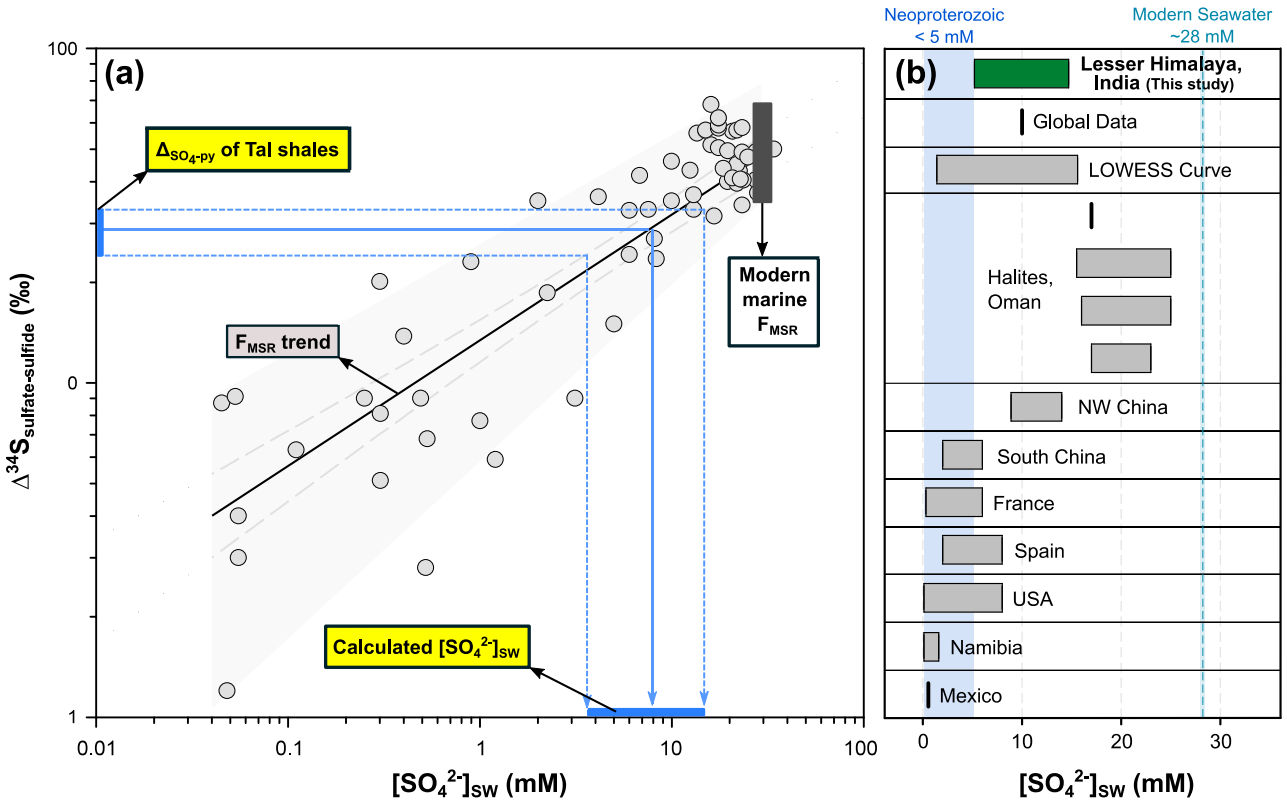

Figure 4.8. (a) *Estimation of seawater $[SO_4^{2-}]$ for the Tal basin using $\Delta^{34}S_{sulfate\text{-}sulfide}$ values using the MSR trend method (Algeo et al., 2015). Compiled data (grey circles) for modern aqueous systems and seawater sulfate concentration are also shown (Algeo et al., 2015).* ***(b)*** *Comparison of our estimated sulfate concentrations with compiled seawater sulfate data from other synchronous global sections and estimates (Horita et al., 2002; Lowenstein et al., 2003; Brennan et al., 2004; Ries et al., 2009; Canfield and Farquhar, 2009; Loyd et al., 2012; Wotte et al., 2012; Algeo et al., 2015; Wu et al., 2015; Zhu et al., 2021; Li et al., 2023).*

4.3. Conclusions

Geochemical and Mo-S isotopic compositions of black shales overlying the Pc-C boundary (Tal Formation, Lesser Himalaya) have been investigated. These datasets have been used to constrain the redox state, seawater sulfate inventory, and areal extent of reducing conditions during this period. The combined data on Fe-speciation, trace elemental enrichments, and Mo isotopes indicate anoxic and ferruginous (iron-rich) deep water conditions in the shelf regions during the deposition of Tal shales. Mo isotopic data estimate a higher areal extent of euxinic waters compared to the modern ocean, possibly due to increased net organic burial during the Pc-C transition. Our calculations based on pyrite-S isotopes yield a seawater sulfate concentration of 8 ± 3 mM. This concentration is higher compared to that of the Neoproterozoic ocean, confirming increased terrestrial input and oxygen in the ocean-atmospheric system during the Pc-C. These observed environmental conditions would have imparted a primary control on the subsequent expansion and diversification of complex life during the early Cambrian.

Chapter 5

Proterozoic Nitrogen cycling in the shallow water environments: An isotopic and modelling perspective from Indian shales

The evolution of eukaryotes during the Proterozoic Eon is considered to have been limited by the availability of fixed nitrogen in the oceans (Anbar and Knoll, 2002; Stüeken et al., 2024). The dominant species of bioavailable nitrogen in the surface oceans and its transformation pathways (Sigman et al., 2009; Ader et al., 2014; Stüeken et al., 2016) are largely dependent on the oceanic redox structure, which showed large temporal and spatial heterogeneity during the Proterozoic Eon. The dominantly anoxic oceanic environments during this Eon under a low-oxygen atmosphere are thought to have limited the bioavailability of nitrate retarding the diversification of early eukaryotes (Stüeken et al., 2024 and reference therein). While multiple studies provide evidence for offshore-onshore variations in nitrogen availability (e.g., Godfrey et al., 2013; Stüeken, 2013), limited studies explore nitrogen cycling in shallow marine environments, which were probably zones of eukaryotic habitats. This work presents the bulk nitrogen and organic carbon data of organic-rich shales from multiple Proterozoic Basins, including the Vindhyan Basin (~1.21 Ga Bijaigarh Formation and ~1.73 Ga Kajrahat Formation), Cuddapah Basin (~1.88 Ga Tadpatri Formation and ~1.66 Ga Cumbum Formation) and the Lesser Himalaya section (immediately above Pc-C boundary (Tal Formation)). These shale samples were deposited in shallow water (shallow to deep subtidal) environments and are suitable for evaluating the effect of marine redox states on continental margin environments. The impact of basinal redox conditions in influencing the modes of N-cycling was assessed using these shale $\delta^{15}N$ data.

5.1. The Modern Nitrogen Cycle

Bioavailable forms of nitrogen in the modern oceans are nitrate (NO_3^-), ammonium (NH_4^+), particulate organic nitrogen (PON), and dissolved organic nitrogen (DON). Abundances and transformation of these complexes are linked by redox reactions mediated by microorganisms (Fig. 5.1; Falkowski, 1997; Sigman et al., 2009; Thomazo and Papineau, 2013). The primary source of nitrogen to the oceans is derived from N_2-fixation processes (126−223 Tg yr^{-1}; Wang et al., 2019), where prokaryotes (and some eukaryotes) reduce N_2 gas to ammonium with the help of nitrogenase enzyme in the photic zone of the ocean (Raymond et al., 2004). Other minor inputs include riverine (~25 Tg yr^{-1}) and atmospheric contributions (~15 Tg yr^{-1}; Algeo et al., 2015). Remineralization of this organic matter produces NH_4^+, which either rapidly gets converted to nitrate by the nitrification process or gets assimilated (Bristow et al., 2016). Removal of nitrogen from the oceans dominantly occurs under suboxic to anoxic conditions as N_2 by (i) denitrification, which happens in the water column (52−66 Tg yr^{-1};

Eugster and Gruber, 2012; DeVries et al., 2012) and/or the sediments (93−164 Tg yr^{-1}; Eugster and Gruber, 2012; DeVries et al., 2012) and (ii) anaerobic oxidation of ammonium (*anammox*) which combines nitrate reduction and ammonium oxidation processes. Additionally, a small portion of this surface productivity (~1%) escapes remineralization and gets buried in the sediments, contributing to the sedimentary organic nitrogen pool. Upon burial, diagenetic processes can redistribute part of the nitrogen pool into clays such as illite and smectite (e.g., Schroeder and McLain, 1998).

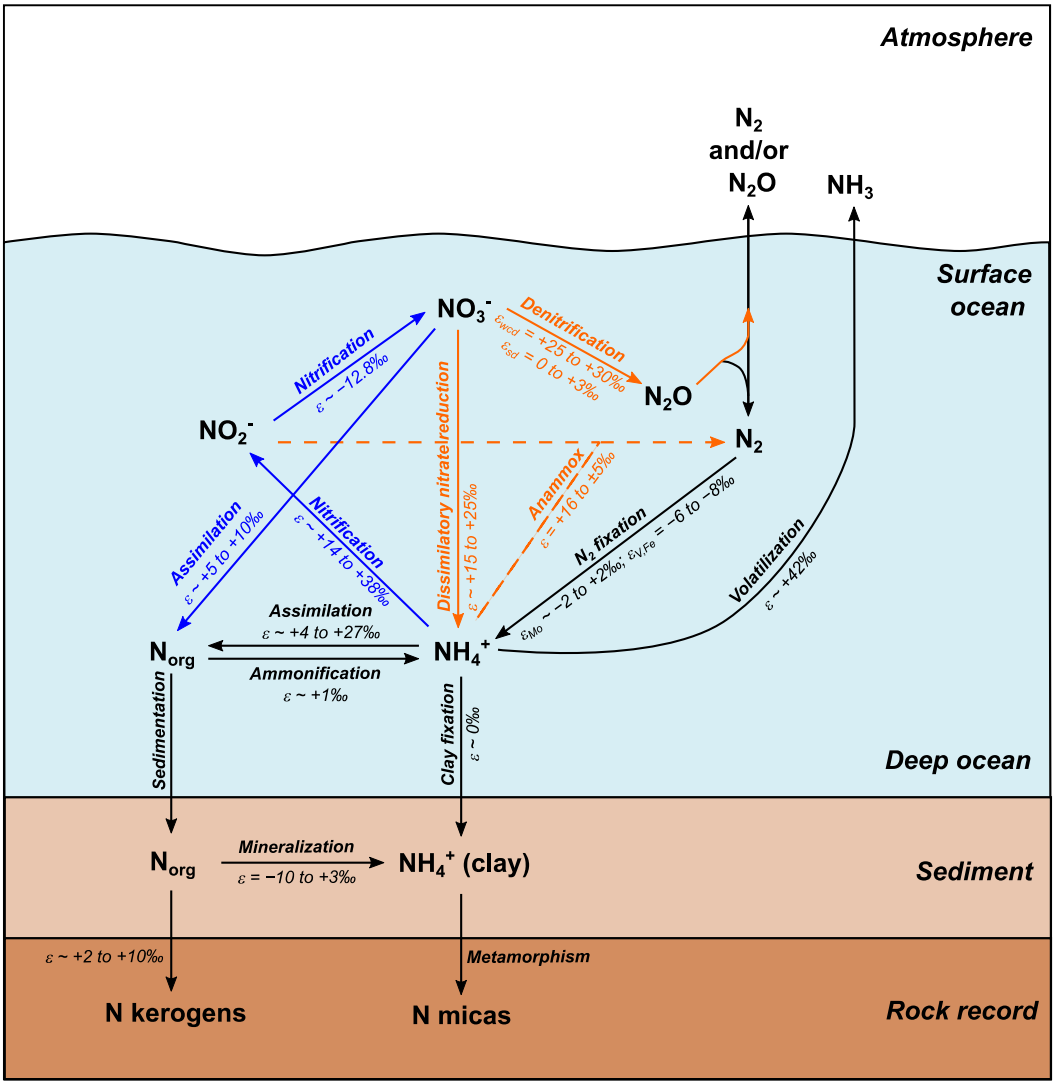

Figure 5.1. *Simplified illustration of the modern marine nitrogen cycle showing the different transformation pathways and associated isotopic fractionation ($\varepsilon \approx \delta^{15}N_{reactant} - \delta^{15}N_{product}$) between various nitrogen species (after Stüeken et al., 2024 and references therein). Blue and orange pathways mark oxic and suboxic-anoxic processes (Stüeken et al., 2016).*

In the marine environment, chemical and biological processes discriminate between the stable isotopes of N (^{14}N and ^{15}N), leading to varying isotopic effects (Sigman et al., 2009). The relative proportion of bioavailable forms and isotopic fractionation during these transformation

processes determine the isotopic composition of primary producers. These include the N_2-fixation process and upwelled nitrate/ammonium (e.g. Sigman et al., 2009; Somes et al., 2010). The N_2-fixation is carried out by aerobic or anaerobic autotrophs, which convert molecular N_2 into NH_4^+. Biological nitrogen fixation using Mo-based *nitrogenase* enzyme imparts small fractionation ($\varepsilon = -2‰$ to $+1‰$; $\varepsilon \approx \delta^{15}N_{reactant} - \delta^{15}N_{product}$) while the involvement of alternate *nitrogenase* containing V or Fe imparts fractionations of $-8‰$ to $-6‰$ (Zerkle et al., 2008; Zhang et al., 2014). Remineralization of these organisms can accumulate NH_4^+ in anoxic conditions, which can either be assimilated by the organisms ($\varepsilon \sim +4‰$ to $+27‰$; Hoch et al., 1992; Pennock et al., 1996; Vo et al., 2013) or be converted into N_2 during *anammox* reaction ($\varepsilon \sim +16‰$ to $+29‰$; Kuypers et al., 2003; Prokopenko et al., 2006). Both these processes lead to a heavier nitrogen pool and subsequent positive $\delta^{15}N$ values in the sediments (Sigman et al., 2009; Brunner et al., 2013). In oxic conditions, this NH_4^+ is rapidly oxidized sequentially to NO_2^- ($\varepsilon = +14‰$ to $+38‰$) and subsequently NO_3^- ($\varepsilon = -12.8‰$; Casciotti, 2009). In the case of partial oxidation, residual NH_4^+ becomes enriched in ^{15}N due to the larger isotope fractionation associated with the first step and imparts a heavier isotopic signal for the biomass (Sigman et al., 2009). In case of the dysoxic or anoxic condition, the resultant NO_3^- is denitrified to N_2 either in the sediments ($\varepsilon_{sd} \sim 0‰$ to $+3‰$) or in the water column ($\varepsilon_{wcd} \sim +25‰$ to $+30‰$), enriching the residual nitrate pool with the heavier isotope (Sigman et al., 2009). This residual nitrate pool is assimilated by organic matter by imparting a fractionation of 0‰ and +10‰ in NO_3^- limited and replete conditions, respectively (Fogel and Cifuentes, 1993; Pennock et al., 1996; Bauersachs et al., 2009). A large number of studies focused on understanding the evolution of the biosphere thus utilize the N-isotopic signature of sedimentary rocks as a proxy for past N-cycling and redox evolution (e.g., Papineau et al., 2009; Busigny et al., 2013; Stüeken et al., 2024). The major source of organic matter to the sediments is associated with the primary productivity in the photic zone. Considering minimal modifications accompanying water column degradation and post-depositional effects, the isotopic signatures of the sedimentary OM should reflect that of the primary producers.

5.2 Results

The carbon and nitrogen isotopic compositions, total organic carbon (TOC) and total nitrogen (TN) contents, along with selected major elemental compositions, for shales from the Vindhyan, Cuddapah and Lesser Himalaya, are provided in Table 5.1. The average TOC of these samples is 1.7 ± 0.9 wt% (n = 73), with a low content of inorganic carbon (0.8 ± 0.5 wt%). The average TN of these shales (0.07 ± 0.02 wt%, n = 73) overlaps with those reported from

other Proterozoic and early Cambrian sections (0.09 ± 0.10 wt%, n = 2668; Stüeken et al., 2024). The (atomic) TOC/TN ratios vary between 14 and 61 (Fig. 5.2a) and are consistently higher than the Redfield ratio (~7; Redfield, 1934).

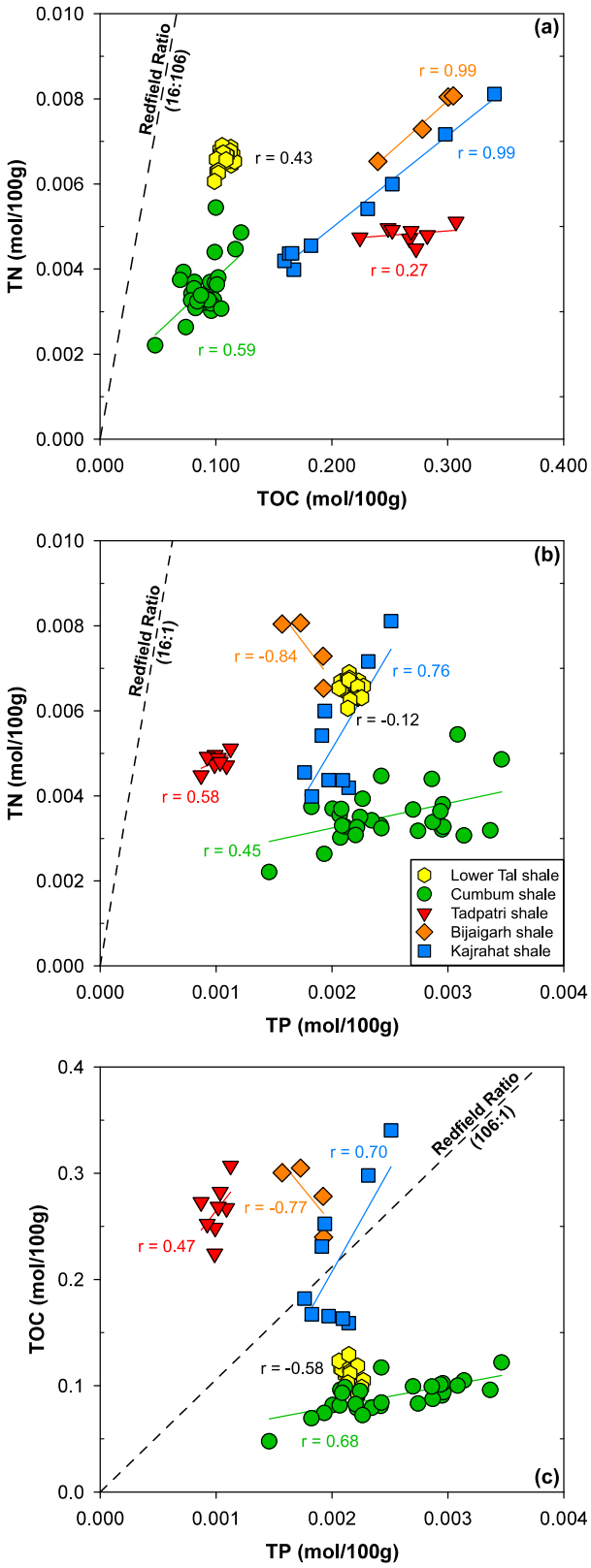

Figure 5.2. *Cross plots between TN, TOC and TP. The expected Redfield ratio associated with normal phytoplankton biomass is also shown for comparison.*

Table 5.1. Elemental and isotopic data for shale samples from selected sedimentary successions of India

Sample ID[#]	TN	TIC	TOC	TP	Fe_T	Al	$\delta^{15}N_{bulk}$ (Air)	$\delta^{13}C_{org}$ (V-PDB)	Fe_{HR}/Fe_T	Fe_{Py}/Fe_{HR}	Mo	U	Mo_{EF}	U_{EF}	P_{EF}
	wt%			µg/g	wt%		‰				µg/g				
Lower Tal Formation, Mussoorie Group															
HM15-10A	0.091	1.03	1.28	670	3.53	7.46	0.93	−31.10	0.50	0.66	15.8	8.0	15.7	3.2	1.1
HM15-10B	0.092	0.97	1.35	662	3.54	7.41	1.45	−31.14	0.49	0.67	16.0	7.9	16.0	3.2	1.1
HM15-11A	0.096	1.01	1.36	665	3.54	7.51	1.00	−31.24	0.50	0.69	15.7	8.2	15.5	3.3	1.1
HM15-11B	0.094	1.01	1.38	643	3.55	7.35	1.01	−31.19	0.49	0.70	15.9	7.8	16.1	3.2	1.1
HM15-12A	0.091	1.06	1.23	654	3.58	7.44	0.77	−31.14	0.48	0.67	15.9	7.5	15.9	3.0	1.1
HM15-12B	0.090	0.95	1.36	658	3.55	7.41	1.17	−31.19	0.46	0.66	15.8	7.2	15.8	2.9	1.1
HM15-13A	0.095	0.93	1.24	668	3.61	7.49	1.17	−31.15	0.49	0.65	15.8	7.8	15.7	3.1	1.1
HM15-13B	0.095	0.89	1.28	664	3.60	7.50	1.12	−31.23	0.49	0.67	15.9	7.1	15.7	2.9	1.1
HM15-14A	0.097	0.96	1.27	665	3.66	7.56	1.13	−31.18	0.52	0.69	16.3	7.7	16.0	3.1	1.1
HM15-14B	0.094	0.94	1.26	691	3.69	7.41	1.07	−31.13	0.46	0.67	16.1	6.6	16.1	2.7	1.2
HM15-15A	0.092	1.02	1.36	664	3.52	7.28	1.13	−31.20	0.47	0.68	15.5	8.1	15.8	3.4	1.1
HM15-15B	0.091	1.08	1.31	645	3.50	7.25	1.13	−31.17	0.48	0.70	15.5	8.1	15.8	3.4	1.1
HM15-16A	0.091	0.94	1.40	638	3.46	7.39	1.06	−29.94	0.45	0.63	15.7	7.8	15.8	3.2	1.1
HM16-16B	0.095	0.96	1.35	666	3.51	7.35	1.45	−30.39	0.43	0.64	15.7	7.6	15.9	3.1	1.1
HM15-17A	0.094	1.03	1.32	670	3.46	7.32	1.03	−31.11	0.48	0.65	16.8	8.1	17.0	3.4	1.1
HM15-17B	0.094	1.07	1.28	665	3.50	7.29	1.07	−29.70	0.47	0.68	16.1	7.6	16.4	3.1	1.1
HM15-18A	0.092	1.06	1.21	704	3.63	7.56	1.32	−31.17	0.46	0.69	16.6	7.8	16.3	3.1	1.2
HM15-18B	0.092	1.00	1.31	688	3.49	7.38	0.93	−30.83	0.48	0.66	17.0	8.3	17.1	3.4	1.2
HM15-20A	0.088	0.98	1.21	688	3.43	7.21	1.12	−30.96	0.45	0.66	13.4	8.1	13.7	3.4	1.2
HM15-20B	0.088	1.01	1.23	699	3.66	7.14	1.15	−31.14	0.50	0.67	14.7	7.5	15.3	3.2	1.2
HM15-21A	0.088	1.02	1.23	668	3.46	7.08	1.42	−31.22	0.51	0.70	13.0	5.0	13.6	2.1	1.2
HM15-21B	0.085	1.00	1.19	662	3.53	7.21	0.86	−31.24	0.54	0.69	14.2	5.8	14.5	2.4	1.1

Table 5.1. *(continued)*

Sample ID[#]	TN	TIC	TOC	TP	Fe_T	Al	$\delta^{15}N_{bulk}$ (Air)	$\delta^{13}C_{org}$ (V-PDB)	Fe_{HR}/Fe_T	Fe_{Py}/Fe_{HR}	Mo	U	Mo_{EF}	U_{EF}	P_{EF}
	wt%			µg/g	wt%		‰				µg/g				
Cumbum Formation, Nallamalai Group, Cuddapah Supergroup															
CDP21-17	0.044	0.49	1.00	850	2.35	7.43	7.60	−30.12	0.55	0.63	6.7	2.7	6.7	1.1	1.4
CDP21-18	0.063	0.12	1.41	751	2.15	9.38	8.03	−29.15	0.38	0.78	5.0	1.9	3.9	0.6	1.0
CDP21-19	0.046	0.19	0.97	750	2.16	7.82	8.06	−30.30	0.43	0.77	7.0	2.6	6.6	1.0	1.2
CDP21-20	0.048	0.25	0.95	726	2.20	8.00	7.67	−30.39	0.41	0.76	7.0	2.7	6.5	1.0	1.1
CDP21-21	0.052	0.13	0.98	621	2.14	7.97	7.50	−30.19	0.53	0.88	6.5	4.3	6.0	1.6	1.0
CDP21-22	0.050	0.14	0.98	640	2.11	8.05	7.64	−30.17	0.37	0.81	6.4	4.5	5.9	1.7	1.0
CDP21-23	0.049	0.09	1.14	695	2.23	7.94	6.95	−30.21	0.43	0.86	7.1	2.7	6.6	1.0	1.1
CDP21-24	0.052	0.06	1.14	644	2.25	8.10	7.67	−30.19	0.67	0.92	7.1	2.2	6.5	0.8	1.0
CDP21-35	0.042	0.81	1.15	642	2.41	7.37	7.39	−29.80	0.46	0.50	8.6	4.1	8.7	1.7	1.1
CDP21-36	0.046	0.97	1.18	654	2.51	7.44	8.21	−29.73	0.60	0.40	9.1	3.8	9.1	1.5	1.1
CDP21-37	0.046	0.86	1.12	647	2.41	7.67	7.70	−29.80	0.61	0.45	6.5	3.1	6.2	1.2	1.1
CDP21-38	0.045	0.82	1.09	914	2.71	7.93	7.38	−31.48	0.91	0.84	7.3	3.2	6.8	1.2	1.4
CDP21-39	0.045	0.65	1.15	1042	2.69	7.99	7.15	−31.52	0.91	0.86	7.5	3.8	6.9	1.4	1.6
CDP21-127	0.046	1.71	1.13	917	2.32	6.65	7.83	−30.74	0.74	0.76	7.7	4.7	8.5	2.1	1.7
CDP21-128	0.043	0.86	1.26	972	2.17	7.22	7.96	−30.85	0.91	0.87	8.0	4.9	8.2	2.0	1.7
CDP21-129	0.046	1.30	0.95	687	2.27	7.61	6.94	−30.68	0.88	0.82	6.4	4.4	6.3	1.7	1.1
CDP21-130	0.051	0.41	1.19	837	2.14	8.07	6.76	−30.48	0.62	0.81	7.8	4.8	7.2	1.8	1.3
CDP21-131	0.031	3.00	0.57	452	2.92	5.09	8.61	−29.97	0.82	0.70	2.7	3.0	3.9	1.8	1.1
CDP21-132	0.043	1.79	0.99	683	2.15	7.06	7.53	−30.37	0.76	0.72	6.0	4.4	6.3	1.9	1.2
CDP21-133	0.045	1.16	1.01	752	2.03	7.36	7.19	−30.33	0.77	0.81	5.8	4.2	5.8	1.7	1.3
CDP21-134	0.037	2.65	0.89	599	2.57	5.65	6.91	−30.49	0.77	0.59	4.9	3.8	6.5	2.0	1.3
CDP21-135	0.055	0.32	0.87	702	2.03	8.65	7.65	−30.56	0.57	0.84	6.3	4.1	5.4	1.4	1.0

Table 5.1. *(continued)*

Sample ID[#]	TN	TIC	TOC	TP	Fe_T	Al	$\delta^{15}N_{bulk}$ (Air)	$\delta^{13}C_{org}$ (V-PDB)	Fe_{HR}/Fe_T	Fe_{Py}/Fe_{HR}	Mo	U	Mo_{EF}	U_{EF}	P_{EF}
	wt%			µg/g	wt%		‰				µg/g				
CDP21-136	0.047	0.88	1.05	889	2.16	7.07	7.06	−30.99	0.65	0.78	6.5	4.1	6.8	1.8	1.6
CDP21-137	0.053	0.85	1.23	916	2.04	7.71	6.35	−30.98	0.64	0.71	7.1	5.0	6.8	1.9	1.5
CDP21-138	0.051	0.96	1.21	909	2.46	7.08	7.05	−30.77	0.49	0.56	7.8	4.7	8.2	2.0	1.6
CDP21-139	0.052	1.57	0.83	565	2.74	7.30	7.70	−30.61	0.58	0.55	5.8	4.0	5.9	1.7	1.0
CDP21-140	0.068	0.26	1.46	1073	2.19	9.03	6.97	−30.87	0.37	0.84	7.5	3.9	6.1	1.3	1.5
CDP21-141	0.062	0.47	1.19	886	2.35	7.89	7.36	−30.68	0.39	0.59	6.3	4.0	5.9	1.5	1.4
CDP21-142	0.076	0.91	1.20	955	2.34	7.86	7.25	−30.21	0.47	0.55	5.6	4.1	5.3	1.6	1.5
Tadpatri Formation, Chitravati Group, Cuddapah Supergroup															
CDP21-99A	0.066	0.42	3.21	338	3.51	8.03	7.04	−33.08	-	-	7.0	5.4	6.5	2.0	0.5
CDP21-99B	0.072	0.85	3.69	349	2.94	8.01	7.13	−32.94	-	-	5.5	5.3	5.1	2.0	0.5
CDP21-100A	0.069	0.26	2.99	308	3.97	9.12	6.66	−32.85	-	-	6.6	6.3	5.4	2.1	0.4
CDP21-100B	0.066	0.19	2.69	306	4.19	9.09	6.09	−32.84	-	-	6.7	5.8	5.4	1.9	0.4
CDP21-101A	0.069	0.64	3.03	286	3.49	8.36	7.53	−33.07	-	-	3.9	5.9	3.5	2.1	0.4
CDP21-101B	0.069	0.53	3.22	316	3.62	8.59	7.31	−33.11	-	-	5.9	6.0	5.1	2.1	0.5
CDP21-102A	0.063	0.62	3.28	270	3.59	8.13	6.95	−33.10	-	-	5.2	5.3	4.8	2.0	0.4
CDP21-102B	0.067	0.66	3.39	321	3.59	8.30	7.58	−33.10	-	-	5.5	5.3	4.9	1.9	0.5
Bijaigarh Formation, Kaimur Group, Vindhyan Supergroup															
VIN22-07A	0.108	0.05	2.88	597	3.39	5.09	2.09	−31.70	0.61	0.46	23.1	20.4	33.7	12.1	1.5
VIN22-07B	0.125	0.11	3.61	486	3.27	5.02	1.55	−31.79	0.61	0.40	23.7	20.7	35.0	12.4	1.2
VIN22-08A	0.113	0.02	3.66	536	3.03	4.98	2.37	−31.77	0.74	0.45	32.8	21.9	48.8	13.3	1.3
VIN22-08B	0.106	0.13	3.34	596	4.31	4.91	3.50	−31.84	0.74	0.63	34.2	21.8	51.6	13.4	1.5

Table 5.1 *(continued)*

Sample ID[#]	TN	TIC	TOC	TP	Fe_T	Al	$\delta^{15}N_{bulk}$ (Air)	$\delta^{13}C_{org}$ (V-PDB)	Fe_{HR}/Fe_T	Fe_{Py}/Fe_{HR}	Mo	U	Mo_{EF}	U_{EF}	P_{EF}
	wt%			µg/g	wt%		‰				µg/g				
Kajrahat Formation, Semri Group, Vindhyan Supergroup															
VIN22-33A	0.062	0.91	2.01	566	1.90	4.91	2.91	−32.69	0.72	0.20	1.8	1.8	2.8	1.1	1.4
VIN22-33B	0.070	0.72	2.19	546	1.96	5.08	3.32	−32.69	0.65	0.23	1.9	1.9	2.8	1.1	1.3
VIN22-34A	0.070	0.85	2.04	-	2.09	5.34	3.68	−32.63	0.68	0.17	1.5	2.1	2.0	1.2	-
VIN22-34B	0.073	0.79	1.91	665	2.10	5.41	3.57	−32.69	0.64	0.22	1.9	1.9	2.6	1.1	1.5
VIN22-35A	0.068	0.86	1.96	649	2.09	5.26	4.69	−32.47	0.72	0.18	1.8	2.1	2.5	1.2	1.5
VIN22-35B	0.068	0.87	1.99	611	2.11	5.27	3.97	−32.56	0.67	0.19	1.6	2.0	2.3	1.1	1.4
VIN22-36A	0.086	0.22	2.78	593	1.67	5.13	3.55	−32.58	0.42	0.35	1.8	2.2	2.6	1.3	1.4
VIN22-36B	0.084	0.01	3.03	601	1.61	5.15	3.57	−32.64	0.38	0.38	1.9	2.2	2.7	1.3	1.5
VIN22-37A	0.122	0.12	4.09	778	2.22	6.83	3.61	−33.02	0.38	0.55	6.2	3.5	6.7	1.5	1.4
VIN22-37B	0.111	0.18	3.58	717	2.12	6.68	4.30	−32.92	0.40	0.48	5.8	3.2	6.5	1.5	1.3

[#]*A and B represent different powdered aliquots of the same sample.*

The phosphorus concentration and (atomic) TOC/TP ratios (Fig. 5.3) of these samples show wide variability between Formations. The average P concentrations for shales from the Lower Tal (668 ± 17 µg/g) and Vindhyan Basin (636 ± 75 µg/g (Kajrahat); 554 ± 53 µg/g (Bijaigarh shales)) are comparable to the UCC (~665 µg/g; Rudnick and Gao, 2003). The corresponding P_{EF}, however, is higher for the Vindhyan shales (~1.3 for Kajrahat and ~1.4 for Bijaigarh shales). Likely, the Cumbum shales show phosphorus enrichment (P_{EF} ~1.3) with an average concentration of 771 ± 154 µg/g. The Tadpatri shales, on the other hand, show low phosphorus content (312 ± 26 µg/g) and enrichment (P_{EF} ~0.5). The average TOC/TP ratio of Kajrahat shales (105 ± 24) is comparable to the Redfield ratio. These ratios for Cumbum (37 ± 6) and Lower Tal (50 ± 3) shales are found lower compared to the Redfield ratio (106), whereas these values for the Tadpatri (265 ± 26) and Bijaigarh (159 ± 30) shales are found higher (Fig. 5.3).

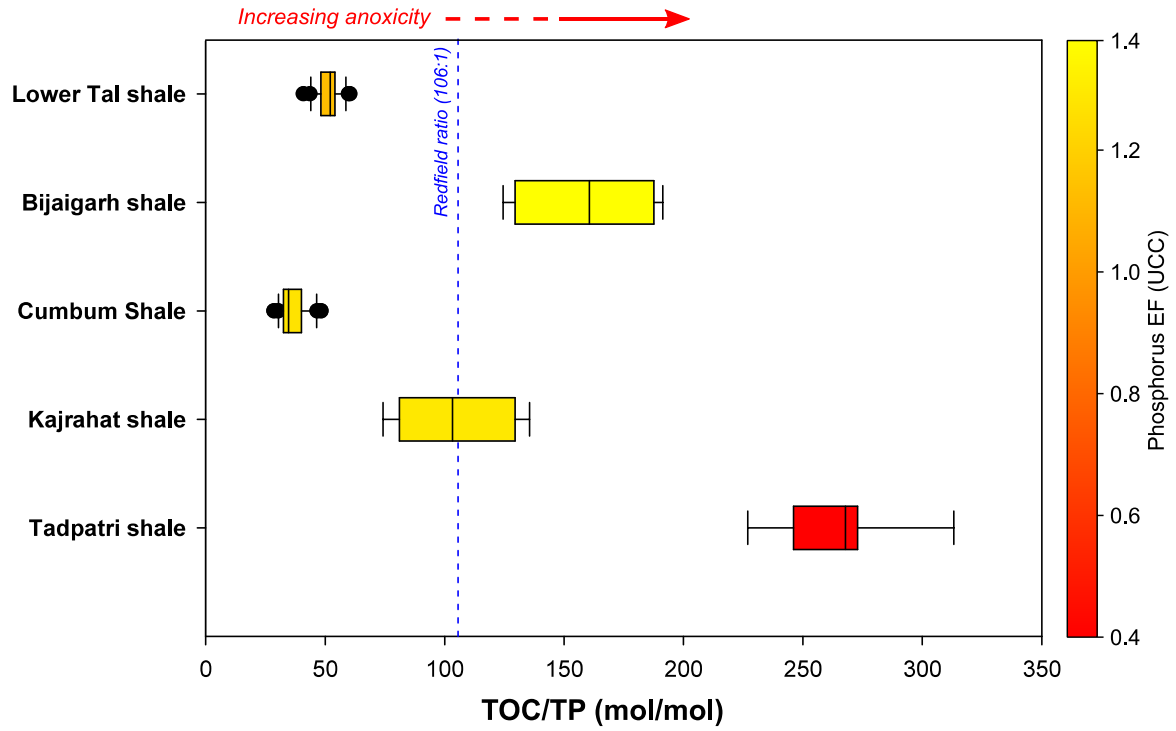

Figure 5.3. *Molar ratio of total organic carbon (TOC) and total phosphorus (TP) in the studied sections. Median values observed for different modern marine environments (after Algeo and Ingall, 2007) are also depicted.*

Redox-sensitive trace elements such as Mo (Mo_{EF} = 2−32) and U (U_{EF} = 1−8) also show considerable enrichment in all the studied shales (Fig. 5.4). The average Fe_{HR}/Fe_T ratios for the Vindhyan (0.60 ± 0.14) and Cuddapah (0.61 ± 0.18) shales are found comparable, whereas that for the Lesser Himalaya is found to be lower (0.48 ± 0.02). These values (Fig. 5.4) are consistently equal to or higher than the values expected for marine sediments deposited under

dysoxic to anoxic conditions ($Fe_{HR}/Fe_T \geq 0.28$; Poulton and Canfield, 2011; Raiswell et al., 2018). In contrast, the Fe_{Py}/Fe_{HR} ratios show wide variation, with the lowest and highest (average) ratios being observed for Kajrahat (0.29 ± 0.14) and Cumbum (0.72 ± 0.14) shales, respectively. Except for some samples from the Cumbum Formation (n = 16), the Fe_{Py}/Fe_T values, however, are consistently lower than the values observed for sediments deposited under euxinic waters ($Fe_{Py}/Fe_T \geq 0.7$; Poulton and Canfield, 2011; Raiswell et al., 2018).

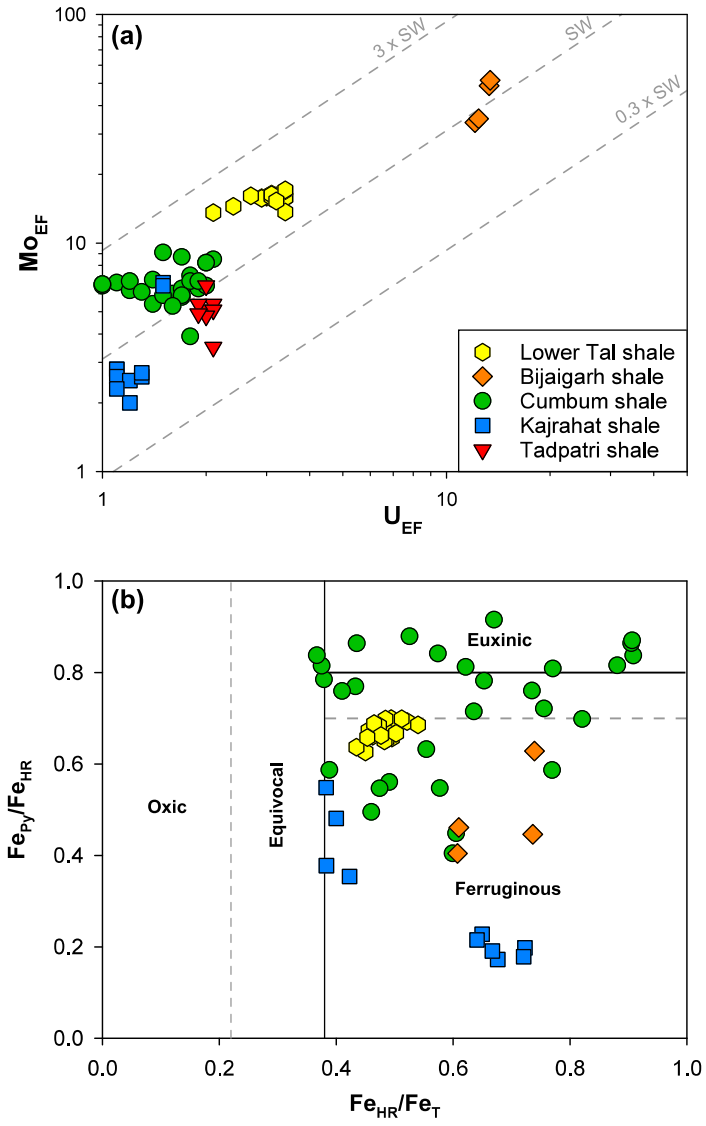

Figure 5.4. *Crossplots between* ***(a)*** *Mo_{EF} and U_{EF}* ***(b)*** *Fe-speciation parameters. Dashed lines in (a) represent the 0.3×, 1× and 3× seawater Mo/U molar ratio.*

The $\delta^{15}N_{bulk}$ values from all the studied samples range between 0.7‰ and 8.6‰ (Fig. 5.5), and broadly overlap with the range observed for modern marine sediments (Tesdal et al., 2013). The Paleoproterozoic shales from the Tadpatri, Kajrahat and Cumbum Formations show systematically enriched $\delta^{15}N_{bulk}$ values (2.9‰ to 8.6‰) than that compared to the

Mesoproterozoic Bijaigarh shales (1.6‰ to 3.5‰) and the early Cambrian (Lower Tal) shales (0.8‰ to 1.4‰; Table 5.1). Variations are minimal within the Formations (<0.5‰), except for the Bijaigarh shales (~0.8‰). The $\delta^{13}C_{org}$ values average 30.7 ± 2.0‰ for the entire studied sample set and overlap with the ranges observed for marine phytoplanktons and autotrophic carbon fixation processes (Hayes, 2001; Schidlowski, 2001). These values also show limited variations within individual Formations (<0.5‰).

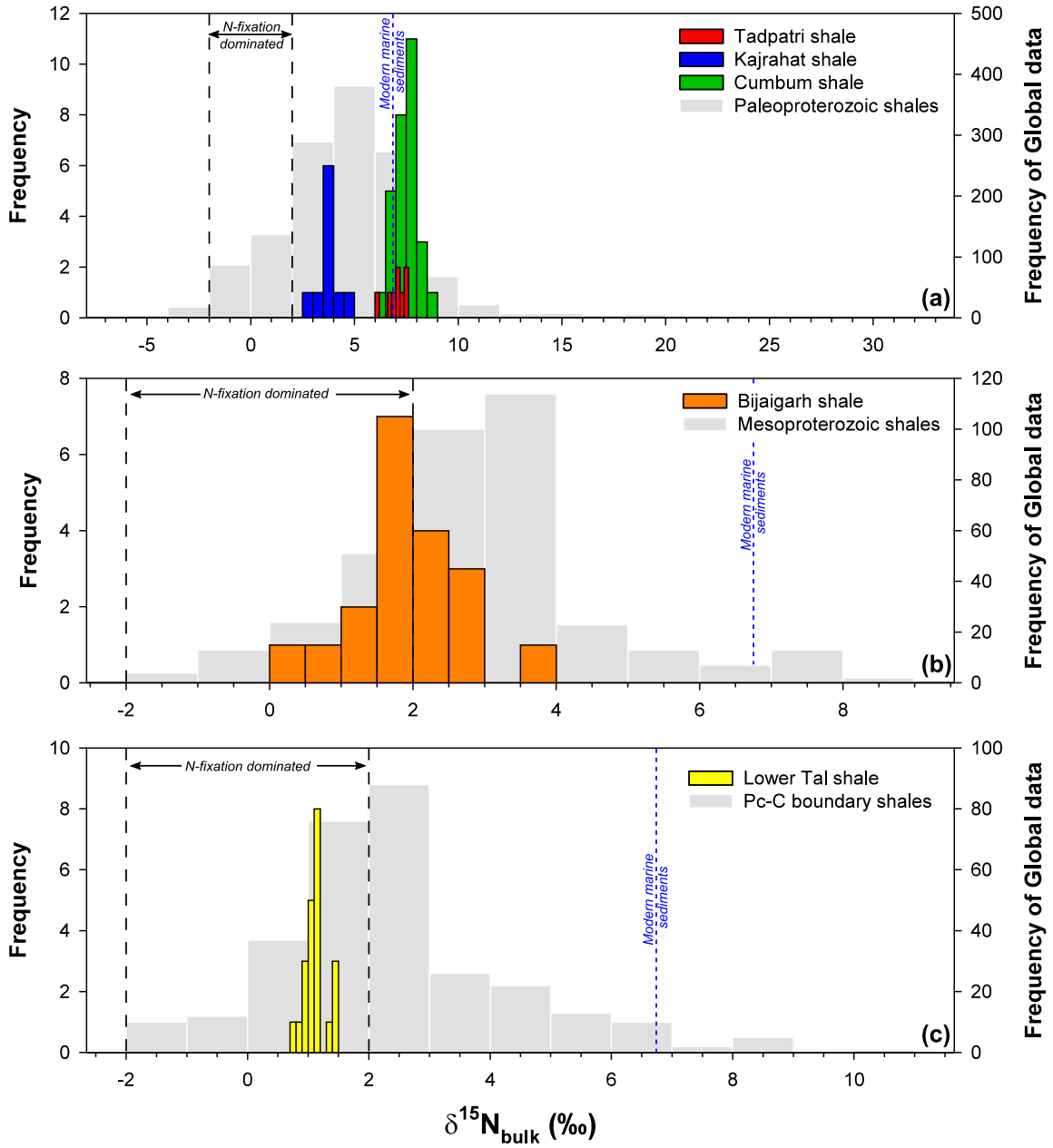

Figure 5.5. *Histogram plot showing the $\delta^{15}N_{bulk}$ distribution of the studied samples along with the global data reported from other* ***(a)*** *Paleoproterozoic,* ***(b)*** *Mesoproterozoic and* ***(c)*** *Pc-C boundary (550–530 Ma) sections (after Stüeken et al., 2024). Additional available data for the Bijaiagarh shales (Gilleaudeau et al., 2020) are also included. The typical range of sedimentary $\delta^{15}N$ values associated with N-fixation-dominated ecosystems (Stüeken et al., 2024) and the average value of modern marine sediments (~6.6‰; Tesdal et al., 2013) are also shown.*

5.3. Discussion

5.3.1. Evaluating post-depositional and metamorphic effects

A major challenge in interpreting isotopic signatures of ancient sedimentary rocks is their low OM content and complex post-depositional history. Evaluation of diagenetic and metamorphic effects is thus required before utilizing biogeochemical signals and redox proxies to determine the sedimentary environment (e.g., Ader et al., 2016). This assessment is done here using TOC/TN ratios and covariations of $\delta^{13}C_{org}$ and $\delta^{15}N_{bulk}$ with TOC, TN concentrations and their ratios (Fig. 5.6).

Nitrogen in marine sediments can exist as either organic-bound or clay-bound phases (e.g., Sigman et al., 2009). During burial diagenesis, OM releases NH_4^+, which is substituted for K^+ in clay minerals (Schroeder and McLain, 1998). Based on studies from modern settings, this remineralization process in the sediments and its fixation into clay minerals can alter the TOC and TN concentrations with minimal changes to the bulk nitrogen isotopic composition (Ader et al., 2016; Stüeken et al., 2016). Specifically, the TOC/TN ratios of primary biomass during remineralization in the water column and sediments increase due to the loss of labile nitrogen phases and, hence, deviate from the Redfield ratio (~7; Redfield, 1934). The samples from our studied section exhibit high (atomic) TOC/TN ratios (between 14 and 61), indicating the possible effect of some of these diagenetic processes. We evaluated the covariation between TN and TOC concentrations to assess the major nitrogen hosting phase (e.g. organic- or clay-bound). The y-intercept of this plot may reflect the amount of clay-bound nitrogen in the samples and hence provide a clue about diagenetic OM remineralization. All the studied sections show a generally positive TN-TOC correlation with a small y-intercept value (Fig. 5.2a, 5.6a), indicating the presence of clay-bound nitrogen possibly mobilized during diagenetic alteration. Further, the Tadpatri shales, in particular, show high y-intercept values (Fig. 5.6a) with the least correlation ($r = 0.27$), suggesting the dominance of clay-bound nitrogen in these samples. This is also supported by the observed significant correlation between their TN and K ($r = 0.71$; $p < 0.05$) concentrations. Since the remineralization and capture of nitrogen into clays is considered to occur under closed conditions (Ader et al., 2016), this process may not have imparted significant modification to the isotopic compositions. Additionally, the contribution of detrital NH_4^+ to the bulk $\delta^{15}N$ of these samples may also be considered negligible since the contribution from terrestrial biomass during the Precambrian is considered to be minimal (Ader et al., 2016; Canfield et al., 2021).

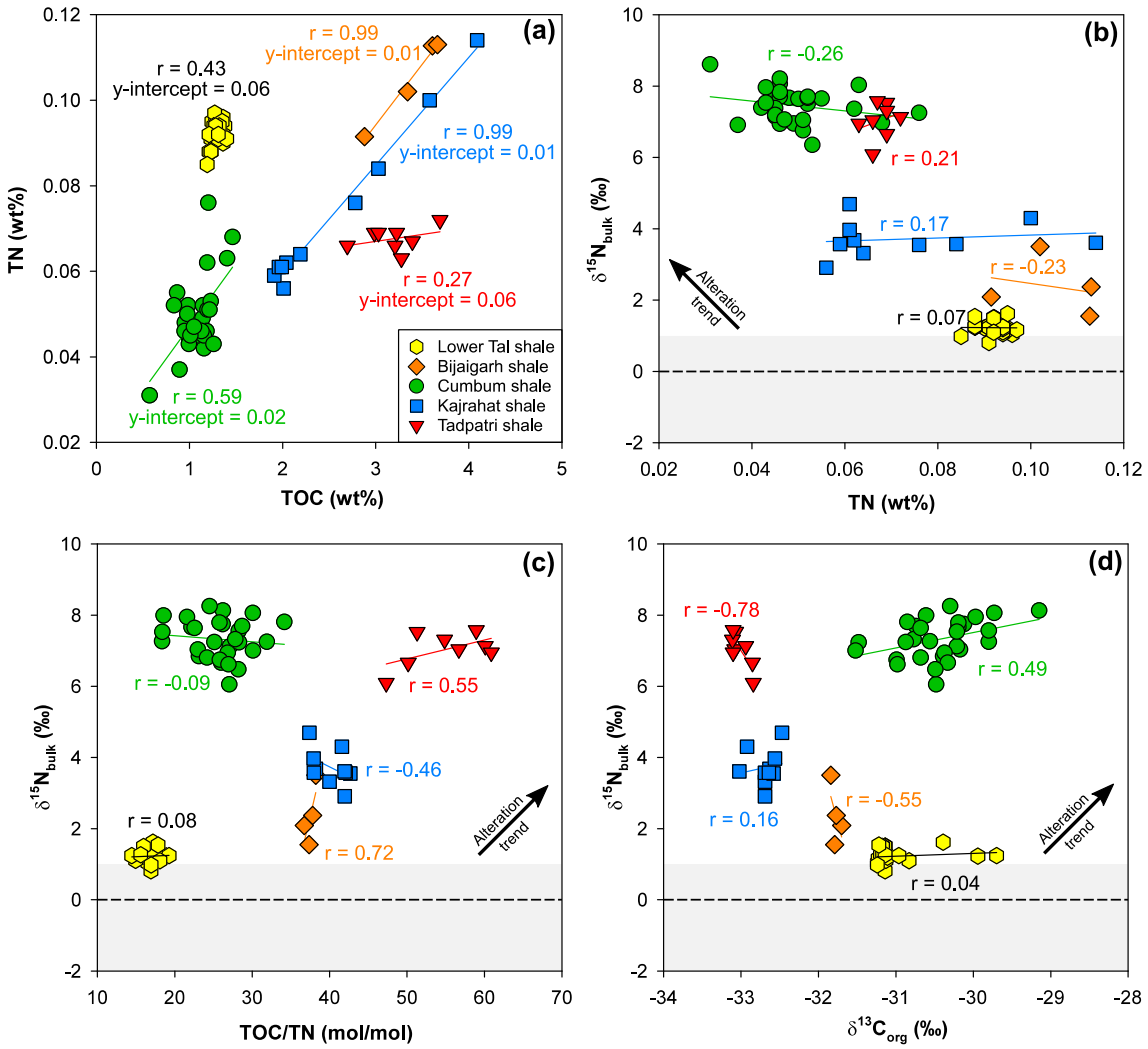

Figure 5.6. *Cross plots showing relations between* ***(a)*** *TN and TOC,* ***(b)*** $\delta^{15}N_{bulk}$ *and TN,* ***(c)*** $\delta^{15}N_{bulk}$ *and TOC/TN, and* ***(d)*** $\delta^{15}N_{bulk}$ *and* $\delta^{13}C_{org}$*. The black arrows depict expected trends resulting from alteration. The grey-shaded region denotes the typical* $\delta^{15}N_{bulk}$ *values associated with N-fixation (Zhang et al., 2014).*

The isotopic effects associated with diagenetic processes on the $\delta^{15}N$ values also depend on the redox state of the depositional condition. Diagenesis in oxic conditions leads to an isotopic enrichment up to ~4‰ (Freudenthal et al., 2001; Lehman et al., 2002), while these changes are minimal in anoxic environments (≤1–2‰; Altabet et al., 1999; Lehman et al., 2002; Thunell et al., 2004). Typically, all the studied shales exhibit deposition under anoxic conditions, as evidenced by the Mo–U enrichments (Fig. 5.4a) and Fe-speciation parameters (Fig. 5.4b). Similarly, a lack of correlation between $\delta^{15}N_{bulk}$ and Fe_{Py}/Fe_{HR} for all the sections ($r < 0.3$) suggests that changing redox conditions had an insignificant effect on the sedimentary $\delta^{15}N$ values. Further, metamorphism and organic matter maturation may elevate the $\delta^{15}N$ by preferentially volatilizing isotopically lighter NH_3 or N_2. These thermal effects may impart variable isotopic enrichments below greenschist (<1‰), within greenschist (1–2‰), for amphibolite (3–4‰) and for upper amphibolite (6–10‰) facies (Bebout and Fogel, 1992; Mingram and Braüer, 2001; Thomazo and Papineau, 2013; Ader et al., 2006; 2016; Stüeken et al., 2016). Similar events may incur the loss of lighter carbon isotopes (^{12}C) during OM degradation, leading to ^{13}C (and $\delta^{13}C_{org}$) enrichment in residual organic matter. Significant metamorphic effects are, therefore, expected to produce positive trends of $\delta^{13}C_{org}$ and TOC/TN with $\delta^{15}N_{bulk}$, and negative trends between $\delta^{15}N_{bulk}$ and TN (Hayes et al., 1983). Our studied sections have only undergone low-grade metamorphism (typically under lower greenschist, e.g., Manikyamba et al., 2008; Singh and Chakraborty, 2022) and thermal maturity (Célérier et al., 2009b; Deb and Pal, 2015), and hence, may not have experienced significant changes in their isotopic compositions. Further, the $\delta^{15}N_{bulk}$ values for all the studied samples show insignificant correlation with TN and TOC/TN, indicating a minimal metamorphic effect on $\delta^{15}N_{bulk}$ (Fig. 5.6b and 5.6c). While the $\delta^{15}N_{bulk}$ and TOC/TN relation doesn't indicate any thermal effects, the Cumbum shale samples exhibit a positive correlation between $\delta^{15}N_{bulk}$ and $\delta^{13}C_{org}$ ($r = 0.49$; $p < 0.01$) values. This relation may be attributed either to the high (lower greenschist to greenschist) grade metamorphism of these samples, its complex deformational history (Saha, 2002; Saha and Chakraborty, 2003; Sheppard et al., 2017), and/or primary biomass signal. Summing up based on available datasets and their trends, the $\delta^{15}N_{bulk}$ values for our studied sections may not have experienced any significant isotopic changes during post-depositional diagenetic and metamorphic processes and, hence, may represent signatures of ocean nitrogen cycling during shale deposition.

5.3.2. Possible Modes of Nitrogen cycling during the Proterozoic

5.3.2.1. Aerobic Nitrogen cycling

The Paleoproterozoic shales (Tadpatri, Kajrahat and Cumbum shales) show enriched (>3‰) $\delta^{15}N_{bulk}$ values, reaching up to 8.6‰. These enriched values do not fall in the typical $\delta^{15}N$ values expected for N-fixation-dominated ecosystems and may be explained by additional transformation mechanisms occurring within these basins. The following scenarios can explain the observed $\delta^{15}N$ enrichment:

(A) Ammonium assimilation: The nitrogen isotopic value of deep-water NH_4^+ in anoxic environments is mostly influenced by remineralization of organic matter and/or rates of other removal pathways (e.g. conversion to N_2 or N_2O; Sigman et al., 2009). This NH_4^+ reservoir gets enriched in $\delta^{15}N$, and primary productivity supported by its upwelling could lead to high $\delta^{15}N$ values in the sediments. Such scenarios have been reported from the late Paleoproterozoic Animikie Basin (Godfrey et al., 2013) and the Aravalli Basin (Papineau et al., 2009).

(B) Non-quantitative nitrification followed by quantitative denitrification: The partial nitrification of NH_4^+ results in the creation of an isotopically light NO_3^- pool and a heavy NH_4^+ pool. Complete denitrification of this NO_3^- pool and the quantitative assimilation of the residual heavy NH_4^+ can result in isotopically heavy biomass and sedimentary $\delta^{15}N$ values.

(C) Partial denitrification/anammox: NO_3^- loss due to denitrification or *anammox* processes in the water column leads to isotopic enrichment. Progressive use of this nitrate can elevate the $\delta^{15}N$ of the nutrient pool and hence, that of the biomass. This scenario, however, requires an abundant nitrate pool and the occurrence of redoxcline in the water column.

Scenario (A) requires the presence of a complementary lighter phase in the deeper parts of these basins or any other contemporaneous sections. While data for these are limited, the occurrence of such heavily depleted $\delta^{15}N$ values is not reported from any contemporaneous global sections apart from one study from the Paleoproterozoic Aravalli Supergroup (Papineau et al., 2009). Therefore, the scenario seems less probable for any of the studied sections. For Scenario (B), the nitrification of ammonium is considered to progress rapidly even under very

low O_2 levels (~1% PAL; Kalvelage et al., 2011; Bristow et al., 2016). The existence of such a situation is only reported from modern environments where seasonal redox stratifications prevail (Granger et al., 2011) and is considered to be unstable over geological timescales (Stüeken, 2013; Kipp et al., 2018). If the redoxcline in these basins were below the surface productive layers, the enriched ammonium may not be available for primary producers, making scenario (B) less likely. Similarly, the non-quantitative denitrification/*anammox* of a large nitrate pool also explains the resultant nitrogen isotopic enrichments (Scenario C). This would require sufficient dissolved O_2 contents and a stable nitrate pool in the surface waters of these basins. Such a mode of N-cycling has been widely invoked to explain the highly enriched values of various Paleo-Mesoproterozoic sections (Kipp et al., 2018; Stüeken et al., 2021; Wang et al., 2023). If scenario (C) were actually true for these sections, the degree of isotopic enrichment can be used to infer the size of the nitrate pool. A larger nitrate pool will lead to lower $\delta^{15}N$ enrichment in the associated biomass. This would also mean the presence of a larger nitrate pool in the Vindhyan (Kajrahat) Basin compared to the Cuddapah (Tadpatri and Cumbum) Basin.

Both scenarios (B) and (C) can explain the observed heavy $\delta^{15}N$ values of these sections. Distinguishing this would require information on the position of chemocline in these basins. While Fe-speciation parameters suggest that the chemocline in all these basins occurred in the water column, their exact position (closer to the surface layers or below the productive zone) is still indefinite. In such a situation, we conclude that scenarios (B) and (C) may be equally likely during the deposition of the Tadpatri, Kajrahat and Cumbum shales. More information on the basin hydrography and water-column structure can help validate the exact dynamics. Altogether, these pieces of evidence confirm the occurrence of aerobic nitrogen cycling in these Paleoproterozoic basins. These inferences are in line with reports from other global sections (Stüeken, 2013; Koehler et al., 2017; Kipp et al., 2018; Cheng et al., 2019; Kang et al., 2023; Wang et al., 2023).

5.3.2.2. Anaerobic cycling

The average $\delta^{15}N_{bulk}$ values of the Bijaigarh (2.4 ± 0.8‰) and Lower Tal shales (1.1 ± 0.2‰) are lower than the Paleoproterozoic shales. These depleted values can be explained by any of the following mechanisms:

(A) The N_2 fixation process contributes to the bulk of bioavailable nitrogen. For this to occur, an anoxic condition inhibiting the production of nitrate is required.

(B) Nitrification and denitrification are quantitative through a water column redox gradient, resulting in a very small amount of NO_3^- for biological uptake. In this case, the final isotopic composition of the biomass is minimally affected by this small NO_3^- pool.

(C) Denitrification is limited to the sediments, such that the nitrate pool has an isotopic composition similar to that of fixed nitrogen.

Scenario (C) is unlikely for the Bijaigarh and Lower Tal shales since these sediments are recognized to have deposited under anoxic (ferruginous) bottom-water conditions, as suggested by the Fe-speciation data. The closeness of the observed values to the atmospheric N_2 (~0‰) and with sedimentary values of fixation-dominated ecosystems (−2‰ to +2‰; Stüeken et al., 2024) indicate a scenario where N_2-fixation signals contributed to the bulk of bioavailable nitrogen (scenarios A and B). Quantitative nitrification and denitrification lead to a small NO_3^- reservoir, limiting the supply of bioavailable nitrogen and causing an increase in N-fixation processes to balance the deficiency. In such a condition, the role of NO_3^- in affecting the $\delta^{15}N$ of the biomass will be negligible. Gilleaudeau et al. (2020) also reported a similar range of $\delta^{15}N_{bulk}$ values (0.3‰ to 2.9‰) for the Bijaigarh shales. They have suggested that these signatures represent a dominant N-fixing system with limited modification from aerobic redox cycling (nitrification and denitrification). Our dataset, while slightly higher than these reported values, overlaps with their range and hence supports this inference. The existence of such a model of N-cycling has been reported from deep water sections of the Mesoproterozoic Bangemall (Koehler et al., 2017) and the Belt (Stüeken, 2013) Supergroups. Overall, we can confirm the occurrence of an anaerobic mode of nitrogen cycling in the Bijaigarh and Tal basins.

5.3.3. Effect of redox conditions on primary productivity

The previous section provides a qualitative assessment of the nitrogen cycling in these basins. Here, we try to develop a quantitative constraint by evaluating the observed sedimentary $\delta^{15}N$ as a function of basinal redox conditions. For this, we follow a numerical modelling approach that captures the effect of changing water column redox conditions in the observed sedimentary isotopic compositions of these samples (Kipp et al., 2018). The method is based

on a steady-state box model, which formulates the marine nitrogen isotopic mass balance (Algeo et al., 2014; Stüeken et al., 2016; Kipp et al., 2018; Kang et al., 2023) and is discussed in detail in the Appendix (Section A5.1). The model results provide a population of sedimentary $\delta^{15}N$ values based on the changing basinal redox conditions. By comparing these model results with the range of $\delta^{15}N_{sed}$ values of our sections, the degree of surface ocean anoxicity (f_{an_sub}) and the resultant proportion of nitrogen assimilators ($f_{assimilators}$) to the sedimentary pool in these basins are reconstructed.

The model output shows a non-linear relationship of $\delta^{15}N_{sed}$ with both f_{an_sub} and $f_{assimilators}$, and is able to reproduce the f_{an_sub} (~0.3%) and corresponding $f_{assimilators}$ (~0.63) values for the present-day ocean system (Fig. 5.7; Kipp et al., 2018; Kang et al., 2023). The highest $\delta^{15}N_{sed}$ values are obtained during intermediate f_{an_sub} values. A highly oxygenated ocean (very low f_{an_sub}) will lead to limited nitrate loss and associated isotopic effects, resulting in $\delta^{15}N_{sed}$ values close to ~0‰. Similarly, a largely reducing ocean with surface ocean anoxia (high f_{an_sub}) high rates of nitrate loss will lead to increased input of N_2-fixers to the marine and sedimentary nitrogen pool, reducing the $\delta^{15}N_{sed}$ values again.

The non-linear relation between f_{an_sub}, and the $\delta^{15}N_{sed}$ provides us with two possible solutions for our $\delta^{15}N_{sed}$ sample ranges (Fig. 5.7a). These solutions reflect two different levels of surface water oxygenation: one characterized by minimal deoxygenation (comparable to modern settings) and the other by significantly higher surface deoxygenation relative to present-day conditions. In the first case of an oxygenated surface water condition, the surface layers in these basins could have sustained a large nitrate pool. The observed high (> 3‰) $\delta^{15}N_{sed}$ values of the Tadpatri, Kajrahat and Cumbum shales can hence be explained by the isotopic effects associated with the incomplete removal of this nitrate pool by denitrification/anammox processes and the utilization of this heavier nitrate by nitrate assimilators (scenario (C) in Section 5.3.2.1). Under such conditions, nitrate assimilators could have dominated the surface productivity and the sedimentary nitrogen pool ($f_{assimilators} > 0.5$) in these basins as well. In the Bijaigarh and Tal basins, the creation of sedimentary $\delta^{15}N$ close to fixation signals (< 3 ‰) in a well-oxygenated basin would require either a small nitrate pool or the redoxcline to be restricted to the sedimentary column (scenarios (A and B) in 5.3.2.2). However, the reconstruction of the sedimentary depositional environment suggests the occurrence of anoxic bottom water and a high degree of redox-sensitive trace element enrichments in these basins,

which could prevent such a mode of N-cycling. Hence, we can dismiss a largely oxygenated environment for the Tal and Bijaigarh shale deposition.

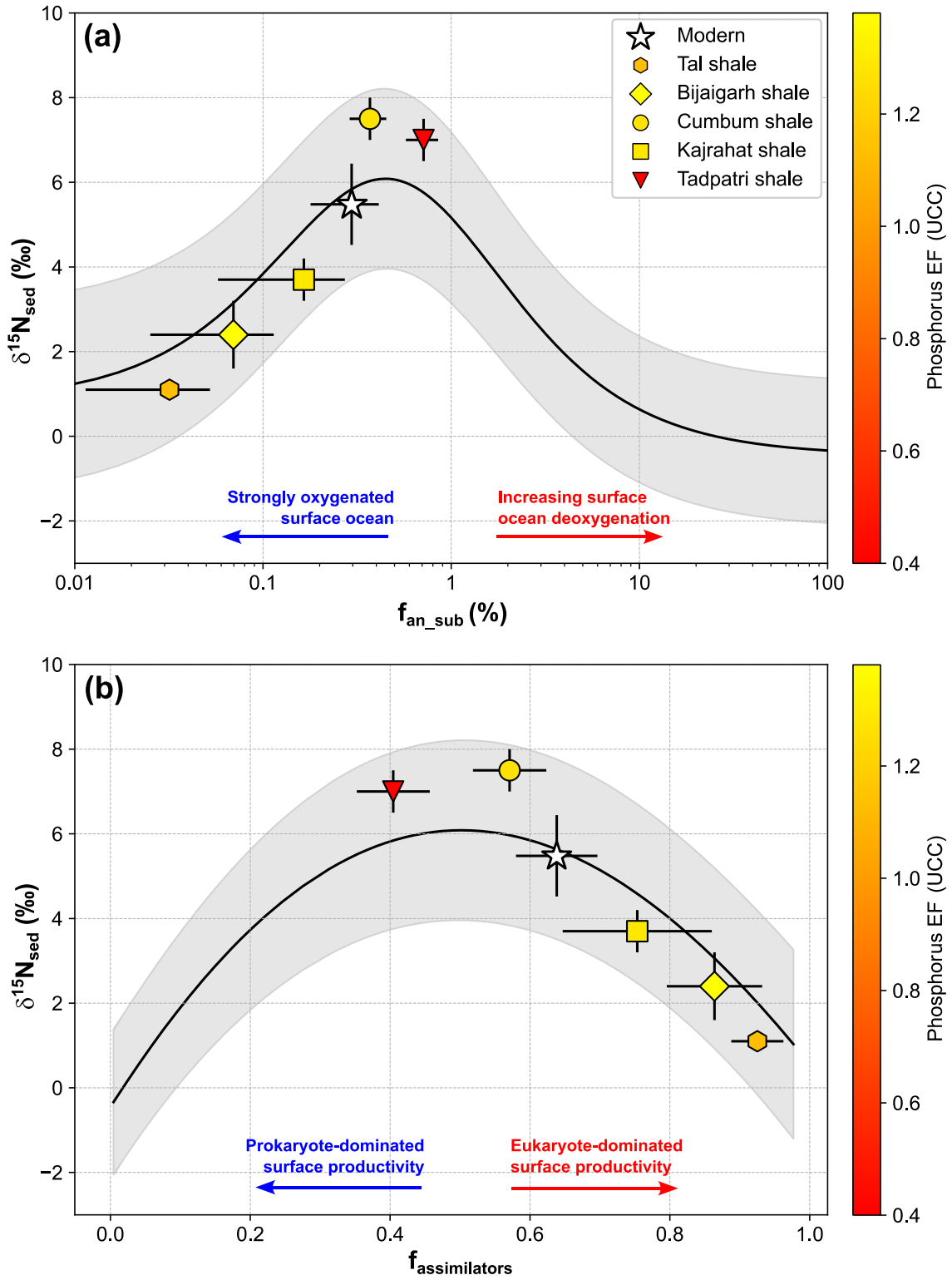

Figure 5.7. *Variation of modelled bulk-rock sedimentary $\delta^{15}N$ values as a function of* ***(a)*** *water-column anoxia and* ***(b)*** *the contribution of nitrogen assimilator ($f_{assimilators}$) to the sedimentary nitrogen pool. The black solid line represents mean values, and the grey shaded regions represent the 2σ range of the modelled result. The f_{an_sub} and $f_{assimilators}$ range depicted for the modern-day ocean are based on the results of the Monte Carlo simulation under modern-day parametrization (Table A5.1).*

Alternatively, the observed sedimentary $\delta^{15}N$ values could have also resulted from high degrees of surface water anoxia in these basins. For such environments to produce enriched $\delta^{15}N_{sed}$ values (> 3‰), denitrification/anammox processes need to have dominated over nitrification processes, leaving ammonium as the dominant bioavailable form for biological uptake. Assimilation of heavy ammonium created due to partial nitrification or supplied from deeper parts of the basin by upwelling can lead to enriched $\delta^{15}N_{sed}$ values similar to those observed in the Tadpatri, Cumbum and Kajrahat basins. However, as described in Section 5.3.2.1, limited reports for ammonium assimilation and the existence of complementary lighter ammonium reservoirs from contemporaneous sections prevent the possibility of a fully anoxic water column structure in these basins. The low sedimentary $\delta^{15}N$ values (< 3‰) observed for the Bijaigarh and Tal basins can also be produced from a dominantly anoxic surface ocean condition. However, this would require the sedimentary nitrogen pool to be composed of a very low proportion of eukaryotic biomass ($f_{assimilators} < 0.1$). This condition seems quite unlikely for the Bijaigarh and Tal sections since evidence for eukaryotic life forms has been reported from both these Basins even before the deposition of these sequences (e.g., Bengtson et al., 2009; Sharma et al., 2021). A more plausible explanation for the low $\delta^{15}N$ could be the absence of significant nitrification or quantitative nitrification-denitrification fluxes in a moderately oxygenated basin, which may have shifted the biomass and sedimentary nitrogen isotopic compositions closer to N-fixation signals in these basins (scenarios (A and B); Section 5.3.2.2).

The above discussion hence supports the presence of aerobic mode of cycling in the Tadpatri, Kajrahat and Cumbum basins (Section 5.3.2.1) and anaerobic modes of nitrogen cycling in the Bijaigarh and Tal basins (Section 5.3.2.2). It has to be noted that these interpretations are primarily based on a broad-scale analysis and are likely to offer a first-order view of nitrogen dynamics in these basins. Several factors, including basinal hydrography, sea-level fluctuations, temporal shifts in terrestrial phosphorus flux, and changes in atmospheric oxygen levels during the shale deposition, may have influenced the regional environments. Further detailed investigations may be required to validate these inferences. Nevertheless, the current discussion, when read in line with previous reports from other global sections, adds to the growing number of evidence in support of an expansive nitrate reservoir in the shallow near-shore surface oceans during the Proterozoic (Kipp et al., 2018; Kang et al., 2023; Wang et al., 2023). As anoxic conditions spread into these surface layers and led to nitrate depletion, a shift towards nitrogen fixation/ammonium assimilation mechanisms likely helped maintain the nitrostat (Stüeken et al., 2024).

5.4. Conclusions

The bulk nitrogen ($\delta^{15}N_{bulk}$) and organic carbon isotopic signatures ($\delta^{13}C_{org}$) of black shales from the Vindhyan, Cuddapah and Lesser Himalaya sedimentary successions were investigated to constrain the modes of nitrogen cycling during the Proterozoic Eon. The nitrogen isotopic signatures for the Bijaigarh and Lower Tal shales overlap with sedimentary $\delta^{15}N$ values characteristic of environments where N-fixing processes using Mo-nitrogenase are dominant. The highly enriched $\delta^{15}N_{bulk}$ values for the Tadpatri, Kajrahat and Cumbum shales suggest the occurrence of aerobic modes of nitrogen cycling in these basins, where processes such as nitrification, denitrification/*anammox* and ammonium assimilation were active. Further, we used a steady-state box model together with our measured shale $\delta^{15}N$ values to assess the effect of increasing water-column deoxygenation on nitrate availability in these settings. Results from this modelling effort support the idea that nitrate assimilators could have prevailed in the surface waters and dominated the organic pool in most of these basins. Further, these observations suggest that basinal redox conditions largely controlled nutrient availability in the Proterozoic oceanic settings and, hence, support the 'nitrostat' concept for developing and expanding eukaryotic habitats.

Chapter 6

Summary

and

Future Perspectives

6.1. Summary

The main objective of this thesis was to reconstruct the redox evolution of the Proterozoic Ocean. This objective was pursued by a detailed geochemical and isotopic investigation of organic-rich shales from different Proterozoic Basins and an early Cambrian section from the Himalaya. Through the application of multiple redox proxies, this research contributes to the current understanding of ocean chemistry during the Proterozoic and Pc-C boundary, and provides new information from the Indian sector.

The studied sequences spanned different time spans within the Proterozoic. The studied sequences from the Vindhyan Basin represent shales from a Paleoproterozoic (~1.73 Ga Kajrahat Formations) and a Mesoproterozoic (~1.21 Ga Bijaigarh shale Formation) section. The shales from the Cuddapah Basin were mostly of Paleoproterozoic age and were collected from the ~1.88 Ga Tadpatri Formation (Chitravati Group) and the ~1.66 Ga Cumbum Formation (Nallamalai Group). In this study, a depositional age of 1658 ± 50 Ma for the Cumbum black shale sequence was established using Re−Os dating. Compared to the previous age information, which was based on radiometric ages derived from detrital zircons and intrusives, this study provides a direct depositional age constraint for this Formation. The Lesser Himalaya sequence represents the Precambrian-Cambrian transition interval from the ~535 Ma Lower Tal Formation (Mussoorie Group).

All the studied sequences showed a reducing depositional environment, which was evident from the enrichment of multiple (e.g., Mo, U, V, Cd) redox-sensitive elements. The Mo and U enrichment (compared to the UCC) in these shales were observed to be lower for the Paleoproterozoic shales (Mo_{EF} ~6 and U_{EF} ~2) compared to the Mesoproterozoic Bijaigarh shales (Mo_{EF} ~42 and U_{EF} ~13) and the early Cambrian Lower Tal shales (Mo_{EF} ~16 and U_{EF} ~3). All these shales were also characterized by low Mo/TOC ($\times 10^{-4}$) ratios, with the ~1.73 Ga Kajrahat shales showing the lowest (1.0 ± 0.3) and the Lower Tal shales showing the highest (12.1 ± 0.8) values. These Mo/TOC values are comparable to modern anoxic and restricted environments, which suggests the possible control of basinal restriction in limiting the trace elemental inventory in these basins.

The Fe-speciation datasets reveal that the Fe associated with sulfide phases (Fe_{Py} ~ 12% to 79%) and carbonate phases (Fe_{carb} ~ 4% to 53%) dominated the total iron pool (Fe_T) of these shale sequences with very minimal association with oxide (Fe_{ox} ~3%) and magnetite phases

(Fe_{mag} ~ 1%). Most of the studied sections also have high proportions of highly reactive iron pools (Fe_{HR} ~ 37% to 91% of total iron) compared to the total iron content (Fe_T). The proportion of iron associated with pyrite (Fe_{Py} = 12% to 79%) and its proportion in the reactive iron pool (Fe_{Py}/Fe_{HR}; ranging between 0.17 and 0.92) show substantial variation between Formations. Altogether, these chemical parameters signify shale deposition under anoxic (ferruginous) bottom-water conditions in all of these basins, with the Cumbum Formation alone displaying signals of intermittent euxinia in the basin.

The Mo isotopic composition ($\delta^{98}Mo$) determined for the Paleoproterozoic Cumbum shales and the early Cambrian Pc-C shales also show considerable differences. The Cumbum shales show limited intraformational variation (+0.43‰ to +1.02‰) and lower average values (+0.7 ± 0.1‰) compared to the Lower Tal shales which show a larger range (+0.99‰ to +1.89‰) and average (+1.5 ± 0.2‰) value. Assuming quantitative Mo sequestration during euxinic bottom water conditions in the Cumbum basin, the average $\delta^{98}Mo$ value of ~ +0.7‰ could be considered as a lower limit for the late Paleoproterozoic global ocean. Similarly, if we assume an average offset of ~0.7‰ associated with the ferruginous deposition in the Tal basin, a $\delta^{98}Mo$ value of ~2.2‰ represents the average Mo isotopic composition of the early Cambrian oceans. This temporal evolution in oceanic Mo isotopic composition, observable from these two datasets, may be related to the gradual rise in the oxic seafloor environments, which preferentially removes lighter Mo from the oceans. Modelling efforts utilizing these $\delta^{98}Mo$ values of euxinic shales from the Cumbum Formation show the presence of extensive euxinic environments during the Paleoproterozoic (~5% of seafloor area), which were an order of magnitude higher than that observed for modern oceans (0.1% to 0.3%). These expanded euxinic environments possibly persisted throughout the Proterozoic, as evidenced by the calculations using reported $\delta^{98}Mo$ values from other global sections.

The oceanic environment close to the Precambrian-Cambrian (Pc-C) boundary appears dynamic with Mo isotopic mass balance calculations revealing the existence of ~2–4 times higher areal extent of sulfidic waters and pyrite burial rates. Evaluation of the seawater sulfate inventory during this interval reveals temporal and spatial variations in seawater chemistry during this transition. These calculations using pyrite-S isotopic values from the Lower Tal shales estimate the seawater sulfate value of 8 ± 3 mM near the Pc-C transition, which is higher than the reported values for the late Neoproterozoic oceans (<5 mM).

Nitrogen isotopic study of these organic-rich shales provides new information on the nitrogen cycling in these basins. The sedimentary $\delta^{15}N$ values were influenced by the rate and balance of nitrification and denitrification/*anammox* processes in these basins, controlled by the bottom-water redox condition. Processes such as nitrification and denitrification/*anammox*, suggestive of aerobic nitrogen cycling, were active in the Paleoproterozoic basins (Tadpatri, Kajrahat, Cumbum). In contrast, anaerobic processes, which lead to N-isotopic composition similar to the N_2-fixation range, were observed from the Mesoproterozoic Bijaigarh shales and the early Cambrian Lower Tal. Attempts to quantify the extent of anoxia on the sedimentary N-isotopic compositions were made using a steady-state Nitrogen isotopic mass balance model, which suggests the possible occurrence of low degrees of surface water anoxia in these anoxic basins. This estimation also supports the idea that N-assimilators (such as eukaryotes) could exist in the shallow oxygenated layers of these anoxic basins. Additionally, the sedimentary $\delta^{15}N$ values were influenced by the rate and balance of nitrification and denitrification/*anammox* processes in these basins, controlled by the bottom-water redox condition.

6.2. Future Perspectives

The major objective of this thesis was to reconstruct the paleoredox conditions of the Proterozoic Ocean, which was achieved by targeting spatially and temporally distinct sedimentary successions from the Proterozoic Basins of India. There are, however, many areas of research that are beyond the scope of this work. Some of the areas that require to be addressed in future works are cited below.

- **Improvement of data resolution**: The interpretations derived from this study provide snapshots of the different paleoenvironmental conditions that persisted in the Proterozoic and Early Cambrian oceans. While multiple Proterozoic sections exist in India, many of these records are still understudied. More investigations combining multiple geochemical proxies can provide new information and improve our understanding of the oxygenation history of the Proterozoic oceans and atmosphere. High-resolution temporal and spatial sampling strategies utilizing well-preserved sections and/or core samples will be beneficial in this regard.

- **Extending the geochemical record**: In this study, we use the Mo isotopic proxy to reconstruct the Proterozoic global ocean euxinia. Application of other novel proxies, such as V and Tl isotopic compositions, which track the low-oxygenated and oxygenated environments, can validate these findings. Similarly, this work utilizes the S-isotopic relationship between sulfides and sulfates to reconstruct basinal seawater sulfate concentrations during the Pc-C boundary. This approach may be expanded to other sections and combined with high-resolution carbonate-associated sulfates (CAS) determinations, which will provide a better reconstruction of the changing sulfate inventory in the Proterozoic.

- **Addition of geochronological data**: Information on the depositional ages of many of the Proterozoic sections is limited. The Re−Os dates from this study provide the first depositional age for the Cumbum Formation, Cuddapah Supergroup. Similar attempts need to be made to improve the geochronological dataset of Indian shales, which has implications for understanding their sedimentation and tectonic histories.

- **Inclusion of Earth System Models and other computational resources**: Earth System Models and Machine Learning algorithms may be utilized to resolve the observed trends of the elemental cycle and predict their probable evolutionary history. The inclusion of such methodologies to explain geochemical datasets may also help identify their controlling factors.

References

Absar, N., Nizamudheen, B.M., Augustine, S., Managave, S. and Balakrishnan, S., 2016. C, O, Sr and Nd isotope systematics of carbonates of Papaghni sub-basin, Andhra Pradesh, India: Implications for genesis of carbonate-hosted stratiform uranium mineralisation and geodynamic evolution of the Cuddapah basin. *Lithos*, 263, pp.88-100.

Acharyya, S.K., 2003. The nature of Mesoproterozoic Central Indian Tectonic Zone with exhumed and reworked older granulites. *Gondwana Research*, *6*(2), pp.197-214.

Ackerman, L., Pašava, J., Šípková, A., Martínková, E., Haluzová, E., Rodovská, Z. and Chrastný, V., 2019. Copper, zinc, chromium and osmium isotopic compositions of the Teplá-Barrandian unit black shales and implications for the composition and oxygenation of the Neoproterozoic-Cambrian ocean. *Chemical Geology*, *521*, pp.59-75.

Ader, M., Cartigny, P., Boudou, J.P., Oh, J.H., Petit, E. and Javoy, M., 2006. Nitrogen isotopic evolution of carbonaceous matter during metamorphism: Methodology and preliminary results. *Chemical Geology*, *232*(3-4), pp.152-169.

Ader, M., Sansjofre, P., Halverson, G.P., Busigny, V., Trindade, R.I., Kunzmann, M. and Nogueira, A.C., 2014. Ocean redox structure across the Late Neoproterozoic Oxygenation Event: a nitrogen isotope perspective. *Earth and Planetary Science Letters*, *396*, pp.1-13.

Ader, M., Thomazo, C., Sansjofre, P., Busigny, V., Papineau, D., Laffont, R., Cartigny, P. and Halverson, G.P., 2016. Interpretation of the nitrogen isotopic composition of Precambrian sedimentary rocks: Assumptions and perspectives. *Chemical Geology*, *429*, pp.93-110.

Agić, H., 2021. Origin and early evolution of the eukaryotes: perspectives from the fossil record. *Prebiotic Chemistry and the Origin of Life*, pp.255-289.

Aharon, P., Schidlowski, M. and Singh, I.B., 1987. Chronostratigraphic markers in the end-Precambrian carbon isotope record of the Lesser Himalaya. *Nature*, *327*(6124), pp.699-702.

Albani, A.E., Bengtson, S., Canfield, D.E., Bekker, A., Macchiarelli, R., Mazurier, A., Hammarlund, E.U., Boulvais, P., Dupuy, J.J., Fontaine, C. and Fürsich, F.T., 2010. Large colonial organisms with coordinated growth in oxygenated environments 2.1 Gyr ago. *Nature*, *466*(7302), pp.100-104.

Alcott, L.J., Krause, A.J., Hammarlund, E.U., Bjerrum, C.J., Scholz, F., Xiong, Y., Hobson, A.J., Neve, L., Mills, B.J., März, C. and Schnetger, B., 2020. Development of iron speciation reference materials for palaeoredox analysis. *Geostandards and Geoanalytical Research*, *44*(3), pp.581-591.

Algeo, T.J. and Ingall, E., 2007. Sedimentary C_{org}: P ratios, paleocean ventilation, and Phanerozoic atmospheric pO_2. *Palaeogeography, Palaeoclimatology, Palaeoecology*, *256*(3-4), pp.130-155.

Algeo, T.J. and Lyons, T.W., 2006. Mo–total organic carbon covariation in modern anoxic marine environments: Implications for analysis of paleoredox and paleohydrographic conditions. *Paleoceanography*, *21*(1).

Algeo, T.J. and Maynard, J.B., 2008. Trace-metal covariation as a guide to water-mass conditions in ancient anoxic marine environments. *Geosphere*, *4*(5), pp.872-887.

Algeo, T.J. and Rowe, H., 2012. Paleoceanographic applications of trace-metal concentration data. *Chemical Geology*, *324*, pp.6-18.

Algeo, T.J. and Tribovillard, N., 2009. Environmental analysis of paleoceanographic systems based on molybdenum–uranium covariation. *Chemical Geology*, *268*(3-4), pp.211-225.

Algeo, T.J., Meyers, P.A., Robinson, R.S., Rowe, H. and Jiang, G.Q., 2014. Icehouse–greenhouse variations in marine denitrification. *Biogeosciences*, *11*(4), pp.1273-1295.

Algeo, T.J., Luo, G.M., Song, H.Y., Lyons, T.W. and Canfield, D.E., 2015. Reconstruction of secular variation in seawater sulfate concentrations. *Biogeosciences*, *12*(7), pp.2131-2151.

Allwood, A.C., Walter, M.R., Kamber, B.S., Marshall, C.P. and Burch, I.W., 2006. Stromatolite reef from the Early Archaean Era of Australia. *Nature*, *441*(7094), pp.714-718.

Altabet, M.A., Pilskaln, C., Thunell, R., Pride, C., Sigman, D., Chavez, F. and Francois, R., 1999. The nitrogen isotope biogeochemistry of sinking particles from the margin of the Eastern North Pacific. *Deep Sea Research Part I: Oceanographic Research Papers*, *46*(4), pp.655-679.

Amthor, J.E., Grotzinger, J.P., Schröder, S., Bowring, S.A., Ramezani, J., Martin, M.W. and Matter, A., 2003. Extinction of Cloudina and Namacalathus at the Precambrian-Cambrian boundary in Oman. *Geology*, *31*(5), pp.431-434.

Anand, M., Gibson, S.A., Subbarao, K.V., Kelley, S.P. and Dickin, A.P., 2003. Early Proterozoic melt generation processes beneath the intra-cratonic Cuddapah Basin, southern India. *Journal of Petrology*, *44*(12), pp.2139-2171.

Anbar, A.D. and Knoll, A.H., 2002. Proterozoic ocean chemistry and evolution: a bioinorganic bridge?. *Science*, *297*(5584), pp.1137-1142.

Anderson, L.D., Delaney, M.L. and Faul, K.L., 2001. Carbon to phosphorus ratios in sediments: Implications for nutrient cycling. *Global Biogeochemical Cycles*, *15*(1), pp.65-79.

Ansari, A.H., Pandey, S.K., Kumar, K., Agrawal, S., Ahmad, S. and Shekhar, M., 2020. Palaeoredox link with the late Neoproterozoic–early Cambrian Bilara carbonate deposition, Marwar Supergroup, India. *Carbonates and Evaporites*, *35*(2), p.38.

Ansari, A.H., Pandey, S.K., Ahmad, S., Sharma, M., Govil, P., Chaddha, A.S. and Sharma, A., 2023. High primary productivity in an Ediacaran shallow marine basin influenced by strong seasonal to perennial upwelling. *Geological Magazine*, *160*(8), pp.1607-1623.

Archer, C. and Vance, D., 2008. The isotopic signature of the global riverine molybdenum flux and anoxia in the ancient oceans. *Nature Geoscience*, *1*(9), pp.597-600.

Arnold, G.L., Anbar, A.D., Barling, J. and Lyons, T.W., 2004. Molybdenum isotope evidence for widespread anoxia in mid-Proterozoic oceans. *Science*, *304*(5667), pp.87-90.

Asael, D., Tissot, F.L., Reinhard, C.T., Rouxel, O., Dauphas, N., Lyons, T.W., Ponzevera, E., Liorzou, C. and Chéron, S., 2013. Coupled molybdenum, iron and uranium stable isotopes as oceanic paleoredox proxies during the Paleoproterozoic Shunga Event. *Chemical Geology*, *362*, pp.193-210.

Asael, D., Rouxel, O., Poulton, S.W., Lyons, T.W. and Bekker, A., 2018. Molybdenum record from black shales indicates oscillating atmospheric oxygen levels in the early Paleoproterozoic. *American Journal of Science*, *318*(3), pp.275-299.

Azmi, R.J., 1983. Microfauna and age of the lower Tal phosphorite of Mussoorie syncline, Garhwal lesser Himalaya, India. *Himalayan Geology*, *11*, pp.373-409.

Azmi, R.J., 1998. Discovery of Lower Cambrian small shelly fossils and brachiopods from the Lower Vindhyan of Son Valley, Central India. *Journal Geological Society of India*, *52*(4), pp.381-389.

Banerjee, D.M., 1985. Proterozoic Stratigraphy of the Indian Platform and the concept of phosphogenic cycles—A Proposal. *Bulletin-Geological survey of Finland*, (331), pp.73-89.

Banerjee, D.M., Schidlowski, M., Siebert, F. and Brasier, M.D., 1997. Geochemical changes across the Proterozoic–Cambrian transition in the Durmala phosphorite mine section, Mussoorie Hills, Garhwal Himalaya, India. *Palaeogeography, Palaeoclimatology, Palaeoecology*, *132*(1-4), pp.183-194.

Barling, J. and Anbar, A.D., 2004. Molybdenum isotope fractionation during adsorption by manganese oxides. *Earth and Planetary Science Letters*, *217*(3-4), pp.315-329.

Barling, J., Arnold, G.L. and Anbar, A.D., 2001. Natural mass-dependent variations in the isotopic composition of molybdenum. *Earth and Planetary Science Letters*, *193*(3-4), pp.447-457.

Bauersachs, T., Schouten, S., Compaoré, J., Wollenzien, U., Stal, L.J. and Sinninghe Damsteé, J.S., 2009. Nitrogen isotopic fractionation associated with growth on dinitrogen gas and nitrate by cyanobacteria. *Limnology and Oceanography*, *54*(4), pp.1403-1411.

Bebout, G.E. and Fogel, M.L., 1992. Nitrogen-isotope compositions of metasedimentary rocks in the Catalina Schist, California: implications for metamorphic devolatilization history. *Geochimica et Cosmochimica Acta*, *56*(7), pp.2839-2849.

Bekker, A., Slack, J.F., Planavsky, N., Krapez, B., Hofmann, A., Konhauser, K.O. and Rouxel, O.J., 2010. Iron formation: the sedimentary product of a complex interplay among mantle, tectonic, oceanic, and biospheric processes. *Economic Geology*, *105*(3), pp.467-508.

Bengtson, S., Belivanova, V., Rasmussen, B. and Whitehouse, M., 2009. The controversial "Cambrian" fossils of the Vindhyan are real but more than a billion years older. *Proceedings of the National Academy of Sciences*, *106*(19), pp.7729-7734.

Berner, R.A., 1970. Sedimentary pyrite formation. *American Journal of Science*, *268*(1), pp.1-23.

Bhargava, O.N., Singh, I, Hans, S.K. and Bassi, U.K., 1998. Early Cambrian trace and trilobite fossils from the Nigali Dhar Syncline (Sirmaur District, Himachal Pradesh), lithostratigraphic correlation and fossil content of the Tal Group. *Himalayan Geology*, *19*(1), pp.89-108

Bhargava, O.N., Frank, W. and Bertle, R., 2011. Late Cambrian deformation in the Lesser Himalaya. *Journal of Asian Earth Sciences*, *40*(1), pp.201-212.

Bhargava, O.N., Singh, B.P., Frank, W. and Tangri, S.K., 2021. Evolution of the Lesser Himalaya in space and time. *Himalayan Geology*, *42*(2), pp.263-289.

Bhatt, D.K., Mamgain, V.D. and Misra, R.S., 1985. Small shelly fossils of Early Cambrian (Tommotian) Age from Chert-Phosphorite Member, Tal Formation, Mussoorie syncline, Lesser Himalaya, India and their chronostratigraphic evaluation. *Journal of the Palaeontological Society of India*, *30*, pp.92-102.

Bhukosh. Geological Survey of India. https://bhukosh.gsi.gov.in/Bhukosh/Public/ (accessed September 2022).

Bickford, M.E., Mishra, M., Mueller, P.A., Kamenov, G.D., Schieber, J. and Basu, A., 2017. U-Pb age and Hf isotopic compositions of magmatic zircons from a rhyolite flow in the Porcellanite Formation in the Vindhyan Supergroup, Son Valley (India): implications for its tectonic significance. *The Journal of Geology*, *125*(3), pp.367-379.

Birck, J.L., Barman, M.R. and Capmas, F., 1997. Re−Os isotopic measurements at the femtomole level in natural samples. *Geostandards newsletter*, *21*(1), pp.19-27.

Brandes, J.A. and Devol, A.H., 2002. A global marine-fixed nitrogen isotopic budget: Implications for Holocene nitrogen cycling. *Global Biogeochemical Cycles*, *16*(4), pp.67-1.

Brasier, M.D. and Singh, P., 1987. Microfossils and Precambrian–Cambrian boundary stratigraphy at Maldeota, Lesser Himalaya. *Geological Magazine*, *124*(4), pp.323-345.

Brasier, M.D., Shields, G., Kuleshov, V.N. and Zhegallo, E.A., 1996. Integrated chemo-and biostratigraphic calibration of early animal evolution: Neoproterozoic–early Cambrian of southwest Mongolia. *Geological Magazine*, *133*(4), pp.445-485.

Brennan, S.T., Lowenstein, T.K. and Horita, J., 2004. Seawater chemistry and the advent of biocalcification. *Geology*, *32*(6), pp.473-476.

Bristow, L.A., Dalsgaard, T., Tiano, L., Mills, D.B., Bertagnolli, A.D., Wright, J.J., Hallam, S.J., Ulloa, O., Canfield, D.E., Revsbech, N.P. and Thamdrup, B., 2016. Ammonium and

nitrite oxidation at nanomolar oxygen concentrations in oxygen minimum zone waters. *Proceedings of the National Academy of Sciences*, *113*(38), pp.10601-10606.

Brocks, J.J., Love, G.D., Summons, R.E., Knoll, A.H., Logan, G.A. and Bowden, S.A., 2005. Biomarker evidence for green and purple sulphur bacteria in a stratified Palaeoproterozoic sea. *Nature*, *437*(7060), pp.866-870.

Brookfield, M.E., 1987. Lithostratigraphic correlation of Blaini Formation (late Proterozoic, Lesser Himalaya, India) with other late Proterozoic tillite sequences. *Geologische Rundschau*, *76*(2), pp.477-484

Brookfield, M.E., 1993. The Himalayan passive margin from Precambrian to Cretaceous times. *Sedimentary Geology*, *84*(1-4), pp.1-35.

Brunner, B., Contreras, S., Lehmann, M.F., Matantseva, O., Rollog, M., Kalvelage, T., Klockgether, G., Lavik, G., Jetten, M.S., Kartal, B. and Kuypers, M.M., 2013. Nitrogen isotope effects induced by anammox bacteria. *Proceedings of the National Academy of Sciences*, *110*(47), pp.18994-18999.

Buick, R., 2007. Did the Proterozoic 'Canfield Ocean'cause a laughing gas greenhouse?. *Geobiology*, *5*(2), pp.97-100.

Buick, R., Des Marais, D.J. and Knoll, A.H., 1995. Stable isotopic compositions of carbonates from the Mesoproterozoic Bangemall Group, northwestern Australia. *Chemical Geology*, *123*(1-4), pp.153-171.

Burke, A., Present, T.M., Paris, G., Rae, E.C., Sandilands, B.H., Gaillardet, J., Peucker-Ehrenbrink, B., Fischer, W.W., McClelland, J.W., Spencer, R.G. and Voss, B.M., 2018. Sulfur isotopes in rivers: Insights into global weathering budgets, pyrite oxidation, and the modern sulfur cycle. *Earth and Planetary Science Letters*, *496*, pp.168-177

Busigny, V., Lebeau, O., Ader, M., Krapež, B. and Bekker, A., 2013. Nitrogen cycle in the Late Archean ferruginous ocean. *Chemical Geology*, *362*, pp.115-130.

Butterfield, N.J., 2015. Proterozoic photosynthesis–a critical review. *Palaeontology*, *58*(6), pp.953-972.

Calvert, S.E. and Pedersen, T.F., 1996. Sedimentary geochemistry of manganese; implications for the environment of formation of manganiferous black shales. *Economic Geology*, *91*(1), pp.36-47.

Campbell, I.H. and Allen, C.M., 2008. Formation of supercontinents linked to increases in atmospheric oxygen. *Nature Geoscience*, *1*(8), pp.554-558.

Canfield, D.E. and Farquhar, J., 2009. Animal evolution, bioturbation, and the sulfate concentration of the oceans. *Proceedings of the National Academy of Sciences*, *106*(20), pp.8123-8127.

Canfield, D.E., Raiswell, R., Westrich, J.T., Reaves, C.M. and Berner, R.A., 1986. The use of chromium reduction in the analysis of reduced inorganic sulfur in sediments and shales. *Chemical geology*, *54*(1-2), pp.149-155.

Canfield, D.E., Farquhar, J. and Zerkle, A.L., 2010. High isotope fractionations during sulfate reduction in a low-sulfate euxinic ocean analog. *Geology*, *38*(5), pp.415-418.

Canfield, D.E., Ngombi-Pemba, L., Hammarlund, E.U., Bengtson, S., Chaussidon, M., Gauthier-Lafaye, F., Meunier, A., Riboulleau, A., Rollion-Bard, C., Rouxel, O. and Asael, D., 2013. Oxygen dynamics in the aftermath of the Great Oxidation of Earth's atmosphere. *Proceedings of the National Academy of Sciences*, *110*(42), pp.16736-16741.

Canfield, D.E., van Zuilen, M.A., Nabhan, S., Bjerrum, C.J., Zhang, S., Wang, H. and Wang, X., 2021. Petrographic carbon in ancient sediments constrains Proterozoic Era atmospheric oxygen levels. *Proceedings of the National Academy of Sciences*, *118*(23), p.e2101544118.

Canfield, D.E., 1998. A new model for Proterozoic ocean chemistry. *Nature*, *396*(6710), pp.450-453.

Canfield, D.E., 2001. Biogeochemistry of sulfur isotopes. *Reviews in mineralogy and geochemistry*, *43*(1), pp.607-636.

Canfield, D.E., 2004. The evolution of the Earth surface sulfur reservoir. *American Journal of Science*, *304*(10), pp.839-861

Casciotti, K.L., 2009. Inverse kinetic isotope fractionation during bacterial nitrite oxidation. *Geochimica et Cosmochimica Acta*, *73*(7), pp.2061-2076.

Célérier, J., Harrison, T.M., Webb, A.A.G. and Yin, A., 2009a. The Kumaun and Garwhal Lesser Himalaya, India: Part 1. Structure and stratigraphy. *Geological Society of America Bulletin*, *121*(9-10), pp.1262-1280.

Célérier, J., Harrison, T.M., Beyssac, O., Herman, F., Dunlap, W.J. and Webb, A.A.G., 2009b. The Kumaun and Garwhal lesser Himalaya, India: Part 2. Thermal and deformation histories. *Geological Society of America Bulletin*, *121*(9-10), pp.1281-1297.

Chakrabarti, R., Basu, A.R. and Chakrabarti, A., 2007. Trace element and Nd-isotopic evidence for sediment sources in the mid-Proterozoic Vindhyan Basin, central India. *Precambrian Research*, *159*(3-4), pp.260-274.

Chakraborty, P.P., Mukhopadhyay, J., Paul, P.P., Banerjee, D.M. and Bera, M.K., 2020. Early atmosphere and hydrosphere oxygenation: Clues from Precambrian paleosols and chemical sedimentary records of India. *Episodes Journal of International Geoscience*, *43*(1), pp.175-186.

Chakraborty, P.P., 2006. Outcrop signatures of relative sea level fall on a siliciclastic shelf: Examples from the Rewa Group of Proterozoic Vindhyan Basin. *Journal of Earth System Science*, *115*, pp.23-36.

Chalapathi Rao, N.V., Miller, J.A., Pyle, D.M., Madhavan, V., 1996. New Proterozoic K–Ar ages for some kimberlites and lamproites from the Cuddapah Basin and Dharwar Craton, South India: evidence for non-contemporaneous emplacement. *Precambrian Research 79*, 363–369.

Chalapathi Rao, N. V., Miller, J. A., Gibson, S. A., Pyle, D. M. & Madhavan, V. 1999. Precise $^{40}Ar/^{39}Ar$ Age Determinations of the Kotakonda Kimberlite and Chelima Lamproite, India: Implication to the Timing of Mafic Dyke Swarm Emplacement in the Eastern Dharwar Craton. *Geological Society of India*, *53*(4), pp.425-432.

Chalapathi Rao, N.V., Wu, F.Y. and Srinivas, M., 2012. Mesoproterozoic emplacement and enriched mantle derivation of the Racherla alkali syenite, Palaeo-Mesoproterozoic Cuddapah Basin, southern India: insights from in situ Sr–Nd isotopic analysis on apatite. *Geological Society, London, Special Publications*, *365*(1), pp.185-195.

Chanda, S.K. and Bhattacharya, A., 1982. Vindhyan sedimentation and palaeogeography: post-Auden developments. In *Geology of Vindhyanchal* (pp. 88-101).

Chatterjee, C., Vadlamani, R. and Kaptan, O.P., 2016. Paleoproterozoic Cordilleran-style accretion along the south eastern margin of the eastern Dharwar Craton: Evidence from the Vinjamuru arc terrane of the Krishna orogen, India. *Lithos*, *263*, pp.122-142.

Chaudhuri, A.K., Saha, D., Deb, G.K., Deb, S.P., Mukherjee, M.K. and Ghosh, G., 2002. The Purana basins of southern cratonic province of India-a case for Mesoproterozoic fossil rifts. *Gondwana Research*, *5*(1), pp.23-33.

Chen, X., Ling, H.F., Vance, D., Shields-Zhou, G.A., Zhu, M., Poulton, S.W., Och, L.M., Jiang, S.Y., Li, D., Cremonese, L. and Archer, C., 2015. Rise to modern levels of ocean oxygenation coincided with the Cambrian radiation of animals. *Nature Communications*, *6*(1), pp.1-7.

Cheng, M., Li, C., Zhou, L., Algeo, T.J., Zhang, F., Romaniello, S., Jin, C.S., Lei, L.D., Feng, L.J. and Jiang, S.Y., 2016. Marine Mo biogeochemistry in the context of dynamically euxinic mid-depth waters: A case study of the lower Cambrian Niutitang shales, South China. *Geochimica et Cosmochimica Acta*, *183*, pp.79-93.

Cheng, M., Li, C., Zhou, L., Feng, L., Algeo, T.J., Zhang, F., Romaniello, S., Jin, C., Ling, H. and Jiang, S., 2017. Transient deep-water oxygenation in the early Cambrian Nanhua Basin, South China. *Geochimica et Cosmochimica Acta*, *210*, pp.42-58.

Cheng, C., Busigny, V., Ader, M., Thomazo, C., Chaduteau, C. and Philippot, P., 2019. Nitrogen isotope evidence for stepwise oxygenation of the ocean during the Great Oxidation Event. *Geochimica et Cosmochimica Acta*, *261*, pp.224-247.

Clarkson, M.O., Poulton, S.W., Guilbaud, R. and Wood, R.A., 2014. Assessing the utility of Fe/Al and Fe-speciation to record water column redox conditions in carbonate-rich sediments. *Chemical Geology*, *382*, pp.111-122.

Claypool, G.E., Holser, W.T., Kaplan, I.R., Sakai, H. and Zak, I., 1980. The age curves of sulfur and oxygen isotopes in marine sulfate and their mutual interpretation. *Chemical Geology*, *28*, pp.199-260.

Cloud, P., 1973. Paleoecological significance of the banded iron-formation. *Economic Geology*, *68*(7), pp.1135-1143.

Cole, D.B., Mills, D.B., Erwin, D.H., Sperling, E.A., Porter, S.M., Reinhard, C.T. and Planavsky, N.J., 2020. On the co-evolution of surface oxygen levels and animals. *Geobiology*, 18(3), pp.260-281.

Colleps, C.L., McKenzie, N.R., Sharma, M., Liu, H., Gibson, T.M., Chen, W. and Stockli, D.F., 2021. Zircon and apatite U-Pb age constraints from the Bundelkhand Craton and Proterozoic strata of central India: Insights into craton stabilization and subsequent basin evolution. *Precambrian Research*, *362*, p.106286.

Collins, A.S., Patranabis-Deb, S., Alexander, E., Bertram, C.N., Falster, G.M., Gore, R.J., Mackintosh, J., Dhang, P.C., Saha, D., Payne, J.L. and Jourdan, F., 2015. Detrital mineral age, radiogenic isotopic stratigraphy and tectonic significance of the Cuddapah Basin, India. *Gondwana Research*, 28(4), pp.1294-1309.

Cook, P.J. and Shergold, J.H., 1984. Phosphorus, phosphorites and skeletal evolution at the Precambrian—Cambrian boundary. *Nature*, *308*(5956), pp.231-236.

Crawford, A.R. and Compston, W., 1973. The age of the Cuddapah and Kurnool systems, southern India. *Journal of the Geological Society of Australia*, *19*(4), pp.453-464.

Creaser, R.A., Papanastassiou, D.A. and Wasserburg, G.J., 1991. Negative thermal ion mass spectrometry of osmium, rhenium and iridium. *Geochimica et Cosmochimica Acta*, *55*(1), pp.397-401.

Creaser, R.A., Sannigrahi, P., Chacko, T. and Selby, D., 2002. Further evaluation of the Re−Os geochronometer in organic-rich sedimentary rocks: A test of hydrocarbon maturation effects in the Exshaw Formation, Western Canada Sedimentary Basin. *Geochimica et Cosmochimica Acta*, *66*(19), pp.3441-3452.

Cremonese, L., Shields-Zhou, G.A., Struck, U., Ling, H.F. and Och, L.M., 2014. Nitrogen and organic carbon isotope stratigraphy of the Yangtze Platform during the Ediacaran–Cambrian transition in South China. *Palaeogeography, Palaeoclimatology, Palaeoecology*, *398*, pp.165-186.

Dahl, T.W., Hammarlund, E.U., Anbar, A.D., Bond, D.P., Gill, B.C., Gordon, G.W., Knoll, A.H., Nielsen, A.T., Schovsbo, N.H. and Canfield, D.E., 2010. Devonian rise in atmospheric oxygen correlated to the radiations of terrestrial plants and large predatory fish. *Proceedings of the National Academy of Sciences*, *107*(42), pp.17911-17915.

Dahl, T.W., Chappaz, A., Hoek, J., McKenzie, C.J., Svane, S. and Canfield, D.E., 2017. Evidence of molybdenum association with particulate organic matter under sulfidic conditions. *Geobiology*, *15*(2), pp.311-323.

Dahl, T.W., Hammarlund, E.U., Rasmussen, C.M.Ø., Bond, D.P. and Canfield, D.E., 2021. Sulfidic anoxia in the oceans during the Late Ordovician mass extinctions–insights from molybdenum and uranium isotopic global redox proxies. *Earth-Science Reviews*, *220*, p.103748.

Danish, M., Tripathy, G.R. and Rahaman, W., 2020. Submarine groundwater discharge to a tropical coastal lagoon (Chilika lagoon, India): An estimation using Sr isotopes. *Marine Chemistry*, *224*, p.103816.

Deb, M. and Pal, T., 2015. Chapter 21 Mineral potential of Proterozoic intracratonic basins in India. *Geological Society, London, Memoirs*, *43*(1), pp.309-325.

Devol, A.H., 2015. Denitrification, anammox, and N_2 production in marine sediments. *Annual Review of Marine Science*, *7*(1), pp.403-423.

DeVries, T., Deutsch, C., Primeau, F., Chang, B. and Devol, A., 2012. Global rates of water-column denitrification derived from nitrogen gas measurements. *Nature Geoscience*, *5*(8), pp.547-550.

Diamond, C.W., Planavsky, N.J., Wang, C. and Lyons, T.W., 2018. What the ~1.4 Ga Xiamaling Formation can and cannot tell us about the mid-Proterozoic ocean. *Geobiology*, *16*(3), pp.219-236.

Dickson, A.J., Cohen, A.S. and Coe, A.L., 2014. Continental margin molybdenum isotope signatures from the early Eocene. *Earth and Planetary Science Letters*, *404*, pp.389-395.

Dickson, A.J., Davies, M., Bagard, M.L. and Cohen, A.S., 2022. Quantifying seawater exchange rates in the Eocene Arctic Basin using osmium isotopes. *Geochemical Perspectives Letters*, *24*, pp.7-11.

Duan, Y., Anbar, A.D., Arnold, G.L., Lyons, T.W., Gordon, G.W. and Kendall, B., 2010. Molybdenum isotope evidence for mild environmental oxygenation before the Great Oxidation Event. *Geochimica et Cosmochimica Acta*, *74*(23), pp.6655-6668.

Erickson, B.E. and Helz, G.R., 2000. Molybdenum (VI) speciation in sulfidic waters: stability and lability of thiomolybdates. *Geochimica et Cosmochimica Acta*, *64*(7), pp.1149-1158.

Eroglu, S., Scholz, F., Frank, M. and Siebert, C., 2020. Influence of particulate versus diffusive molybdenum supply mechanisms on the molybdenum isotope composition of continental margin sediments. *Geochimica et Cosmochimica Acta*, *273*, pp.51-69.

Erwin, D.H., Laflamme, M., Tweedt, S.M., Sperling, E.A., Pisani, D. and Peterson, K.J., 2011. The Cambrian conundrum: early divergence and later ecological success in the early history of animals. *Science*, *334*(6059), pp.1091-1097.

Esser, B.K. and Turekian, K.K., 1993. The osmium isotopic composition of the continental crust. *Geochimica et Cosmochimica Acta*, *57*(13), pp.3093-3104.

Etienne, J.L., Allen, P.A., Guerroué, E.L., Heaman, L., Ghosh, S.K. and Islam, R., 2011. Chapter 31 The Blaini Formation of the Lesser Himalaya, NW india. *Geological Society, London, Memoirs*, *36*(1), pp.347-355.

Eugster, O. and Gruber, N., 2012. A probabilistic estimate of global marine N-fixation and denitrification. *Global Biogeochemical Cycles*, *26*(4).

Fakhraee, M., Tarhan, L.G., Reinhard, C.T., Crowe, S.A., Lyons, T.W. and Planavsky, N.J., 2023. Earth's surface oxygenation and the rise of eukaryotic life: Relationships to the Lomagundi positive carbon isotope excursion revisited. *Earth-Science Reviews*, *240*, p.104398.

Falkowski, P.G., 1997. Evolution of the nitrogen cycle and its influence on the biological sequestration of CO_2 in the ocean. *Nature*, *387*(6630), pp.272-275.

Farrell, Ú.C., Samawi, R., Anjanappa, S., Klykov, R., Adeboye, O.O., Agic, H., Ahm, A.S.C., Boag, T.H., Bowyer, F., Brocks, J.J. and Brunoir, T.N., 2021. The sedimentary geochemistry and paleoenvironments project. *Geobiology*, *19*(6), pp.545-556.

Feng, L., Li, C., Huang, J., Chang, H. and Chu, X., 2014. A sulfate control on marine mid-depth euxinia on the early Cambrian (ca. 529–521 Ma) Yangtze platform, South China. *Precambrian Research*, *246*, pp.123-133.

Fike, D.A. and Grotzinger, J.P., 2008. A paired sulfate–pyrite $\delta^{34}S$ approach to understanding the evolution of the Ediacaran–Cambrian sulfur cycle. *Geochimica et Cosmochimica Acta*, *72*(11), pp.2636-2648.

Fike, D.A. and Grotzinger, J.P., 2010. A $\delta^{34}S_{SO4}$ approach to reconstructing biogenic pyrite burial in carbonate-evaporite basins: An example from the Ara Group, Sultanate of Oman. *Geology*, *38*(4), pp.371-374.

Fike, D.A., Bradley, A.S. and Rose, C.V., 2015. Rethinking the ancient sulfur cycle. *Annual Review of Earth and Planetary Sciences*, *43*, pp.593-622.

Fogel, M.L. and Cifuentes, L.A., 1993. Isotope fractionation during primary production. In *Organic geochemistry: principles and applications* (pp. 73-98). Boston, MA: Springer US.

Frausto da Silva, J.J.R. and Williams, R.J.P., 2001. *The biological chemistry of the elements: the inorganic chemistry of life*. Oxford University Press.

French, J.E., Heaman, L.M., Chacko, T. and Srivastava, R.K., 2008. 1891–1883 Ma Southern Bastar–Cuddapah mafic igneous events, India: A newly recognized large igneous province. *Precambrian research*, *160*(3-4), pp.308-322.

Freudenthal, T., Wagner, T., Wenzhöfer, F., Zabel, M. and Wefer, G., 2001. Early diagenesis of organic matter from sediments of the eastern subtropical Atlantic: evidence from stable nitrogen and carbon isotopes. *Geochimica et Cosmochimica Acta*, *65*(11), pp.1795-1808.

Fu, Y., Dong, L., Li, C., Qu, W., Pei, H., Qiao, W. and Shen, B., 2016. New Re−Os isotopic constrains on the formation of the metalliferous deposits of the Lower Cambrian Niutitang Formation. *Journal of Earth Science*, *27*, pp.271-281.

Georgiev, S., Stein, H.J., Hannah, J.L., Bingen, B., Weiss, H.M. and Piasecki, S., 2011. Hot acidic Late Permian seas stifle life in record time. *Earth and Planetary Science Letters*, *310*(3-4), pp.389-400.

German, C.R. and Elderfield, H., 1990. Application of the Ce anomaly as a paleoredox indicator: the ground rules. *Paleoceanography*, *5*(5), pp.823-833.

Ghosh, S.K., Pandey, A.K., Pandey, P., Ray, Y. and Sinha, S., 2012. Soft-sediment deformation structures from the Paleoproterozoic Damtha Group of Garhwal Lesser Himalaya, India. *Sedimentary Geology*, *261*, pp.76-89.

Ghosh, S.K., Jalal, P. and Islam, R., 2016. Sedimentologic attributes of the Proterozoic siliciclastic packages of the Garhwal–Kumaun Lesser Himalaya, India: Implication for their relationship and palaeobasinal conditions. *Journal of the Geological Society of India*, *87*, pp.661-678.

Gilleaudeau, G.J., Sahoo, S.K., Kah, L.C., Henderson, M.A. and Kaufman, A.J., 2018. Proterozoic carbonates of the Vindhyan Basin, India: Chemostratigraphy and diagenesis. *Gondwana Research*, *57*, pp.10-25.

Gilleaudeau, G.J., Romaniello, S.J., Luo, G., Kaufman, A.J., Zhang, F., Klaebe, R.M., Kah, L.C., Azmy, K., Bartley, J.K., Zheng, W. and Knoll, A.H., 2019. Uranium isotope evidence for limited euxinia in mid-Proterozoic oceans. *Earth and Planetary Science Letters*, 521, pp.150-157.

Gilleaudeau, G.J., Sahoo, S.K., Ostrander, C.M., Owens, J.D., Poulton, S.W., Lyons, T.W. and Anbar, A.D., 2020. Molybdenum isotope and trace metal signals in an iron-rich Mesoproterozoic ocean: A snapshot from the Vindhyan Basin, India. *Precambrian Research*, *343*, p.105718.

Godfrey, L.V., Poulton, S.W., Bebout, G.E. and Fralick, P.W., 2013. Stability of the nitrogen cycle during development of sulfidic water in the redox-stratified late Paleoproterozoic Ocean. *Geology*, *41*(6), pp.655-658.

Goldberg, T., Archer, C., Vance, D. and Poulton, S.W., 2009. Mo isotope fractionation during adsorption to Fe (oxyhydr) oxides. *Geochimica et Cosmochimica Acta*, *73*(21), pp.6502-6516.

Goldberg, T., Archer, C., Vance, D., Thamdrup, B., McAnena, A. and Poulton, S.W., 2012. Controls on Mo isotope fractionations in a Mn-rich anoxic marine sediment, Gullmar Fjord, Sweden. *Chemical Geology*, *296*, pp.73-82.

Goldberg, T., Gordon, G., Izon, G., Archer, C., Pearce, C.R., McManus, J., Anbar, A.D. and Rehkämper, M., 2013. Resolution of inter-laboratory discrepancies in Mo isotope data: an intercalibration. *Journal of Analytical Atomic Spectrometry*, *28*(5), pp.724-735.

Gomes, M.L. and Hurtgen, M.T., 2013. Sulfur isotope systematics of a euxinic, low-sulfate lake: Evaluating the importance of the reservoir effect in modern and ancient oceans. *Geology*, *41*(6), pp.663-666.

Gopalan, K., Kumar, A., Kumar, S. and Vijayagopal, B., 2013. Depositional history of the Upper Vindhyan succession, central India: time constraints from Pb–Pb isochron ages of its carbonate components. *Precambrian Research*, *233*, pp.108-117.

Goswami, V., Singh, S.K. and Bhushan, R., 2012. Dissolved redox sensitive elements, Re, U and Mo in intense denitrification zone of the Arabian Sea. *Chemical Geology*, *291*, pp.256-268.

Goswami, V., Singh, S.K. and Bhushan, R., 2014. Impact of water mass mixing and dust deposition on Nd concentration and ε_{Nd} of the Arabian Sea water column. *Geochimica et Cosmochimica Acta*, *145*, pp.30-49.

Goswami, V., Singh, S.K., Bhushan, R. and Rai, V.K., 2022. Spatial distribution of Mo and δ^{98}Mo in waters of the northern Indian Ocean: Role of suboxia and particle-water interactions on lighter Mo in the Bay of Bengal. *Geochimica et Cosmochimica Acta*, *324*, pp.174-193.

Granger, J., Prokopenko, M.G., Sigman, D.M., Mordy, C.W., Morse, Z.M., Morales, L.V., Sambrotto, R.N. and Plessen, B., 2011. Coupled nitrification-denitrification in sediment of the eastern Bering Sea shelf leads to ^{15}N enrichment of fixed N in shelf waters. *Journal of Geophysical Research: Oceans*, *116*(C11).

Gregory, L.C., Meert, J.G., Pradhan, V., Pandit, M.K., Tamrat, E. and Malone, S.J., 2006. A paleomagnetic and geochronologic study of the Majhgawan kimberlite, India: implications for the age of the Upper Vindhyan Supergroup. *Precambrian Research*, *149*(1-2), pp.65-75.

Grotzinger, J.P., Bowring, S.A., Saylor, B.Z. and Kaufman, A.J., 1995. Biostratigraphic and geochronologic constraints on early animal evolution. *Science*, *270*(5236), pp.598-604.

Hammer, Ø., Harper, D.A. and Ryan, P.D., 2001. PAST: Paleontological statistics software package for education and data analysis. *Palaeontologia electronica*, *4*(1), p.9.

Han, W., Feng, L., Li, H. and Liu, W., 2017. Bulk δ^{15}N measurements of organic-rich rock samples by elemental analyzer/isotope ratio mass spectrometry with enhanced oxidation ability. *Rapid Communications in Mass Spectrometry*, *31*(1), pp.16-20.

Hannah, J.L., Bekker, A., Stein, H.J., Markey, R.J. and Holland, H.D., 2004. Primitive Os and 2316 Ma age for marine shale: implications for Paleoproterozoic glacial events and the rise of atmospheric oxygen. *Earth and Planetary Science Letters*, *225*(1-2), pp.43-52.

Hannah, J.L., Stein, H.J., Zimmerman, A., Yang, G., Markey, R.J. and Melezhik, V.A., 2006. Precise 2004±9 Ma Re–Os age for Pechenga black shale: comparison of sulfides and organic material. *Geochimica et Cosmochimica Acta*, *18*(70), p.A228.

Hawkesworth, C., Cawood, P., Kemp, T., Storey, C. and Dhuime, B., 2009. A matter of preservation. *Science*, *323*(5910), pp.49-50.

Hayes, J.M., Wedeking, K.W. and Kaplan, I.R., 1983. Precambrian organic geochemistry-Preservation of the record.

Hayes, J.M., 2001. Fractionation of carbon and hydrogen isotopes in biosynthetic processes. *Reviews in mineralogy and geochemistry*, *43*, pp.225-278.

He, T., Zhu, M., Mills, B.J., Wynn, P.M., Zhuravlev, A.Y., Tostevin, R., Pogge von Strandmann, P.A., Yang, A., Poulton, S.W. and Shields, G.A., 2019. Possible links between extreme oxygen perturbations and the Cambrian radiation of animals. *Nature Geoscience*, *12*(6), pp.468-474.

Helz, G.R., Miller, C.V., Charnock, J.M., Mosselmans, J.F.W., Pattrick, R.A.D., Garner, C.D. and Vaughan, D.J., 1996. Mechanism of molybdenum removal from the sea and its concentration in black shales: EXAFS evidence. *Geochimica et Cosmochimica Acta*, *60*(19), pp.3631-3642.

Hoch, M.P., Fogel, M.L. and Kirchman, D.L., 1992. Isotope fractionation associated with ammonium uptake by a marine bacterium. *Limnology and oceanography*, *37*(7), pp.1447-1459.

Hoffman, P.F., Abbot, D.S., Ashkenazy, Y., Benn, D.I., Brocks, J.J., Cohen, P.A., Cox, G.M., Creveling, J.R., Donnadieu, Y., Erwin, D.H. and Fairchild, I.J., 2017. Snowball Earth climate dynamics and Cryogenian geology-geobiology. *Science Advances*, *3*(11), p.e1600983.

Hofmann, H.J., Grey, K., Hickman, A.H. and Thorpe, R.I., 1999. Origin of 3.45 Ga coniform stromatolites in Warrawoona group, Western Australia. *Geological Society of America Bulletin*, *111*(8), pp.1256-1262.

Holland HD (1984) The Chemical Evolution of the Atmosphere and Oceans. Princeton, NJ: Princeton University Press.

Holland, H.D., 2002. Volcanic gases, black smokers, and the Great Oxidation Event. *Geochimica et Cosmochimica acta*, *66*(21), pp.3811-3826.

Holland, H.D., 2006. The oxygenation of the atmosphere and oceans. *Philosophical Transactions of the Royal Society B: Biological Sciences*, *361*(1470), pp.903-915.

Horita, J., Zimmermann, H. and Holland, H.D., 2002. Chemical evolution of seawater during the Phanerozoic: Implications from the record of marine evaporites. *Geochimica et Cosmochimica Acta*, *66*(21), pp.3733-3756.

Hu, Z. and Gao, S., 2008. Upper crustal abundances of trace elements: A revision and update. *Chemical Geology*, *253*(3-4), pp.205-221.

Hughes, N.C., Peng, S., Bhargava, O.N., Ahluwalia, A.D., Walia, S., Myrow, P.M. and Parcha, S.K., 2005. Cambrian biostratigraphy of the Tal Group, Lesser Himalaya, India, and early

Tsanglangpuan (late early Cambrian) trilobites from the Nigali Dhar syncline. *Geological Magazine*, *142*(1), pp.57-80.

Hughes, N.C., 2016. The Cambrian palaeontological record of the Indian subcontinent. *Earth-Science Reviews*, *159*, pp.428-461.

Ingall, E. and Jahnke, R., 1994. Evidence for enhanced phosphorus regeneration from marine sediments overlain by oxygen depleted waters. *Geochimica et Cosmochimica Acta*, *58*(11), pp.2571-2575.

Javaux, E.J. and Lepot, K., 2018. The Paleoproterozoic fossil record: implications for the evolution of the biosphere during Earth's middle-age. *Earth-Science Reviews*, *176*, pp.68-86.

Javaux, E.J., Knoll, A.H. and Walter, M.R., 2001. Morphological and ecological complexity in early eukaryotic ecosystems. *Nature*, *412*(6842), pp.66-69.

Jayananda, M., Peucat, J.J., Chardon, D., Rao, B.K., Fanning, C.M. and Corfu, F., 2013. Neoarchean greenstone volcanism and continental growth, Dharwar Craton, southern India: Constraints from SIMS U–Pb zircon geochronology and Nd isotopes. *Precambrian Research*, *227*, pp.55-76.

Jiang, G., Sohl, L.E. and Christie-Blick, N., 2003. Neoproterozoic stratigraphic comparison of the Lesser Himalaya (India) and Yangtze block (south China): Paleogeographic implications. *Geology*, *31*(10), pp.917-920.

Jiang, S.Y., Yang, J.H., Ling, H.F., Chen, Y.Q., Feng, H.Z., Zhao, K.D. and Ni, P., 2007. Extreme enrichment of polymetallic Ni–Mo–PGE–Au in Lower Cambrian black shales of South China: an Os isotope and PGE geochemical investigation. *Palaeogeography, Palaeoclimatology, Palaeoecology*, *254*(1-2), pp.217-228.

Jin, C., Li, C., Algeo, T.J., Planavsky, N.J., Cui, H., Yang, X., Zhao, Y., Zhang, X. and Xie, S., 2016. A highly redox-heterogeneous ocean in South China during the early Cambrian (~ 529–514 Ma): Implications for biota-environment co-evolution. *Earth and Planetary Science Letters*, *441*, pp.38-51.

Joy, S., Jelsma, H., Tappe, S. and Armstrong, R., 2015. SHRIMP U–Pb zircon provenance of the Sullavai Group of Pranhita–Godavari Basin and Bairenkonda Quartzite of Cuddapah Basin, with implications for the Southern Indian Proterozoic tectonic architecture. *Journal of Asian Earth Sciences*, *111*, pp.827-839.

Kagoshima, T., Sano, Y., Takahata, N., Maruoka, T., Fischer, T.P. and Hattori, K., 2015. Sulphur geodynamic cycle. *Scientific Reports*, *5*(1), pp.1-6.

Kah, L.C., Lyons, T.W. and Frank, T.D., 2004. Low marine sulphate and protracted oxygenation of the Proterozoic biosphere. *Nature*, *431*(7010), pp.834-838.

Kale, V.S., Saha, D., Patrabnis-Deb, S., Sesha Sai, V.V., Tripathy, V. and Patil-Pillai, S., 2020. Cuddapah Basin, India: A collage of proterozoic subbasins and terranes. *Proceedings of the Indian National Science Academy*, *86*(1), p.137.

Kalvelage, T., Jensen, M.M., Contreras, S., Revsbech, N.P., Lam, P., Günter, M., LaRoche, J., Lavik, G. and Kuypers, M.M., 2011. Oxygen sensitivity of anammox and coupled N-cycle processes in oxygen minimum zones. *PloS one*, *6*(12), p.e29299.

Kampschulte, A. and Strauss, H., 2004. The sulfur isotopic evolution of Phanerozoic seawater based on the analysis of structurally substituted sulfate in carbonates. *Chemical Geology*, *204*(3-4), pp.255-286.

Kang, J., Gill, B., Reid, R., Zhang, F. and Xiao, S., 2023. Nitrate limitation in early Neoproterozoic oceans delayed the ecological rise of eukaryotes. *Science Advances*, *9*(12), p.eade9647.

Kaufman, A.J., Jiang, G., Christie-Blick, N., Banerjee, D.M. and Rai, V., 2006. Stable isotope record of the terminal Neoproterozoic Krol platform in the Lesser Himalayas of northern India. *Precambrian Research*, *147*(1-2), pp.156-185.

Keeling, R.F., Körtzinger, A. and Gruber, N., 2010. Ocean deoxygenation in a warming world. *Annual Review of Marine Science*, *2*(1), pp.199-229.

Kendall, B. and Ostrander, C.M., 2025. Oxygenation of the Proterozoic Earth's surface: An evolving story. In: A. Anbar and D. Weis, eds. *Treatise on Geochemistry* (3rd ed.). Elsevier, pp. 297-336.

Kendall, B.S., Creaser, R.A., Ross, G.M. and Selby, D., 2004. Constraints on the timing of Marinoan "Snowball Earth" glaciation by ^{187}Re–^{187}Os dating of a Neoproterozoic, post-glacial black shale in Western Canada. *Earth and Planetary Science Letters*, *222*(3-4), pp.729-740.

Kendall, B., Creaser, R.A., Gordon, G.W. and Anbar, A.D., 2009. Re–Os and Mo isotope systematics of black shales from the Middle Proterozoic Velkerri and Wollogorang Formations, McArthur Basin, northern Australia. *Geochimica et Cosmochimica Acta*, 73(9), pp.2534-2558.

Kendall, B., Gordon, G.W., Poulton, S.W. and Anbar, A.D., 2011. Molybdenum isotope constraints on the extent of late Paleoproterozoic ocean euxinia. *Earth and Planetary Science Letters*, *307*(3-4), pp.450-460.

Kendall, B., Komiya, T., Lyons, T.W., Bates, S.M., Gordon, G.W., Romaniello, S.J., Jiang, G., Creaser, R.A., Xiao, S., McFadden, K. and Sawaki, Y., 2015. Uranium and molybdenum isotope evidence for an episode of widespread ocean oxygenation during the late Ediacaran Period. *Geochimica et Cosmochimica Acta*, *156*, pp.173-193.

Kendall, B., Dahl, T.W. and Anbar, A.D., 2017. The stable isotope geochemistry of molybdenum. *Reviews in Mineralogy and Geochemistry*, *82*(1), pp.683-732.

Kessler, A.J., Bristow, L.A., Cardenas, M.B., Glud, R.N., Thamdrup, B. and Cook, P.L., 2014. The isotope effect of denitrification in permeable sediments. *Geochimica et Cosmochimica Acta*, *133*, pp.156-167.

Khelen, A.C., Manikyamba, C., Tang, L., Santosh, M., Subramanyam, K.S.V. and Singh, T.D., 2020. Detrital zircon U-Pb geochronology of stromatolitic carbonates from the greenstone belts of Dharwar Craton and Cuddapah basin of Peninsular India. *Geoscience Frontiers*, *11*(1), pp.229-242.

Kikumoto, R., Tahata, M., Nishizawa, M., Sawaki, Y., Maruyama, S., Shu, D., Han, J., Komiya, T., Takai, K. and Ueno, Y., 2014. Nitrogen isotope chemostratigraphy of the Ediacaran and Early Cambrian platform sequence at Three Gorges, South China. *Gondwana Research*, *25*(3), pp.1057-1069.

King, E.K. and Pett-Ridge, J.C., 2018. Reassessing the dissolved molybdenum isotopic composition of ocean inputs: The effect of chemical weathering and groundwater. *Geology*, *46*(11), pp.955-958.

Kipp, M.A., Stüeken, E.E., Yun, M., Bekker, A. and Buick, R., 2018. Pervasive aerobic nitrogen cycling in the surface ocean across the Paleoproterozoic Era. *Earth and Planetary Science Letters*, *500*, pp.117-126.

Klinkhammer, G.P. and Palmer, M.R., 1991. Uranium in the oceans: where it goes and why. *Geochimica et Cosmochimica Acta*, *55*(7), pp.1799-1806.

Knoll, A.H. and Carroll, S.B., 1999. Early animal evolution: emerging views from comparative biology and geology. *Science*, *284*(5423), pp.2129-2137.

Koehler, M.C., Stüeken, E.E., Kipp, M.A., Buick, R. and Knoll, A.H., 2017. Spatial and temporal trends in Precambrian nitrogen cycling: A Mesoproterozoic offshore nitrate minimum. *Geochimica et Cosmochimica Acta*, *198*, pp.315-337.

Krissansen-Totton, J., Buick, R. and Catling, D.C., 2015. A statistical analysis of the carbon isotope record from the Archean to Phanerozoic and implications for the rise of oxygen. *American Journal of Science*, *315*(4), pp.275-316.

Kumar, A., Gopalan, K. and Rajagopalan, G., 2001. Age of the Lower Vindhyan sediments, central India. *Current Science*, *81*(7), pp.806-809.

Kuypers, M.M., Sliekers, A.O., Lavik, G., Schmid, M., Jørgensen, B.B., Kuenen, J.G., Sinninghe Damsté, J.S., Strous, M. and Jetten, M.S., 2003. Anaerobic ammonium oxidation by anammox bacteria in the Black Sea. *Nature*, *422*(6932), pp.608-611.

Lakshminarayana, G. and Bhattacharjee, S., 2000. Shallow marine siliciclastic sedimentation in the middle Proterozoic Gandikota Formation, Cuddapah basin, Andhra Pradesh. *Geological Society of India*, *55*(1), pp.65-76.

Lakshminarayana, G., Bhattacharjee, S. and Kumar, A., 1999. Palaeocurrents and depositional setting in the Banganapalle Formation, Kurnool sub-basin, Cuddapah basin, Andhra Pradesh. *Journal Geological Society of India*, *53*(2), pp.255-259.

Lakshminarayana, G., Bhattacharjee, S. and Ramanaidu, K.V., 2001. Sedimentation and stratigraphic framework in the Cuddapah Basin. *Geol. Surv. India Spec. Publ*, *55*, pp.31-58.

Lan, Z., Pandey, S.K., Zhang, S., Sharma, M., Gao, Y. and Wu, S., 2021. Precambrian crustal evolution in Northern Indian Block: evidence from detrital zircon U-Pb ages and Hf-isotopes. *Precambrian Research*, *361*, p.106238.

LaRowe, D.E., Burwicz, E., Arndt, S., Dale, A.W. and Amend, J.P., 2017. Temperature and volume of global marine sediments. *Geology*, *45*(3), pp.275-278.

Lehmann, M.F., Bernasconi, S.M., Barbieri, A. and McKenzie, J.A., 2002. Preservation of organic matter and alteration of its carbon and nitrogen isotope composition during simulated and in situ early sedimentary diagenesis. *Geochimica et Cosmochimica Acta*, *66*(20), pp.3573-3584.

Lenton, T.M., Boyle, R.A., Poulton, S.W., Shields-Zhou, G.A. and Butterfield, N.J., 2014. Co-evolution of eukaryotes and ocean oxygenation in the Neoproterozoic era. *Nature Geoscience*, *7*(4), pp.257-265.

Li, J. and Yin, L., 2019. Rhenium–osmium isotope measurements in marine shale reference material SBC-1: Implications for method validation and quality control. *Geostandards and Geoanalytical Research*, *43*(3), pp.497-507.

Li, D.A., Ling, H.F., Jiang, S.Y., Pan, J.Y., Chen, Y.Q., Cai, Y.F. and Feng, H.Z., 2009. New carbon isotope stratigraphy of the Ediacaran–Cambrian boundary interval from SW China: implications for global correlation. *Geological Magazine*, *146*(4), pp.465-484.

Li, C., Shi, W., Cheng, M., Jin, C. and Algeo, T.J., 2020. The redox structure of Ediacaran and early Cambrian oceans and its controls. *Science Bulletin*, *65*(24), pp.2141-2149.

Li, Z., Cole, D.B., Newby, S.M., Owens, J.D., Kendall, B. and Reinhard, C.T., 2021. New constraints on mid-Proterozoic ocean redox from stable thallium isotope systematics of black shales. *Geochimica et Cosmochimica Acta*, *315*, pp.185-206.

Li, S., Lang, X., Wang, H., Zhu, S., Zhao, K. and Hou, M., 2023. Pyrite Sulfur Isotope Systematics Suggest Low Marine Sulfate Levels across the Ediacaran–Cambrian Transition. *Minerals*, *13*(2), p.227.

Liu, Z.R.R., Zhou, M.F. and Wang, W., 2021. Mercury anomalies across the Ediacaran–Cambrian boundary: Evidence for a causal link between continental erosion and biological evolution. *Geochimica et Cosmochimica Acta*, *304*, pp.327-346.

Love, G.D., Grosjean, E., Stalvies, C., Fike, D.A., Grotzinger, J.P., Bradley, A.S., Kelly, A.E., Bhatia, M., Meredith, W., Snape, C.E. and Bowring, S.A., 2009. Fossil steroids record the appearance of Demospongiae during the Cryogenian period. *Nature*, *457*(7230), pp.718-721.

Lowenstein, T.K., Hardie, L.A., Timofeeff, M.N. and Demicco, R.V., 2003. Secular variation in seawater chemistry and the origin of calcium chloride basinal brines. *Geology*, *31*(10), pp.857-860.

Lowenstein, T.K., Kendall, B. and Anbar, A., 2013. The geologic history of seawater. In *The Oceans and Marine Geochemistry* (pp. 569-622). Elsevier Inc..

Loyd, S.J., Marenco, P.J., Hagadorn, J.W., Lyons, T.W., Kaufman, A.J., Sour-Tovar, F. and Corsetti, F.A., 2012. Sustained low marine sulfate concentrations from the Neoproterozoic to the Cambrian: Insights from carbonates of northwestern Mexico and eastern California. *Earth and Planetary Science Letters*, *339*, pp.79-94.

Lu, X., Kendall, B., Stein, H.J. and Hannah, J.L., 2017. Temporal record of osmium concentrations and $^{187}Os/^{188}Os$ in organic-rich mudrocks: Implications for the osmium geochemical cycle and the use of osmium as a paleoceanographic tracer. *Geochimica et Cosmochimica Acta*, *216*, pp.221-241.

Lu, X., Edwards, C.T. and Kendall, B., 2023. No evidence for expansion of global ocean euxinia during the base Stairsian mass extinction event (Tremadocian, Early Ordovician). *Geochimica et Cosmochimica Acta*, *341*, pp.116-131.

Luo, G., Ono, S., Huang, J., Algeo, T.J., Li, C., Zhou, L., Robinson, A., Lyons, T.W. and Xie, S., 2015. Decline in oceanic sulfate levels during the early Mesoproterozoic. *Precambrian Research*, *258*, pp.36-47.

Luo, G., Junium, C.K., Izon, G., Ono, S., Beukes, N.J., Algeo, T.J., Cui, Y., Xie, S. and Summons, R.E., 2018. Nitrogen fixation sustained productivity in the wake of the Palaeoproterozoic Great Oxygenation Event. *Nature Communications*, *9*(1), p.978.

Luo, J., Long, X., Bowyer, F.T., Mills, B.J., Li, J., Xiong, Y., Zhu, X., Zhang, K. and Poulton, S.W., 2021. Pulsed oxygenation events drove progressive oxygenation of the early Mesoproterozoic ocean. *Earth and Planetary Science Letters*, *559*, p.116754.

Lyons, T.W., Anbar, A.D., Severmann, S., Scott, C. and Gill, B.C., 2009. Tracking euxinia in the ancient ocean: a multiproxy perspective and Proterozoic case study. *Annual Review of Earth and Planetary Sciences*, *37*(1), pp.507-534.

Lyons, T.W., Reinhard, C.T. and Planavsky, N.J., 2014. The rise of oxygen in Earth's early ocean and atmosphere. *Nature*, *506*(7488), pp.307-315.

Lyons, T.W., Diamond, C.W., Planavsky, N.J., Reinhard, C.T. and Li, C., 2021. Oxygenation, life, and the planetary system during Earth's middle history: An overview. *Astrobiology*, 21(8), pp.906-923.

Lyons, T.W., Tino, C.J., Fournier, G.P., Anderson, R.E., Leavitt, W.D., Konhauser, K.O. and Stüeken, E.E., 2024. Co-evolution of early Earth environments and microbial life. *Nature Reviews Microbiology*, pp.1-15.

Ma, P., Guo, H., Du, Y., Yu, W., Jin, S. and Xu, L., 2023. Dynamic seawater redox status in the early Mesoproterozoic: Evidence from trace elements and sulfur isotopic compositions of carbonate associated sulfate in multiple sections. *Precambrian Research*, *385*, p.106953.

Malone, S.J., Meert, J.G., Banerjee, D.M., Pandit, M.K., Tamrat, E., Kamenov, G.D., Pradhan, V.R. and Sohl, L.E., 2008. Paleomagnetism and detrital zircon geochronology of the

Upper Vindhyan Sequence, Son Valley and Rajasthan, India: A ca. 1000 Ma closure age for the Purana Basins?. *Precambrian Research*, *164*(3-4), pp.137-159.

Mandal, A., Tripathy, G.R., Goswami, V., Ackerman, L., Parcha, S.K. and Chandra, R., 2021. Re–Os and Sr Isotopic Study of Permian–Triassic Sedimentary Rocks from the Himalaya: Shale Chronology and Carbonate Diagenesis. *Minerals*, *11*(4), p.417.

Mandal, S., Choudhury, T.R., Das, A., Sarkar, S. and Banerjee, S., 2022. Shallow marine glauconitization during the Proterozoic in response to intrabasinal tectonics: A study from the Proterozoic Lower Bhander Sandstone, Central India. *Precambrian Research*, *372*, p.106596.

Manikyamba, C., Kerrich, R., Gonzalez-Alvarez, I., Mathur, R. and Khanna, T.C., 2008. Geochemistry of Paleoproterozoic black shales from the Intracontinental Cuddapah basin, India: implications for provenance, tectonic setting, and weathering intensity. *Precambrian Research*, *162*(3-4), pp.424-440.

März, C., Poulton, S.W., Beckmann, B., Küster, K., Wagner, T. and Kasten, S., 2008. Redox sensitivity of P cycling during marine black shale formation: dynamics of sulfidic and anoxic, non-sulfidic bottom waters. *Geochimica et Cosmochimica Acta*, *72*(15), pp.3703-3717.

Mazumdar, A. and Banerjee, D.M., 2001. Regional variations in the carbon isotopic composition of phosphorite from the Early Cambrian Lower Tal Formation, Mussoorie Hills, India. *Chemical Geology*, *175*(1-2), pp.5-15.

Mazumdar, A., Banerjee, D.M., Schidlowski, M. and Balaram, V., 1999. Rare-earth elements and stable isotope geochemistry of early Cambrian chert-phosphorite assemblages from the Lower Tal Formation of the Krol Belt (Lesser Himalaya, India). *Chemical geology*, *156*(1-4), pp.275-297.

Mazumdar, A., Goldberg, T. and Strauss, H., 2008. Abiotic oxidation of pyrite by Fe (III) in acidic media and its implications for sulfur isotope measurements of lattice-bound sulfate in sediments. *Chemical Geology*, *253*(1-2), pp.30-37.

McArthur, J.M., Algeo, T.J., Van de Schootbrugge, B., Li, Q. and Howarth, R.J., 2008. Basinal restriction, black shales, Re−Os dating, and the Early Toarcian (Jurassic) oceanic anoxic event. *Paleoceanography*, *23*(4).

McKenzie, N.R., Hughes, N.C., Myrow, P.M., Xiao, S. and Sharma, M., 2011. Correlation of Precambrian–Cambrian sedimentary successions across northern India and the utility of isotopic signatures of Himalayan lithotectonic zones. *Earth and Planetary Science Letters*, *312*(3-4), pp.471-483.

McKenzie, N.R., Hughes, N.C., Myrow, P.M., Banerjee, D.M., Deb, M. and Planavsky, N.J., 2013. New age constraints for the Proterozoic Aravalli–Delhi successions of India and their implications. *Precambrian Research*, *238*, pp.120-128.

McManus, J., Nägler, T.F., Siebert, C., Wheat, C.G. and Hammond, D.E., 2002. Oceanic molybdenum isotope fractionation: Diagenesis and hydrothermal ridge-flank alteration. *Geochemistry, Geophysics, Geosystems, 3*(12), pp.1-9.

Meijerink, A.M.J., Rao, D.P. and Rupke, J., 1984. Stratigraphic and structural development of the Precambrian Cuddapah Basin, SE India. *Precambrian Research*, *26*(1), pp.57-104.

Menard, H.W. and Smith, S.M., 1966. Hypsometry of ocean basin provinces. *Journal of Geophysical Research, 71*(18), pp.4305-4325.

Mentel, M. and Martin, W., 2008. Energy metabolism among eukaryotic anaerobes in light of Proterozoic ocean chemistry. *Philosophical Transactions of the Royal Society B: Biological Sciences*, *363*(1504), pp.2717-2729.

Middelburg, J.J., Klaver, G., Nieuwenhuize, J., Wielemaker, A., de Haas, W., Vlug, T. and van der Nat, J.F., 1996. Organic matter mineralization in intertidal sediments along an estuarine gradient. *Marine Ecology Progress Series*, *132*, pp.157-168.

Miller, C., Klötzli, U., Frank, W., Thöni, M. and Grasemann, B., 2000. Proterozoic crustal evolution in the NW Himalaya (India) as recorded by circa 1.80 Ga mafic and 1.84 Ga granitic magmatism. *Precambrian Research*, *103*(3-4), pp.191-206.

Miller, C.A., Peucker-Ehrenbrink, B., Walker, B.D. and Marcantonio, F., 2011. Re-assessing the surface cycling of molybdenum and rhenium. *Geochimica et Cosmochimica Acta*, *75*(22), pp.7146-7179.

Mills, D.B. and Canfield, D.E., 2014. Oxygen and animal evolution: Did a rise of atmospheric oxygen "trigger" the origin of animals? *BioEssays*, *36*(12), pp.1145-1155.

Mills, D.B., Simister, R.L., Sehein, T.R., Hallam, S.J., Sperling, E.A. and Crowe, S.A., 2024. Constraining the oxygen requirements for modern microbial eukaryote diversity. *Proceedings of the National Academy of Sciences*, *121*(2), p.e2303754120.

Mingram, B. and Bräuer, K., 2001. Ammonium concentration and nitrogen isotope composition in metasedimentary rocks from different tectonometamorphic units of the European Variscan Belt. *Geochimica et Cosmochimica Acta*, *65*(2), pp.273-287.

Mishra, D.C., 2011. Long hiatus in Proterozoic sedimentation in India: Vindhyan, Cuddapah and Pakhal Basins—A plate tectonic model. *Journal of the Geological Society of India*, *77*, pp.17-25.

Mishra, M., Bickford, M.E. and Basu, A., 2018. U-Pb age and chemical composition of an ash bed in the Chopan Porcellanite Formation, Vindhyan Supergroup, India. *The Journal of Geology*, *126*(5), pp.553-560.

Mitra, R., Chakrabarti, G. and Shome, D., 2018. Geochemistry of the Palaeo–Mesoproterozoic Tadpatri shales, Cuddapah Basin, India: Implications on provenance, paleoweathering and paleoredox conditions. *Acta Geochimica*, *37*, pp.715-733.

Mondal, M.E.A., Goswami, J.N., Deomurari, M.P. and Sharma, K.K., 2002. Ion microprobe $^{207}Pb/^{206}Pb$ ages of zircons from the Bundelkhand massif, northern India: implications for crustal evolution of the Bundelkhand–Aravalli protocontinent. *Precambrian Research*, *117*(1-2), pp.85-100.

Morford, J.L. and Emerson, S., 1999. The geochemistry of redox sensitive trace metals in sediments. *Geochimica et Cosmochimica Acta*, *63*(11-12), pp.1735-1750.

Morse, J.W. and Luther Iii, G.W., 1999. Chemical influences on trace metal-sulfide interactions in anoxic sediments. *Geochimica et Cosmochimica Acta*, *63*(19-20), pp.3373-3378.

Motomura, K., Bekker, A., Bleeker, W., Ikehara, M., Sano, T., Guilmette, C., Lin, Y. and Kiyokawa, S., 2024. Nitrogen isotope gradient on continental margins during the late Paleoproterozoic. *Geochimica et Cosmochimica Acta*, *371*, pp.144-161.

Mukherjee, I., Deb, M., Large, R.R., Halpin, J., Meffre, S., Ávila, J. and Belousov, I., 2020. Pyrite textures, trace elements and sulfur isotope chemistry of Bijaigarh Shales, Vindhyan Basin, India and their implications. *Minerals*, *10*(7), p.588.

Mukherjee, S., Das, P., Ghosh, G., Bose, S., Dev, J.A., Das, K. and Tomson, J.K., 2023. Petrography, geochemistry and detrital zircon geochronology of the Srisailam Quartzite Formation, Cuddapah Basin, India: Implications for depositional age, correlation and provenance. *Precambrian Research*, *387*, p.106978.

Murthy, Y.G.K., Babu Rao, V., Guptasarma, D., Rao, J.M., Rao, M.N. and Bhattacharji, S., 1987. Tectonic, petrochemical and geophysical studies of mafic dyke swarms around the Proterozoic Cuddapah basin, South India. *Mafic dyke swarms*, *34*, pp.303-316.

Nagaraja Rao, B.K., Rajurkar, S.T., Ramalingaswamy, G., and Ravindra Babu, B., 1987. Stratigraphy, Structure and Evolution of the Cuddapah Basin. In: Radhakrishna, B.P. (ed.) Purana basins of peninsular India (Middle to Late Proterozoic). *Memoirs of the Geological Society of India*, *6*, pp.33-86.

Nägler, T.F., Neubert, N., Böttcher, M.E., Dellwig, O. and Schnetger, B., 2011. Molybdenum isotope fractionation in pelagic euxinia: Evidence from the modern Black and Baltic Seas. *Chemical Geology*, 289(1-2), pp.1-11.

Nägler, T.F., Anbar, A.D., Archer, C., Goldberg, T., Gordon, G.W., Greber, N.D., Siebert, C., Sohrin, Y. and Vance, D., 2014. Proposal for an international molybdenum isotope measurement standard and data representation. *Geostandards and Geoanalytical Research*, *38*(2), pp.149-151.

Nakagawa, Y., Takano, S., Firdaus, M.L., Norisuye, K., Hirata, T., Vance, D. and Sohrin, Y., 2012. The molybdenum isotopic composition of the modern ocean. *Geochemical Journal*, *46*(2), pp.131-141.

Neely, R.A., Gislason, S.R., Ólafsson, M., McCoy-West, A.J., Pearce, C.R. and Burton, K.W., 2018. Molybdenum isotope behaviour in groundwaters and terrestrial hydrothermal systems, Iceland. *Earth and Planetary Science Letters*, *486*, pp.108-118.

Negi, M., Saha, S., Ghosh, S.K. and Rai, S.K., 2023. Provenance and sedimentation age of the Proterozoic clastic succession of the Garhwal-Kumaon Lesser Himalaya, NW-India: Clues from U–Pb zircon and Sr–Nd isotopes. *Geological Journal*, *58*(2), pp.605-619.

Neubert, N., Nägler, T.F. and Böttcher, M.E., 2008. Sulfidity controls molybdenum isotope fractionation into euxinic sediments: Evidence from the modern Black Sea. *Geology*, *36*(10), pp.775-778.

Noordmann, J., Weyer, S., Montoya-Pino, C., Dellwig, O., Neubert, N., Eckert, S., Paetzel, M. and Böttcher, M.E., 2015. Uranium and molybdenum isotope systematics in modern euxinic basins: Case studies from the central Baltic Sea and the Kyllaren fjord (Norway). *Chemical Geology*, *396*, pp.182-195.

Och, L.M. and Shields-Zhou, G.A., 2012. The Neoproterozoic oxygenation event: Environmental perturbations and biogeochemical cycling. *Earth-Science Reviews*, *110*(1-4), pp.26-57.

Ossa, F.O., Eickmann, B., Hofmann, A., Planavsky, N.J., Asael, D., Pambo, F. and Bekker, A., 2018. Two-step deoxygenation at the end of the Paleoproterozoic Lomagundi Event. *Earth and Planetary Science Letters*, *486*, pp.70-83.

Ostrander, C.M., Nielsen, S.G., Owens, J.D., Kendall, B., Gordon, G.W., Romaniello, S.J. and Anbar, A.D., 2019. Fully oxygenated water columns over continental shelves before the Great Oxidation Event. *Nature Geoscience*, *12*(3), pp.186-191.

Ostrander, C.M., Johnson, A.C. and Anbar, A.D., 2021. Earth's first redox revolution. *Annual Review of Earth and Planetary Sciences*, *49*(1), pp.337-366.

Owens, J.D., Reinhard, C.T., Rohrssen, M., Love, G.D. and Lyons, T.W., 2016. Empirical links between trace metal cycling and marine microbial ecology during a large perturbation to Earth's carbon cycle. *Earth and Planetary Science Letters*, *449*, pp.407-417.

Oxburgh, R., 1998. Variations in the osmium isotope composition of sea water over the past 200,000 years. *Earth and Planetary Science Letters*, *159*(3-4), pp.183-191.

Pan, W., Cao, M., Du, Y., Cheng, M., Zhou, Y.Q., Algeo, T.J., Zhao, M.Y., Thibault, N., Li, C., Wei, G.Y. and Dahl, T.W., 2021. Paired U and Mo isotope evidence for pervasive anoxia in the Cryogenian early interglacial ocean. *Precambrian Research*, *361*, p.106244.

Pandey, S.K., Singh, D., Sharma, M., Ahmad, S. and Bhan, U., 2024. A new palaeobiological assemblage from the Son Valley Bhander Group and its implications on the age of the upper Vindhyans of India. *Palaeoworld*, *33*(4), pp.801-828.

Pang, K., Tang, Q., Yuan, X.L., Wan, B. and Xiao, S., 2015. A biomechanical analysis of the early eukaryotic fossil Valeria and new occurrence of organic-walled microfossils from the Paleo-Mesoproterozoic Ruyang Group. *Palaeoworld*, *24*(3), pp.251-262.

Pant, C.C. and Goswami, P.K., 2002. The Proterozoic Bhumiadhar Member (Blaini Formation), Nainital Hills: an example of storm-dominated regressive offshore sedimentation in Krol

Belt, Kumaun Lesser Himalaya. *Aspects of geology and environment of Himalaya*, pp.112-127.

Papineau, D., Purohit, R., Goldberg, T., Pi, D., Shields, G.A., Bhu, H., Steele, A. and Fogel, M.L., 2009. High primary productivity and nitrogen cycling after the Paleoproterozoic phosphogenic event in the Aravalli Supergroup, India. *Precambrian Research*, *171*(1-4), pp.37-56.

Partin, C.A., Bekker, A., Planavsky, N.J. and Lyons, T.W., 2015. Euxinic conditions recorded in the ca. 1.93 Ga Bravo Lake Formation, Nunavut (Canada): Implications for oceanic redox evolution. *Chemical Geology*, *417*, pp.148-162.

Patranabis-Deb, S., Saha, D. and Tripathy, V., 2012. Basin stratigraphy, sea-level fluctuations and their global tectonic connections—evidence from the Proterozoic Cuddapah Basin. *Geological Journal*, *47*(2-3), pp.263-283.

Paul, P.P., 2017. Autogenic and allogenic controls on late paleoproterozoic continental and marine sedimentation clues from Gwalior rift basin central India.

Paulmier, A. and Ruiz-Pino, D., 2009. Oxygen minimum zones (OMZs) in the modern ocean. *Progress in Oceanography*, *80*(3-4), pp.113-128.

Payne, J.L., Boyer, A.G., Brown, J.H., Finnegan, S., Kowalewski, M., Krause Jr, R.A., Lyons, S.K., McClain, C.R., McShea, D.W., Novack-Gottshall, P.M. and Smith, F.A., 2009. Two-phase increase in the maximum size of life over 3.5 billion years reflects biological innovation and environmental opportunity. *Proceedings of the National Academy of Sciences*, *106*(1), pp.24-27.

Pearce, C.R., Cohen, A.S. and Parkinson, I.J., 2009. Quantitative separation of molybdenum and rhenium from geological materials for isotopic determination by MC-ICP-MS. *Geostandards and Geoanalytical Research*, *33*(2), pp.219-229.

Pennock, J.R., Velinsky, D.J., Ludlam, J.M., Sharp, J.H. and Fogel, M.L., 1996. Isotopic fractionation of ammonium and nitrate during uptake by Skeletonema costatum: Implications for $\delta^{15}N$ dynamics under bloom conditions. *Limnology and Oceanography*, *41*(3), pp.451-459.

Peucker-Ehrenbrink, B. and Jahn, B.M., 2001. Rhenium-osmium isotope systematics and platinum group element concentrations: Loess and the upper continental crust. *Geochemistry, Geophysics, Geosystems*, *2*(10).

Peucker-Ehrenbrink, B. and Ravizza, G., 2000. The marine osmium isotope record. *Terra Nova*, *12*(5), pp.205-219.

Pi, D.H., Liu, C.Q., Shields-Zhou, G.A. and Jiang, S.Y., 2013. Trace and rare earth element geochemistry of black shale and kerogen in the early Cambrian Niutitang Formation in Guizhou province, South China: Constraints for redox environments and origin of metal enrichments. *Precambrian Research*, *225*, pp.218-229.

Planavsky, N.J., McGoldrick, P., Scott, C.T., Li, C., Reinhard, C.T., Kelly, A.E., Chu, X., Bekker, A., Love, G.D. and Lyons, T.W., 2011. Widespread iron-rich conditions in the mid-Proterozoic ocean. *Nature*, *477*(7365), pp.448-451.

Pogge von Strandmann, P.A., Stüeken, E.E., Elliott, T., Poulton, S.W., Dehler, C.M., Canfield, D.E. and Catling, D.C., 2015. Selenium isotope evidence for progressive oxidation of the Neoproterozoic biosphere. *Nature Communications*, *6*(1), pp.1-10.

Poulson Brucker, R.L., McManus, J., Severmann, S. and Berelson, W.M., 2009. Molybdenum behavior during early diagenesis: Insights from Mo isotopes. *Geochemistry, Geophysics, Geosystems*, *10*(6).

Poulson, R.L., Siebert, C., McManus, J. and Berelson, W.M., 2006. Authigenic molybdenum isotope signatures in marine sediments. *Geology*, *34*(8), pp.617-620.

Poulton, S.W. and Canfield, D.E., 2005. Development of a sequential extraction procedure for iron: implications for iron partitioning in continentally derived particulates. *Chemical Geology*, *214*(3-4), pp.209-221.

Poulton, S.W. and Canfield, D.E., 2011. Ferruginous conditions: a dominant feature of the ocean through Earth's history. *Elements*, *7*(2), pp.107-112.

Poulton, S.W. and Raiswell, R., 2002. The low-temperature geochemical cycle of iron: from continental fluxes to marine sediment deposition. *American Journal of Science*, *302*(9), pp.774-805.

Poulton, S.W., Fralick, P.W. and Canfield, D.E., 2004. The transition to a sulphidic ocean∼ 1.84 billion years ago. *Nature*, *431*(7005), pp.173-177.

Poulton, S.W., Fralick, P.W. and Canfield, D.E., 2010. Spatial variability in oceanic redox structure 1.8 billion years ago. *Nature Geoscience*, 3(7), pp.486-490.

Prokopenko, M.G., Hammond, D.E., Berelson, W.M., Bernhard, J.M., Stott, L. and Douglas, R., 2006. Nitrogen cycling in the sediments of Santa Barbara basin and Eastern Subtropical North Pacific: Nitrogen isotopes, diagenesis and possible chemosymbiosis between two lithotrophs (Thioploca and Anammox)—"riding on a glider". *Earth and Planetary Science Letters*, *242*(1-2), pp.186-204.

Proud, R., Cox, M.J. and Brierley, A.S., 2017. Biogeography of the global ocean's mesopelagic zone. *Current Biology*, *27*(1), pp.113-119.

Qin, Z., Xu, D., Kendall, B., Zhang, X., Ou, Q., Wang, X., Li, J. and Liu, J., 2022. Molybdenum isotope-based redox deviation driven by continental margin euxinia during the early Cambrian. *Geochimica et Cosmochimica Acta*, *325*, pp.152-169.

Qiu, Y., Qin, L., Huang, F., Zhao, T. and Li, Y., 2022. Early prosperity of iron bacteria at the end of the Paleoproterozoic era. *Geophysical Research Letters*, *49*(9), p.e2022GL097877.

Raab, M. and Spiro, B., 1991. Sulfur isotopic variations during seawater evaporation with fractional crystallization. *Chemical Geology: Isotope Geoscience Section*, *86*(4), pp.323-333.

Rai, Vibhuti. and Singh, I.B., 1983. Tal Formation, Mussoorie area, India. *Journal of the Palaeontological, Society of India*, *28*, pp.114-117.

Rai, A.K., Pandey, U.K., Zakaulla, S. and Parihar, P.S., 2015. New 1.9-2.0 Ga, Pb-Pb (PbSL), Age of Dolomites from Vempalle Formation, Lower Cuddapah Supergroup, Eastern Dharwar Craton, India. *Journal of the Geological Society of India*, *86*, pp.131-136.

Raiswell, R. and Anderson, T.F., 2005. Reactive iron enrichment in sediments deposited beneath euxinic bottom waters: constraints on supply by shelf recycling. *Geological Society, London, Special Publications*, *248*(1), pp.179-194.

Raiswell, R. and Canfield, D.E., 1998. Sources of iron for pyrite formation in marine sediments. *American Journal of Science*, *298*(3), pp.219-245.

Raiswell, R. and Canfield, D.E., 2012. The iron biogeochemical cycle past and present. *Geochemical Perspectives*, *1*(1), pp.1-2.

Raiswell, R., Newton, R., Bottrell, S.H., Coburn, P.M., Briggs, D.E., Bond, D.P. and Poulton, S.W., 2008. Turbidite depositional influences on the diagenesis of Beecher's Trilobite Bed and the Hunsrück Slate; sites of soft tissue pyritization. *American Journal of Science*, *308*(2), pp.105-129.

Raiswell, R., Hardisty, D.S., Lyons, T.W., Canfield, D.E., Owens, J.D., Planavsky, N.J., Poulton, S.W. and Reinhard, C.T., 2018. The iron paleoredox proxies: A guide to the pitfalls, problems and proper practice. *American Journal of Science*, *318*(5), pp.491-526.

Ramakrishnan, M. and Vaidyanadhan, R., 2008. Geology of India (Vol. 1, pp. 261-333). Bangalore: *Geological Society of India*.

Rao, B., 1994. Time of early sedimentation and volcanism in the Proterozoic Cuddapah basin, South India: evidence from the Rb−Sr age of Pulivendla mafic sill. *Geological Society of India Memoirs.*, *329*.

Rasmussen, B., Bose, P.K., Sarkar, S., Banerjee, S., Fletcher, I.R. and McNaughton, N.J., 2002. 1.6 Ga U−Pb zircon age for the Chorhat Sandstone, lower Vindhyan, India: Possible implications for early evolution of animals. *Geology*, *30*(2), pp.103-106.

Ravizza, G. and Turekian, K.K., 1989. Application of the ^{187}Re–^{187}Os system to black shale geochronometry. *Geochimica et Cosmochimica Acta*, *53*(12), pp.3257-3262.

Ravizza, G.E. and Zachos, J.C., 2003. Records of Cenozoic ocean chemistry. *Treatise on geochemistry*, *6*, p.625.

Ray, J.S., Martin, M.W., Veizer, J. and Bowring, S.A., 2002. U−Pb zircon dating and Sr isotope systematics of the Vindhyan Supergroup, India. *Geology*, *30*(2), pp.131-134.

Ray, J.S., Veizer, J. and Davis, W.J., 2003. C, O, Sr and Pb isotope systematics of carbonate sequences of the Vindhyan Supergroup, India: age, diagenesis, correlations and implications for global events. *Precambrian Research*, *121*(1-2), pp.103-140.

Ray, J.S., 2006. Age of the Vindhyan Supergroup: a review of recent findings. *Journal of Earth System Science*, *115*, pp.149-160.

Raymond, J., Siefert, J.L., Staples, C.R. and Blankenship, R.E., 2004. The natural history of nitrogen fixation. *Molecular Biology and Evolution*, *21*(3), pp.541-554.

Redifield, A., 1934. On the proportions of organic derivatives in sea water and their relation to the composition of plankton. *James Johnstone Memorial Volume*, pp.176-192.

Reinhard, C.T., Planavsky, N.J., Robbins, L.J., Partin, C.A., Gill, B.C., Lalonde, S.V., Bekker, A., Konhauser, K.O. and Lyons, T.W., 2013. Proterozoic ocean redox and biogeochemical stasis. *Proceedings of the National Academy of Sciences*, *110*(14), pp.5357-5362.

Reinhard, C.T., Planavsky, N.J., Olson, S.L., Lyons, T.W. and Erwin, D.H., 2016. Earth's oxygen cycle and the evolution of animal life. *Proceedings of the National Academy of Sciences*, *113*(32), pp.8933-8938.

Reinhard, C.T., Planavsky, N.J., Gill, B.C., Ozaki, K., Robbins, L.J., Lyons, T.W., Fischer, W.W., Wang, C., Cole, D.B. and Konhauser, K.O., 2017. Evolution of the global phosphorus cycle. *Nature*, *541*(7637), pp.386-389.

Richards, A., Argles, T., Harris, N., Parrish, R., Ahmad, T., Darbyshire, F. and Draganits, E., 2005. Himalayan architecture constrained by isotopic tracers from clastic sediments. *Earth and Planetary Science Letters*, *236*(3-4), pp.773-796.

Ries, J.B., Fike, D.A., Pratt, L.M., Lyons, T.W. and Grotzinger, J.P., 2009. Superheavy pyrite in the terminal Proterozoic Nama Group, southern Namibia: a consequence of low seawater sulfate at the dawn of animal life. *Geology*, *37*(8), pp.743-746.

Robbins, L.J., Lalonde, S.V., Planavsky, N.J., Partin, C.A., Reinhard, C.T., Kendall, B., Scott, C., Hardisty, D.S., Gill, B.C., Alessi, D.S. and Dupont, C.L., 2016. Trace elements at the intersection of marine biological and geochemical evolution. *Earth-Science Reviews*, *163*, pp.323-348.

Robinson, R.S., Kienast, M., Luiza Albuquerque, A., Altabet, M., Contreras, S., De Pol Holz, R., Dubois, N., Francois, R., Galbraith, E., Hsu, T.C. and Ivanochko, T., 2012. A review of nitrogen isotopic alteration in marine sediments. *Paleoceanography*, *27*(4).

Rooney, A.D., Selby, D., Houzay, J.P. and Renne, P.R., 2010. Re–Os geochronology of a Mesoproterozoic sedimentary succession, Taoudeni basin, Mauritania: implications for basin-wide correlations and Re–Os organic-rich sediments systematics. *Earth and Planetary Science Letters*, *289*(3-4), pp.486-496.

Rooney, A.D., Chew, D.M. and Selby, D., 2011. Re–Os geochronology of the Neoproterozoic–Cambrian Dalradian Supergroup of Scotland and Ireland: implications for

Neoproterozoic stratigraphy, glaciations and Re–Os systematics. *Precambrian Research, 185*(3-4), pp.202-214.

Rooney, A.D., Hnatyshin, D., Toma, J., Saintilan, N.J., Millikin, A.E., Selby, D. and Creaser, R.A., 2024. Application of the ^{187}Re–^{187}Os geochronometer to crustal materials: Systematics, methodology, data reporting, and interpretation. *Geological Society of America Bulletin*.

Rooze, J. and Meile, C., 2016. The effect of redox conditions and bioirrigation on nitrogen isotope fractionation in marine sediments. *Geochimica et Cosmochimica Acta, 184*, pp.227-239.

Rudge, J.F., Reynolds, B.C. and Bourdon, B., 2009. The double spike toolbox. *Chemical Geology*, *265*(3-4), pp.420-431.

Rudnick, R.L. and Gao, S., 2003. Composition of the continental crust. Treatise on Geochemistry, vol. 3. *Treatise on Geochemistry*, pp.1-64.

Ruttenberg, K.C. and Berner, R.A., 1993. Authigenic apatite formation and burial in sediments from non-upwelling, continental margin environments. *Geochimica et Cosmochimica Acta*, *57*(5), pp.991-1007.

Ruttenberg, K.C., 1992. Development of a sequential extraction method for different forms of phosphorus in marine sediments. *Limnology and Oceanography*, *37*(7), pp.1460-1482.

Saha, D. and Chakraborty, S., 2003. Deformation pattern in the Kurnool and Nallamalai Groups in the northeastern part (Palnad area) of the Cuddapah Basin, South India and its implication on Rodinia/Gondwana tectonics. *Gondwana Research, 6*(4), pp.573-583.

Saha, D. and Tripathy, V., 2012. Palaeoproterozoic sedimentation in the Cuddapah Basin, south India and regional tectonics: a review. *Geological Society, London, Special Publications*, *365*(1), pp.161-184.

Saha, D. and Patranabis-Deb, S., 2014. Proterozoic evolution of Eastern Dharwar and Bastar Cratons, India–an overview of the intracratonic basins, craton margins and mobile belts. *Journal of Asian Earth Sciences, 91*, pp.230-251.

Saha, D., Chakraborti, S. and Tripathy, V., 2010. Intracontinental thrusts and inclined transpression along eastern margin of the East Dharwar Craton, India. *Journal of the Geological Society of India*, 75, pp.323-337.

Saha, D., Patranabis-Deb, S. and Collins, A.S., 2016. Proterozoic stratigraphy of southern Indian Cratons and Global context. In *Stratigraphy & Timescales* (Vol. 1, pp. 1-59). Academic Press.

Saha, D., 2002. Multi-stage deformation in the Nallamalai Fold Belt, Cuddapah basin, South India-Implications for Mesoproterozoic tectonism along southeastern margin of India. *Gondwana Research*, *5*(3), pp.701-719.

Sahoo, S.K., Planavsky, N.J., Jiang, G., Kendall, B., Owens, J.D., Wang, X., Shi, X., Anbar, A.D. and Lyons, T.W., 2016. Oceanic oxygenation events in the anoxic Ediacaran ocean. *Geobiology*, *14*(5), pp.457-468.

Samanta, A., Tripathy, G.R., Nath, B.N., Bhushan, R., Panchang, R., Bharti, N. and Shrivastava, A., 2022. Holocene variability in chemical weathering and ocean redox state: A reconstruction using sediment geochemistry of the Arabian Sea. *Journal of Asian Earth Sciences*, *224*, p.105029.

Sarangi, S., Gopalan, K. and Kumar, S., 2004. Pb–Pb age of earliest megascopic, eukaryotic alga bearing Rohtas Formation, Vindhyan Supergroup, India: implications for Precambrian atmospheric oxygen evolution. *Precambrian Research*, *132*(1-2), pp.107-121.

Sarkar, A., Chakraborty, P.P., Mishra, B., Bera, M.K., Sanyal, P. and Paul, S., 2010. Mesoproterozoic sulphidic ocean, delayed oxygenation and evolution of early life: sulphur isotope clues from Indian Proterozoic basins. *Geological Magazine*, *147*(2), pp.206-218.

Sarkar, S. and Banerjee, S., 2020. A Synthesis of Depositional Sequence of the Proterozoic Vindhyan Supergroup in Son Valley.

Sastry, M.A. and Moitra, A.K., 1984. Vindhyan stratigraphy—A review. *Memoirs of the Geological Survey of India*, *116*(1-2), pp.109-148.

Scheller, E.L., Dickson, A.J., Canfield, D.E., Korte, C., Kristiansen, K.K. and Dahl, T.W., 2018. Ocean redox conditions between the snowballs–Geochemical constraints from Arena Formation, East Greenland. *Precambrian Research*, 319, pp.173-186.

Schidlowski, M., 2001. Carbon isotopes as biogeochemical recorders of life over 3.8 Ga of Earth history: evolution of a concept. *Precambrian Research*, *106*(1-2), pp.117-134.

Schroeder, P.A. and McLain, A.A., 1998. Illite-smectites and the influence of burial diagenesis on the geochemical cycling of nitrogen. *Clay Minerals*, *33*(4), pp.539-546.

Scott, C. and Lyons, T.W., 2012. Contrasting molybdenum cycling and isotopic properties in euxinic versus non-euxinic sediments and sedimentary rocks: Refining the paleoproxies. *Chemical Geology*, *324*, pp.19-27.

Scott, C., Lyons, T.W., Bekker, A., Shen, Y.A., Poulton, S.W., Chu, X.L. and Anbar, A.D., 2008. Tracing the stepwise oxygenation of the Proterozoic ocean. *Nature*, *452*(7186), pp.456-459.

Scott, C., Wing, B.A., Bekker, A., Planavsky, N.J., Medvedev, P., Bates, S.M., Yun, M. and Lyons, T.W., 2014. Pyrite multiple-sulfur isotope evidence for rapid expansion and contraction of the early Paleoproterozoic seawater sulfate reservoir. *Earth and Planetary Science Letters*, *389*, pp.95-104.

Selby, D. and Creaser, R.A., 2003. Re–Os geochronology of organic rich sediments: an evaluation of organic matter analysis methods. *Chemical Geology*, *200*(3-4), pp.225-240.

Selby, D. and Creaser, R.A., 2005. Direct radiometric dating of the Devonian-Mississippian time-scale boundary using the Re−Os black shale geochronometer. Geology, 33(7), pp.545-548.

Sai, V.S., Khanna, T.C. and Reddy, N.R.K., 2016. Red beds in the Cuddapah Basin, eastern Dharwar Craton, India: Implications for the initiation of sedimentation during the Proterozoic Oxygenation event. *Journal of Indian Geophysical Union*, *20*(3), pp.342-350.

Shang, M., Tang, D., Shi, X., Zhou, L., Zhou, X., Song, H. and Jiang, G., 2019. A pulse of oxygen increase in the early Mesoproterozoic ocean at ca. 1.57–1.56 Ga. *Earth and Planetary Science Letters*, 527, p.115797.

Sharma, A. and Chakraborty, P.P., 2024. Recent findings from Proterozoic basins of Peninsular India and roadmap ahead. *Proceedings of the Indian National Science Academy*, pp.1-12.

Sharma, M. and Shukla, Y., 2012. Occurrence of helically coiled microfossil Obruchevella in the Owk Shale of the Kurnool Group and its significance. *Journal of Earth System Science*, *121*, pp.755-768.

Sharma, M., Shukla, Y. and Sergeev, V.N., 2021. Microfossils from the Krol 'A'of the Lesser Himalaya, India: Additional supporting data for its early Ediacaran age. Palaeoworld, 30(4), pp.610-626.

Sharma, K.K., Rameshwar Rao, D., Azmi, R.J., Gopalan, K. and Pantulu, G.V.C., 1991. Precambrian-Cambrian boundary in the Tal Formation of Garhwal Lesser Himalaya: Rb-Sr age evidence from black shales underlying phosphorites. *Current Science (Bangalore)*, *62*(7), pp.528-530.

Sharma, M., Rosenberg, E.J. and Butterfield, D.A., 2007. Search for the proverbial mantle osmium sources to the oceans: Hydrothermal alteration of mid-ocean ridge basalt. *Geochimica et Cosmochimica Acta*, *71*(19), pp.4655-4667.

Sheen, A.I., Kendall, B., Reinhard, C.T., Creaser, R.A., Lyons, T.W., Bekker, A., Poulton, S.W. and Anbar, A.D., 2018. A model for the oceanic mass balance of rhenium and implications for the extent of Proterozoic ocean anoxia. *Geochimica et Cosmochimica Acta*, *227*, pp.75-95.

Sheppard, S., Rasmussen, B., Zi, J.W., Soma Sekhar, V., Srinivasa Sarma, D., Ram Mohan, M., Krapež, B., Wilde, S.A. and McNaughton, N.J., 2017. U–Pb dating of metamorphic monazite establishes a Pan-African age for tectonism in the Nallamalai Fold Belt, India. *Journal of the Geological Society*, *174*(6), pp.1062-1069.

Shields, G.A., 2007. A normalised seawater strontium isotope curve: possible implications for Neoproterozoic-Cambrian weathering rates and the further oxygenation of the Earth. *EEarth*, *2*(2), pp.35-42.

Shukla, Y., Sharma, M. and Sergeev, V.N., 2020. Organic walled microfossils from the Neoproterozoic Owk Shale, Kurnool Group, South India. *Palaeoworld*, *29*(3), pp.490-511.

Shukla, A.D., George, B.G. and Ray, J.S., 2020. Evolution of the Proterozoic Vindhyan Basin, Rajasthan, India: insights from geochemical provenance of siliciclastic sediments. *International Geology Review*, *62*(2), pp.153-167.

Siebert, C., Nägler, T.F. and Kramers, J.D., 2001. Determination of molybdenum isotope fractionation by double-spike multicollector inductively coupled plasma mass spectrometry. *Geochemistry, Geophysics, Geosystems*, *2*(7).

Siebert, C., Nägler, T.F., von Blanckenburg, F. and Kramers, J.D., 2003. Molybdenum isotope records as a potential new proxy for paleoceanography. *Earth and Planetary Science Letters*, *211*(1-2), pp.159-171.

Sigman, D.M., Karsh, K.L. and Cas, K.L., *Ocean Process Tracers: Nitrogen Isotopes in the Ocean. 2009* [online].

Sindhuja, C.S., Manikyamba, C., Saha, S., Narayanan, S. and Sridhar, B., 2022. Geochemical and carbon isotopic studies of carbonaceous phyllites from Dharwar Craton, India–Reconstruction of Precambrian depositional environment. *Precambrian Research*, 372, p.106575.

Singh, A.K. and Chakraborty, P.P., 2022. Shales of Palaeo-Mesoproterozoic Vindhyan Basin, central India: insight into sedimentation dynamics of Proterozoic shelf. *Geological Magazine*, *159*(2), pp.247-268.

Singh, S.K., Trivedi, J.R. and Krishnaswami, S., 1999. Re−Os isotope systematics in black shales from the Lesser Himalaya: Their chronology and role in the $^{187}Os/^{188}Os$ evolution of seawater. *Geochimica et Cosmochimica Acta*, *63*(16), pp.2381-2392.

Singh, A.K., Chakraborty, P.P. and Sarkar, S., 2018. Redox structure of Vindhyan hydrosphere. *Current Science*, *115*(7), pp.1334-1341.

Soetaert, K., Petzoldt, T. and Setzer, R. W., 2010. Solving differential equations in R: package deSolve. *Journal of Statistical Software, 33*, 1–25.

Soetaert, K. and Petzoldt, T., 2010. Inverse modelling, sensitivity and Monte Carlo analysis in R using package FME. *Journal of Statistical Software, 33*, 1–28.

Somasekhar, V., Ramanaiah, S. and Sarma, D.S., 2018. Geochemical characterization of the siliciclastic rocks of Chitravati Group, Cuddapah Supergroup: Implications for provenance and depositional environment. *Journal of Earth System Science*, *127*, pp.1-27.

Somes, C.J., Schmittner, A., Galbraith, E.D., Lehmann, M.F., Altabet, M.A., Montoya, J.P., Letelier, R.M., Mix, A.C., Bourbonnais, A. and Eby, M., 2010. Simulating the global distribution of nitrogen isotopes in the ocean. *Global Biogeochemical Cycles*, *24*(4).

Song, H., Tong, J., Algeo, T.J., Song, H., Qiu, H., Zhu, Y., Tian, L., Bates, S., Lyons, T.W., Luo, G. and Kump, L.R., 2014. Early Triassic seawater sulfate drawdown. *Geochimica et Cosmochimica Acta*, *128*, pp.95-113.

Sperling, E.A., Frieder, C.A., Raman, A.V., Girguis, P.R., Levin, L.A. and Knoll, A.H., 2013. Oxygen, ecology, and the Cambrian radiation of animals. *Proceedings of the National Academy of Sciences*, *110*(33), pp.13446-13451.

Sperling, E.A., Wolock, C.J., Morgan, A.S., Gill, B.C., Kunzmann, M., Halverson, G.P., Macdonald, F.A., Knoll, A.H. and Johnston, D.T., 2015. Statistical analysis of iron geochemical data suggests limited late Proterozoic oxygenation. *Nature*, *523*(7561), pp.451-454.

Srivastava, R.N., Srivastava, A.K., Singh, K.N. and Redcliffe, R.P., 2003. Sedimentation and depositional environment of the Chopan porcellanite Formation, Semri group, Vindhyan supergroup in parts of Sonbhadra district, Uttar Pradesh. *Journal of the Palaeontological Society of India*, *48*, pp.167-179.

Stockey, R.G., Cole, D.B., Planavsky, N.J., Loydell, D.K., Frýda, J. and Sperling, E.A., 2020. Persistent global marine euxinia in the early Silurian. *Nature Communications*, 11(1), p.1804.

Stolper, D.A. and Keller, C.B., 2018. A record of deep-ocean dissolved O_2 from the oxidation state of iron in submarine basalts. *Nature*, *553*(7688), pp.323-327.

Stüeken, E.E., Kipp, M.A., Koehler, M.C. and Buick, R., 2016. The evolution of Earth's biogeochemical nitrogen cycle. *Earth-Science Reviews*, *160*, pp.220-239.

Stüeken, E.E., de Castro, M., Krotz, L., Brodie, C., Iammarino, M. and Giazzi, G., 2020. Optimized switch-over between CHNS abundance and CNS isotope ratio analyses by elemental analyzer-isotope ratio mass spectrometry: Application to six geological reference materials. *Rapid Communications in Mass Spectrometry*, *34*(18), p.e8821.

Stüeken, E.E., Kuznetsov, A.B., Vasilyeva, I.M., Krupenin, M.T. and Bekker, A., 2021. Transient deep-water oxygenation recorded by rare Mesoproterozoic phosphorites, South Urals. *Precambrian Research*, *360*, p.106242.

Stüeken, E.E., Pellerin, A., Thomazo, C., Johnson, B.W., Duncanson, S. and Schoepfer, S.D., 2024. Marine biogeochemical nitrogen cycling through Earth's history. *Nature Reviews Earth & Environment*, pp.1-16.

Stüeken, E.E., 2013. A test of the nitrogen-limitation hypothesis for retarded eukaryote radiation: Nitrogen isotopes across a Mesoproterozoic basinal profile. *Geochimica et Cosmochimica Acta*, *120*, pp.121-139.

Sweere, T., van den Boorn, S., Dickson, A.J. and Reichart, G.J., 2016. Definition of new trace-metal proxies for the controls on organic matter enrichment in marine sediments based on Mn, Co, Mo and Cd concentrations. *Chemical Geology*, *441*, pp.235-245.

Tan, Z., Jia, W., Li, J., Yin, L., Wang, S., Wu, J. and Song, J., 2021. Geochemistry and molybdenum isotopes of the basal Datangpo Formation: Implications for ocean-redox conditions and organic matter accumulation during the Cryogenian interglaciation. *Palaeogeography, Palaeoclimatology, Palaeoecology*, *563*, p.110169.

Tanaka, E., Yasukawa, K., Ohta, J. and Kato, Y., 2022. Enhanced continental chemical weathering during the multiple early Eocene hyperthermals: New constraints from the southern Indian Ocean. *Geochimica et Cosmochimica Acta*, 331, pp.192-211.

Taylor, S.R. and McLennan, S.M., 1985. The continental crust: its composition and evolution. Blackwell Scientific Publications.

Tesdal, J.E., Galbraith, E.D. and Kienast, M., 2013. Nitrogen isotopes in bulk marine sediment: linking seafloor observations with subseafloor records. *Biogeosciences*, *10*(1), pp.101-118.

Thomazo, C. and Papineau, D., 2013. Biogeochemical cycling of nitrogen on the early Earth. *Elements*, *9*(5), pp.345-351.

Thompson, J., Poulton, S.W., Guilbaud, R., Doyle, K.A., Reid, S. and Krom, M.D., 2019. Development of a modified SEDEX phosphorus speciation method for ancient rocks and modern iron-rich sediments. *Chemical Geology*, *524*, pp.383-393.

Thunell, R.C., Sigman, D.M., Muller-Karger, F., Astor, Y. and Varela, R., 2004. Nitrogen isotope dynamics of the Cariaco Basin, Venezuela. *Global Biogeochemical Cycles*, *18*(3).

Timothy, D.A. and Calvert, S.E., 1998. Systematics of variations in excess Al and Al/Ti in sediments from the central equatorial Pacific. *Paleoceanography*, *13*(2), pp.127-130.

Tissot, F.L. and Dauphas, N., 2015. Uranium isotopic compositions of the crust and ocean: Age corrections, U budget and global extent of modern anoxia. *Geochimica et Cosmochimica Acta*, 167, pp.113-143.

Tostevin, R., Turchyn, A.V., Farquhar, J., Johnston, D.T., Eldridge, D.L., Bishop, J.K. and McIlvin, M., 2014. Multiple sulfur isotope constraints on the modern sulfur cycle. *Earth and Planetary Science Letters*, *396*, pp.14-21.

Tostevin, R., Wood, R.A., Shields, G.A., Poulton, S.W., Guilbaud, R., Bowyer, F., Penny, A.M., He, T., Curtis, A., Hoffmann, K.H. and Clarkson, M.O., 2016. Low-oxygen waters limited habitable space for early animals. *Nature Communications*, *7*(1), p.12818.

Tribovillard, N., Riboulleau, A., Lyons, T. and Baudin, F., 2004. Enhanced trapping of molybdenum by sulfurized marine organic matter of marine origin in Mesozoic limestones and shales. *Chemical Geology*, *213*(4), pp.385-401.

Tribovillard, N., Algeo, T.J., Lyons, T. and Riboulleau, A., 2006. Trace metals as paleoredox and paleoproductivity proxies: an update. *Chemical geology*, *232*(1-2), pp.12-32.

Tribovillard, N., Algeo, T.J., Baudin, F. and Riboulleau, A.J.C.G., 2012. Analysis of marine environmental conditions based onmolybdenum–uranium covariation—Applications to Mesozoic paleoceanography. *Chemical Geology*, *324*, pp.46-58.

Tripathy, V. and Saha, D., 2010. Structure and low grade metamorphism of the east central part of the Proterozoic Nallamalai fold belt, South India-thrust stacking and discontinuous

metamorphic gradients along eastern margin of east Dharwar Craton. *Indian Journal of Geology*, *80*(1-4), pp.173-188.

Tripathy, G.R. and Singh, S.K., 2010. Chemical erosion rates of river basins of the Ganga system in the Himalaya: Reanalysis based on inversion of dissolved major ions, Sr, and $^{87}Sr/^{86}Sr$. *Geochemistry, Geophysics, Geosystems*, *11*(3).

Tripathy, G.R. and Singh, S.K., 2015. Re–Os depositional age for black shales from the Kaimur Group, Upper Vindhyan, India. *Chemical Geology*, *413*, pp.63-72.

Tripathy, G.R., Singh, S.K. and Ramaswamy, V., 2014. Major and trace element geochemistry of Bay of Bengal sediments: Implications to provenances and their controlling factors. *Palaeogeography, Palaeoclimatology, Palaeoecology*, *397*, pp.20-30.

Tripathy, G.R., Hannah, J.L. and Stein, H.J., 2018. Refining the Jurassic-Cretaceous boundary: Re−Os geochronology and depositional environment of Upper Jurassic shales from the Norwegian Sea. *Palaeogeography, Palaeoclimatology, Palaeoecology*, *503*, pp.13-25.

Turner, C.C., Meert, J.G., Pandit, M.K. and Kamenov, G.D., 2014. A detrital zircon U–Pb and Hf isotopic transect across the Son Valley sector of the Vindhyan Basin, India: implications for basin evolution and paleogeography. *Gondwana Research*, *26*(1), pp.348-364.

Uveges, B.T., Izon, G., Ono, S., Beukes, N.J. and Summons, R.E., 2023. Reconciling discrepant minor sulfur isotope records of the Great Oxidation Event. *Nature Communications*, *14*(1), p.279.

Vadlamani, R., Hashmi, S., Chatterjee, C., Ji, W.Q. and Wu, F.Y., 2014. Initiation of the intra-cratonic Cuddapah basin: evidence from Paleoproterozoic (1995 Ma) anorogenic porphyritic granite in Eastern Dharwar Craton basement. *Journal of Asian Earth Sciences*, *79*, pp.235-245.

Valdiya, K.S., 1969. Stromatolites of the Lesser Himalayan carbonate formations and the Vindhyans. *Journal Geological Society of India*, *10*(1), pp.1-25.

Valdiya, K.S., 1980. Geology of Kumaun Lesser Himalaya. Wadia Institute of Himalayan Geology, Dehradun (UK), India, pp. 291.

Valdiya, K.S., 2015. *The making of India: geodynamic evolution*. Springer.

Venkatakrishnan, R. and Dotiwalla, F.E., 1987. The Cuddapah salient: a tectonic model for the Cuddapah basin, India, based on Landsat image interpretation. *Tectonophysics*, *136*(3-4), pp.237-253.

Venugopal, A., Tripathy, G.R., Goswami, V., Ghosh, S.K. and Singh, D., 2023. Oceanic Redox State During the Early Cambrian: Insights From Mo-S Isotopes and Geochemistry of Himalayan Shales. *Geochemistry, Geophysics, Geosystems*, *24*(12), p.e2023GC011182.

Vermeesch, P., 2018. IsoplotR: A free and open toolbox for geochronology. *Geoscience Frontiers*, *9*(5), pp.1479-1493.

Virdi, N.S., 1995. Proterozoic sedimentological cycles and the geotectonic evolution of the southern margin of the proto-tethys: evidence from the western Himalaya. *Indian Journal of Petroleum Geology*, *4*, pp.45-73.

Vo, J., Inwood, W., Hayes, J.M. and Kustu, S., 2013. Mechanism for nitrogen isotope fractionation during ammonium assimilation by Escherichia coli K12. *Proceedings of the National Academy of Sciences*, *110*(21), pp.8696-8701.

Völkening, J., Walczyk, T. and Heumann, K.G., 1991. Osmium isotope ratio determinations by negative thermal ionization mass spectrometry. *International Journal of Mass Spectrometry and Ion Processes*, *105*(2), pp.147-159.

Wabo, H., Beukes, N.J., Patranabis-Deb, S., Saha, D., Belyanin, G. and Kramers, J., 2022. Paleomagnetic and $^{40}Ar/^{39}Ar$ age constraints on the timing of deposition of deep-water carbonates of the Kurnool Group (Cuddapah basin) and correlation across Proterozoic Purana successions of Southern India. *Journal of Asian Earth Sciences*, *223*, p.104984.

Wang, J., Chen, D., Yan, D., Wei, H. and Xiang, L., 2012. Evolution from an anoxic to oxic deep ocean during the Ediacaran–Cambrian transition and implications for bioradiation. *Chemical Geology*, *306*, pp.129-138.

Wang, D., Ling, H.F., Struck, U., Zhu, X.K., Zhu, M., He, T., Yang, B., Gamper, A. and Shields, G.A., 2018. Coupling of ocean redox and animal evolution during the Ediacaran-Cambrian transition. *Nature Communications*, *9*(1), pp.1-8.

Wang, W.L., Moore, J.K., Martiny, A.C. and Primeau, F.W., 2019. Convergent estimates of marine nitrogen fixation. *Nature*, *566*(7743), pp.205-211.

Wang, H., Zhang, Z., Li, C., Algeo, T.J., Cheng, M. and Wang, W., 2020. Spatiotemporal redox heterogeneity and transient marine shelf oxygenation in the Mesoproterozoic ocean. *Geochimica et Cosmochimica Acta*, *270*, pp.201-217.

Wang, X., Zhang, S., Ye, Y., Ma, S., Su, J., Wang, H. and Canfield, D.E., 2023. Nitrogen cycling during the Mesoproterozoic as informed by the 1400 million year old Xiamaling Formation. *Earth-Science Reviews*, p.104499.

Wang, C., Lechte, M.A., Reinhard, C.T., Asael, D., Cole, D.B., Halverson, G.P., Porter, S.M., Galili, N., Halevy, I., Rainbird, R.H. and Lyons, T.W., 2022. Strong evidence for a weakly oxygenated ocean–atmosphere system during the Proterozoic. *Proceedings of the National Academy of Sciences*, *119*(6), p.e2116101119.

Wei, G.Y., Planavsky, N.J., He, T., Zhang, F., Stockey, R.G., Cole, D.B., Lin, Y.B. and Ling, H.F., 2021. Global marine redox evolution from the late Neoproterozoic to the early Paleozoic constrained by the integration of Mo and U isotope records. *Earth-Science Reviews*, *214*, p.103506.

Wen, H., Carignan, J., Zhang, Y., Fan, H., Cloquet, C. and Liu, S., 2011. Molybdenum isotopic records across the Precambrian-Cambrian boundary. *Geology*, *39*(8), pp.775-778.

Wen, H., Carignan, J., Chu, X., Fan, H., Cloquet, C., Huang, J., Zhang, Y. and Chang, H., 2014. Selenium isotopes trace anoxic and ferruginous seawater conditions in the Early Cambrian. *Chemical Geology*, *390*, pp.164-172.

Wen, H., Fan, H., Zhang, Y., Cloquet, C. and Carignan, J., 2015. Reconstruction of early Cambrian ocean chemistry from Mo isotopes. *Geochimica et Cosmochimica Acta*, *164*, pp.1-16.

Wille, M., Nägler, T.F., Lehmann, B., Schröder, S. and Kramers, J.D., 2008. Hydrogen sulphide release to surface waters at the Precambrian/Cambrian boundary. *Nature*, *453*(7196), pp.767-769.

Wotte, T., Strauss, H., Fugmann, A. and Garbe-Schönberg, D., 2012. Paired $\delta^{34}S$ data from carbonate-associated sulfate and chromium-reducible sulfur across the traditional Lower–Middle Cambrian boundary of W-Gondwana. *Geochimica et Cosmochimica Acta*, *85*, pp.228-253.

Wu, N., Farquhar, J. and Fike, D.A., 2015. Ediacaran sulfur cycle: Insights from sulfur isotope measurements ($\Delta^{33}S$ and $\delta^{34}S$) on paired sulfate–pyrite in the Huqf Supergroup of Oman. *Geochimica et Cosmochimica Acta*, *164*, pp.352-364.

Xu, L., Lehmann, B., Mao, J., Nägler, T.F., Neubert, N., Böttcher, M.E. and Escher, P., 2012. Mo isotope and trace element patterns of Lower Cambrian black shales in South China: Multi-proxy constraints on the paleoenvironment. *Chemical Geology*, *318*, pp.45-59.

Xu, D., Qin, Z., Wang, X., Li, J., Shi, X., Tang, D. and Liu, J., 2023. Extensive sea-floor oxygenation during the early Mesoproterozoic. *Geochimica et Cosmochimica Acta*, *354*, pp.186-196.

Xu, L., Lechte, M., Shi, X., Zheng, W., Zhou, L., Huang, K., Zhou, X. and Tang, D., 2024. Large Igneous Province Emplacement Triggered an Oxygenation Event at ∼1.4 Ga: Evidence From Mercury and Paleo-Productivity Proxies. *Geophysical Research Letters*, *51*(2), p.e2023GL106654.

Yang, G., Hannah, J.L., Zimmerman, A., Stein, H.J. and Bekker, A., 2009. Re–Os depositional age for Archean carbonaceous slates from the southwestern Superior Province: challenges and insights. *Earth and Planetary Science Letters*, *280*(1-4), pp.83-92.

Yang, S., Lu, X., Chen, X., Zheng, W., Owens, J.D., Young, S.A. and Kendall, B., 2023. Uranium and molybdenum isotope evidence for globally extensive marine euxinia on continental margins and in epicontinental seas during the Devonian-Carboniferous Hangenberg Crisis. *Geochimica et Cosmochimica Acta*, *352*, pp.133-156.

Yang, H., Shi, X., Xu, L., Sun, L., Xie, B., Zhou, L., Huang, K., Zhou, X. and Tang, D., 2024. 1.44 Ga Oxygenation Event: Evidence From the Southern Margin of North China. *Journal of Geophysical Research: Biogeosciences*, *129*(4), p.e2023JG007787.

Ye, Y., Wang, H., Wang, X., Zhai, L., Wu, C., Canfield, D.E. and Zhang, S., 2020. Tracking the evolution of seawater Mo isotopes through the Ediacaran–Cambrian transition. *Precambrian Research*, *350*, p.105929.

Ye, Y., Zhang, S., Wang, H., Wang, X., Tan, C., Li, M., Wu, C. and Canfield, D.E., 2021. Black shale Mo isotope record reveals dynamic ocean redox during the Mesoproterozoic Era. *Geochemical Perspectives Letters*, *18*, pp.16-21.

Yin, L., Li, J., Tian, H. and Long, X., 2018. Rhenium–osmium and molybdenum isotope systematics of black shales from the Lower Cambrian Niutitang Formation, SW China: Evidence of a well oxygenated ocean at ca. 520 Ma. *Chemical Geology*, *499*, pp.26-42.

Zachariah, J.K., Rao, Y.B., Srinivasan, R. and Gopalan, K., 1999. Pb, Sr and Nd isotope systematics of uranium mineralised stromatolitic dolomites from the Proterozoic Cuddapah Supergroup, south India: constraints on age and provenance. *Chemical Geology*, *162*(1), pp.49-64.

Zerkle, A.L., Junium, C.K., Canfield, D.E. and House, C.H., 2008. Production of ^{15}N-depleted biomass during cyanobacterial N_2-fixation at high Fe concentrations. *Journal of Geophysical Research: Biogeosciences*, *113*(G3).

Zerkle, A.L., Poulton, S.W., Newton, R.J., Mettam, C., Claire, M.W., Bekker, A. and Junium, C.K., 2017. Onset of the aerobic nitrogen cycle during the Great Oxidation Event. *Nature*, *542*(7642), pp.465-467.

Zhang, X., Sigman, D.M., Morel, F.M. and Kraepiel, A.M., 2014. Nitrogen isotope fractionation by alternative nitrogenases and past ocean anoxia. *Proceedings of the National Academy of Sciences*, *111*(13), pp.4782-4787.

Zhang, K., Zhu, X., Wood, R.A., Shi, Y., Gao, Z. and Poulton, S.W., 2018. Oxygenation of the Mesoproterozoic ocean and the evolution of complex eukaryotes. *Nature Geoscience*, *11*(5), pp.345-350.

Zheng, Y., Anderson, R.F., Van Geen, A. and Fleisheir, M.Q., 2002. Preservation of non-lithogenic particulate uranium in marine sediments. *Geochimica et Cosmochimica Acta*, *66*(17), pp.3085-3092.

Zhu, M.Y., Babcock, L.E. and Peng, S.C., 2006. Advances in Cambrian stratigraphy and paleontology: integrating correlation techniques, paleobiology, taphonomy and paleoenvironmental reconstruction. *Palaeoworld*, *15*(3-4), pp.217-222.

Zhu, B., Becker, H., Jiang, S.Y., Pi, D.H., Fischer-Gödde, M. and Yang, J.H., 2013. Re–Os geochronology of black shales from the Neoproterozoic Doushantuo Formation, Yangtze platform, south China. *Precambrian Research*, *225*, pp.67-76.

Zhu, G., Li, T., Huang, T., Zhao, K., Tang, W., Wang, R., Lang, X. and Shen, B., 2021. Quantifying the seawater sulfate concentration in the Cambrian ocean. *Frontiers in Earth Science*, *9*, p.767857.

Appendix

Table A3.1. Additional geochemical data for the Cumbum shales

Sample ID	Na	K	Ca	Mg	Si	Ti	Fe_{carb}	Fe_{ox}	Fe_{mag}	Fe_{Py}	V	Cr	Ni	Cu	Zn	Ba
	wt%										µg/g					
CDP21-17	0.38	3.53	0.69	1.31	31.38	0.32	0.39	0.06	0.03	0.82	191	74	41	24	49	406
CDP21-18	0.04	4.57	0.13	1.41	29.33	0.36	0.12	0.04	0.01	0.64	235	100	39	48	56	160
CDP21-19	0.38	3.97	0.16	1.13	31.63	0.36	0.17	0.02	0.02	0.72	191	85	42	35	73	523
CDP21-20	0.38	4.00	0.19	1.17	31.61	0.36	0.18	0.02	0.02	0.68	190	88	42	32	53	752
CDP21-21	0.38	3.97	b.d.l	1.05	31.97	0.35	0.10	0.02	0.02	0.99	179	104	40	36	78	1319
CDP21-22	0.37	3.96	b.d.l	1.06	31.93	0.35	0.11	0.02	0.02	0.65	180	103	40	35	68	1319
CDP21-23	0.45	3.89	b.d.l	1.00	31.84	0.34	0.09	0.02	0.02	0.84	184	95	46	41	63	1074
CDP21-24	0.45	3.85	b.d.l	1.03	31.63	0.34	0.09	0.02	0.02	1.38	180	90	46	41	58	696
CDP21-35	0.84	3.06	1.20	1.69	29.65	0.33	0.48	0.05	0.03	0.55	185	81	41	28	61	605
CDP21-36	0.78	3.08	1.42	1.83	28.64	0.33	0.84	0.04	0.02	0.61	187	81	42	25	73	574
CDP21-37	0.74	3.34	1.27	1.73	29.03	0.34	0.76	0.03	0.02	0.65	232	93	41	28	121	1060
CDP21-38	0.06	3.97	1.13	1.64	28.02	0.30	0.37	0.03	0.00	2.06	166	83	49	21	42	1507
CDP21-39	0.06	4.07	0.91	1.51	28.12	0.30	0.31	0.02	0.00	2.11	173	94	52	23	42	3481
CDP21-127	0.31	3.17	2.16	1.96	27.69	0.28	0.38	0.02	0.01	1.30	190	87	42	24	54	2689
CDP21-128	0.34	3.47	0.98	1.41	29.56	0.30	0.23	0.02	0.01	1.71	214	91	48	34	67	2332
CDP21-129	0.34	3.59	1.74	1.87	27.62	0.31	0.34	0.02	0.00	1.63	179	95	40	26	40	2943
CDP21-130	0.45	3.91	0.54	1.25	29.62	0.33	0.23	0.02	0.01	1.08	191	102	41	41	72	2382
CDP21-131	0.22	2.39	4.91	3.24	24.71	0.24	0.69	0.02	0.01	1.67	106	64	42	33	50	1279
CDP21-132	0.26	3.34	2.52	2.20	27.20	0.30	0.43	0.02	0.00	1.17	176	85	38	24	53	2586
CDP21-133	0.34	3.52	1.22	1.55	29.27	0.31	0.28	0.01	0.00	1.26	167	89	42	25	55	1681
CDP21-134	0.22	2.71	4.22	2.92	25.87	0.26	0.78	0.03	0.01	1.16	119	64	37	16	35	3690
CDP21-135	0.16	4.42	0.29	1.26	29.82	0.33	0.16	0.02	0.00	0.98	186	100	39	26	43	3083
CDP21-136	0.22	3.56	1.00	1.38	30.51	0.32	0.28	0.02	0.01	1.10	134	80	34	23	42	3383
CDP21-137	0.19	3.95	1.18	1.54	29.39	0.32	0.34	0.02	0.01	0.92	208	91	36	23	39	3777
CDP21-138	0.21	3.40	1.43	1.68	29.44	0.32	0.48	0.03	0.02	0.68	196	83	46	26	74	3121
CDP21-139	0.24	3.62	2.11	2.06	28.02	0.33	0.66	0.03	0.02	0.87	154	86	45	26	123	3026
CDP21-140	0.32	4.42	b.d.	1.09	29.89	0.33	0.10	0.02	0.02	0.67	205	105	47	45	71	1428
CDP21-141	0.31	3.79	0.67	1.35	30.13	0.34	0.33	0.03	0.02	0.54	228	91	44	28	56	1208
CDP21-142	0.47	3.69	1.31	1.67	29.23	0.35	0.45	0.03	0.02	0.61	204	94	48	39	138	856

Table A3.2. Input parameters used for the Mo isotopic modelling

Parameter	Unit	Value	References
Area of modern seafloor	m^2	3.6×10^{14}	(1)
Mass of seawater	kg	1.41×10^{21}	(2)
Concentration of Mo in modern seawater ($[Mo]_{sw}$)	nmol kg^{-1}	105	(3)
Isotopic composition of Mo in modern seawater ($\delta^{98}Mo_{SW}$)	‰	+2.34	(4)

Parameter	Unit	Min Value	Max Value	References
Riverine flux (F_{riv})	mol yr^{-1}	18.8×10^7	30.0×10^7	(1), (5)
Riverine isotopic composition ($\delta^{98}Mo_{riv}$)	‰	+0.2	+0.8	(6)
Accumulation rate in euxinic settings (b_{eux})	mol m^{-2} yr^{-1}	5×10^{-5}	1.25×10^{-4}	(1), (5)
Accumulation rate in broadly reducing settings (b_{interm})	mol m^{-2} yr^{-1}	2.61×10^{-5}	2.81×10^{-5}	(1), (5)
Accumulation rate in oxic settings (b_{oxic})	mol m^{-2} yr^{-1}	2.08×10^{-7}	2.87×10^{-7}	(1), (5)
Fractionation factor in euxinic settings ($\Delta^{98}Mo_{eux}$)	‰	−0.8	0	(6)
Fractionation factor in broadly reducing settings ($\Delta^{98}Mo_{interm}$)	‰	−1.0	−0.9	*This study*
Fractionation factor in oxic settings ($\Delta^{98}Mo_{oxic}$)	‰	−3.0	−2.8	(7), (8)
Local fractionation factors in euxinic settings ($\Delta^{98}Mo_{eux.loc}$)	‰	−0.8	0	(6)
Local accumulation rates factors in euxinic settings ($b_{eux.loc}$)	mol m^{-2} yr^{-1}	5×10^{-5}	1.25×10^{-4}	(1), (5)

References

(1) Reinhard et al., 2013 (2) Stockey et al., 2020 (3) Morford and Emerson, 1999 (4) Nägler et al., 2014 (5) Scott et al., 2008 (6) Dahl et al., 2021 (7) Kendall et al., 2017 (8) Dahl et al., 2017

Table A3.3. Summary of the δ^{98}Mo compilation data for shales deposited in euxinic settings.

Age	δ^{98}Mo ‰				Counts*	Reference
Ma	Mean	Median	Min	Max		
500	+0.95	+0.96	+0.92	+0.98	3	(1)
519	+1.34	+1.07	+1.02	+1.94	3	(1), (2)
520	+0.72	+0.70	−0.68	+2.19	14	(1), (2), (3)
521	+0.81	+0.81	−0.89	+1.97	45	(2), (3), (4), (5)
526	+1.16	+1.15	+0.86	+1.49	4	(6)
529	+1.42	+1.66	+0.11	+1.76	8	(7)
532	+0.99	+0.96	+0.17	+1.86	4	(4)
551	+0.51	+0.39	−0.02	+1.32	8	(2), (8)
560	+0.08	+0.44	−1.98	+2.24	54	(8)
576	+0.43	+0.14	−0.34	+1.66	13	(9)
591	+0.02	+0.01	−1.12	+1.40	15	(9)
633	−0.44	−0.50	−1.49	+0.54	13	(5), (8)
641	+0.80	+0.81	+0.39	+1.15	8	(9)
659	+0.68	+0.63	+0.10	+1.48	19	(10)
660	−0.35	−0.20	−1.60	+0.70	6	(11)
742	+0.97	+0.97	+0.81	+1.13	2	(1)
1210	+0.86	+0.86	+0.54	+1.18	2	(12)
1332	+0.35	+0.49	−0.11	+0.66	3	(13)
1361	+0.94	+0.94	+0.85	+1.04	6	(14)
1392	+0.57	+0.40	+0.07	+1.74	25	(15)
1658	***+0.65***	***+0.66***	***+0.52***	***+0.85***	***16***	***This study***
1730	+0.68	+0.73	+0.29	+0.99	4	(14)
1836	+0.78	+0.93	+0.20	+1.29	28	(16)
1930	+0.62	+0.60	+0.55	+0.70	13	(17)
1980	+0.68	+0.62	+0.51	+1.27	13	(18)
2060	+0.71	+0.72	+0.32	+1.11	19	(19)
2083	+0.68	+0.56	+0.41	+1.24	4	(20)
2150	+1.23	+1.19	+0.70	+1.70	11	(19)
2320	+0.31	+0.17	−0.34	+1.25	6	(19)
2480	+1.15	+1.11	+0.79	+1.54	17	(21)
2500	+1.36	+1.35	+0.99	+1.80	14	(22)

**Only euxinic shales are considered*

References

(1) Dahl et al., 2010 (2) Chen et al., 2015 (3) Qin et al., 2022 (4) Wen et al., 2015 (5) Ye et al., 2020 (6) Cheng et al., 2016 (7) Cheng et al., 2017 (8) Ostrander et al., 2019 (9) Kendall et al., 2015 (10) Pan et al., 2021 (11) Scheller et al., 2018 (12) Gilleaudeau et al., 2020 (13) Ye et al., 2021 (14) Kendall et al., 2009 (15) Diamond et al., 2018 (16) Kendall et al., 2011 (17) Partin et al., 2015 (18) Asael et al., 2013 (19) Asael et al., 2018 (20) Canfield et al., 2013 (21) Ostrander et al., 2021 (22) Duan et al., 2010

Table A3.4. Estimated areal extent of ocean redox state for the Proterozoic Eon. These model results are based on present and literature-available δ^{98}Mo data for shales deposited in euxinic settings.

Age	A_{oxic}				A_{interm}				A_{eux}				Modelled A_{eux} / Modern A_{eux}[#]
Ma	Mean	Median	32nd Quantile	68th Quantile	Mean	Median	32nd Quantile	68th Quantile	Mean	Median	32nd Quantile	68th Quantile	
500	37.2%	34.9%	17.5%	53.1%	45.2%	43.4%	27.2%	60.7%	10.3%	1.6%	0.6%	5.0%	5.3
519	41.0%	40.4%	21.6%	58.9%	45.7%	44.0%	27.2%	62.4%	5.8%	0.6%	0.3%	1.6%	2.1
520	34.8%	31.5%	15.0%	49.7%	42.3%	39.4%	23.4%	57.7%	15.7%	3.2%	0.8%	12.6%	10.5
521	34.8%	31.5%	15.0%	49.7%	42.3%	39.5%	23.4%	57.8%	15.7%	3.2%	0.8%	12.6%	10.5
526	38.5%	37.0%	19.2%	55.0%	46.0%	44.6%	28.0%	62.2%	8.0%	1.0%	0.4%	2.5%	3.3
529	35.0%	31.8%	15.3%	50.1%	43.0%	40.6%	24.4%	58.6%	14.7%	2.5%	0.8%	10.0%	8.4
532	35.2%	32.0%	15.4%	50.3%	43.2%	40.7%	24.6%	58.8%	14.3%	2.5%	0.8%	10.0%	8.4
551	33.9%	30.2%	14.3%	48.2%	42.4%	39.8%	23.9%	57.8%	16.5%	4.0%	1.3%	12.6%	13.3
560	34.8%	31.5%	15.0%	49.7%	42.2%	39.4%	23.4%	57.7%	15.7%	3.2%	0.8%	12.6%	10.5
576	34.6%	31.2%	14.8%	49.3%	42.4%	39.7%	23.7%	57.9%	15.7%	3.2%	1.0%	12.6%	10.5
591	34.0%	30.4%	14.4%	48.5%	42.2%	39.5%	23.5%	57.5%	16.6%	4.0%	1.0%	12.6%	13.3
633	28.4%	23.6%	8.9%	40.3%	34.8%	29.9%	15.9%	47.2%	29.8%	15.8%	7.9%	39.8%	52.8
641	33.8%	30.1%	14.3%	48.0%	43.7%	41.9%	25.7%	59.2%	15.2%	3.2%	1.0%	12.6%	10.5
659	34.6%	31.2%	14.9%	49.2%	42.9%	40.5%	24.4%	58.4%	15.2%	3.2%	1.0%	10.0%	10.5
660	29.5%	25.0%	10.1%	41.9%	37.4%	33.3%	18.2%	51.0%	26.1%	12.6%	5.0%	31.6%	42.0
742	36.2%	33.3%	17.0%	51.4%	45.9%	44.9%	28.4%	61.8%	10.6%	1.6%	0.5%	5.0%	5.3
1210	34.9%	31.7%	15.5%	49.5%	44.4%	42.8%	26.4%	60.1%	13.4%	2.5%	0.8%	7.9%	8.4
1332	29.3%	24.7%	10.1%	41.4%	37.3%	33.1%	18.1%	50.9%	26.4%	12.6%	6.3%	31.6%	42.0
1361	35.9%	32.8%	16.3%	51.0%	45.8%	44.8%	28.0%	61.5%	10.9%	1.6%	0.6%	5.0%	5.3
1392	34.9%	31.7%	15.2%	49.9%	42.9%	40.4%	24.3%	58.4%	14.8%	2.5%	0.8%	10.0%	8.4

[#]*Calculated using modern euxinic seafloor areal extent of 0.3%*

Table A3.4 *(continued)*

Age	A_{oxic}				A_{interm}				A_{eux}				Modelled A_{eux} / Modern A_{eux}[#]
Ma	Mean	Median	32nd Quantile	68th Quantile	Mean	Median	32nd Quantile	68th Quantile	Mean	Median	32nd Quantile	68th Quantile	
1658	**32.3%**	**28.0%**	**12.6%**	**45.9%**	**42.9%**	**40.7%**	**24.6%**	**58.4%**	**17.7%**	**5.0%**	**1.6%**	**15.8%**	**16.7**
1730	32.4%	28.3%	13.0%	46.1%	42.4%	39.9%	24.0%	57.7%	18.0%	5.0%	1.6%	15.8%	16.7
1836	34.1%	30.6%	14.6%	48.5%	43.0%	40.7%	24.7%	58.5%	15.6%	3.2%	1.0%	12.6%	10.5
1930	31.6%	27.5%	12.0%	44.4%	42.0%	39.9%	23.8%	57.0%	19.3%	6.3%	2.5%	20.0%	21.0
1980	35.1%	31.9%	15.6%	50.0%	44.5%	42.8%	26.4%	60.2%	13.1%	2.0%	0.8%	7.9%	6.7
2060	33.3%	29.6%	13.8%	47.3%	43.2%	41.0%	25.0%	58.6%	16.3%	4.0%	1.3%	12.6%	13.3
2083	31.4%	27.2%	11.6%	44.9%	41.6%	38.8%	23.4%	56.5%	19.8%	6.3%	2.5%	20.0%	21.0
2150	37.7%	35.4%	18.1%	54.1%	45.4%	43.9%	27.2%	61.6%	9.4%	1.3%	0.4%	3.2%	4.2
2320	33.4%	29.8%	13.9%	47.7%	41.8%	39.1%	23.1%	57.0%	17.5%	5.0%	1.3%	15.8%	16.7
2480	38.0%	36.0%	18.6%	54.3%	45.9%	44.6%	27.9%	62.2%	8.7%	1.0%	0.4%	3.2%	3.3
2500	40.5%	39.9%	21.2%	58.1%	45.8%	44.4%	27.4%	62.3%	6.1%	0.6%	0.3%	1.6%	2.1

[#]*Calculated using modern euxinic seafloor areal extent of 0.3%*

Table A4.1. Additional geochemical data for black shale samples from the (lower) Tal Formation and Neoproterozoic shale sequence (Chandpur Formation) from Lesser Himalaya.

Sample ID[#]	Na	Mg	Si	K	Ca	Ti	Sr	Ba	Sc	Th
	wt%						µg/g			
Tal Formation, Lesser Himalaya (Shale sequence overlying the Pc-C boundary)										
HM15-10A	0.91	2.04	26.88	2.85	2.43	0.41	90	479	11.0	13.0
HM15-10B	0.94	2.04	26.99	2.82	2.35	0.41	89	457	11.2	13.5
HM15-11A	0.94	2.04	27.24	2.84	2.31	0.41	85	419	10.6	13.5
HM15-11B	0.92	2.01	27.19	2.80	2.27	0.41	83	392	11.1	12.7
HM15-12A	0.94	2.03	27.04	2.86	2.34	0.41	91	524	11.6	13.6
HM15-12B	0.97	2.03	27.01	2.81	2.34	0.41	83	422	10.8	13.8
HM15-13A	0.95	2.02	27.17	2.85	2.06	0.41	69	481	11.4	13.8
HM15-13B	0.98	2.03	27.12	2.84	2.01	0.41	65	467	11.5	12.7
HM15-14A	0.94	2.06	26.52	2.83	2.30	0.41	81	539	12.1	13.6
HM15-14B	0.94	2.06	26.72	2.86	2.35	0.41	82	393	11.3	11.7
HM15-15A	0.92	1.97	27.12	2.78	2.47	0.41	67	761	12.8	14.5
HM15-15B	0.92	1.98	27.27	2.79	2.43	0.41	95	668	12.4	14.1
HM15-16A	0.90	1.99	26.95	2.76	2.24	0.40	80	497	11.5	13.8
HM15-16B	0.94	2.00	27.03	2.80	2.29	0.41	83	516	11.4	12.6
HM15-17A	0.92	2.00	26.96	2.75	2.46	0.40	85	512	11.2	13.0
HM15-17B	0.92	2.01	27.13	2.83	2.38	0.41	81	462	11.6	12.6
HM15-18A	0.92	2.08	27.89	2.87	2.50	0.42	90	608	12.4	13.6
HM15-18B	0.93	2.01	26.83	2.82	2.45	0.40	88	586	12.0	14.0
HM15-20A	0.88	2.10	26.89	2.77	2.65	0.40	91	651	11.9	13.5
HM15-20B	0.94	2.08	28.12	2.90	2.59	0.42	82	389	11.2	12.8
HM15-21A	1.03	1.97	27.11	2.67	2.39	0.40	85	424	10.8	11.4
HM15-21B	1.00	2.00	27.04	2.67	2.41	0.40	86	447	10.7	12.6
Chandpur Formation, Lesser Himalaya										
HM15-01A	0.47	1.33	24.52	5.84	0.24	0.67	6	80	2.6	5.5
HM15-01B	0.46	1.34	24.48	5.76	0.23	0.67	8	43	2.8	6.5
HM15-01C	0.46	1.31	24.31	5.80	0.21	0.68	16	138	6.9	9.5
HM15-02A	0.44	1.19	29.68	3.93	0.10	0.47	11	60	3.2	5.3
HM15-02B	0.40	1.31	25.08	5.54	0.22	0.64	9	54	3.5	6.5
HM15-02C	0.41	1.36	23.95	6.01	0.20	0.69	5	51	2.9	6.5
HM15-03A	0.58	1.24	29.33	3.57	0.12	0.45	15	120	6.0	7.5
HM15-03B	0.57	1.26	29.49	3.62	0.12	0.46	37	337	13.9	13.6
HM15-03C	0.54	1.28	29.01	3.70	0.10	0.45	28	242	10.1	10.6

[#]A, B, and C stand for different powdering aliquots of the shale sample.

Table A4.2. REE concentration data for black shale samples from the (lower) Tal Formation and the Neoproterozoic shale sequence (Chandpur Formation) from Lesser Himalaya.

Sample ID[#]	La	Ce	Pr	Nd	Sm	Eu	Gd	Tb	Dy	Ho	Er	Tm	Yb	Lu	Y	Ce/Ce*
	µg/g															
Tal Formation, Lesser Himalaya (Shale sequence overlying the Pc-C boundary)																
HM15-10A	36.2	72.2	8.5	30.4	5.7	1.1	5.0	0.8	4.5	0.9	2.6	0.4	2.4	0.4	26.2	0.99
HM15-10B	37.2	74.3	8.7	32.4	5.9	1.1	4.7	0.8	4.5	0.9	2.6	0.4	2.5	0.4	25.9	1.00
HM15-11A	35.7	73.0	8.2	30.7	5.5	1.0	4.8	0.8	4.1	0.9	2.5	0.4	2.3	0.4	25.7	1.03
HM15-11B	35.9	72.5	8.6	30.6	5.6	1.0	5.0	0.7	4.3	0.9	2.6	0.4	2.4	0.4	24.9	1.00
HM15-12A	37.7	72.5	8.5	30.7	5.7	1.1	4.9	0.7	4.3	0.9	2.7	0.4	2.4	0.4	25.2	0.98
HM15-12B	32.4	65.8	7.6	27.4	5.3	1.0	4.4	0.7	3.8	0.8	2.7	0.4	2.4	0.4	26.0	1.01
HM15-13A	31.6	60.9	7.1	26.3	5.4	1.0	4.1	0.6	3.8	0.8	2.6	0.4	2.2	0.4	27.1	0.98
HM15-13B	32.2	64.5	7.4	27.3	5.3	1.0	4.2	0.7	3.8	0.8	2.6	0.4	2.2	0.4	24.6	1.01
HM15-14A	34.3	69.0	8.2	29.4	5.7	1.0	4.8	0.7	4.2	0.9	2.6	0.4	2.5	0.4	25.7	0.99
HM15-14B	34.0	67.7	7.8	29.5	5.5	1.1	4.7	0.7	4.2	0.9	2.6	0.4	2.4	0.4	20.9	1.00
HM15-15A	25.8	49.2	6.1	21.5	5.7	1.1	3.5	0.6	3.1	0.6	2.8	0.4	1.9	0.4	27.9	0.95
HM15-15B	36.4	71.1	8.4	30.8	5.7	1.1	4.9	0.7	4.4	0.9	2.7	0.4	2.5	0.4	27.7	0.98
HM15-16A	33.4	67.8	8.0	29.4	5.4	1.0	4.7	0.7	4.3	0.8	2.5	0.4	2.3	0.4	25.4	1.00
HM15-16B	34.9	69.4	8.2	29.8	5.6	1.1	4.7	0.7	4.4	0.9	2.6	0.4	2.4	0.4	24.8	0.99
HM15-17A	31.3	63.3	7.5	27.9	5.4	1.0	4.3	0.7	4.1	0.8	2.6	0.4	2.3	0.4	26.1	1.00
HM15-17B	31.1	63.4	7.3	27.5	5.3	1.0	4.6	0.7	4.0	0.8	2.5	0.4	2.2	0.4	24.3	1.02
HM15-18A	37.6	71.2	8.5	30.5	6.1	1.2	5.2	0.8	4.4	0.9	2.8	0.4	2.7	0.4	25.6	0.96
HM15-18B	33.7	67.1	7.9	29.1	5.7	1.1	4.8	0.8	4.3	0.9	2.7	0.4	2.5	0.4	27.2	0.99
HM15-20A	28.4	55.3	6.8	24.4	5.5	1.1	4.6	0.7	4.1	0.8	2.5	0.4	2.2	0.4	24.9	0.96
HM15-20B	27.1	55.7	6.5	24.6	5.3	1.0	4.1	0.6	3.9	0.8	2.5	0.4	2.2	0.4	23.8	1.01
HM15-21A	28.3	55.9	6.6	23.8	4.9	1.0	4.2	0.6	3.7	0.8	2.4	0.4	2.3	0.4	19.5	0.99
HM15-21B	23.3	47.3	5.4	20.5	4.3	0.9	3.8	0.6	3.7	0.8	2.3	0.4	2.3	0.4	23.2	1.02
Chandpur Formation, Lesser Himalaya																
HM15-01A	28.8	64.5	8.5	33.6	6.5	1.0	3.9	0.4	1.5	0.2	0.5	0.1	0.5	0.1	4.1	0.99
HM15-01B	47.5	102.0	12.3	47.0	8.6	1.3	5.0	0.5	2.0	0.3	0.8	0.1	0.7	0.1	6.2	1.02
HM15-01C	51.1	110.5	13.0	49.2	9.2	1.6	6.2	0.7	3.2	0.5	1.5	0.2	1.3	0.2	13.6	1.03
HM15-02A	18.8	42.4	5.2	18.9	3.2	0.6	2.1	0.2	1.1	0.2	0.5	0.1	0.5	0.1	3.8	1.03
HM15-02B	35.6	75.3	9.3	37.1	7.4	1.2	4.2	0.4	1.8	0.3	0.7	0.1	0.7	0.1	5.5	1.00
HM15-02C	36.1	75.2	9.8	36.5	6.6	1.1	3.9	0.4	1.5	0.2	0.5	0.1	0.5	0.1	3.6	0.96
HM15-03A	22.3	45.3	5.4	20.4	3.5	0.6	2.3	0.3	1.7	0.3	0.9	0.1	1.0	0.1	8.3	1.00
HM15-03B	41.8	81.3	9.3	33.8	6.0	1.1	4.9	0.8	4.4	0.9	2.6	0.4	2.5	0.4	24.9	0.99
HM15-03C	9.6	20.1	2.1	6.7	1.0	0.2	0.7	0.1	0.8	0.2	0.8	0.2	1.1	0.2	18.5	1.07

[#]A, B, and C stand for different powdering aliquots of the shale sample.

Table A4.3. Results from Principal Component Analysis (PCA) of the geochemical data for the black shales from the Tal Formation.

Elements		PC 1	PC 2	PC 3	PC 4	PC 5	PC 6
	Eigen Value	6.5	4.9	3.8	3.6	1.5	1.1
	Cumulative Variance (%)	25.9	45.7	60.8	75.3	81.2	85.8
	Possible sources	Organic Matter	Sulfide reduction	Carbonates	Clastic supply	Macronutrient	Carbonate-rich clasts
TN		0.68	0.20	−0.43	−0.07	0.16	−0.15
TIC		0.03	−0.30	0.66	0.00	0.32	0.49
TOC		0.44	−0.29	−0.32	−0.48	0.31	−0.24
P		−0.01	0.20	0.40	0.71	−0.17	−0.22
S		−0.30	0.71	−0.28	0.02	−0.28	0.33
Al		0.75	0.41	−0.34	0.01	−0.15	0.14
Si		−0.05	−0.05	0.28	0.62	0.61	0.12
Ti		0.28	0.30	−0.01	0.80	0.34	0.10
Na		−0.69	0.45	−0.25	−0.10	0.18	0.21
K		0.68	0.34	−0.03	0.55	0.12	−0.04
Fe_T		0.20	0.65	−0.26	0.60	−0.03	0.17
Mn		0.65	−0.16	−0.27	0.05	−0.32	0.12
Ca		−0.14	−0.38	0.78	0.28	−0.17	0.00
Mg		0.30	0.39	0.32	0.58	−0.38	−0.29
V		0.58	0.54	0.36	−0.42	0.11	0.03
Cr		0.53	−0.59	−0.37	0.07	0.00	0.18
Co		0.37	0.67	0.43	−0.41	−0.12	0.06
Ni		0.69	−0.03	0.46	−0.32	0.31	−0.06
Cu		0.24	0.81	0.15	−0.42	−0.06	0.17
Zn		0.73	−0.01	0.40	−0.12	−0.05	−0.29
Mo		0.82	0.16	−0.22	−0.03	0.13	0.2
Th		0.56	−0.58	−0.16	0.11	−0.22	0.36
U		0.87	−0.43	0.05	0.09	−0.02	−0.07
Sr		0.10	0.09	0.88	−0.29	−0.17	0.23
Ba		0.20	−0.74	0.04	0.18	−0.33	0.26

A5.1. Nitrogen isotopic Model details

The modelling approach considers two primary oceanic nitrogen reservoirs (Fig. A5.1). The first reservoir N_{fix_amm} consists of organic nitrogen of diazotrophic organisms (N_{fixers}) and ammonium formed by OM remineralization. The second reservoir N_{assm_nit} is comprised of organic nitrogen from the nitrate-assimilating organisms ($N_{assimilators}$) and nitrate. Nitrogen fixation (F_{fix}) contributes to the bulk of the nitrogen flux to the N_{fix_amm} with subordinate contributions from rivers (F_{river}) and atmospheric deposition (F_{depo}). Remineralization of organic matter and its nitrification supplies nitrate to the N_{assm_nit}. Output fluxes from the N_{assm_nit} are through denitrification and *anammox* reactions in the water column (F_{wcd}) and sediments (F_{sd}). A small portion of both the fixers (F_{fixer_burial}) and assimilators ($F_{assimilator\_burial}$) gets buried in the sediments.

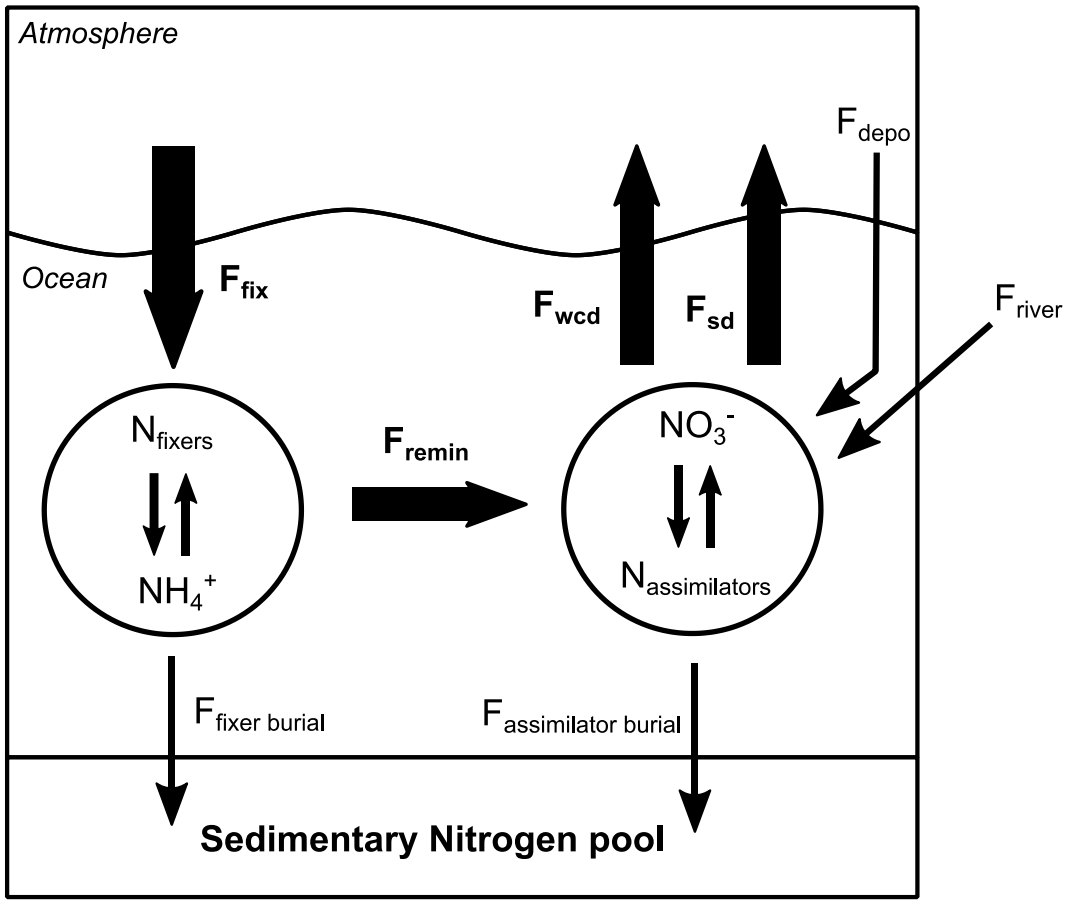

Figure A5.1. *Box model framework of the marine nitrogen cycle (after Kipp et al., 2018).*

Under steady-state conditions, the input and output fluxes of both these reservoirs may be considered to be in balance and can be described by the following isotopic mass balance equations:

$$F_{fix} \times \left(\delta^{15}N_{atm} + \varepsilon_{fix}\right) = F_{remin} \times \delta^{15}N_{fix\_amm} + F_{fixer\_burial} \times \delta^{15}N_{fix\_amm} \quad \text{(A5.1)}$$

$$F_{remin} \times \delta^{15}N_{fix\_amm} = F_{wcd} \times \left(\delta^{15}N_{assm\_nit} + \varepsilon_{wcd}\right) + F_{sd} \times \left(\delta^{15}N_{assm\_nit} + \varepsilon_{sd}\right) - F_{assimilator\_burial} \times \delta^{15}N_{assm\_nit} + F_{river} \times \delta^{15}N_{river} + F_{depo} \times \delta^{15}N_{depo} \quad \text{(A5.2)}$$

For the modern ocean, the flux of sedimentary denitrification processes (F_{sd}) is considered to be ~2.4 times higher than the water column denitrification (F_{wcd}; Brandes and Devol, 2002; DeVries et al., 2012; Devol, 2015). We also consider that the net isotopic effect associated with burial (ε_{burial}) and remineralization-nitrification ($\varepsilon_{remineralization/nitrification}$) processes were negligible (~0‰; Kipp et al., 2018).

By combining the burial fluxes from the two major reservoirs, the nitrogen isotopic composition of the sediments is calculated as:

$$\delta^{15}N_{sed} = \frac{\delta^{15}N_{fixer\_burial} \times F_{fixer\_burial} + \delta^{15}N_{assimilator\_burial} \times F_{assimilator\_burial}}{F_{fixer\_burial} + F_{assimilator\_burial}} \quad \text{(A5.3)}$$

Equations A5.1 to A5.3 are solved using the *SymPy* package in Python. A Monte Carlo simulation approach (n = 10,000 iterations) was used to include the ranges of isotopic effects ($\varepsilon = \delta^{15}N_{product} - \delta^{15}N_{reactant}$) associated with fixation (ε_{fix} = −2‰ to +1‰; Zhang et al., 2014), sedimentary denitrification/*annamox* (ε_{sd} = −3‰ to 0‰; Kessler et al., 2014; Rooze and Meile, 2016) and water column denitrification (ε_{wcd} = −30‰ to −22‰; Devol, 2015). Under modern-day parametrization (Table A5.1), the model simulations yield $\delta^{15}N$ values between +2.8‰ to +8.1‰ with an average of +5.5 ± 1.0‰ (Fig. A5.2). This average value overlaps with the range of modern marine sediments (mode 5–6‰ with a standard deviation of ±2.5‰; Tesdal et al., 2013) and is comparable to the previous studies utilizing this approach (+2.6‰ to +7.3‰ (Kipp et al., 2018) and +2.7‰ to +6.9‰ (Kang et al., 2023)).

The model was then modified to include the effect of changing water-column anoxia on the sedimentary nitrogen isotopic compositions (after Kipp et al., 2018). For this, the denitrification terms were expanded as:

$$F_{sd} + F_{wcd} = (V_{pore} + k_{sd}) + (V_{anoxic\_suboxic} + k_{wcd}) \quad \text{(A5.4)}$$

Here, V_{pore} and $V_{anoxic\_suboxic}$ are the volumes of the sedimentary pore water (LaRowe et al., 2017) and water column environments (suboxic-to-anoxic cores of oxygen-minimum zones in the modern ocean; Keeling et al., 2009) where denitrification proceeds. k_{sd} and k_{wcd} are the volumetric flux constants associated with each of these environments (Table A5.1; Kipp et al., 2018). To simulate the changing water-column redox conditions, V_{pore} was assumed to be a fixed value while $V_{anoxic\_suboxic}$ was set to vary. As described by Kipp et al. (2018), we consider increasing anoxia in the top 1 km of the oceans defined as:

$$f_{an\_sub}\ (\%) = \frac{V_{anoxic\_suboxic}}{V_{\text{modern\_ocean\_1km}}} \times 100 \quad \text{(A5.5)}$$

where $V_{modern\_ocean\_1km}$ is the volume of the upper 1 km of the modern ocean (2.4×10^8 km^3; Proud et al., 2017) denoting the average depth of present-day oxygen minimum zones (Paulmier and Ruiz-Pino, 2009; Kipp et al., 2018), and the term f_{an_sub} provides the percentage of the upper 1 km ocean that is anoxic. The burial flux from the N_{assm_nit} reservoir ($F_{assimilator\_burial}$), which is the contribution of eukaryotic biomass into the sediments, was set to vary as a function of water column anoxia and changing rates of denitrification as:

$$F_{assimilator\_burial} \propto \frac{1}{F_{sd} + F_{wcd}} \quad \text{(A5.6)}$$

Further, we calculate the proportion of $F_{assimilator\_burial}$ to the total organic matter, which provides the contribution of nitrate burial to the sedimentary pool as:

$$f_{assimilator} = \frac{F_{assimilator\_burial}}{F_{total\_burial}} \quad \text{(A5.7)}$$

The model outputs show a non-linear relationship of $\delta^{15}N_{sed}$ with both f_{an_sub} and $f_{assimilators}$, with f_{an_sub} ~ 0.3% and a corresponding $f_{assimilator}$ of ~0.63 for the present-day oceans. The highest $\delta^{15}N_{sed}$ values are obtained during intermediate f_{an_sub} values. A highly oxygenated ocean (very low f_{an_sub}) will lead to limited nitrate loss and associated isotopic effects, resulting in $\delta^{15}N_{sed}$ values close to 0‰. Similarly, a largely reducing ocean with surface ocean anoxia (high f_{an_sub}) and high rates of nitrate loss will lead to increased input of N_2-fixers to the marine and sedimentary nitrogen pool, reducing the $\delta^{15}N_{sed}$ values again.

Previous studies have shown that the inclusion of the riverine (F_{river}) and atmospheric deposition fluxes (F_{depo}) to these marine reservoirs impart minimal effect on the model-derived sedimentary $\delta^{15}N$ values (Kipp et al., 2018; Kang et al., 2023). Similarly, the difference in body size between prokaryotes and eukaryotes complicates their mineralization potential and induces differences in burial efficiencies. Following Kang et al. (2023), the burial efficiencies of the eukaryotes were considered to be higher by a factor of 2 than that of the prokaryotes, although their sensitivity analysis suggests that values up to 5 times can still reproduce modern-day ranges. We recognize that all these assumptions introduce uncertainties, but this approach still offers a first-order understanding of nitrogen dynamics in these basins (Kipp et al., 2018; Kang et al., 2023).

Table A5.1. Model parameters used for the box model calculations

Parameter	Value	Unit	References
F_{fix}	205	Tg N yr^{-1}	Algeo et al., 2014
F_{depo}	15	Tg N yr^{-1}	Algeo et al., 2014
F_{river}	25	Tg N yr^{-1}	Algeo et al., 2014
$F_{total\ burial}$	25	Tg N yr^{-1}	Algeo et al., 2014
$\delta^{15}N_{air}$	0	‰	Zhang et al., 2014
$\delta^{15}N_{river}$	6.4	‰	Algeo et al., 2014
$\delta^{15}N_{depo}$	−4	‰	Algeo et al., 2014
ε_{fix}	−2 to +1	‰	Zhang et al., 2014
ε_{wcd}	−30 to −22	‰	Devol, 2015
ε_{sd}	−3 to 0	‰	Kessler et al., 2014; Rooze and Meile, 2016
ε_{burial}	0	‰	Robinson et al., 2012
$\varepsilon_{remineralization/nitrification}$	0	‰	Robinson et al., 2012
V_{pore}	8.46×10^{7}	km^3	LaRowe et al., 2017
$V_{anoxic\_suboxic}$	4.61×10^{5}	km^3	Keeling et al., 2009
V_{1km_ocean}	2.40×10^{8}	km^3	Proud et al., 2017
k_{sd}	1.84×10^{-6}	Tg km^{-3} yr^{-1}	*Calculated*
k_{wcd}	1.40×10^{-4}	Tg km^{-3} yr^{-1}	*Calculated*

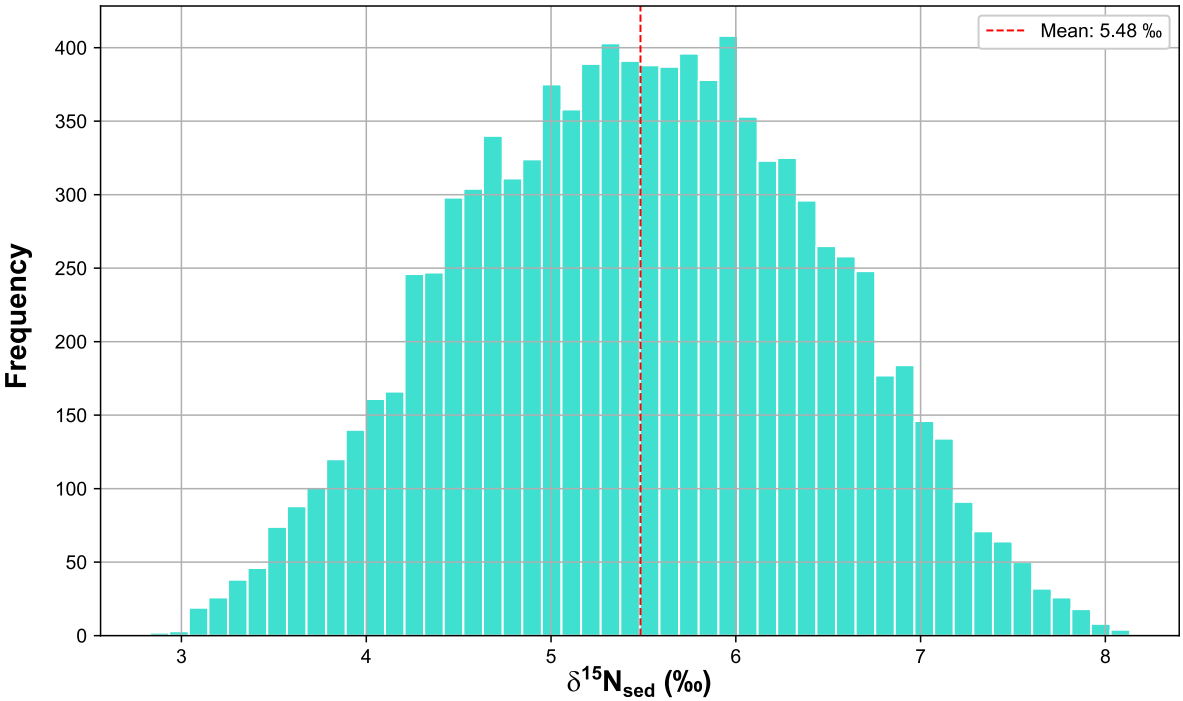

Figure A5.2. *Frequency distribution showing the results of the Monte Carlo simulation under modern-day parametrization. The red dashed line depicts the average value of this population.*

List of Publications

1. **Venugopal, A.**, Tripathy, G.R., Goswami, V., Ghosh, S.K. and Singh, D., 2023. Oceanic Redox State During the Early Cambrian: Insights From Mo-S Isotopes and Geochemistry of Himalayan Shales. *Geochemistry, Geophysics, Geosystems*, *24*(12), p.e2023GC011182. https://doi.org/10.1029/2023GC011182

2. **Venugopal, A.**, Tripathy, G.R., Goswami, V., Khan, T. and Ackerman, L., Unravelling the extent of ocean euxinia during the late Paleoproterozoic: Constraints from Re−Os and Mo isotopes. (*under review*)

Manuscripts in Preparation

1. **Venugopal, A.,** Tripathy, G.R., Goswami, V. and Singh, B.P., Proterozoic Nitrogen cycling in the shelf environments: An isotopic and modelling perspective from organic-rich shales

Conference Abstracts

1. **Venugopal, A.,** Tripathy, G.R., Goswami, V. and Khan, T., 2024, April. Tracking the Mesoproterozoic Ocean anoxia: Inferences from Mo isotopic study of black shales from Cuddapah Basin, India. *In EGU General Assembly Conference Abstracts (p. 14361).*

2. **Venugopal, A.,** Tripathy, G.R. and Khan, T., 2023, December. Stable isotopic ($\delta^{15}N$ and $\delta^{34}S$) evidence for Mesoproterozoic ocean redox state: A study of organic-rich shales from the Cuddapah Basin, India. *In AGU Fall Meeting Abstracts (Vol. 2023, No. 1517, pp. PP31F-1517).*

3. **Venugopal, A.,** Tripathy, G.R., and Ghosh, S.K., 2023, February. Oceanic redox state and sulfate concentration during the early Cambrian period: A sulfur isotopic study of Himalayan shales. *In Frontiers in Geoscience Research Conference (FGRC) 2023.*

4. **Venugopal, A.,** Rout, R.K. and Tripathy, G.R., 2023, January. Carrier phases of Rare Earth elements in Archean Banded Iron Formation from Singhbhum Craton, India. *In Geology: Emerging Methods and Applications (GEMS) 2023.*